UNIVERSITY OF THESSALY
SCHOOL OF ENGINEERING
DEPARTMENT OF MECHANICAL ENGINEERING

GASEOUS TRANSPORT PHENOMENA IN RAREFIED CONDITIONS VIA DETERMINISTIC AND STOCHASTIC METHODS WITH APPLICATIONS IN VACUUM AND FUSION ENGINEERING

Nikos Vasileiadis

Diploma in Mechanical Engineering, University of Thessaly, 2016

M.Sc. in Mechanical Engineering, University of Thessaly, 2017

Submitted in partial fulfillment of the requirements for the degree of Doctor of Philosophy in Mechanical Engineering at the University of Thessaly

Volos, 2021

Certified by the members of the Dissertation Committee:

1^{st} member (Supervisor)	Prof. Dimitris Valougeorgis Professor in the Department of Mechanical Engineering University of Thessaly
2^{nd} member	Prof. Nikos Pelekasis Professor in the Department of Mechanical Engineering University of Thessaly
3^{rd} member	Prof. Vasilis Bontozoglou Professor in the Department of Mechanical Engineering University of Thessaly
4^{th} member	Prof. Kostas Papadimitriou Professor in the Department of Mechanical Engineering University of Thessaly
5^{th} member	Prof. Theodoros Karakasidis Professor in the Department of Physics University of Thessaly
6^{th} member	Prof. Ioannis Kominis Assistant Professor in the School of Applied Mathematical and Physical Sciences National Technical University of Athens
7^{th} member	Prof. Livio Gibelli Lecturer in the Department of Mechanical Engineering University of Edinburgh

Dedicated to my family

Acknowledgements

First and foremost, I would like to express my sincere gratitude to my supervisor Prof. Dimitris Valougeorgis for his continuous guidance and support of my research. He has been an inspirational and motivational, as well as, an understanding and patient mentor throughout our collaboration for my Ph.D. study.

I would also like to express my gratitude to the rest of the thesis committee: Prof. Nikos Pelekasis, Prof. Vasilis Bontozoglou, Prof. Kostas Papadimitriou, Prof. Theodoris Karakasidis, Prof. Giannis Kominis and Prof. Livio Gibelli, for dedicating their time to review my thesis and provide useful and insightful comments.

Besides the thesis committee, I would like to thank all my friends and colleagues at the Laboratory of Transport Phenomena and Process Equipment. Firstly, I would like to offer my special gratitude to Serafeim Misdanitis for collaborating to advance his rarefied gas network solver ARIADNE. In addition, I would like to thank Dr. Sarantis Pantazis for providing me the opportunity to work in extension of his general 3D DSMC solver PROGRESS. I would also like to express my gratitude to Dr. Steryios Naris, Dr. Christos Tantos and Dr. John Lihnaropoulos for sharing their knowledge with me. Special thanks to Dr. Giorgos Tatsios, Dr. Alexandros Tsimpoukis, Dr. Guillermo Lopez-Quesada, Alireza Sharifi and Thanasis Basdanis for all the stimulating discussions and great times we had during our collaboration.

I am eternally grateful to my parents, Giannis and Eleni and to my brother Neoklis for their continuous support and motivation. Finally, I would like to express my special thanks to my friends both in Volos and Thessaloniki for their support and for the fun times we had.

This work has been carried out within the framework of the EUROfusion Consortium and has received funding from the Euratom research and training programme 2014-2018 and 2019-2020 under grant agreement No 633053. The computational work has been performed in the CINECA HPC facility MARCONI and the GRNET HPC facility ARIS.

GASEOUS TRANSPORT PHENOMENA IN RAREFIED CONDITIONS VIA DETERMINISTIC AND STOCHASTIC METHODS WITH APPLICATIONS IN VACUUM AND FUSION ENGINEERING

Nikos Vasileiadis
University of Thessaly, April 2021
Supervisor: Professor D. Valougeorgis

In the last decades technology is increasingly moving towards micro- and nano-scale, developing smaller devices. In addition, vacuum systems and aerosol flows play a critical role in the semiconductor and microelectromechanical systems (MEMS) industry, as well as in some of the most significant large scale scientific and technological achievements, such as particle accelerators and fusion reactors. Consequently, the theoretical and computational investigation of gaseous transport phenomena in rarefied conditions is increasingly attracting considerable attention. These phenomena are far from local equilibrium and the classical Navier-Stokes-Fourier equations are not applicable, since the gas does not behave as a continuum medium. In this case, the molecular nature of gases must be taken into consideration and kinetic modeling, as described by the Boltzmann equation (BE), is required.

In the present work, sophisticated deterministic and stochastic kinetic modeling software tools are developed on the basis of the well-established Discrete Velocity Method (DVM) and the Direct Simulation Monte Carlo (DSMC) method, respectively. These software tools are validated in several benchmarks and implemented to tackle a number of diverse subjects related to gaseous transport phenomena under rarefied conditions.

As already mentioned, the basis of kinetic theory is the Boltzmann equation. However, its computational solution is associated with a formidable computational effort and thus, it is usually circumvented by solving suitable kinetic models that replace the exact Boltzmann collision operator with simplified expressions. Here, the linearized Boltzmann equation for the hard-sphere intermolecular potential is numerically solved for the first time at the Laboratory of Transport Phenomena and Process Equipment. The computational solution of the Boltzmann equation is validated by computing the heat conductivity and dynamic viscosity for a hard-sphere gas, as well as by solving the planar fully-developed Poiseuille and thermal creep rarefied gas flows. In all benchmark cases an excellent agreement has been observed with results presented in the literature. Then, the linearized Boltzmann equation is implemented to simulate

the planar fully-developed rarefied gas flow due to a harmonically oscillating pressure gradient in the whole range of gas rarefaction and oscillation frequency. In this type of flows, kinetic models have been widely used and thus, the solution of the Boltzmann equation is considered necessary to validate them. The Poiseuille coefficient, which is related to the mass flow rate and the macroscopic velocity distribution are provided. The Boltzmann equation results are in very good agreement with the ones provided by the Bhatnagar, Gross and Krook (BGK) model justifying the use of kinetic models for simulating pressure-driven oscillatory rarefied gas flows. In addition, the obtained results properly recover the analytical slip solution and the steady-state solution in the corresponding flow regimes. The Poiseuille coefficient and velocity distribution are said to be in phase with the pressure gradient for low oscillation frequencies. However, as the oscillation frequency is increased the macroscopic quantities always lag the pressure gradient and decrease in amplitude. The Poiseuille coefficient shows a non-monotonic trend with respect to the gas rarefaction and a local maximum may be observed for some intermediate value of the gas rarefaction parameter depending on the oscillation frequency. At very high frequencies, a plug-flow mode in the channel center and a velocity overshoot near the two plates is observed based on the Boltzmann equation. This behavior has been well-established in the viscous regime and has been recently also observed in rarefied conditions based on the BGK model.

Gas flows coupled with gas injection and suction through permeable surfaces are considered as fundamental problems in the viscous regime and have been extensively investigated due to their important role in many technological applications, such as filtration systems, membrane gas permeators, detritiation systems and biological applications. However, these flows have not been studied under rarefied conditions and thus, there is both theoretical and technological interest for their investigation. In the present work, the fully-developed pressure and temperature driven rarefied gas flow between two parallel permeable plates with gas injection and suction through the bottom and top plate, respectively, is investigated. In addition, the fully-developed rarefied gas flow over a permeable plate with downward suction is studied. In the former flow configuration, the Shakhov (S) kinetic model equation and the Boltzmann equation are implemented, while for the latter one the S kinetic model is employed. In the case of the permeable channel flow, the full-range acceleration scheme is implemented for the S model, which is far superior to the non accelerated one in terms of computational effort for large values of the rarefaction parameter. Furthermore, the Poiseuille, mechanocaloric, thermal creep and reduced heat flux coefficients, which are related to

the mass and heat flow rates due to the pressure and temperature gradients are provided. In addition, the macroscopic velocity, heat flux and shear stress distributions are presented. Moreover, the Onsager-Casimir reciprocity relation for the mechanocaloric and thermal creep coefficients is proven theoretically for an arbitrary injection velocity and is used to validate the numerical accuracy of the obtained results. The Boltzmann and S equation results for the kinetic coefficients show a great agreement, justifying the use of kinetic models for the simulation of rarefied gas flows coupled with gas injection or suction through permeable surfaces. In addition, the kinetic results properly recover the analytical solutions provided in the free-molecular and slip regimes. Regarding the behavior of the kinetic coefficients, the Poiseuille coefficient is monotonically decreased when the injection velocity is increased and tends to a constant value at the hydrodynamic regime. Moreover, as the injection velocity is increased, the well-known Knudsen minimum vanishes. The rest of the kinetic coefficients, are also decreased as the injection velocity is increased and for high injection velocity values the mechanocaloric and thermal creep coefficients change sign. This peculiar behavior is also confirmed by the asymptotic solution in the free-molecular regime. In the case of the flow over a permeable plate, the boundary layer thickness, as well as, the macroscopic velocity, shear stress and heat flux distributions are presented. In addition, the analytical solutions in the slip and hydrodynamic regimes are also provided for comparison purposes. The boundary layer thickness is inversely proportional to the suction velocity as predicted by the analytical solutions in the slip and hydrodynamic regimes. Furthermore, an excellent agreement between the kinetic, slip and hydrodynamic results is observed outside of the boundary layer, while inside the boundary layer only the kinetic results are considered accurate.

Some of the most significant scientific and technological achievements depend on the smooth operation of vast vacuum systems. At the Laboratory of Transport Phenomena and Process Equipment, the ARIADNE code has been developed by S. Misdanitis by integrating a kinetic database containing the mass flow rates through tubes computed via the BGK and Ellipsoidal-Statistical (ES) kinetic models in a typical gas network solver. In the present work, the ARIADNE code for simulating steady-state rarefied gas networks in the whole range of the Knudsen number, is advanced and is then implemented in a time-dependent hybrid algorithm to simulate the transient response of gas distribution systems. The developed codes are validated based on a gas expansion apparatus developed by Physikalische-Technische Bundesanstalt and a benchmark network operating in the free-molecular regime. The obtained results are in excellent

agreement in the first benchmark with results reported in the literature and in the second benchmark with the well-established Test Particle Monte Carlo (TPMC) code Molflow+. In addition, the ARIADNE code is used to demonstrate the implementation of the Monte Carlo (MC) uncertainty propagation analysis method to vacuum systems. The aforementioned second benchmark network is assumed to operate under steady-state conditions and the uncertainty of the pumped throughput with respect to the pipe radius, pipe length, vessel pressure and pump pumping speed uncertainties is computed in the whole range of gas rarefaction. The capabilities of the aforementioned developed gas network codes are then demonstrated by simulating the ITER primary pumping system during the burn and dwell phases under steady-state and time-dependent conditions, respectively. In the burn phase, several operating scenarios are investigated and both qualitative and quantitative results, including the gas flow paths through the divertor, as well as, the pumped and backflow throughputs, are presented. The pumped throughput depends almost linearly on the number of operating cryopumps, while both the pumped and backflow throughputs are increased as the average torus pressure is increased. Regarding the envisaged cyclic pumping/regeneration mode, the total pumped throughput is almost equal in all possible pump setups and the individual pump throughputs are well balanced. In the dwell phase, several operating scenarios are investigated and the temporal evolution of the torus pressure is presented. In addition, an analytical solution for the case of constant torus effective pumping speed is provided. A parametric study of the torus pressure at the end of the dwell phase shows that it is independent of the initial torus pressure and linearly depends on the initial outgassing rate. This behavior is also validated based on the aforementioned analytical solution. Moreover, the torus pressure at the end of the dwell phase is almost linearly dependent on the number of operating pumps. Furthermore, the torus pressure at the end of the dwell phase is below the required pressure in a wide range of the torus temperature and initial outgassing, for the highest outgassing decay index value. However, the required pressure is only marginally achieved when all six available cryopumps are utilized for the lowest outgassing decay index value.

Aerosol flows under rarefied conditions have attracted considerable attention in the last decades due to their importance in several applications in the semiconductor and MEMS industry, as well as due to their tentative importance in fusion technology. Here, the general 3D DSMC solver PROGRESS, which has been developed by Dr. S. Pantazis at the Laboratory of Transport Phenomena and Process Equipment, is appropriately modified in order to simulate the transport of solid particles in a

rarefied gas. In addition, several advancements, including the implementation of the Variable Soft Sphere (VSS) intermolecular potential, are made. The capabilities of the developed code are demonstrated and validated based on three benchmark cases, including thermophoresis, as well as translational and rotational Brownian motion. The thermophoresis benchmark considers a rigid spherical particle suspended in a rarefied gas between two parallel plates kept at slightly different temperatures. The heat flux between the two plates and the thermophoretic force experienced by the solid particle due to the imposed temperature gradient are presented in terms of the gas rarefaction from the free-molecular up to the slip regime. In addition, approximate closed form expressions for the heat flux and the thermophoretic force found in the literature are presented and a new simple expression for the thermophoretic parameter, which tends to the correct analytical values in the free-molecular and viscous regimes, is formulated. An excellent agreement is observed between the obtained results and the ones reported in the literature, while the presented approximate expressions can provide the heat flux and thermophoretic force with an accuracy of about 10%. In the translational and rotational Brownian motion benchmarks the random translational movement or rotation, respectively, of a spherical particle suspended in a free-molecular gas is studied. The translational displacement and velocity distributions, as well as the rotational ones are presented. In addition, the translational and rotational diffusion coefficients derived from the aforementioned displacement distributions are presented with respect to the spherical particle radius. In all cases, the obtained results are found to be in excellent agreement with the analytical ones.

In the present work, certain advancements in kinetic modeling are made and sophisticated software tools are developed to model and simulate several diverse gaseous transport phenomena in rarefied conditions. It is hoped, that this effort will prove to be useful, at some extend, to the scientific rarefied gas community and support the design and optimization of applications, devices and systems in vacuum engineering and fusion technology.

ΦΑΙΝΟΜΕΝΑ ΜΕΤΑΦΟΡΑΣ ΑΕΡΙΩΝ ΣΕ ΑΡΑΙΟΠΟΙΗΜΕΝΕΣ ΣΥΝΘΗΚΕΣ ΜΕΣΩ ΝΤΕΤΕΡΜΙΝΙΣΤΙΚΩΝ ΚΑΙ ΣΤΟΧΑΣΤΙΚΩΝ ΜΕΘΟΔΟΛΟΓΙΩΝ ΜΕ ΕΦΑΡΜΟΓΕΣ ΣΤΗΝ ΤΕΧΝΟΛΟΓΙΑ ΚΕΝΟΥ ΚΑΙ ΣΥΝΤΗΞΗΣ

Νίκος Βασιλειάδης
Πανεπιστήμιο Θεσσαλίας, Απρίλιος 2021
Επιβλέπων: Καθηγητής Δ. Βαλουγεώργης

Τις τελευταίες δεκαετίες η τεχνολογία μεταβαίνει όλο και περισσότερο στην μίκρο- και νάνο-κλίμακα, δημιουργώντας συνεχώς μικρότερες διατάξεις και συσκευές. Επιπλέον, τα συστήματα κενού και οι ροές αεροζόλ παίζουν κρίσιμο ρόλο στην βιομηχανία ημιαγωγών και μικροηλεκτρομηχανικών συστημάτων (MEMS) αλλά και σε κάποια από τα πιο σημαντικά επιστημονικά και τεχνολογικά επιτεύγματα μεγάλης κλίμακας, όπως οι επιταχυντές σωματιδίων και οι αντιδραστήρες πυρηνικής σύντηξης. Συνεπώς, η θεωρητική και υπολογιστική μελέτη φαινομένων μεταφοράς αραιοποιημένων αερίων αποκτά όλο και περισσότερη προσοχή. Τα συγκεκριμένα φαινόμενα βρίσκονται εκτός τοπικής θερμοδυναμικής ισορροπίας και οι κλασσικές εξισώσεις Navier-Stokes-Fourier δεν είναι πλέον εφαρμόσιμες, καθώς το αέριο δεν συμπεριφέρεται ως συνεχές μέσο. Σε αυτήν την περίπτωση, η μοριακή φύση των αερίων πρέπει να ληφθεί υπόψη και η χρήση κινητικής θεωρίας, όπως αυτή περιγράφεται από την εξίσωση Boltzmann (BE), είναι αναγκαία.

Στην παρούσα εργασία, αναπτύσσονται εξελιγμένα εργαλεία λογισμικού κινητικής μοντελοποίησης βασισμένα στην ντετερμινιστική μέθοδο διακριτών ταχυτήτων (DVM) καθώς και στην στοχαστική μέθοδο απευθείας μοντελοποίησης Monte Carlo (DSMC). Τα ανεπτυγμένα εργαλεία λογισμικού πιστοποιούνται και χρησιμοποιούνται για την μελέτη διαφόρων φαινομένων μεταφοράς αερίων υπό αραιοποιημένες συνθήκες.

Όπως προαναφέρθηκε, η εξίσωση Boltzmann καθιστά την βάση της κινητικής θεωρίας των αερίων. Ωστόσο, η υπολογιστική της λύση συνδέεται με ένα αυξημένο υπολογιστικό κόστος και συνήθως παρακάμπτεται μέσω της επίλυσης κατάλληλων κινητικών μοντέλων που αντικαθιστούν τον ακριβή όρο ενδομοριακών συγκρούσεων της εξίσωσης Boltzmann με απλουστευμένες εκφράσεις. Στα πλαίσια της διατριβής, η γραμμικοποιημένη εξίσωση Boltzmann με ενδομοριακό δυναμικό σκληρών σφαιρών επιλύεται για πρώτη φορά στο Εργαστήριο Φυσικών και Χημικών Διεργασιών. Η σωστή υπολογιστική επίλυση της εξίσωσης Boltzmann επιβεβαιώνεται βάσει του υπολογισμού της θερμικής αγωγιμότητας και του δυναμικού ιξώδους για ένα αέριο σκληρών σφαιρών, καθώς και βάσει της επίλυσης της πλήρους ανεπτυγμένης ροής μεταξύ παράλληλων πλακών λόγω βαθμίδων πίεσης και θερμοκρασίας. Σε όλα τα εξεταζόμενα προβλήματα τα εξαγόμενα αποτελέσματα είναι

σε πλήρη συμφωνία με την βιβλιογραφία. Στην συνέχεια, η εξίσωση Boltzmann χρησιμοποιείται για την μοντελοποίηση της πλήρους ανεπτυγμένης ροής μεταξύ παράλληλων πλακών λόγω αρμονικά ταλαντωτικής βαθμίδας πίεσης. Σε ροές τέτοιου τύπου, έχουν χρησιμοποιηθεί εκτενώς κινητικά μοντέλα, καθιστώντας την επίλυση της εξίσωσης Boltzmann αναγκαία για την πιστοποίηση τους. Παρουσιάζονται η αδιάστατη μαζική παροχή καθώς και η κατανομή της μακροσκοπικής ταχύτητας του αερίου. Τα αποτελέσματα της εξίσωσης Boltzmann είναι σε πολύ καλή συμφωνία με τα αποτελέσματα του κινητικού μοντέλου των Bhatnagar, Gross και Krook (BGK), δικαιολογώντας την χρήση κινητικών μοντέλων σε ταλαντωτικές ροές αερίων. Επιπλέον, τα εξαγόμενα αποτελέσματα επιβεβαιώνονται από τα αναλυτικά αποτελέσματα στην περιοχή ολίσθησης και στην περιοχή σταθερής ροής. Για χαμηλές συχνότητες ταλάντωσης ο συντελεστής Poiseuille και η μακροσκοπική ταχύτητα βρίσκονται σε φάση με την βαθμίδα πίεσης. Ωστόσο, καθώς η συχνότητα ταλάντωσης αυξάνεται η διαφορά φάσης των μακροσκοπικών ποσοτήτων αυξάνεται, ενώ το πλάτος τους μειώνεται. Ο συντελεστής Poiseuille εμφανίζει μια μη μονοτονική συμπεριφορά σε σχέση με την αραιοποίηση του αερίου και ανάλογα την συχνότητα ταλάντωσης είναι πιθανόν να εμφανίσει ένα τοπικό μέγιστο για κάποια ενδιάμεση τιμή της παραμέτρου αραιοποίησης. Σε πολύ υψηλές συχνότητες ταλάντωσης, η εξίσωση Boltzmann δείχνει ότι η ροή στο κέντρο του καναλιού είναι ανιξώδης ενώ η ροή κοντά στα τοιχώματα χαρακτηρίζεται από υψηλή ταχύτητα. Η συγκεκριμένη συμπεριφορά είναι ευρέως γνωστή στην υδροδυναμική περιοχή ενώ έχει παρατηρηθεί πρόσφατα σε αραιοποιημένες συνθήκες βάσει του μοντέλου BGK .

Οι ροές αερίων οι οποίες περιλαμβάνουν την έγχυση ή αναρρόφηση αερίου μέσω πεπρατών επιφανειών θεωρούνται ως βασικά προβλήματα στην υδροδυναμική περιοχή και έχουν μελετηθεί εκτενώς λόγω της χρησιμότητας τους σε διάφορες τεχνολογικές εφαρμογές όπως συστήματα φίλτρων, διαπερατές μεμβράνες αερίου, συστήματα απαγωγής τριτίου και βιολογικές εφαρμογές. Ωστόσο, οι συγκεκριμένες ροές δεν έχουν ερευνηθεί υπό αραιοποιημένες συνθήκες και άρα η μελέτη τους έχει θεωρητικό και πρακτικό ενδιαφέρον. Στην παρούσα εργασία μελετάται η πλήρως ανεπτυγμένη ροή μεταξύ δύο παράλληλων διαπερατών πλακών λόγω βαθμίδων πίεσης και θερμοκρασίας, με έγχυση και αναρρόφηση αερίου από την κάτω και πάνω πλακά, αντίστοιχα. Επίσης, μελετάται η πλήρως ανεπτυγμένη ροή πάνω από μία διαπερατή πλάκα που αναρροφά αέριο. Στην πρώτη ροή χρησιμοποιούνται το κινητικό μοντέλο Shakhov (S) καθώς και η εξίσωση Boltzmann ενώ στην δεύτερη ροή γίνεται χρήση μόνο του κινητικού μοντέλου S. Στην ροή μέσω διαπερατού καναλιού εφαρμόζεται το αριθμητικό σχήμα επιτάχυνσης για το κινητικό μοντέλο S το οποίο είναι αρκετά γρηγορότερο από το σχήμα χωρίς επιτάχυνση

για μεγάλες τιμές της παραμέτρου αραιοποίησης. Στην εν λόγω ροή, παρουσιάζονται οι αδιάστατες ολικές μαζικές παροχές και θερμορροές λόγω βαθμίδας πίεσης και θερμοκρασίας. Επίσης, παρουσιάζονται οι κατανομές της μακροσκοπικής ταχύτητας, θερμορροής και διατμητικής τάσης. Επιπλέον, η σχέση Onsager-Casimir για την ισότητα της μαζικής παροχής λόγω βαθμίδας θερμοκρασίας και της θερμορροής λόγω βαθμίδας πίεσης αποδεικνύεται θεωρητικά για οποιαδήποτε τιμή της ταχύτητας έγχυσης και χρησιμοποιείται για την επιβεβαίωση των αριθμητικών αποτελεσμάτων. Τα αποτελέσματα της εξίσωσης Boltzmann και του κινητικού μοντέλου S για τις αδιάστατες παροχές βρίσκονται σε πολύ καλή συμφωνία, δικαιολογώντας την χρήση κινητικών μοντέλων σε ροές αερίων που περιλαμβάνουν έγχυση ή αναρρόφηση μέσω διαπερατών επιφανειών. Επίσης, τα παραπάνω αποτελέσματα επιβεβαιώνονται από τις αναλυτικές λύσεις στην ελεύθερη μοριακή περιοχή και στην περιοχή ολίσθησης. Η μαζική παροχή λόγω βαθμίδας πίεσης μειώνεται μονοτονικά καθώς η ταχύτητα έγχυσης αυξάνεται και τείνει να γίνει σταθερή στο υδροδυναμικό όριο. Επιπλέον, το γνωστό ελάχιστο που παρατηρείται στην μαζική παροχή (ελάχιστο Knudsen) εξαφανίζεται καθώς η ταχύτητα έγχυσης αυξάνεται. Η μαζική παροχή λόγω βαθμίδας θερμοκρασίας καθώς και οι θερμορροές λόγω βαθμίδας πίεσης ή θερμοκρασίας μειώνονται καθώς η ταχύτητα έγχυσης αυξάνεται. Για αρκετά μεγάλες τιμές της ταχύτητας έγχυσης η μαζική παροχή και η θερμορροή λόγω βαθμίδας θερμοκρασίας και πίεσης, αντίστοιχα, αλλάζουν κατεύθυνση. Η συγκεκριμένη συμπεριφορά επιβεβαιώνεται από την ασυμπτωτική λύση στην ελεύθερη μοριακή περιοχή. Στην ροή πάνω από διαπερατή πλάκα, παρουσιάζονται το πάχος του οριακού στρώματος καθώς και οι κατανομές της μακροσκοπικής ταχύτητας, θερμορροής και διατμητικής τάσης. Επίσης, παρουσιάζονται συγκριτικά οι αναλυτικές λύσεις στην περιοχή ολίσθησης και στην υδροδυναμική περιοχή. Το πάχος του οριακού στρώματος είναι αντιστρόφως ανάλογο της ταχύτητας αναρρόφησης, όπως προβλέπεται από τις αναλυτικές λύσεις. Επιπλέον, εκτός του οριακού στρώματος υπάρχει άριστη συμφωνία μεταξύ των κινητικών και αναλυτικών αποτελεσμάτων, ενώ εντός του οριακού στρώματος μόνο τα κινητικά αποτελέσματα θεωρούνται ακριβή.

Όπως αναφέρθηκε κάποια από τα πιο σημαντικά επιστημονικά και τεχνολογικά επιτεύγματα βασίζονται στην ομαλή λειτουργία τεράστιων συστημάτων κενού. Στο Εργαστήριο Φυσικών και Χημικών Διεργασιών, ο κώδικας ARIADNE έχει αναπτυχθεί από τον Σ. Μισδανίτη κάνοντας χρήση μιας κινητικής βάσης δεδομένων, η οποία περιέχει τις μαζικές παροχές δια μέσω αγωγών υπολογισμένες βάσει των κινητικών μοντέλων BGK και Ellipsoidal-Statistical (ES), σε έναν τυπικό επιλύτη δικτύων αερίου. Στην εν λόγω εργασία, ο κώδικας ARIADNE για την μοντελοποίηση δικτύων αερίου σταθερών συνθηκών σε όλο το εύρος αραιοποίησης, εξελίσσεται περαιτέρω και χρησιμοποιείται σε

έναν υβριδικό κώδικα για την μοντελοποίηση δικτύων αερίου τα οποία λειτουργούν υπό χρονομεταβαλλόμενες συνθήκες. Οι ανεπτυγμένοι κώδικες πιστοποιούνται με βάση την διάταξη διαστολής αερίου σε κενό που έχει κατασκευαστεί στη Physikalische-Technische Bundesanstalt και με βάση ένα δίκτυο αερίου το οποίο λειτουργεί στην ελεύθερη μοριακή περιοχή. Τα εξαγόμενα αποτελέσματα με βάση τους ανεπτυγμένους κώδικες βρίσκονται σε άριστη συμφωνία με την βιβλιογραφία στο πρώτο δίκτυο και με τον κώδικα Test Particle Monte Carlo (TPMC) Molflow+ στο δεύτερο δίκτυο. Επιπλέον, ο κώδικας ARIADNE χρησιμοποιείται για την εφαρμογή της μεθόδου ανάλυσης αβεβαιοτήτων Monte Carlo (MC) σε συστήματα κενού. Το προαναφερθέν δεύτερο δίκτυο θεωρείται ότι λειτουργεί υπό σταθερές συνθήκες και υπολογίζεται η αβεβαιότητα της αντλούμενης παροχής σε σχέση με την αβεβαιότητα της ακτίνας των σωλήνων, του μήκους των σωλήνων, της πίεσης των δοχείων και της ταχύτητας άντλησης της αντλίας σε ολόκληρο το εύρος αραιοποίησης. Στη συνέχεια, οι δυνατότητες των προαναφερθέντων κωδίκων προβάλλονται προσομοιώνοντας το βασικό σύστημα άντλησης του αντιδραστήρα σύντηξης ITER κατά τις φάσεις καύσης και εκκένωσης, υπό χρονικά σταθερές και μεταβαλλόμενες συνθήκες, αντίστοιχα. Για την φάση εκκένωσης μελετώνται διαφορετικά σενάρια λειτουργίας και παρουσιάζονται ποιοτικά και ποσοτικά αποτελέσματα για την ροή του αερίου δια μέσου του συστήματος άντλησης, για την αντλούμενη μαζική παροχή αλλά και για την μαζική παροχή που επιστρέφει στον τόρο. Η αντλούμενη μαζική παροχή εξαρτάται σχεδόν γραμμικά από τον αριθμό αντλιών που βρίσκονται σε λειτουργία, ενώ η αντλούμενη παροχή και η παροχή που επιστρέφει στον τόρο αυξάνονται καθώς αυξάνεται η μέση πίεση του τόρου. Όσο αφορά τον κυκλικό τρόπο λειτουργίας των αντλιών που έχει προταθεί, η ολική αντλούμενη μαζική παροχή είναι σχεδόν ίση σε όλα τα πιθανά σενάρια λειτουργίας και ισομοιρασμένη στις αντλίες που βρίσκονται σε λειτουργία. Για την φάση εκκένωσης μελετώνται επίσης διάφορα σενάρια λειτουργίας και παρουσιάζεται η χρονική εξέλιξη της πίεσης του τόρου. Επιπλέον, παρουσιάζεται η αναλυτική λύση για την χρονική εξέλιξη της πίεσης του τόρου στην περίπτωση που η ταχύτητα άντλησης του τόρου είναι σταθερή. Η παραμετρική ανάλυση της τελικής πίεσης του τόρου μετά το πέρας της φάσης εκκένωσης δείχνει ότι η τελική πίεση είναι ανεξάρτητη της αρχικής πίεσης του τόρου και εξαρτάται γραμμικά από τον αρχικό ρυθμό εκρόφησης. Τα συγκεκριμένα αποτελέσματα επιβεβαιώνονται από την προαναφερθείσα αναλυτική λύση. Επίσης, η τελική πίεση του τόρου εξαρτάται σχεδόν γραμμικά από τον αριθμό αντλιών που λειτουργούν. Επιπλέον, η τελική πίεση του τόρου βρίσκεται κάτω από την επιθυμητή σε ένα μεγάλο εύρος της θερμοκρασίας και του αρχικού ρυθμού εκρόφησης του τόρου για την μεγαλύτερη τιμή του συντελεστή απόσβεσης της εκρόφησης. Αντίθετα, όταν ο συντελεστής απόσβεσης

παίρνει την μικρότερη τιμή του, η επιθυμητή τελική πίεση μπορεί να επιτευχθεί οριακά μόνο στην περίπτωση που λειτουργούν και οι έξι διαθέσιμες κρυογενικές αντλίες.

Οι ροές αεροζόλ υπό αραιοποιημένες συνθήκες έχουν αποκτήσει σημαντική προσοχή τις τελευταίες δεκαετίες λόγω της σημαντικότητας τους σε μία πληθώρα εφαρμογών στην βιομηχανία ημιαγωγών και MEMS, καθώς και λόγω της πιθανής εφαρμογής τους στην τεχνολογία πυρηνικής σύντηξης. Στην παρούσα εργασία ο γενικός τριδιάστατος κώδικας DSMC PROGRESS, που έχει αναπτυχθεί από τον Δρ. Σ. Πανταζή στο εργαστήριο Φυσικών και Χημικών Διεργασιών τροποποιείται κατάλληλα για την προσομοίωση της μεταφοράς στερεών σωματιδίων δια μέσου ενός αραιοποιημένου αερίου. Επιπλέον, πραγματοποιούνται αρκετές προσθήκες στον κώδικα, συμπεριλαμβανομένης της εφαρμογής του ενδομοριακού δυναμικού μεταβλητά μαλακών σφαιρών (VSS). Οι δυνατότητες του ανεπτυγμένου κώδικα αποδεικνύονται και επιβεβαιώνονται επιλύοντας τρία προβλήματα αναφοράς, που συμπεριλαμβάνουν το πρόβλημα θερμοφόρησης, καθώς και τα προβλήματα μεταφορικής και περιστροφικής κίνησης Brown. Στο πρόβλημα θερμοφόρησης εξετάζεται ένα στερεό σφαιρικό σωματίδιο το οποίο αιωρείται σε ένα αραιοποιημένο αέριο μεταξύ δύο παράλληλων πλακών μικρής θερμοκρασιακής διαφοράς. Η θερμορροή μεταξύ των πλακών καθώς και η θερμοφορητική δύναμη που επιδρά στο σωματίδιο λόγω της βαθμίδας θερμοκρασίας παρουσιάζονται σε σχέση με την αραιοποίηση του αερίου από την ελεύθερη μοριακή περιοχή ως την περιοχή ολίσθησης. Επίσης, παρουσιάζονται προσεγγιστικές εκφράσεις για την θερμορροή και την θερμοφορητική δύναμη που υπάρχουν στην βιβλιογραφία αλλά και προτείνεται μια νέα απλή έκφραση για τον θερμοφορητικό συντελεστή, η οποία τείνει στα σωστά όρια στην ελεύθερη μοριακή και στην υδροδυναμική περιοχή. Τα αποτελέσματα του ανεπτυγμένου κώδικα είναι σε άριστη συμφωνία με την βιβλιογραφία, ενώ οι προαναφερθείσες εκφράσεις μπορούν να προσεγγίσουν την θερμορροή και την δύναμη με μια ακρίβεια της τάξης του 10%. Στο πρόβλημα μεταφορικής και περιστροφικής κίνησης Brown, μελετάται η τυχαία κίνηση ή περιστροφή, αντίστοιχα ενός στερεού σφαιρικού σωματιδίου στην ελεύθερη μοριακή περιοχή. Παρουσιάζονται, οι κατανομές μεταφορικής μετατόπισης και ταχύτητας καθώς και οι αντίστοιχες περιστροφικές. Επιπλέον, παρουσιάζεται ο μεταφορικός και περιστροφικός συντελεστής διάχυσης σε σχέση με την ακτίνα του σωματιδίου, οι οποίοι υπολογίζονται από τις προαναφερθείσες κατανομές μετατόπισης. Σε όλες τις περιπτώσεις τα παρουσιαζόμενα αποτελέσματα είναι σε άριστη συμφωνία με τα αναλυτικά.

Στην παρούσα εργασία, γίνονται ορισμένες καινοτομίες στην κινητική μοντελοποίηση, και αναπτύσσονται εξελιγμένα εργαλεία λογισμικού για την μοντελοποίηση και προσομοίωση διαφορετικών φαινομένων μεταφοράς αερίων υπό αραιοποιημένες συνθήκες. Η

συγκεκριμένη προσπάθεια, δύναται να φανεί χρήσιμη στην επιστημονική κοινότητα δυναμικής αραιοποιημένων αερίων, καθώς και να υποβοηθήσει την σχεδίαση και βελτιστοποίηση εφαρμογών, συσκευών και συστημάτων στην τεχνολογία κενού και σύντηξης.

Contents

List of Tables

List of Figures

Chapter 1

Introduction

1.1 General concepts

Over the years the investigation of rarefied gas flows has attracted significant attention in the scientific community due to their importance in several industrial processes and technological applications. Typical examples of rarefied gas flows include high altitude flows, such as the reentry of orbiting vehicles and satellite propulsion [1, 2]. In addition, gas rarefaction plays a significant role in vacuum systems where the pressure may range from rough vacuum down to ultra-high vacuum. These systems are found in several technological fields and applications, including electrical engineering and semiconductor technologies, medicine and medical engineering, physical and chemical vapor deposition processes, drying and degassing processes, vacuum metallurgy and food packaging [3]. In addition, rarefied gas flows play an integral part in the calibration process of industrial pressure gauges, and secondary pressure standards in the intermediate pressure range, which is usually performed by force-balanced pressure gauges [4, 5]. Moreover, vacuum pumping is a critical aspect of many of the aforementioned applications, and huge effort has been made to model various vacuum pumps [6–8]. Furthermore, the design and optimization of some of the largest vacuum gas pumping systems is critical for the smooth operation of fusion reactor and particle accelerator facilities [9–11]. Rarefied gas flows through permeable media have recently attracted significant attention due to their tentative importance in filtration systems [12], membrane gas permeators [13, 14], detritiation systems [15, 16] and biological applications [17, 18]. Furthermore, aerosol flows in rarefied gases are found in clean room technology, semiconductor wafer and microelectromechanical systems

(MEMS) protection [19–21], as well as in fusion reactor facilities for reactor plasma and tritiated dust control [22–25].

In the aforementioned applications gaseous transport phenomena occur at low pressures, where intermolecular collisions rarely occur, or in miniaturized systems, where the characteristic flow lengths are very small. In such systems, the gas mean free path i.e. the average distance travelled by the gas molecules between collisions is comparable to a characteristic length of the flow and the gas is said to be far from local equilibrium. In addition, non-equilibrium gas transport phenomena also occur in flows characterized by steep gradients of macroscopic quantities, such as, in Knudsen layers and shock waves. Under these conditions, the continuum medium assumption fails, the Navier-Stokes-Fourier equations collapse and the molecular nature of the gas must be taken into consideration. Consequently, the implementation of kinetic theory, as described by the Boltzmann equation, is required.

The solution of the exact Boltzmann equation is a formidable task even with today's computational power and parallelization techniques. Thus, both deterministic and stochastic methods have been proposed to circumvent the solution of the exact Boltzmann equation. In the deterministic approach, suitable kinetic models that replace the complex Boltzmann collision operator with simplified expressions have been proposed [26–28]. The Discrete Velocity Method (DVM) [29], is widely used to solve these kinetic models, applying discretization procedures in the physical, molecular velocity and time spaces. In the stochastic approach the Direct Simulation Monte Carlo (DSMC) method has been proposed [30]. In the DSMC method, the motion and collision of gas particles are decoupled over each discrete time step and simulator particles, that represent a large number of real gas molecules, are implemented to emulate the physics of the Boltzmann equation.

The present dissertation is focused on the development of sophisticated deterministic and stochastic kinetic modeling software tools, as well as, on their implementation to simulate several diverse subjects related to gaseous transport phenomena under rarefied conditions.

1.2 Dissertation structure and contents

The present dissertation tackles a number of diverse topics related to non-equillibrium gas transport phenomena. These topics include the computational solution of novel rarefied gas flow configurations, as well as, the development and implementation of novel

and advanced kinetic codes. Following Chapters 1 and 2, where a brief introduction in the field of rarefied gas dynamics and a review of the relative literature are presented, respectively, the investigated topics are covered in Chapters 3-7, while in Chapter 8 the dissertation is concluded. In Chapters 3-7, where each of the investigated topics are presented, there is some repetition, mainly related to the formulation of each problem, which is considered to be necessary for completeness and clarity. The detailed structure of the dissertation is as follows:

In **Chapter 2**, a review of the relative theoretical background is presented. First the flow regimes with respect to the rarefaction parameter are presented. The Boltzmann equation, kinetic models and boundary conditions, as well as the implemented numerical methods are reviewed. Next, a brief review of rarefied flows through capillaries and gas distribution systems is provided. Then, the relative literature on aerosol flows under rarefied conditions is surveyed.

In **Chapter 3**, the linearized Boltzmann equation based on the hard-sphere intermolecular potential is computationally solved. The integration of the exact linearized Boltzmann collision operator is validated based on the computation of the heat conductivity and viscosity coefficients. The solution of the exact Boltzmann equation is validated based on the planar fully-developed Poiseuille and thermal creep rarefied gas flow. Then, the linearized Boltzmann equation is implemented to simulate the oscillatory planar fully-developed Poiseuille rarefied gas flow. The BGK kinetic model is also implemented and is compared to the Boltzmann equation.

In **Chapter 4**, novel rarefied gas flow configurations with gas injection and suction through permeable surfaces, are investigated. The fully-developed Poiseuille and thermal creep flow between two parallel permeable plates with gas injection and suction at the bottom and top plate, respectively, is investigated based on the S kinetic model and the Boltzmann equation. In addition, the fully-developed flow over a permeable plate with downward suction is investigated based on the S model.

In **Chapter 5**, the developed codes for simulating steady-state and time-dependent gas distribution systems of arbitrary size are presented. A brief overview of the geometrical and operational data in a gas network is provided. The developed steady-state gas network code ARIADNE and the hybrid time-dependent gas network code are described in detail. Then, the hybrid time-dependent code, which implements the ARIADNE code in each time step is validated based on two benchmark gas networks. Next, the MC uncertainty propagation analysis method is implemented in a

gas distribution network operating under steady-state conditions to obtain the pumped throughput uncertainty with respect to the uncertainty of the input quantities.

In **Chapter 6**, the developed network codes are implemented to simulate the rarefied neutral gas flow in the ITER primary pumping system during the burn and dwell phases. The simulation of the ITER primary pumping system is based on a gas network model, which consists of thousands of piping elements that approximates the actual gas flow path though the divertor. The most important quantities from the engineering point of view, namely the pumped and backflow throughputs in the burn phase, as well as, the final torus pressure in the dwell phase are presented.

In **Chapter 7**, the developed 3D aerosol code, which is based on the DSMC method, is presented. First, the developed code structure is described in detail and then, the code is validated via three benchmark cases. The first benchmark focuses on the thermophoretic force exerted on a solid particle suspended in a rarefied gas between two parallel infinite plates kept at unequal temperatures. The two remaining benchmarks focus on the translational and rotational Brownian motion of a solid particle suspended in a rarefied gas in the free-molecular regime.

In **Chapter 8**, the dissertation is concluded by providing a brief overview of Chapters 3-7 along with the main findings and achievements. In addition, tentative extensions of the present work in the future are proposed.

1.3 Novelty and scientific contributions

As mentioned in Section 1.2 the present dissertation includes the computational solution of novel rarefied gas flow configurations, as well as, the development and implementation of advanced kinetic codes. The most significant findings and novelties of the present Ph.D. thesis may be outlined as follows:

- Computational solution of the linearized Boltzmann equation based on the hard-sphere molecules for the planar fully-developed rarefied gas flow due to a harmonically oscillating pressure gradient.

- Novel investigation of the fully-developed Poiseuille and thermal creep rarefied gas flow between parallel permeable plates with gas injection and suction from the bottom and top plate in the whole range of gas rarefaction based on the linearized Boltzmann equation and the S kinetic model.

Section 1.3

- Proof of the Onsager-Casimir reciprocity relation for the mechanocaloric effect and thermal creep coefficients in the fully-developed Poiseuille and thermal creep rarefied gas flow through a permeable channel for arbitrary values of the gas injection/suction velocity.
- Derivation of analytical and asymptotic solutions in the free-molecular regime for the fully-developed Poiseuille and thermal creep rarefied gas flow through a permeable channel.
- Novel investigation of the fully-developed rarefied gas flow over a permeable plate with downward suction based on the S kinetic model.
- Implementation of a robust loop and pseudoloop extraction algorithm to a steady-state kinetic modeling code for simulating gas distribution systems of arbitrary size in the whole range of the Knudsen number.
- Advancement of the aforementioned steady-state code to simulate gas distribution systems with an arbitrary number of pumps.
- Development of a time-dependent kinetic modeling code for simulating the transient response of gas distribution systems of arbitrary size in the whole range of the Knudsen number.
- Demonstration of the MC uncertainty propagation analysis method for a gas distribution system operating under steady-state conditions in the whole range of the Knudsen number.
- Implementation of the developed gas network codes to model, simulate and provide useful insight for the ITER primary pumping system during the burn and dwell phases.
- Development of an advanced 3D aerosol code, based on the stochastic DSMC method, capable of simulating the transport of solid spherical particles through a rarefied gas in complex geometries.
- Validation of the developed 3D aerosol code on the basis of thermophoresis between two parallel plates, as well as, translational and rotational Brownian motion.

Chapter 2

Literature review

2.1 The Knudsen number and flow regimes

Rarefied or non-equilibrium gas flows are mainly characterized by the Knudsen number introduced by Knudsen [31], defined as

$$Kn = \frac{\lambda}{L}, \tag{2.1}$$

where λ is the mean free path, which is defined as the mean distance travelled by a gas particle between successive collisions, while L is a characteristic length of the flow or a length scale of a macroscopic quantity φ given by $L = \varphi / (\partial\varphi/\partial x)$. The mean free path for a monoatomic hard-sphere gas is written as [32]

$$\lambda = \frac{1}{\sqrt{2}\pi d^2 n}, \tag{2.2}$$

where d is the molecular diameter and n is the gas number density. The Knudsen number may also be written with respect to the Mach number Ma and Reynolds number Re as

$$Kn = \sqrt{\frac{\pi\gamma}{2}}\frac{Ma}{Re}, \tag{2.3}$$

with γ denoting the specific heat ratio of the gas. Instead of the Knudsen number, the gas rarefaction parameter, which is inversely proportional to the equivalent mean free path [33], is frequently used in the literature to characterize the level of gas rarefaction:

$$\delta = \frac{PL}{\mu v_0} \sim \frac{1}{Kn} \tag{2.4}$$

The quantity μ denotes the gas dynamic viscosity at temperature T and $v_0 = \sqrt{2R_gT}$ is the most probable molecular speed, with $R_g = k_B/m$ denoting the specific gas constant (k_B is the Boltzmann constant and m is the molecular mass).

The following flow regimes may be identified in terms of the Knudsen number or the gas rarefaction [34]:

1. $Kn \leq 10^{-3}$ ($\delta \geq 10^3$): The gas is in the hydrodynamic or viscous regime. The gas may be considered as continuum medium and typical CFD modeling may be implemented.

2. $10^{-3} < Kn \leq 10^{-1}$ ($10 \leq \delta < 10^3$): The gas is in slip regime. The gas may still be considered as continuum medium in the bulk of the flow and typical CFD modeling along with the appropriate velocity slip and temperature jump boundary conditions may be implemented.

3. $10^{-1} < Kn \leq 10$ ($0.1 \leq \delta < 10$): The gas is in the transition regime. The typical CFD approaches fail and the molecular nature of the gas must be taken into account. The use of kinetic theory, as described by the Boltzmann equation, is required.

4. $Kn > 10$ ($\delta < 0.1$): The gas is in the free-molecular regime. Intermolecular collisions are very rare and kinetic theory, omitting intermolecular interaction, may be implemented.

It is worthwhile to mention that, the aforementioned flow regime limits are indicative and only provide an estimation of the actual gas rarefaction. It is also noted that, in contrast to CFD modeling, kinetic theory is valid in the whole range of the Knudsen number, such as that the Navier-Stokes, Burnett and super Burnett equations may be derived from the Boltzmann equation. However, due to the higher computational cost, kinetic modeling is usually implemented in the free-molecular, transition and early slip regimes, while in the late slip and hydrodynamic regimes typical CFD modeling is preferred.

2.2 Boltzmann equation, kinetic models and boundary conditions

In 1859 Maxwell [35] introduced the idea that all gas molecules move at different speeds and introduced the statistical approach to gaseous mediums. Then, in 1860 [36]

he also introduced the concept of the distribution function $f(t, \boldsymbol{r}, \boldsymbol{\xi})$, which is defined as the probability that a gas molecule is around position $\boldsymbol{r}$ with a molecular velocity around $\boldsymbol{\xi}$ at time t. Maxwell then proceeded to derive the distribution function that describes a gas in equilibrium and his findings were corrected by Boltzmann a few years later. The Maxwell-Boltzmann distribution (usually called Maxwell or Maxwellian distribution) is a Gaussian distribution with respect to the local gas macroscopic quantities

$$f^M(t, \boldsymbol{r}, \boldsymbol{\xi}) = n(t, \boldsymbol{r}) \left[\frac{m}{2\pi k_B T(t, \boldsymbol{r})}\right]^{3/2} \exp\left\{-\frac{m[\boldsymbol{\xi} - \boldsymbol{u}(t, \boldsymbol{r})]^2}{2k_B T(t, \boldsymbol{r})}\right\}, \tag{2.5}$$

where n, T and $\boldsymbol{u}$ are the local gas number density, temperature and macroscopic velocity vector, respectively. In 1870 Boltzmann derived the integro-differential transport equation for the distribution function [37], which bears his name and is written as

$$\frac{\partial f}{\partial t} + \boldsymbol{\xi} \cdot \frac{\partial f}{\partial \boldsymbol{r}} + \boldsymbol{F} \cdot \frac{\partial f}{\partial \boldsymbol{\xi}} = Q(f, f'), \tag{2.6}$$

where $\boldsymbol{F}$ is the acceleration associated with an externally imposed force field and Q is the collision operator given by

$$Q(f, f') = \iiint (f' f'_1 - f f_1) g b db d\varepsilon d\boldsymbol{\xi}_1, \tag{2.7}$$

where, $g = |\boldsymbol{\xi} - \boldsymbol{\xi}_1|$ is the relative collision velocity, b is the impact parameter and ε is the azimuthal angle. The left hand side of the Boltzmann equation describes the streaming motion of the gas molecules along a trajectory, while the right hand side describes the effect of intermolecular collisions taking gas molecules in or out of the streaming trajectory. Inside the collision operator, the first term in the parenthesis is known as the gain term and corresponds to the molecules that obtain a molecular velocity around $\boldsymbol{\xi}$ due to a collision. On the other hand, the second term is known as the loss term and corresponds to the molecules that initially have a molecular velocity around $\boldsymbol{\xi}$ and are scattered to a different molecular velocity after a collision. The derivation of the Boltzmann equation includes two important assumptions [38]. The first is that only binary intermolecular collisions are considered, limiting the implementation of the Boltzmann equation to dilute gases. The second assumption is that of molecular chaos or as called by Boltzmann "Stosszahlansatz", which states that the distribution function f is uncorrelated to the distribution function f_1 and

allows a two-particle distribution to be substituted by the product of two one-particle distributions.

Another significant advancement made by Boltzmann is the introduction of the H-Theorem, which states that the H-function defined as

$$H = \int f \log f d\boldsymbol{\xi}, \tag{2.8}$$

is a non-increasing function of time $dH/dt \leq 0$ [32]. It is noted that, the Maxwellian distribution f^M corresponds to the special equilibrium case $dH/dt = 0$. The H-Theorem is related to the second law of thermodynamics stating the irreversibility of macroscopic processes and the increase of entropy due to intermolecular collisions.

The solution of the Boltzmann equation leads to the distribution function, which provides the position and molecular velocity of the gas molecules with respect to time. The macroscopic quantities are obtained as moments of the distribution function:

- Number density
$$n\left(t, \boldsymbol{r}\right) = \int f d\boldsymbol{\xi} \tag{2.9}$$

- Velocity vector
$$\boldsymbol{u}\left(t, \boldsymbol{r}\right) = \frac{1}{n} \int \boldsymbol{\xi} f d\boldsymbol{\xi} \tag{2.10}$$

- Pressure
$$P\left(t, \boldsymbol{r}\right) = \frac{m}{3} \int \left(\boldsymbol{\xi} - \boldsymbol{u}\right)^2 f d\boldsymbol{\xi} \tag{2.11}$$

- Stress Tensor
$$P_{ij}\left(t, \mathbf{r}\right) = m \int \left(\xi_i - u_i\right)\left(\xi_i - u_i\right) f d\boldsymbol{\xi} \tag{2.12}$$

- Temperature
$$T\left(t, \boldsymbol{r}\right) = \frac{m}{3k_B n} \int \left(\boldsymbol{\xi} - \boldsymbol{u}\right)^2 f d\boldsymbol{\xi} \tag{2.13}$$

- Heat flux vector
$$\boldsymbol{q}\left(t, \boldsymbol{r}\right) = \frac{m}{2} \int \left(\boldsymbol{\xi} - \boldsymbol{u}\right)^2 \left(\boldsymbol{\xi} - \boldsymbol{u}\right) \, f d\boldsymbol{\xi} \tag{2.14}$$

The combination of Eqs. (2.11) and (2.13) yields the ideal gas law

$$P = n k_B T. \tag{2.15}$$

In order to deal with the significant computational effort required for the solution of the Boltzmann equation several kinetic collision models, that replace the Boltzmann

five-fold integral collision operator with simplified expressions, have been proposed. In general, a collision model should satisfy the collision invariants, namely the mass, momentum and energy invariants, while it should also satisfy the H-Theorem and provide the correct values for the transport coefficients.

The first kinetic model for monoatomic gases is the one proposed by Bhatnagar, Gross and Krook (BGK) [26], that has also been independently proposed by Welander [39]. The BGK model replaces the Boltzmann collision integral with the simple expression

$$Q_{BGK} = v\left(f^M - f\right), \tag{2.16}$$

where $v = P/\mu$ is the collision frequency, which is assumed to be independent of the molecular velocity. The BGK model assumes that a particle relaxes to the Maxwellian distribution after a single collision. In addition, it satisfies the collision invariants and the H-Theorem. However, its major drawback is that it cannot provide the correct values for the gas viscosity and thermal conductivity simultaneously (it provides a Prandlt number $\mathrm{Pr} = 1$ instead of the correct one, which is $\mathrm{Pr} = 2/3$). Consequently, it is well-known that it cannot accurately tackle flow configurations where mass and heat transfer phenomena are coupled. Despite these pitfalls, the BGK model has been widely used in the literature due to its simplicity providing accurate results in the whole range of the Knudsen number [40].

The kinetic model proposed by Shakhov (S) [27] is a generalization of the BGK model and replaces the Boltzmann collision term with the simplified expression:

$$Q_S = v\left\{f^M\left[1 + \frac{2m}{5n(k_BT)^2}\left(1-\mathrm{Pr}\right)\boldsymbol{q}\cdot\left(\boldsymbol{\xi}-\boldsymbol{u}\right)\left(\frac{m(\boldsymbol{\xi}-\boldsymbol{u})^2}{2k_BT} - \frac{5}{2}\right)\right] - f\right\} \tag{2.17}$$

The S model satisfies the collision invariants and provides the correct value for the transport coefficients. However, it has been only proven to satisfy the H-Theorem in its linearized form. Although, the H-Theorem has not been proven for the S model it is generally regarded as a reliable model and has been widely used in the literature providing accurate results in the whole range of the Knudsen number for various flow configurations [40].

Another widely used kinetic model is the Ellipsoidal-Statistical (ES) model proposed by Holway [28], which replaces the Boltzmann collision integral with

$$Q_{ES} = v\,\mathrm{Pr}\left\{f^M\left[\frac{n}{\pi^{3/2}}\sqrt{|A|}\exp\left[-\sum_{i,j=1}^{3}\left(\xi_i-u_i\right)\left(\xi_j-u_j\right)A_{ij}\right]\right] - f\right\}, \tag{2.18}$$

where,

$$A_{ij} = \left[\frac{2k_B T \delta_{K,ij}}{m \Pr} - \frac{2\left(1 - \Pr\right) P_{ij}}{nm \Pr} \right]^{-1}, \tag{2.19}$$

with $\delta_{K,ij}$ denoting the Kronecker delta. The ES model satisfies the collision invariants and the H-Theorem and also provides the correct values for the transport coefficients. However, it involves a higher computational cost compared to the BGK and S model equations.

In the present dissertation, monoatomic gas flows are considered, implementing the Boltzmann equation, as well as the BGK, S and ES kinetic model equations. In the literature, in addition to monoatomic kinetic models several kinetic models have been suggested for polyatomic gases [28, 41, 42] and gas mixtures [43–45].

The Boltzmann equation, as well as suitable kinetic model equations must be accompanied by the correct boundary conditions. In kinetic theory the boundary conditions are defined by the gas-surface interaction law through the scattering kernel $R\left(\boldsymbol{\xi}', \boldsymbol{\xi}\right)$. The scattering kernel represents the probability that a gas molecule with incident velocity $\boldsymbol{\xi}'$ is scattered from boundary with outgoing velocity $\boldsymbol{\xi}$. The most extensively used gas-surface interaction law is the diffuse-specular reflection law proposed by Maxwell [36]. In the case of purely diffuse reflection the gas molecules are assumed to be fully accommodated and the outgoing velocity $\boldsymbol{\xi}$ is independent of the incident velocity $\boldsymbol{\xi}'$. The reflected molecules follow a Maxwellian distribution, characterized by the boundary temperature T_w and the scattering kernel is written as

$$R_d\left(\boldsymbol{\xi}', \boldsymbol{\xi}\right) = \frac{\boldsymbol{\xi} \cdot \boldsymbol{n}}{2\pi (R_g T_w)^2} \exp\left[-\frac{\boldsymbol{\xi}^2}{2R_g T_w} \right], \tag{2.20}$$

where $\boldsymbol{n}$ denotes the unit vector normal to the boundary facing towards the flow domain. In the case of purely specular reflection the outgoing velocity $\boldsymbol{\xi}$ depends on the incident velocity $\boldsymbol{\xi}'$. More, specifically, the velocity component normal to the wall is reversed, while the two tangential components remain the same. The specular scattering kernel is written as

$$R_s\left(\boldsymbol{\xi}', \boldsymbol{\xi}\right) = \delta_D\left[\boldsymbol{\xi}' - \boldsymbol{\xi} + 2\left(\boldsymbol{\xi} \cdot \boldsymbol{n}\right) \boldsymbol{n} \right], \tag{2.21}$$

where δ_D denotes the Dirac function. The Maxwell diffuse-specular scattering kernel is obtained by combining the diffuse and specular reflection kernels as

$$R\left(\boldsymbol{\xi}', \boldsymbol{\xi}\right) = a R_d\left(\boldsymbol{\xi}', \boldsymbol{\xi}\right) + \left(1 - a\right) R_s\left(\boldsymbol{\xi}', \boldsymbol{\xi}\right), \tag{2.22}$$

where a is the accommodation coefficient and denotes the fraction of molecules that are reflected diffusively, while the quantity $(1 - a)$ denotes the fraction of molecules that are reflected specularly.

In the present work, the Maxwell diffuse-specular boundary conditions are considered. However, more advanced gas-surface interaction laws have been proposed in the literature. More specifically, the kernel proposed by Epstein [46] is a generalization of the diffuse-specular Maxwell scattering kernel, taking into account the dependence of the accommodation coefficient on the incident molecular velocity. The Cercignani-Lampis scattering kernel [47] and its extensions introduced by Lord [48, 49], sufficiently differ from the Maxwell and Epstein kernels and take into account both normal and tangential accommodation. These more advanced scattering kernels may be applied in specific flow configurations, where a more detailed description of the gas-surface interaction is required.

2.3 Numerical methods

The most extensively used methodologies for the numerical solution of the Boltzmann equation and aforementioned kinetic models are the Discrete Velocity Method (DVM) [29] and the Direct Simulation Monte Carlo (DSMC) method [30]. In the present work, both methods are implemented to tackle novel rarefied gas flows and are integrated into sophisticated codes that may model and simulate several non-equilibrium gaseous transport phenomena.

The DVM is a deterministic method that has been widely used by the scientific community of rarefied gas dynamics to numerically solve the exact Boltzmann equation, as well as kinetic model equations. In DVM the continuum molecular velocity spectrum is replaced by a set of discrete molecular velocities. This discretization leads to a set of ordinary or partial differential equations, with each equation corresponding to a specific discrete molecular velocity. This set of differential equations is usually tackled by implementing a second order finite difference scheme, leading to a system of algebraic equations, which is then solved in an iterative manner, by implementing the so-called marching schemes. The detailed formulation and implementation of the DVM for several prototype rarefied gas flows is provided in [33]. In the present dissertation, the DVM is implemented for the computational solution of the linearized Boltzmann equation, as well as the BGK and S model equations in Chapters 3 and 4.

A well-established drawback of the aforementioned iterative scheme is the slow convergence rate at the slip and hydrodynamic regimes [50, 51]. In order to overcome this pitfall, synthetic acceleration schemes, which couple the kinetic equation with a system of moment equations, have been developed [50]. These moment equations are constructed using full-range orthogonal polynomials and are solved coupled with the kinetic equations for the interior spatial nodes. Full-range synthetic acceleration schemes have been implemented mainly in linearized fully-developed flows. In Chapter 4, the full-range synthetic acceleration scheme is implemented in the S model for the solution of the pressure and temperature driven fully-developed rarefied gas flow between parallel permeable plates with uniform injection/suction in the whole range of the Knudsen number.

The DSMC method has been proposed by Bird [30] as a stochastic or probabilistic approach for solving the Boltzmann equation. In DSMC a large number of simulator particles is used to simulate the behavior of the real gas particles and emulate the physics of the Boltzmann equation. The essential DSMC approximation is the decoupling of the molecular motion and the intermolecular collisions over a small time step. The free motion of simulator particles is performed in a deterministic manner, while the intermolecular collisions are performed in a stochastic one. The simulator particles are indexed in the cells or subcells, that discretize the flow domain so that intermolecular collisions only occur between close neighbours. The macroscopic quantities of interest are taken as averages of the simulator particle properties in each cell. In [52] it has been proven that the DSMC method tends to the solution of the Boltzmann equation as the number of simulator particles approaches infinity. In Chapter 7, a 3D aerosol code is developed, by appropriately modifying the DSMC method in order to simulate the transport of solid particles through a rarefied gas.

2.4 Pressure driven rarefied gas flow through capillaries

The pressure driven rarefied gas flow through a capillary has attracted considerable attention over the years due to its significant role in vacuum systems and equipment, which are widely implemented in several technological applications and industrial processes. In addition, certain pressure driven capillary rarefied gas flows are frequently used as benchmark problems for new numerical methods due to their simplicity [40].

The first investigation of rarefied gas flow through a capillary is attributed to Knudsen, who in 1909, studied the free-molecular gas flow through capillaries of infinite length and arbitrary cross-section [53], as well as the free-molecular flow through an orifice [31]. One year later, Smoluchowski corrected Knudsen's findings for non-circular capillaries and provided a solution for a long rectangular duct [54]. The next significant contribution was made by Clausing who derived and solved via suitable approximations the integral equation for the free-molecular gas transport through a circular capillary of finite length [55]. The accurate evaluation of the Clausing integral equation was provided much later by DeMarcus and Hopper [56], implementing several improved numerical techniques. Clausing's integral equation is not easily extended to capillaries of arbitrary cross-section and thus, Monte Carlo techniques have been developed in order to tackle such flows [57, 58]. A more detailed survey of the free-molecular flow through a capillary is presented in [59].

As computers evolved, the simulation of pressure driven flows through capillaries was extended from the free-molecular to the transition and slip regimes. Some of the earliest works considered the fully-developed pressure driven rarefied gas flow between parallel plates. More specifically, this flow was tackled by the infinite capillary theory, via the BGK and S model equations [60–62], as well as via the Boltzmann equation [63–67]. In addition, the infinite capillary theory has been implemented in capillaries of circular [68–72], rectangular [50, 73, 74], ellipsoidal [75], triangular [72, 76, 77] and trapezoidal [72] cross-sections. The range of infinite capillary theory was later extended from very long capillaries to capillaries of moderate length by considering the effects of the tube inlet and outlet and introducing the appropriate end effect corrections [78, 79]. The investigation of the pressure driven rarefied gas flow through capillaries was then extended to short capillaries, distinguishing between the low and high speed flow case due to small and large pressure difference, respectively. The most significant works concerning the small pressure difference case, include the low speed flow through orifices and short tubes [80, 81]. Regarding the large pressure difference case, the works investigating the high speed flow through orifices [82–86] and short tubes [87–89] are distinguished.

2.5 Vacuum systems

The main purpose of the investigation of pressure driven rarefied gas flows through capillaries is the implementation of the obtained findings to simulate complex vacuum

systems. However, the literature on vacuum system simulation techniques is rather scarce. The so-called electric-hydraulic analogy is frequently used in the free-molecular and viscous limits [59, 90]. In this classical approach, the gas network is replaced by an equivalent electric circuit, where current and voltage correspond to gas flow rate and pressure respectively. Then, the steady-state or the transient response of the equivalent electric circuit may be simulated by typical integrated circuit codes. However, this methodology is valid only when the whole gas pipe network operates either in the free-molecular or viscous regimes. Another more general approach has been elaborated in the ITERVAC code, developed at the Institute of Technical Physics in the Karlsruhe Institute of Technology [91, 92]. Interpolating between available solutions in the free-molecular and viscous regimes reliable semi-empirical expressions to compute the conductance through various pipe elements have been derived and implemented in ITERVAC in order to model gas pumping systems operating under various vacuum conditions. However, ITERVAC is subject to steady-state conditions, as well as to certain theoretical simplifications. Recently, an approach for simulating nanofluidic networks of long and narrow channels via a hybrid molecular-continuum method is presented in [93], based on the multiscale method proposed in [94, 95]. Computational savings are primarily achieved by exploiting length scale separation. Hybrid approaches are promising and must be investigated in multiscale physics problems. Of course, the applicability of these approaches in large vacuum systems is yet to be determined.

At the Laboratory of Transport Phenomena and Process Equipment at the University of Thessaly (UTH), an in-house code has been developed by S. Misdanitis for simulating steady-state gas distribution systems in the whole range of the Knudsen number [96, 97]. This is achieved by integrating a dense kinetic database providing the flow rates through pipe elements of various geometries subject to any pressure difference into a typical gas network solver. The flow rates are computed via kinetic modeling and are considered as very accurate since they are solely based on theoretical principles.

In Chapter 5, several advancements made in the UTH steady-state network code, including the ability to simulate gas pumps with arbitrary characteristic curves is described. In addition, the development of a time-dependent gas network code, which implements the steady-state network code in each time step is described in Chapter 5. The effectiveness of the developed network codes is demonstrated in Chapter 6, where the ITER primary pumping system is simulated during the burn and dwell phases.

2.6 Aerosol flows under rarefied conditions

Over the years aerosol flows have attracted considerable attention in the hydrodynamic regime due to their significant role in a variety of industrial processes, including pneumatic transport, fluidized beds and pollution control [98]. Moreover, in the last decades the interest in simulating aerosol flows under rarefied conditions has been renewed due to their importance in aerosol thermal precipitators, gas cleaning, clean room technologies, semiconductor wafer and MEMS protection from particle contaminant deposition [19–21], as well as in fusion reactor plasma control and tritiated dust safety [22–25].

In the literature, several works regarding the forces exerted on a solid particle suspended in a rarefied gas are found. These works mostly consider the drag and thermophoretic force exerted on a spherical solid particle moving through a gas having a constant temperature gradient. Some of the earliest works investigated the drag and thermophoretic force on a spherical particle either in the free-molecular or slip regime [99–102]. The investigation of drag and thermophoresis was later extended in the whole range of the Knudsen number by implementing the Boltzmann equation for hard-sphere molecules and suitable kinetic models [103–106], as well as the DSMC method [19–21]. Moreover, the effect of the gas-surface interaction law on the drag and thermophoretic force has been recently investigated in [107, 108].

However, literature on simulating the transport of solid particles through a rarefied gas is rather limited. One approach has been presented in [19], where the DSMC method is implemented and the computation of momentum and heat transfer from the incident gas molecules to the solid particle is performed via two Green's functions. This approach is computationally very efficient, as it only introduces few additional computations to the typical DSMC method. However, it is limited to a single particle that is very small compared to the flow length scales. In [109] a more general approach based on the DSMC method for simulating the transport of a solid particle of arbitrary geometry through a rarefied gas has been suggested. In the proposed approach, a two-way coupling between the gas and the solid particle transport is implemented. More specifically, both the solid particle transport and the surrounding gas flow are governed by the solid-gas collisions. This method is computationally more expensive, however it is applicable to any solid particle size and also accurately captures the gas-solid interaction.

In Chapter 7, the latter approach is coupled with an in-house 3D DSMC code, developed by Dr. S. Pantazis at the Laboratory of Transport Phenomena and Process Equipement, in order to simulate the transport of a solid spherical particle through a rarefied gas.

Chapter 3

The linearized Boltzmann equation

3.1 Introduction

In order to accurately simulate rarefied gas flows in the whole range of gas rarefaction the Boltzmann equation [32, 110, 111] must be implemented. However, even with today's computational power the direct numerical solution of the Boltzmann equation is a formidable task. More specifically, the most computationally demanding task is the computation of the Boltzmann equation collision kernel, which describes the variation of the distribution function due to the gas particle collisions. To circumvent this pitfall, kinetic models [26–28] that replace the exact Boltzmann collision operator with simplified expressions have been widely used to tackle a variety of rarefied gas flows. However, since all proposed kinetic models are approximations of the Boltzmann equation they introduce some approximation error. It is evident that, the solution of the Boltzmann equation for some fundamental problems is necessary in order to validate the proposed models and their ability to accurately capture the behavior of the Boltzmann equation. In this work, the linearized Boltzmann equation is tackled for the first time in the Laboratory of Transport Phenomena and Process Equipment. The hard-sphere intermolecular potential is used in all cases, since it simplifies the expression of the collision operator and significantly reduces the involved computational cost [111].

In Section 3.3, the transport coefficients, namely the heat conductivity and viscosity are computed as a benchmark problem. These coefficients have been already computed with great accuracy in the literature in many works [112–115] for the hard-sphere potential. In addition, it is mentioned here that a great advancement in the computation of the transport coefficients has been made in [116], where the Boltzmann collision

integral has been computed for an arbitrary intermolecular potential. The computation of the heat conductivity and viscosity is considered as an important benchmark for the numerical solution of the linearized Boltzmann equation and more specifically, for the validation of the numerical integration performed for the linearized collision operator.

Next, in Section 3.4 the linearized Boltzmann equation is implemented for the simulation of the planar fully-developed Poiseuille and thermal creep rarefied gas flows. These two classical problems are excellent benchmarks and frequently used to validate novel kinetic models and numerical methods [67]. The main results of these problems are the kinetic coefficients, namely the Poiseuille, mechanocaloric, thermal creep and reduced heat flux coefficients. These coefficients have been computed in many works based on the hard–sphere Boltzmann equation [63–66], as well as, based on kinetic models [60–62]. Moreover, a significant addition to the previous works has been the computation of the kinetic coefficients for the planar Poiseuille and thermal creep problems based on the linearized Boltzmann equation by implementing the (6-12) Lennard-Jones intermolecular potential [67]. In order to validate the numerical solution of the linearized Boltzmann equation the kinetic coefficients are computed in a wide range of the rarefaction parameter δ and compared with corresponding linearized BE, BGK and S model results reported in the literature [67].

The BGK kinetic model has been successfully implemented to simulate a variety of oscillatory pressure driven rarefied gas flows [117, 118]. However, although the linearized Boltzmann equation has been used and compared to the BGK model in rarefied gas flows driven by oscillating walls [119], it has never been applied to rarefied gas flows driven by an oscillating pressure gradient. In Section 3.5, the linearized Boltzmann equation is implemented for the investigation of the oscillatory planar fully-developed Poiseuille rarefied gas flow. The Poiseuille coefficient amplitude and phase angle are provided in a wide range of the two parameters characterizing the flow, namely the rarefaction parameter δ and the oscillation parameter θ. The obtained results are compared with the analytical solution in the slip regime, as well as, with the steady-state results provided in Section 3.4 for large values of θ. Moreover, they are compared to corresponding results obtained via the BGK model in order to validate its accuracy in this type of flows. In addition, the amplitude and phase angle, as well as, as the temporal evolution of the macroscopic velocity are provided for indicative values of the gas rarefaction and oscillation frequency.

3.2 Linearization of the Boltzmann equation

In linear kinetic theory, the gas is weakly disturbed from the equilibrium state described by the global Maxwellian distribution function

$$f_0^M(\boldsymbol{\xi}) = \frac{n_0}{\pi^{3/2} v_0^3} \exp\left[-\left(\frac{\boldsymbol{\xi}}{v_0}\right)^2\right], \tag{3.1}$$

where n_0 is the equilibrium number density, $\boldsymbol{\xi}$ is the molecular velocity vector and $v_0 = \sqrt{2R_g T_0}$ is the most probable molecular speed, with $R_g = k_B/m$ denoting the specific gas constant (k_B is the Boltzmann constant and m is the molecular mass) and T_0 being the equilibrium temperature. The non-equilibrium distribution function is then linearized with respect to the global Maxwellian as

$$f\left(\tilde{t}, \tilde{\boldsymbol{r}}, \boldsymbol{\xi}\right) = f_0^M(\boldsymbol{\xi})\left(1 + h\left(\tilde{t}, \tilde{\boldsymbol{r}}, \boldsymbol{\xi}\right) X\right), \quad X \ll 1, \tag{3.2}$$

where $\tilde{t}$ is the independent time variable, $\tilde{\boldsymbol{r}}$ is the spatial velocity vector and X is a small linearization parameter. The linearized Boltzmann equation is then obtained by substituting Eq. (3.2) in the full Boltzmann equation

$$\frac{\partial h\left(\tilde{t}, \tilde{\boldsymbol{r}}, \boldsymbol{\xi}\right)}{\partial \tilde{t}} + \boldsymbol{\xi} \cdot \frac{\partial h\left(\tilde{t}, \tilde{\boldsymbol{r}}, \boldsymbol{\xi}\right)}{\partial \tilde{\boldsymbol{r}}} = \tilde{L}'(h). \tag{3.3}$$

The quantity $\tilde{L}'(h)$ denotes the linearized Boltzmann collision operator, which for a finite total collision cross-section is written as

$$\tilde{L}'(h) = \int f_0^M(\boldsymbol{\xi}) \tilde{K}'(\boldsymbol{\xi}, \boldsymbol{\xi}_1)\, h\left(\tilde{t}, \tilde{\boldsymbol{r}}, \boldsymbol{\xi}_1\right) d\boldsymbol{\xi}_1 - \tilde{K}_0'(\boldsymbol{\xi})\, h\left(\tilde{t}, \tilde{\boldsymbol{r}}, \boldsymbol{\xi}\right), \tag{3.4}$$

where

$$\begin{aligned} \tilde{K}'(\boldsymbol{\xi}, \boldsymbol{\xi}_1) = \tilde{g} \int_0^{2\pi} \int_0^{\pi} \exp\left[-\left(\frac{\tilde{g}}{v_0}\cot(\chi/2)\right)^2 + \frac{2\,|\boldsymbol{\xi} \times \boldsymbol{\xi}_1|}{v_0^2}\cot(\chi/2)\cos\varepsilon\right] \times \\ \left[\tilde{\sigma}\left(\frac{\tilde{g}}{\sin(\chi/2)}, \chi\right) + \tilde{\sigma}\left(\frac{\tilde{g}}{\sin(\chi/2)}, \pi - \chi\right)\right] \frac{\sin\chi}{\sin^4(\chi/2)} d\chi d\varepsilon - \tilde{g}\tilde{\sigma}_t \end{aligned} \tag{3.5}$$

and

$$\tilde{K}_0'(\boldsymbol{\xi}) = \tilde{\sigma}_t \int \tilde{g} f_0^M(\boldsymbol{\xi}_1)\, d\boldsymbol{\xi}_1. \tag{3.6}$$

In this notation, $\tilde{K}_0'(\boldsymbol{\xi})$ is the collision frequency, $\tilde{g} = |\boldsymbol{\xi} - \boldsymbol{\xi}_1|$ is the binary collision relative velocity, χ is the scattering angle and ε is the azimuthal angle. The quantity $d^2\tilde{\sigma}(\tilde{g}, \chi)$ denotes the differential collision cross-section which depends on the intermolecular potential, while $\tilde{\sigma}_t$ denotes the total collision cross-section given by

$$\tilde{\sigma}_t = 2\pi \int_0^{2\pi} \tilde{\sigma}(g, \chi) \sin\chi d\chi. \tag{3.7}$$

Specifically, for a monoatomic gas and the hard-sphere intermolecular potential, which is implemented throughout this chapter, the differential cross-section and the total collision cross-section are analytically given by

$$\tilde{\sigma} = \frac{d^2}{4}, \;\; \tilde{\sigma}_t = \pi d^2, \tag{3.8}$$

where d is the molecular diameter. In addition, the kernel $\tilde{K}'(\boldsymbol{\xi})$ can be integrated analytically to yield the simple closed form expression

$$\tilde{K}'(\boldsymbol{\xi}) = \pi d^2 \tilde{g} \left\{ 2\left(\frac{v_0}{\tilde{g}}\right)^2 \exp\left[\left(\frac{|\boldsymbol{\xi} \times \boldsymbol{\xi}_1|}{v_0 \tilde{g}}\right)^2\right] - 1 \right\}. \tag{3.9}$$

It is noted that, for $\tilde{g} = 0$ (i.e. $\boldsymbol{\xi} = \boldsymbol{\xi}_1$) the linearized Boltzmann collision operator is singular. To overcome this, the collision invariants $\Psi = (1, \boldsymbol{\xi}, \xi^2)$ may be used as described in [116] to rewrite the collision operator as

$$\tilde{L}'(h) = \int f_0^M(\boldsymbol{\xi}) \tilde{K}'(\boldsymbol{\xi}, \boldsymbol{\xi}_1) \left[h\left(\tilde{t}, \tilde{\boldsymbol{r}}, \boldsymbol{\xi}_1\right) - \frac{\Psi(\boldsymbol{\xi}_1)}{\Psi(\boldsymbol{\xi})} h\left(\tilde{t}, \tilde{\boldsymbol{r}}, \boldsymbol{\xi}\right) \right] d\boldsymbol{\xi}_1. \tag{3.10}$$

Since the expression inside the brackets is zero when $\boldsymbol{\xi} = \boldsymbol{\xi}_1$, the corresponding computations can be omitted.

At this point it is convenient to introduce the dimensionless quantities

$$t = \tilde{t}\frac{v_0}{H}, \;\; \boldsymbol{r} = \frac{\tilde{\boldsymbol{r}}}{H}, \;\; \boldsymbol{c} = \frac{\boldsymbol{\xi}}{v_0}, \;\; g = \frac{\tilde{g}}{v_0}, \;\; \sigma = \frac{\tilde{\sigma}}{d^2}, \;\; \sigma_t = \frac{\tilde{\sigma}_t}{d^2}, \tag{3.11}$$

where H is taken to be some reference length of the investigated flow. The dimensionless linearized Boltzmann equation becomes

$$\frac{\partial h(t, \boldsymbol{r}, \boldsymbol{c})}{\partial t} + \boldsymbol{c} \cdot \frac{\partial h(t, \boldsymbol{r}, \boldsymbol{c})}{\partial \boldsymbol{r}} = n_0 H d^2 L'(h), \tag{3.12}$$

with the linearized Boltzmann collision operator written as

$$L'(h) = \frac{1}{\pi^{3/2}} \int K'(\boldsymbol{c}, \boldsymbol{c}_1) \left[h(t, \boldsymbol{r}, \boldsymbol{c}_1) - \frac{\Psi(\boldsymbol{c}_1)}{\Psi(\boldsymbol{c})} h(t, \boldsymbol{r}, \boldsymbol{c}) \right] e^{-\boldsymbol{c}_1^2} d\boldsymbol{c}_1, \tag{3.13}$$

where

$$K'(\boldsymbol{c}, \boldsymbol{c}_1) = \pi g \left\{ \frac{2}{g^2} \exp\left[\left(\frac{|\boldsymbol{c} \times \boldsymbol{c}_1|}{g} \right)^2 \right] - 1 \right\}. \tag{3.14}$$

The formulation of the linearized Boltzmann equation is now properly defined by the Eqs. (3.12)-(3.14). It is reminded here that, the term containing the collision frequency $K_0'(\boldsymbol{c})$, which in the present notation is given by

$$K_0'(\boldsymbol{c}) = \frac{1}{\sqrt{\pi}} \int g e^{-\boldsymbol{c}_1^2} d\boldsymbol{c}_1, \tag{3.15}$$

has been used to rewrite $L'(h)$.

3.3 Test Case I: Transport coefficients

3.3.1 Governing equations and numerical scheme

In this section, the methodology for computing the transport coefficients, namely the heat conductivity and viscosity, based on the linearized Boltzmann equation is described. The heat conductivity $\tilde{\kappa}$ and viscosity $\tilde{\mu}$, according to [32, 110, 120], are calculated as

$$\tilde{\kappa} = \frac{k_B v_0}{\pi^{3/2} d^2} \int A(\boldsymbol{c}) c_x^2 \left(\boldsymbol{c}^2 - \frac{5}{2} \right) e^{-\boldsymbol{c}^2} d\boldsymbol{c}, \tag{3.16}$$

$$\tilde{\mu} = \frac{m v_0}{\pi^{3/2} d^2} \int B(\boldsymbol{c}) c_x^2 c_y^2 e^{-\boldsymbol{c}^2} d\boldsymbol{c}, \tag{3.17}$$

where the functions $A(\boldsymbol{c})$ and $B(\boldsymbol{c})$ satisfy the integral equations

$$L'(A(\boldsymbol{c}) c_x) + c_x \left(\boldsymbol{c}^2 - \frac{5}{2} \right) = 0, \tag{3.18}$$

$$L'(B(\boldsymbol{c}) c_x c_y) + 2 c_x c_y = 0. \tag{3.19}$$

However, since c_x is one of the collision invariants, the function $A(\boldsymbol{c})$ is not completely defined by Eq. (3.18). Assuming that the gas is at rest the additional constraint becomes

$$\int A(\boldsymbol{c}) c_x^2 e^{-\boldsymbol{c}^2} d\boldsymbol{c} = 0. \tag{3.20}$$

At this stage, the required computational effort for the solution of Eqs. (3.18)-(3.20) can be reduced, as described in [121], by introducing cylindrical coordinates, eliminating one of the molecular velocity components

$$c_x = c_x, \quad c_y = c_r \cos\theta, \quad c_z = c_r \sin\theta. \tag{3.21}$$

Substituting Eq. (3.21) in Eq. (3.18) yields

$$L_1 \left(A \left(c_x, c_r \right) c_x \right) + c_x \left(\boldsymbol{c}^2 - \frac{5}{2} \right) = 0. \tag{3.22}$$

Then, substituting Eq. (3.21) and $\Psi = 1$ (mass conservation) the linearized collision operator from Eq. (3.13) is written as

$$\begin{aligned} L_1 \left(h \right) = \frac{1}{\pi^{3/2}} \int_{-\infty}^{+\infty} \int_{0}^{+\infty} K_1 \left(c_x, c_r, c_{1,x}, c_{1,r} \right) \times \\ \left[h \left(c_{1,x}, c_{1,r} \right) - h \left(c_x, c_r \right) \right] c_{1,r} e^{-\left(c_{1,x}^2 + c_{1,r}^2 \right)} dc_{1,r} dc_{1,x}, \end{aligned} \tag{3.23}$$

where

$$K_1 \left(c_x, c_r, c_{1,x}, c_{1,r} \right) = 2 \int_{0}^{\pi} K \left(c_x, c_r, c_{1,x}, c_{1,r}, \beta \right) d\beta, \tag{3.24}$$

with $K \left(c_x, c_r, c_{1,x}, c_{1,r}, \beta \right)$ given by Eq. (3.14) and $\beta = \theta_1 - \theta$. In addition, the constraint (3.20) may be readily deduced:

$$\int_{-\infty}^{+\infty} \int_{0}^{+\infty} A \left(c_x, c_r \right) c_x^2 dc_r dc_x = 0 \tag{3.25}$$

Operating in the same manner on Eq. (3.19), it is reduced to:

$$L_2 \left(B \left(c_x, c_r \right) c_x \right) + 2 c_x c_r = 0 \tag{3.26}$$

Substituting Eq. (3.21) and $\Psi = c_y$ (momentum conservation in y direction) the linearized collision operator from Eq. (3.13) is written as

$$\begin{aligned} L_2 \left(h \right) = \frac{1}{\pi^{3/2}} \int_{-\infty}^{+\infty} \int_{0}^{+\infty} K_2 \left(c_x, c_r, c_{1,x}, c_{1,r} \right) \times \\ \left[h \left(c_{1,x}, c_{1,r} \right) - h \left(c_x, c_r \right) \right] c_{1,r}^2 e^{-\left(c_{1,x}^2 + c_{1,r}^2 \right)} dc_{1,r} dc_{1,x}, \end{aligned} \tag{3.27}$$

where

$$K_2\left(c_x, c_r, c_{1,x}, c_{1,r}\right) = 2\int_0^{\pi} K\left(c_x, c_r, c_{1,x}, c_{1,r}, \beta\right)\cos\beta d\beta. \tag{3.28}$$

Next, it is convenient to present the heat conductivity and viscosity in dimensionless form:

$$\kappa = \frac{\tilde{\kappa}d^2}{k_B v_0} = 2\pi\int_{-\infty}^{+\infty}\int_0^{+\infty} A\left(c_x, c_r\right) c_r c_x^2\left(c_x^2 + c_r^2 - \frac{5}{2}\right) e^{-\left(c_x^2+c_r^2\right)} dc_r dc_x \tag{3.29}$$

$$\mu = \frac{\tilde{\mu}d^2}{m v_0} = \pi\int_{-\infty}^{+\infty}\int_0^{+\infty} B\left(c_x, c_r\right) c_r^3 c_x^2 e^{-\left(c_x^2+c_r^2\right)} dc_r dc_x \tag{3.30}$$

The deterministic numerical solution of Eqs. (3.22) and (3.26) is based on the discrete velocity method. The continuum molecular velocity $c_x \in (-\infty, \infty)$ is split into the negative part $c_x \in (-\infty, 0]$ and the positive part $c_x \in [0, \infty)$. The positive part of c_x is replaced by $Nc_x/2$ discrete velocities, which are taken to be the roots of the half-range Hermite polynomials of degree $Nc_x/2$ [122]. The negative part is also replaced by $Nc_x/2$ discrete velocities, which are taken to be symmetrical to the positive part with respect to the origin. In total, Nc_x discrete molecular velocities are used for the discretization of c_x and each discrete velocity has its own weight Wc_x. In a similar manner, the continuum molecular velocity $c_r \in (0, \infty]$, is replaced by Nc_r discrete velocities, which are taken to be the roots of the half-range Hermite polynomials of degree Nc_r having their own weights Wc_r. In addition, the angle $\beta \in [0, \pi]$ is replaced by N_β discrete angles with weights $W\beta$, The discrete angles are taken to be the roots of the Legendre polynomials of degree N_β and are transformed from $[-1, 1]$ to $[0, \pi]$.

The discretized set of equations for the heat conductivity become

$$\sum_k\sum_m L_{1,ijkm}\left(A_{km}c_{xk} - A_{ij}c_{xi}\right) + c_{xi}\left[c_{xi}^2 + c_{rj}^2 - \frac{5}{2}\right] = 0, \tag{3.31}$$

$$L_{1,ijkm} = \frac{1}{\pi^{3/2}} K_{1,ijkm} c_{rm} e^{-\left(c_{xk}^2 + c_{rm}^2\right)} W c_{xk} W c_{rm}, \tag{3.32}$$

$$K_{1,ijkm} = 2\sum_b K_{ijkmb} W\beta_b, \tag{3.33}$$

where the kernel K_{ijkmb} is given in Eq. (3.14). The discretized form of the additional constraint (3.25) is written as

$$\sum_i \sum_j A_{ij} c_{xi}^2 W c_{xi} W c_{rj} = 0. \tag{3.34}$$

Then, Eq. (3.31) along with the additional constraint (3.34) form a linear system of algebraic equations of rank $Nc_x \times Nc_r$, which is numerically solved by implementing the LU decomposition method with partial pivoting [123]. The dimensionless heat conductivity is then simply calculated as

$$\kappa = \frac{2}{\sqrt{\pi}} \sum_i \sum_j A_{ij} c_{xi}^2 c_{rj} \left(c_{xi}^2 + c_{rj}^2 - \frac{5}{2} \right) e^{-(c_{xi}^2 + c_{rj}^2)} W c_{xi} W c_{rj}. \tag{3.35}$$

The discretized equations for the viscosity are written as

$$\sum_k \sum_m L_{2,ijkm} \left(B_{km} c_{xk} - B_{ij} c_{xi} \right) + 2 c_{xi} c_{rj} = 0, \tag{3.36}$$

$$L_{2,ijkm} = \frac{1}{\pi^{3/2}} K_{2,ijkm} c_{rm}^2 e^{-(c_{xk}^2 + c_{rm}^2)} W c_{xk} W c_{rm}, \tag{3.37}$$

$$K_{2,ijkm} = 2 \sum_b K_{ijkmb} \cos \beta_b W \beta_b. \tag{3.38}$$

The linear system of algebraic equations, which is formed by Eq. (3.36) has also rank $Nc_x \times Nc_r$ and is solved in the same manner. Then, the dimensionless viscosity is calculated as

$$\mu = \frac{1}{\sqrt{\pi}} \sum_i \sum_j B_{ij} c_{xi}^2 c_{rj}^3 e^{-(c_{xi}^2 + c_{rj}^2)} W c_{xi} W c_{rj}. \tag{3.39}$$

3.3.2 Heat conductivity and viscosity

For the hard-sphere potential, the dimensionless heat conductivity and viscosity have been obtained by various methods [112–115] and their reported values are

$$\kappa = 0.479305, \quad \mu = 0.126668. \tag{3.40}$$

In the present work, for the computation of the transport coefficients various grids have been investigated. In all investigated cases, the relation $Nc_x = 2Nc_r$ holds, as it has been found to provide the best results for the transport coefficients. In addition, a total of 100 total discrete angles ($N\beta = 100$) are required to accurately compute

the kernels K_1 and K_2. The optimal grid has been found to be $Nc_x = 2Nc_r = 100$. The computed values for the dimensionless heat conductivity and viscosity with the aforementioned grid have been found to be

$$\kappa = 0.479307, \quad \mu = 0.126668. \tag{3.41}$$

It is evident that, the exact Boltzmann collision operator is computed with great accuracy, providing the heat conductivity and viscosity in excellent agreement with the ones found in the literature. The heat conductivity and viscosity, are equal to the ones reported in the literature, up to five and six significant digits, respectively.

3.4 Test Case II: Planar Poiseuille and thermal creep fully-developed flow

3.4.1 Governing equations and numerical scheme

Consider a monoatomic gas confined between two parallel infinite plates located at $\tilde{y} = \pm H/2$. The gas is driven by a small pressure gradient X_P and a small temperature gradient X_T along the longitudinal $\tilde{x}$ direction

$$X_a = \frac{H}{a}\frac{da}{d\tilde{x}}, \quad a = P, T, \tag{3.42}$$

where P and T are the local pressure and temperature, respectively. Since $X_a \ll 1$ the gas flow may be treated as isothermal and fully-developed [33].

The flow is fully characterized by the rarefaction parameter

$$\delta = \frac{P_0 H}{\tilde{\mu} v_0}, \tag{3.43}$$

where P_0 is the equilibrium pressure, $\tilde{\mu}$ is the gas viscosity at the equilibrium temperature T_0 and $v_0 = \sqrt{2R_g T_0}$ is the most probable molecular speed ($R_g = k_B/m$ is the specific gas constant, with k_B denoting the Boltzmann constant and m the gas molecular mass).

At this point, it is convenient to introduce the dimensionless physical and velocity space variables

$$x = \frac{\tilde{x}}{H}, \quad y = \frac{\tilde{y}}{H}, \quad \boldsymbol{c} = \frac{\boldsymbol{\xi}}{v_0}. \tag{3.44}$$

The total dimensionless macroscopic quantities of interest in the longitudinal direction, namely the velocity and heat flux can be written as a linear superposition of the pressure and temperature driven flow due to the smallness of the driving gradients as follows:

$$u_x\left(y\right)=\frac{\tilde{u}_x\left(\tilde{y}\right)}{v_0}=u_{x,P}\left(y\right)X_P+u_{x,T}\left(y\right)X_T \tag{3.45}$$

$$q_x\left(y\right)=\frac{\tilde{q}_x\left(\tilde{y}\right)}{v_0P_0}=q_{x,P}\left(y\right)X_P+q_{x,T}\left(y\right)X_T \tag{3.46}$$

Here, $\tilde{u}_x$ and $\tilde{q}_x$ are the total velocity and heat flux, respectively. The specific dimensionless macroscopic quantities for the pressure and temperature driven problems in Eqs. (3.45)-(3.46) are given by

$$u_{x,a}\left(y\right)=\frac{\tilde{u}_{x,a}\left(\tilde{y}\right)}{v_0X_a},\quad q_{x,a}\left(y\right)=\frac{\tilde{q}_{x,a}\left(\tilde{y}\right)}{v_0P_0X_a},\quad a=P,T. \tag{3.47}$$

In addition, the mass and heat flow rates can be computed by introducing the dimensionless kinetic coefficients [67]

$$\begin{aligned} G_P&=-2\int\limits_{-1/2}^{1/2}u_{x,P}dy,\quad G_T=2\int\limits_{-1/2}^{1/2}u_{x,T}dy,\\ Q_P&=2\int\limits_{-1/2}^{1/2}q_{x,P}dy,\quad Q_T=-2\int\limits_{-1/2}^{1/2}q_{x,T}dy. \end{aligned} \tag{3.48}$$

In this notation the kinetic coefficients G_P, G_T, Q_P and Q_T are taken to be positive. The quantities G_P and G_T represent the dimensionless flow rate in the pressure and temperature driven cases respectively, while Q_P and Q_T represent the corresponding dimensionless heat flow rates. In the literature G_P is the Poiseuille coefficient, G_T is the thermal creep coefficient, Q_P is the mechanocaloric coefficient and Q_T is the reduced heat flux coefficient. In [124–127] it has been shown, that the cross coefficients G_T and Q_P obey the Onsager-Casimir reciprocity relation $G_T=Q_P$, which has been utilized here to validate the accuracy of the presented results.

The gas is weakly disturbed from its equilibrium state and the unknown distribution function can be linearized as

$$f=f_0^M\left[1+X_P\left(h_P+h_{R,P}\right)+X_T\left(h_T+h_{R,T}\right)\right], \tag{3.49}$$

where h_P and h_T are the unknown so-called perturbed distribution functions, while $h_{R,P}$ and $h_{R,T}$ are the reference perturbations given by

$$h_{R,P} = x, \quad h_{R,T} = x\left(c^2 - \frac{5}{2}\right). \tag{3.50}$$

The steady-state linearized Boltzmann equation for the aforementioned configuration is written in dimensionless form as

$$c_y \frac{\partial h_a(y, \boldsymbol{c})}{\partial y} = 2\mu\delta L'_a(h_a) + s'_a(\boldsymbol{c}), \tag{3.51}$$

where $s'_a(\boldsymbol{c})$ denotes the source term for the pressure and temperature driven flow

$$s'_P(\boldsymbol{c}) = -c_x, \quad s'_T(\boldsymbol{c}) = -c_x\left(\boldsymbol{c}^2 - \frac{5}{2}\right). \tag{3.52}$$

The linearized collision operator $L'_a(h_a)$ reads

$$L'_a(h_a) = \frac{1}{\pi^{3/2}} \int K'(\boldsymbol{c}, \boldsymbol{c}_1) \left[h_a(y, \boldsymbol{c_1}) - \frac{c_{1,y}}{c_y} h_a(y, \boldsymbol{c})\right] e^{-\boldsymbol{c}_1^2} d\boldsymbol{c}_1, \tag{3.53}$$

where $\Psi = c_y$ (momentum conservation in the y direction) has been used and the kernel $K'(\boldsymbol{c}, \boldsymbol{c}_1)$ is given by Eq. (3.14). At the two infinite plates, purely diffuse gas-surface interaction is assumed

$$h_a(-1/2, c_x, c_y > 0, c_z) = 0, \quad h_a(1/2, c_x, c_y < 0, c_z) = 0. \tag{3.54}$$

The macroscopic quantities of interest, namely the velocity and heat flux are given as the moments of the perturbed distribution function

$$u_{x,a}(y) = \frac{1}{\pi^{3/2}} \int c_x h_a(y, \boldsymbol{c})\, e^{-\boldsymbol{c}^2} d\mathbf{c}, \tag{3.55}$$

$$q_{x,a}(y) = \frac{1}{\pi^{3/2}} \int c_x \left(\boldsymbol{c}^2 - \frac{5}{2}\right) h_a(y, \boldsymbol{c})\, e^{-\boldsymbol{c}^2} d\mathbf{c}. \tag{3.56}$$

At this stage, in order to reduce the required computational effort for the solution of Eq. (3.51) the number of molecular velocity components may be reduced, as described in [63], by introducing cylindrical coordinates

$$c_x = c_r \sin\theta, \quad c_y = c_y, \quad c_z = c_r \cos\theta. \tag{3.57}$$

Then, the perturbed distribution function can be written as

$$h_a\left(y, c_x, c_y, c_z\right) = \psi_a\left(y, c_y, c_r\right)\cos\theta. \tag{3.58}$$

Substituting Eqs. (3.57) and (3.58) in the linearized Boltzmann equation (3.51), it yields

$$c_y\frac{\partial\psi_a}{\partial y} = 2\mu\delta L_a\left(\psi_a\right) + s_a\left(c_y, c_r\right), \quad s_P = -c_r, \quad s_T = -c_r\left(c_y^2 + c_r^2 - \frac{5}{2}\right), \tag{3.59}$$

where the linearized collision operator becomes

$$\begin{gathered} L_\alpha\left(\psi_\alpha\right) = \frac{1}{\pi^{3/2}}\int_{-\infty}^{+\infty}\int_{0}^{+\infty}\hat{K}\left(c_y, c_r, c_{1,y}, c_{1,r}\right)\times \\ \left[\psi_\alpha\left(y, c_{1,y}, c_{1,r}\right) - \frac{c_{1,y}}{c_y}\psi_\alpha\left(y, c_y, c_r\right)\right] c_{1,r}e^{-\left(c_{1,y}^2 + c_{1,r}^2\right)}dc_{1,r}dc_{1,y}, \end{gathered} \tag{3.60}$$

while

$$\hat{K}\left(c_y, c_r, c_{1,y}, c_{1,r}\right) = 2\int_0^\pi K\left(c_y, c_r, c_{1,y}, c_{1,r}, \beta\right)\,\cos\beta d\beta. \tag{3.61}$$

The kernel $K\left(c_y, c_r, c_{1,y}, c_{1,r}, \beta\right)$ is given by Eq. (3.14). The corresponding boundary conditions are readily deduced:

$$\psi_a\left(-1/2, c_y > 0, c_r\right) = 0, \quad \psi_a\left(1/2, c_y < 0, c_r\right) = 0 \tag{3.62}$$

Performing the corresponding mathematical manipulations on Eq. (3.55) and (3.56) the velocity and heat flux are written as

$$u_{x,a}\left(y\right) = \frac{1}{\sqrt{\pi}}\int_{-\infty}^{+\infty}\int_{0}^{+\infty}c_r^2\psi_a(y, c_y, c_r)e^{-\left(c_y^2 + c_r^2\right)}dc_r dc_y, \tag{3.63}$$

$$q_{x,a}\left(y\right) = \frac{1}{\sqrt{\pi}}\int_{-\infty}^{+\infty}\int_{0}^{+\infty}c_r^2\left(c_y^2 + c_r^2 - \frac{5}{2}\right)\psi_a(y, c_y, c_r)e^{-\left(c_y^2 + c_r^2\right)}dc_r dc_y. \tag{3.64}$$

The formulation of the linearized Boltzmann equation (3.59) with the corresponding boundary conditions (3.62) is now complete. The numerical solution is based on the discrete velocity method and is the same for the pressure and temperature driven configurations. Thus, the subscript $a = P, T$ is omitted for the discretized equations. The discretization of the velocity space has been thoroughly addressed in Section 3.3.1.

The discretization of the physical space is based on a second order central difference scheme, where the flow domain $y \in [-1/2, 1/2]$ is divided into Ny evenly distributed segments.

Based on the above discretization Eq. (3.59) is written as

$$\begin{aligned} c_{yk}\frac{\psi^{(n)}_{l+1,km}-\psi^{(n)}_{l,km}}{\Delta y}+\mu\delta K_{0,km}\left(\psi^{(n)}_{l+1,km}+\psi^{(n)}_{l,km}\right) \\ =\mu\delta\sum_{i=1}^{Nc_x}\sum_{j=1}^{Nc_y}L_{ijkm}\left[\psi^{(n-1)}_{l+1,ij}+\psi^{(n-1)}_{l,ij}-\frac{c_{rj}}{c_{rm}}\left(\psi^{(n-1)}_{l+1,km}+\psi^{(n-1)}_{l,km}\right)\right] \\ +\mu\delta K_{0,km}\left(\psi^{(n-1)}_{l+1,km}+\psi^{(n-1)}_{l,km}\right)+s_{km}, \end{aligned} \tag{3.65}$$

where $\psi^{(n)}_{l,km}=\psi\left(y_l,c_{xk},c_{rm}\right)$ is the reduced distribution in the nth iteration. The discretized collision kernel reads

$$L_{ijkm}=\frac{1}{\pi^{3/2}}K_{ijkm}c_{rj}e^{-\left(c^2_{yi}+c^2_{rj}\right)}Wc_{yi}Wc_{rj},\quad K_{ijkm}=2\sum_{b=1}^{N_b}K_{ijkmb}\cos\beta_b W\beta_b. \tag{3.66}$$

It is reminded here that, K_0 denotes the collision frequency given by Eq. (3.15). The macroscopic velocity and heat flux are obtained from Eqs. (3.63) and (3.64):

$$u^{(n)}_{x,l}=\frac{1}{\sqrt{\pi}}\sum_{k=1}^{Nc_y}\sum_{m=1}^{Nc_r}c^2_{rm}\psi^{(n)}_{l,km}e^{-\left(c^2_{yk}+c^2_{rm}\right)}Wc_{rm}Wc_{yk} \tag{3.67}$$

$$q^{(n)}_{x,l}=\frac{1}{\sqrt{\pi}}\sum_{k=1}^{Nc_y}\sum_{m=1}^{Nc_r}c^2_{rm}\left(c^2_{yk}+c^2_{rm}-\frac{5}{2}\right)\psi^{(n)}_{l,km}e^{-\left(c^2_{yk}+c^2_{rm}\right)}Wc_{rm}Wc_{yk} \tag{3.68}$$

The kinetic coefficients G and Q are then computed by Eq. (3.48) using Simpson rule. The iterative scheme is concluded when the following criteria are fulfilled

$$\frac{1}{2}\left(\left|u^{(n)}_{x,l}-u^{(n-1)}_{x,l}\right|+\left|q^{(n)}_{x,l}-q^{(n-1)}_{x,l}\right|\right)<\varepsilon,\quad l=1,2,...,Ny+1, \tag{3.69}$$

where ε is the tolerance parameter. It is noted here that, as the iterative scheme converges the two terms containing K_0 cancel each other out. However, they are essential for the stability of the numerical scheme [67].

3.4.2 Kinetic coefficients

The planar fully-developed Poiseuille and thermal creep flow is simulated in a wide range of the gas rarefaction parameter. The computed kinetic coefficients are presented and compared with corresponding results in the literature based on the linearized hard-sphere Boltzmann equation, as well as, on the BGK and S kinetic models [67]. The presented results have been obtained with a set of $Nc_y = 2Nc_r = 160$ discrete velocities and $Ny = 500$ segments.

In Table 3.1 the Poiseuille coefficient G_P is presented in tabulated form with respect to the rarefaction parameter δ. As it is seen, the Poiseuille coefficient is decreased as the rarefaction coefficient is increased up to $\delta \sim 1$ and then it is increased. The minimum at $\delta \sim 1$ is well-known in the literature as the Knudsen minimum or Knudsen paradox. An excellent agreement is observed between the present BE results and the BE results reported in [67]. The highest absolute relative deviation between the two works is 0.2%. In addition, the BGK and S kinetic models, which provide similar results for G_P [40], are in great agreement with the BE results, with the highest deviation below 5%.

The thermal creep G_T and mechanocaloric coefficients Q_P are provided in Table 3.2. The Onsager-Casimir relation $G_T = Q_P$ is satisfied to at least six significant digits validating the accuracy of the obtained results. The thermal creep coefficient is monotonically decreased as the rarefaction parameter is increased. The BE results of the present work and these of [67] are again in excellent agreement, with a highest deviation of 1%. The BGK model, which cannot provide the correct Prandtl number, significantly underestimates G_T and shows a highest deviation of 26% with the BE results. The corresponding deviations for the S model drop below 10%.

In Table 3.3 the reduced heat flux coefficient Q_T is presented with respect to the rarefaction parameter. It is also, monotonically decreased as the rarefaction parameter is increased. An excellent agreement between the present results and the ones in [67] is also observed here, with a highest deviation of 0.3%. Similar to G_T, the BGK model is unable to accurately capture Q_T and significantly underestimates it. The highest deviation between the BGK and BE results is up to 33%, while the corresponding deviations for the S model are significantly lower reaching up to 5.5%.

3.5 Oscillatory planar Poiseuille fully-developed flow

3.5.1 Governing equations and numerical scheme

Consider a monoatomic gas confined between two infinite parallel plates located at $\tilde{y} = \pm H/2$. The gas is disturbed by a small oscillatory pressure gradient along the longitudinal $\tilde{x}$ direction

$$\frac{dP\left(\tilde{t},\tilde{x}\right)}{d\tilde{x}} = \frac{dP\left(\tilde{x}\right)}{d\tilde{x}}\cos\left(\omega\tilde{t}\right) = \mathbb{R}\left[\frac{dP\left(\tilde{x}\right)}{d\tilde{x}}e^{-i\omega\tilde{t}}\right], \tag{3.70}$$

where ω is the oscillation frequency, $\tilde{t}$ is the time variable, $\mathbb{R}$ denotes the real part of a complex quantity and $i = \sqrt{-1}$ is the imaginary unit. The amplitude $dP\left(\tilde{x}\right)/d\tilde{x}$ of the oscillating pressure gradient is assumed to be small and thus, the gas flow may be treated as isothermal and fully-developed [117, 118, 128].

The two parameters characterizing the flow are the rarefaction parameter and the oscillation parameter [129]. The gas rarefaction parameter is given by

$$\delta = \frac{P_0 H}{\tilde{\mu} v_0}, \tag{3.71}$$

while the oscillation parameter is written as

$$\theta = \frac{P_0}{\tilde{\mu}\omega}, \tag{3.72}$$

where the quantity $P_0/\tilde{\mu}$ approximates the collision frequency. Thus, small values of θ correspond to high oscillation of the pressure gradient, while large values of θ correspond to low oscillation of the pressure gradient. At this point it is useful to point out the distinct flow regimes. The flow is in the slip and hydrodynamic regime when $\delta \gg 1$ and $\theta \gg 1$, i.e. the channel height and the collision frequency are much larger than the equivalent mean free path and the oscillation frequency, respectively [129]. The flow is said to be in the free-molecular regime for $\delta \ll 1$ and in the high-speed oscillation regime for $\theta \ll 1$.

Next, it is convenient to introduce the dimensionless time, spatial and molecular velocity variables

$$t = \tilde{t}\omega, \;\; \boldsymbol{r} = \frac{\tilde{\boldsymbol{r}}}{H}, \;\; \boldsymbol{c} = \frac{\boldsymbol{\xi}}{v_0}, \tag{3.73}$$

as well as, the dimensionless local pressure gradient amplitude

$$X_P = \frac{H}{P}\frac{dP}{d\tilde{x}} \ll 1. \tag{3.74}$$

The most important macroscopic quantity of interest is the velocity, which may be written in complex notation as

$$u_x(y) = \frac{\tilde{u}_x(y)}{v_0 X_P} = u_{x,\mathrm{Re}}(y) + u_{x,\mathrm{Im}}(y)\, i = u_{x,A}(y) \exp\left[i u_{x,P}(y)\right]. \tag{3.75}$$

The subscripts Re and Im correspond to the real and imaginary parts, while the subscripts A and P correspond to the amplitude and phase angle, respectively. Then, the time-dependent form of the macroscopic velocity is readily calculated

$$u_x(t, y) = \frac{\tilde{u}_x\left(\tilde{t}, \tilde{y}\right)}{v_0 X_P} = u_{x,A}(y) \cos\left[t - u_{x,P}(y)\right]. \tag{3.76}$$

In addition, the Poiseuille coefficient, which is also of major practical importance, is written in complex notation

$$G(\delta, \theta) = G_{\mathrm{Re}}(\delta, \theta) + i G_{\mathrm{Im}}(\delta, \theta) = G_A(\delta, \theta) \exp\left[i G_P(\delta, \theta)\right] \tag{3.77}$$

and is computed by

$$G(\delta, \theta) = -2 \int_{-1/2}^{1/2} u_x(y)\, dy. \tag{3.78}$$

Due to the smallness of the pressure gradient amplitude the unknown distribution function can be linearized as

$$f = f_0^M \left[1 + X_P (h + h_R)\right], \;\; h_R = x\mathbb{R}\left(e^{-it}\right), \tag{3.79}$$

where h is the unknown perturbed distribution function, while h_R is the reference perturbation. Substituting Eq. (3.79) into (3.12) yields the dimensionless linearized

Boltzmann equation for the investigated flow configuration

$$\frac{\delta}{\theta}\frac{\partial h\left(t,y,\boldsymbol{c}\right)}{\partial t}+c_{y}\frac{\partial h\left(t,y,\boldsymbol{c}\right)}{\partial y}=2\mu\delta L'\left(h\right)-c_{x}\mathbb{R}\left(e^{-it}\right), \tag{3.80}$$

where the linearized collision operator has already been given in detail in Section 3.4.

The computational effort required to solve the time-dependent form of the linearized Boltzmann equation can be significantly reduced by introducing the complex perturbed distribution function $h\left(y,\mathbf{c}\right)$

$$h\left(t,y,\boldsymbol{c}\right)=\mathbb{R}\left[h\left(y,\boldsymbol{c}\right)e^{-it}\right]. \tag{3.81}$$

Then Eq. (3.80) is rewritten in complex notation as

$$c_{y}\frac{\partial h\left(y,\boldsymbol{c}\right)}{\partial y}-i\frac{\delta}{\theta}h\left(y,\boldsymbol{c}\right)=2\mu\delta L'\left(h\right)-c_{x}. \tag{3.82}$$

The macroscopic velocity is given in terms of the complex distribution $h\left(y,\boldsymbol{c}\right)$

$$u_{x}\left(y\right)=\frac{1}{\pi^{3/2}}\int c_{x}h\left(y,\boldsymbol{c}\right)e^{-\boldsymbol{c}^{2}}d\boldsymbol{c}. \tag{3.83}$$

Similar to Section 3.4 cylindrical coordinates may be introduced in order to reduce the computation effort required for the solution of Eq. (3.82)

$$c_{x}=c_{r}\sin\theta,\quad c_{y}=c_{y},\quad c_{z}=c_{r}\cos\theta. \tag{3.84}$$

The complex perturbed distribution function is written as

$$h\left(y,c_{x},c_{y},c_{z}\right)=\psi\left(y,c_{y},c_{r}\right)\cos\theta. \tag{3.85}$$

Substituting Eqs. (3.84) and (3.85) in Eq. (3.82), yields

$$c_{y}\frac{\partial\psi}{\partial y}+i\frac{\delta}{\theta}\psi=2\mu\delta L\left(\psi\right)-c_{r}, \tag{3.86}$$

where the linearized collision operator is given by Eq. (3.60). At the two infinite plates, purely diffuse gas-surface interaction is assumed and the corresponding boundary conditions are readily deduced

$$\psi\left(-1/2,c_{y}>0,c_{r}\right)=0,\quad\psi\left(1/2,c_{y}<0,c_{r}\right)=0. \tag{3.87}$$

Performing the corresponding mathematical manipulations on the macroscopic velocity, yields

$$u_x(y) = \frac{1}{\sqrt{\pi}} \int_{-\infty}^{+\infty} \int_{0}^{+\infty} c_r^2 \psi(y, c_y, c_r) e^{-\left(c_y^2 + c_r^2\right)} dc_r dc_y. \tag{3.88}$$

The formulation of the linearized Boltzmann equation (3.86) with the corresponding boundary conditions (3.87) is now complete. The numerical solution is based on the discrete velocity method and the discretization of the physical and molecular velocity space have been thoroughly addressed in Sections 3.3 and 3.4, respectively.

The discretized form of (3.86) is written as

$$\begin{aligned} c_{yk} \frac{\psi_{l+1,km}^{(n)} - \psi_{l,km}^{(n)}}{\Delta y} + \mu\delta K_{0,km} \left(\psi_{l+1,km}^{(n)} + \psi_{l,km}^{(n)}\right) + i\frac{\delta}{2\theta} \left(\psi_{l+1,km}^{(n)} + \psi_{l,km}^{(n)}\right) \\ = \mu\delta \sum_{i=1}^{Nc_x} \sum_{j=1}^{Nc_y} L_{ijkm} \left[\psi_{l+1,ij}^{(n-1)} + \psi_{l,ij}^{(n-1)} - \frac{c_{rj}}{c_{rm}} \left(\psi_{l+1,km}^{(n-1)} + \psi_{l,km}^{(n-1)}\right)\right] \\ + \mu\delta K_{0,km} \left(\psi_{l+1,km}^{(n-1)} + \psi_{l,km}^{(n-1)}\right) - c_{rm}, \end{aligned} \tag{3.89}$$

where $\psi_{l,km}^{(n)} = \psi(y_l, c_{xk}, c_{rm})$ is the reduced complex distribution in the nth iteration. The discretized collision kernel is given by Eq. (3.66). The macroscopic velocity is obtained from Eq. (3.88):

$$u_{x,l}^{(n)} = \frac{1}{\sqrt{\pi}} \sum_{k=1}^{Nc_y} \sum_{m=1}^{Nc_r} c_{rm}^2 \psi_{l,km}^{(n)} e^{-\left(c_{yk}^2 + c_{rm}^2\right)} W c_{rm} W c_{yk} \tag{3.90}$$

The Poiseuille coefficient $G(\delta, \theta)$ is calculated by Eq. (3.78) using Simpson rule. The iterative map is concluded when the following criteria for the macroscopic quantities is fulfilled

$$\left|u_{x,l}^{(n)} - u_{x,l}^{(n-1)}\right| < \varepsilon, \quad l = 1, 2, ..., Ny + 1. \tag{3.91}$$

3.5.2 Complex Poiseuille coefficient and macroscopic velocity

The oscillatory fully-developed Poiseuille flow between two infinite parallel plates is simulated in a wide range of the gas rarefaction and oscillation parameters based on the linearized hard-sphere Boltzmann equation. The computed amplitude and phase angle for the Poiseuille coefficient, as well as, results for the macroscopic velocity distribution are provided. The presented results have been obtained with a set of $Nc_y = 2Nc_r = 160$ discrete velocities and $Ny = 2000$ segments in the physical space.

The increased number of $Ny = 2000$ segments used here, compared to the $Ny = 500$ segments used for the steady-state Poiseuille flow, is required for the numerical accuracy of the presented results. More specifically, a sawtooth-like behavior appears in regions where the macroscopic quantities exhibit steep gradients, when a coarser physical space grid is used. In addition, in order to validate the accuracy of the BGK model equation in this type of flows [117, 118] the corresponding BGK results for the Poiseuille coefficient are provided and compared to the BE ones. The formulation of the BGK model for the investigated flow configuration has been given in [118] and is omitted here.

In Tables 3.4 and 3.5 the Poiseuille coefficient amplitude $G_A(\delta, \theta)$ and $G_A^{(BGK)}(\delta, \theta)$ based on the BE and the BGK model are provided in a wide range of the rarefaction parameter $\delta \in [10^{-2}, 10^2]$ and the oscillation parameter $\theta = [0.1, 1, 10, 50, 10^2]$. In addition, in Table 3.4, $G_A^{(s)}(\delta, \theta)$ is provided based on the slip regime analytical solution (A.11) for $\delta \geq 1$ and $\theta = [50, 10^2]$. Furthermore, the steady-state Poiseuille coefficient that has been reported for $\delta \leq 10$ in Table 3.1, is also provided in the last column of Table 3.4 for comparison purposes. A very good agreement can be observed between $G_A(\delta, \theta)$ and $G_A^{(s)}(\delta, \theta)$ for $\delta \geq 10$. More importantly, it can be confirmed that the agreement between the BE and the slip results is improved as both δ and θ are increased. However, even for $\theta = [50, 10^2]$ the deviations between the two approaches become significant as δ is decreased. This comparison, demonstrates the ability of the BE to recover the analytical slip solution at high values of both δ and θ, as well as, the range of validity of the slip results. Next, $G_A(\delta, \theta)$ for $\theta = 10^2$, is compared to the corresponding steady-state Poiseuille coefficient. The agreement is excellent for small and intermediate values of the rarefaction parameter ($\delta \leq 5$), however, it quickly deteriorates as δ is further increased. Thus it is evident that, in order to properly recover the steady-state solution $\theta \gg \delta$ must be fulfilled, in addition to $\theta \gg 1$. Furthermore, comparing the Poiseuille coefficient amplitude based on the BE and BGK model an excellent agreement is observed. More specifically, the two approaches are in excellent agreement for small values of θ and start to slightly deviate as θ is increased i.e. as the steady-state is approached. The largest relative deviations ($<5\%$) are found at $\theta = 100$ and are similar to the ones reported for the steady-state Poiseuille flow in Section 3.4.

Continuing the discussion in Table 3.4, the behavior of $G_A(\delta, \theta)$ is analyzed in the whole range of δ and θ. The dependency of $G_A(\delta, \theta)$ with respect to θ is simple, since it can be easily confirmed that for a specific δ, $G_A(\delta, \theta)$ is monotonically increased as θ

is increased. However, the behavior of $G_A(\delta,\theta)$ with respect to δ is more complex. For small values of the oscillation parameter ($\theta \leq 1$), the Poiseuille coefficient amplitude is monotonically decreased as δ is increased. At larger values of θ, as δ is increased $G_A(\delta,\theta)$ is decreased until $\delta \sim 1$, where it exhibits a local minimum. Then, as δ is further increased $G_A(\delta,\theta)$ tends to a maximum at some δ (depending on θ) and it is then again decreased. It is noted that, the above behavior described for the Poiseuille coefficient amplitude is in agreement with the one reported in [117, 118, 130].

In Tables 3.6 and 3.7 the Poiseuille coefficient phase angle $G_P(\delta,\theta)$ and $G_P^{(BGK)}(\delta,\theta)$ based on the BE and BGK model respectively, are provided in a wide range of the rarefaction parameter $\delta \in [10^{-2}, 10^2]$ and the oscillation parameter $\theta = [0.1, 1, 10, 50, 10^2]$. In addition, in the two last columns of Table 3.6, $G_P^{(s)}(\delta,\theta)$ obtained from the analytical solution (A.11) is provided for $\delta \geq 1$ and $\theta = [50, 10^2]$. The presented phase angles, vary between zero and $\pi/2$, which correspond to the no phase and maximum phase difference between the flow rate and the pressure gradient. The comparison between the kinetic and slip regimes phase angle results is great and in accordance with the remarks previously made for the amplitudes. Furthermore, the comparison between the BE and BGK model phase angle results is also in agreement with the remarks made for the amplitudes. The largest relative deviations between the two approaches reach 23% for $\theta = 10^2$ and $\delta = 10^{-2}$. It is noted that, even though these discrepancies are quite large, they are found in regions where the phase angle is close to zero and thus, they are not considered to be of significant importance.

Next, the dependency of the Poiseuille coefficient phase angle on δ and θ is discussed. As expected, for any given δ the phase angle $G_P(\delta,\theta)$ is increased as θ is decreased i.e. the phase difference between the flow rate and the pressure gradient is increased as the oscillation frequency is increased. In addition, for a specific θ, the phase angle is very close to zero at the free-molecular limit and is increased as δ is increased, tending to the maximum phase angle difference of $\pi/2$ at the viscous limit. It is noted that similar to the Poiseuille coefficient amplitude, the above remarks for the phase angle are in accordance with the ones made in [117, 118, 130].

Moving on, the velocity distribution amplitude $u_{x,A}(y)$ and phase angle $u_{x,P}(y)$ are plotted in Fig. 3.1 for indicative values of the rarefaction parameter $\delta = [0.1, 1, 10]$ and the oscillation parameter $\theta = [0.1, 1, 10]$. It is observed that, for some combinations of δ and θ ($\delta = 0.1$ and $\theta \geq 0.1$, $\delta = 1$ and $\theta \geq 1$, $\delta = 10$ and $\theta \geq 10$) the velocity amplitude has the typical steady-state Poiseuille velocity profile, where the velocity maximum appears in the channel center. The corresponding phase angles show the

same trend in the opposite direction with a minimum forming in the channel center. However, for a given δ as the oscillation parameter is decreased ($\delta = 1$ and $\theta < 1$, $\delta = 10$ and $\theta < 10$), the bulk of the velocity at the channel center tends to become flat, while it exhibits a maximum in the region close to the two plates. The corresponding phase angles in these cases are also flat in the channel center and rapidly change close to the plates. At a specific δ the thickness of this region is reduced as θ is decreased and the velocity amplitude and phase gradients become steeper. In the aforementioned cases, the flow consists of the inviscid piston flow in the channel center dominated by inertia forces and the frictional Stokes wall layer dominated by viscous forces. This flow description, including the velocity overshoot inside the Stokes layer, is known as the "Richardson effect" and has been observed in the viscous limit [128, 131, 132], as well as, under rarefied conditions [117, 118, 130].

The time evolution of the velocity distribution $u_x(t, y)$ at specific timeframes over an oscillation period $t \in [0, 2\pi)$ for $\delta = 10$ and $\theta = [0.1, 1, 10, 10^2]$ is plotted in Fig 3.2. For $\theta = 0.1$, the two layer flow, with the bulk of the velocity oscillating in a plug-flow and the velocity overshoot close to the plates can be clearly seen. In addition, it is observed that, the position of the velocity extrema is not constant but it is shifting with time. The described effects are reduced as the oscillation parameter is increased and at $\theta = 10^2$ they completely vanish. More specifically, at $\theta = 10^2$ the velocity profile is the typical one (velocity extrema in the channel center) and only slightly lags the pressure gradient.

3.6 Concluding remarks

The exact Boltzmann collision operator is computed and the Boltzmann equation is solved based on the hard-sphere intermolecular potential. First, the computation of the Boltzmann collision operator has been benchmarked by calculating the heat conductivity and viscosity. The obtained results have been found to be equal to the ones found in the literature to at least 5 significant digits. Then, the solution of the BE is validated by simulating the planar Poiseuille and thermal creep flows. The kinetic coefficients, namely the Poiseuille, mechanocaloric, thermal creep and reduced heat flux coefficients are obtained and compared with the ones found in the literature providing an excellent agreement. In addition, a comparison between the BE and the BGK and S kinetic models is presented to give an idea of the expected discrepancies for the most-widely used kinetic models.

Then, having established confidence in the accuracy of the numerical solution of the BE, the methodology is implemented for simulating the oscillatory planar Poiseuille flow. The Poiseuille coefficient amplitude and phase angle are presented in a wide range of the rarefaction parameter δ and the oscillation parameter θ. The obtained results reproduce the analytical slip solution for large values of both δ and θ. In addition, they tend to the steady-state results for large values of θ, as long as, $\delta \ll \theta$. Moreover, they are compared to corresponding results obtained via the BGK model providing an excellent agreement. Based on the above comparison it is confirmed that, the simulation of pressure driven oscillatory flows via the BGK model is reliable. The Poiseuille coefficient amplitude and phase angle behavior with respect δ and θ has been found to be in accordance with the one described in the literature. In addition, the amplitude and phase angle, as well as, as the temporal evolution of the macroscopic velocity are provided for indicative values of δ and θ. The velocity overshoot near the two plates, that has been well-established in the viscous regime and more recently under rarefied conditions based on the BGK model, also appears in the BE results.

Table 3.1 Poiseuille coefficient G_P with respect to δ.

δ	LBE	LBE [67]	BGK [67]	S [67]
0.01	2.911	2.905	3.049	3.051
0.02	2.586	2.589	2.711	2.714
0.05	2.200	2.200	2.302	2.307
0.1	1.950	1.950	2.032	2.039
0.2	1.746	1.746	1.808	1.817
0.5	1.561	1.561	1.601	1.614
1	1.507	1.507	1.538	1.553
2	1.564	1.564	1.594	1.610
5	1.954	1.954	1.988	2.002
10	2.730	2.730	2.760	2.772

Table 3.2 Thermal creep and mechanocaloric coefficients $G_T = Q_P$ with respect to δ.

δ	LBE	LBE [67]	BGK [67]	S [67]
0.01	1.320	1.307	1.236	1.247
0.02	1.152	1.155	1.061	1.078
0.05	0.944	0.944	0.845	0.872
0.1	0.800	0.800	0.695	0.733
0.2	0.666	0.666	0.558	0.607
0.5	0.504	0.504	0.398	0.463
1	0.389	0.389	0.295	0.365
2	0.281	0.281	0.206	0.274
5	0.158	0.158	0.114	0.164
10	0.090	0.090	0.066	0.098

Table 3.3 Reduced heat flux coefficient Q_T with respect to δ

δ	LBE	LBE [67]	BGK [67]	S [67]
0.01	6.385	6.366	6.673	6.733
0.02	5.598	5.603	5.808	5.900
0.05	4.609	4.608	4.679	4.830
0.1	3.904	3.904	3.845	4.054
0.2	3.235	3.235	3.041	3.311
0.5	2.392	2.392	2.060	2.391
1	1.783	1.783	1.418	1.753
2	1.221	1.221	0.900	1.189
5	0.632	0.632	0.435	0.616
10	0.347	0.347	0.233	0.341

Table 3.4 Poiseuille coefficient amplitude $G_A(\delta,\theta)$ based on the BE in terms of the rarefaction parameter δ and oscillation parameter θ.

δ	$G_A(\delta,\theta)$					$G_A^{(s)}(\delta,\theta)$		$G_{ss}(\delta)$
	$\theta=0.1$	$\theta=1$	$\theta=10$	$\theta=50$	$\theta=100$	$\theta=50$	$\theta=100$	$\theta\to\infty$
0.01	1.872	2.797	2.910	2.911	2.911	-	-	2.911
0.02	1.530	2.467	2.585	2.586	2.586	-	-	2.586
0.05	1.089	2.066	2.198	2.200	2.200	-	-	2.200
0.1	7.693(-1)	1.789	1.948	1.950	1.950	-	-	1.950
0.2	4.801(-1)	1.529	1.743	1.746	1.746	-	-	1.746
0.5	2.038(-1)	1.165	1.554	1.561	1.561	-	-	1.561
1	9.995(-2)	8.295(-1)	1.489	1.506	1.507	1.154	1.154	1.507
2	5.000(-2)	4.865(-1)	1.494	1.561	1.563	1.319	1.320	1.564
5	2.000(-2)	1.978(-1)	1.388	1.916	1.944	1.789	1.813	1.954
10	1.000(-2)	9.926(-2)	8.895(-1)	2.357	2.620	2.299	2.550	2.730
20	5.000(-3)	4.980(-2)	4.659(-1)	1.989	3.117	1.976	3.093	-
50	2.000(-3)	1.997(-2)	1.940(-1)	9.050(-1)	1.726	9.031(-1)	1.723	-
100	1.000(-3)	9.991(-3)	9.846(-2)	4.747(-1)	9.241(-1)	4.744(-1)	9.231(-1)	-

Table 3.5 Poiseuille coefficient amplitude $G_A(\delta,\theta)$ based on the BGK model in terms of the rarefaction parameter δ and oscillation parameter θ.

δ	$G_A^{(BGK)}(\delta,\theta)$				
	$\theta=0.1$	$\theta=1$	$\theta=10$	$\theta=50$	$\theta=100$
0.01	1.872	2.878	3.047	3.050	3.050
0.02	1.527	2.536	2.709	2.711	2.711
0.05	1.086	2.115	2.300	2.302	2.302
0.1	7.682(-1)	1.822	2.030	2.033	2.033
0.2	4.796(-1)	1.546	1.804	1.808	1.808
0.5	2.038(-1)	1.168	1.594	1.602	1.602
1	9.995(-2)	8.288(-1)	1.519	1.538	1.538
2	5.000(-2)	4.845(-1)	1.521	1.592	1.594
5	2.000(-2)	1.978(-1)	1.397	1.951	1.981
10	1.000(-2)	9.925(-2)	8.889(-1)	2.380	2.654
20	5.000(-3)	4.980(-2)	4.660(-1)	1.991	3.127
50	2.000(-3)	1.996(-2)	1.940(-1)	9.058(-1)	1.728
100	1.000(-3)	9.992(-3)	9.849(-2)	4.747(-1)	9.247(-1)

Table 3.6 Poiseuille coefficient phase angle $G_P(\delta,\theta)$ based on the BE in terms of the rarefaction parameter δ and oscillation parameter θ.

δ	$G_P(\delta,\theta)$					$G_P^{(s)}(\delta,\theta)$	
	$\theta=0.1$	$\theta=1$	$\theta=10$	$\theta=50$	$\theta=100$	$\theta=50$	$\theta=100$
0.01	4.514(-1)	1.396(-1)	1.580(-2)	3.165(-3)	1.583(-3)	-	-
0.02	5.525(-1)	1.665(-1)	1.884(-2)	3.773(-3)	1.887(-3)	-	-
0.05	7.490(-1)	2.228(-1)	2.522(-2)	5.051(-3)	2.526(-3)	-	-
0.1	9.542(-1)	2.935(-1)	3.344(-2)	6.700(-3)	3.350(-3)	-	-
0.2	1.195	4.075(-1)	4.750(-2)	9.519(-3)	4.760(-3)	-	-
0.5	1.454	6.701(-1)	8.600(-2)	1.726(-2)	8.632(-3)	-	-
1	1.515	9.645(-1)	1.515(-1)	3.055(-2)	1.528(-2)	2.317(-2)	1.159(-2)
2	1.543	1.259	2.985(-1)	6.147(-2)	3.077(-2)	5.345(-2)	2.674(-2)
5	1.560	1.463	7.793(-1)	1.954(-1)	9.863(-2)	1.874(-1)	9.456(-2)
10	1.565	1.517	1.221	5.246(-1)	2.822(-1)	5.190(-1)	2.787(-1)
20	1.568	1.544	1.417	1.079	7.650(-1)	1.078	7.637(-1)
50	1.570	1.560	1.512	1.418	1.339	1.419	1.339
100	1.571	1.565	1.542	1.498	1.464	1.498	1.464

Table 3.7 Poiseuille coefficient phase angle $G_P(\delta,\theta)$ based on the BGK model in terms of the rarefaction parameter δ and oscillation parameter θ.

δ	$G_P^{(BGK)}(\delta,\theta)$				
	$\theta=0.1$	$\theta=1$	$\theta=10$	$\theta=50$	$\theta=100$
0.01	4.563(-1)	1.623(-1)	1.948(-2)	3.906(-3)	1.953(-3)
0.02	5.573(-1)	1.909(-1)	2.281(-2)	4.572(-3)	2.286(-3)
0.05	7.512(-1)	2.484(-1)	2.956(-2)	5.925(-3)	2.963(-3)
0.1	9.550(-1)	3.183(-1)	3.797(-2)	7.611(-3)	3.806(-3)
0.2	1.196	4.295(-1)	5.203(-2)	1.043(-2)	5.217(-3)
0.5	1.454	6.852(-1)	9.029(-2)	1.813(-2)	9.067(-3)
1	1.516	9.749(-1)	1.561(-1)	3.149(-2)	1.575(-2)
2	1.543	1.263	3.056(-1)	6.303(-2)	3.155(-2)
5	1.560	1.463	7.906(-1)	2.000(-1)	1.010(-1)
10	1.565	1.517	1.224	5.319(-1)	2.868(-1)
20	1.568	1.545	1.416	1.085	7.690(-1)
50	1.570	1.559	1.506	1.425	1.345
100	1.571	1.567	1.555	1.485	1.477

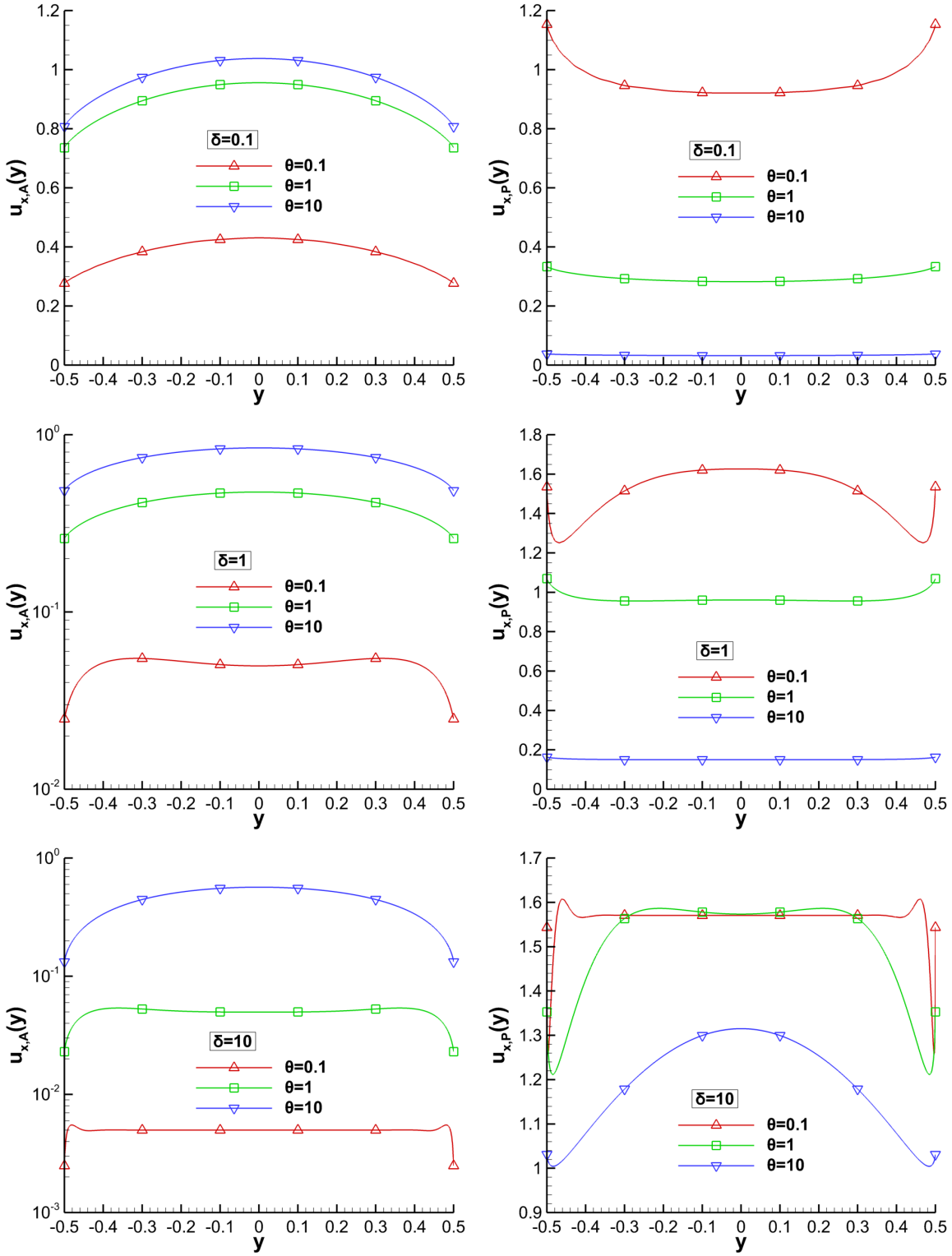

Figure 3.1 Velocity amplitude $u_{x,A}$ (left) and phase angle $u_{x,P}$ (right) for $\delta = [0.1, 1, 10]$ and $\theta = [0.1, 1, 10]$.

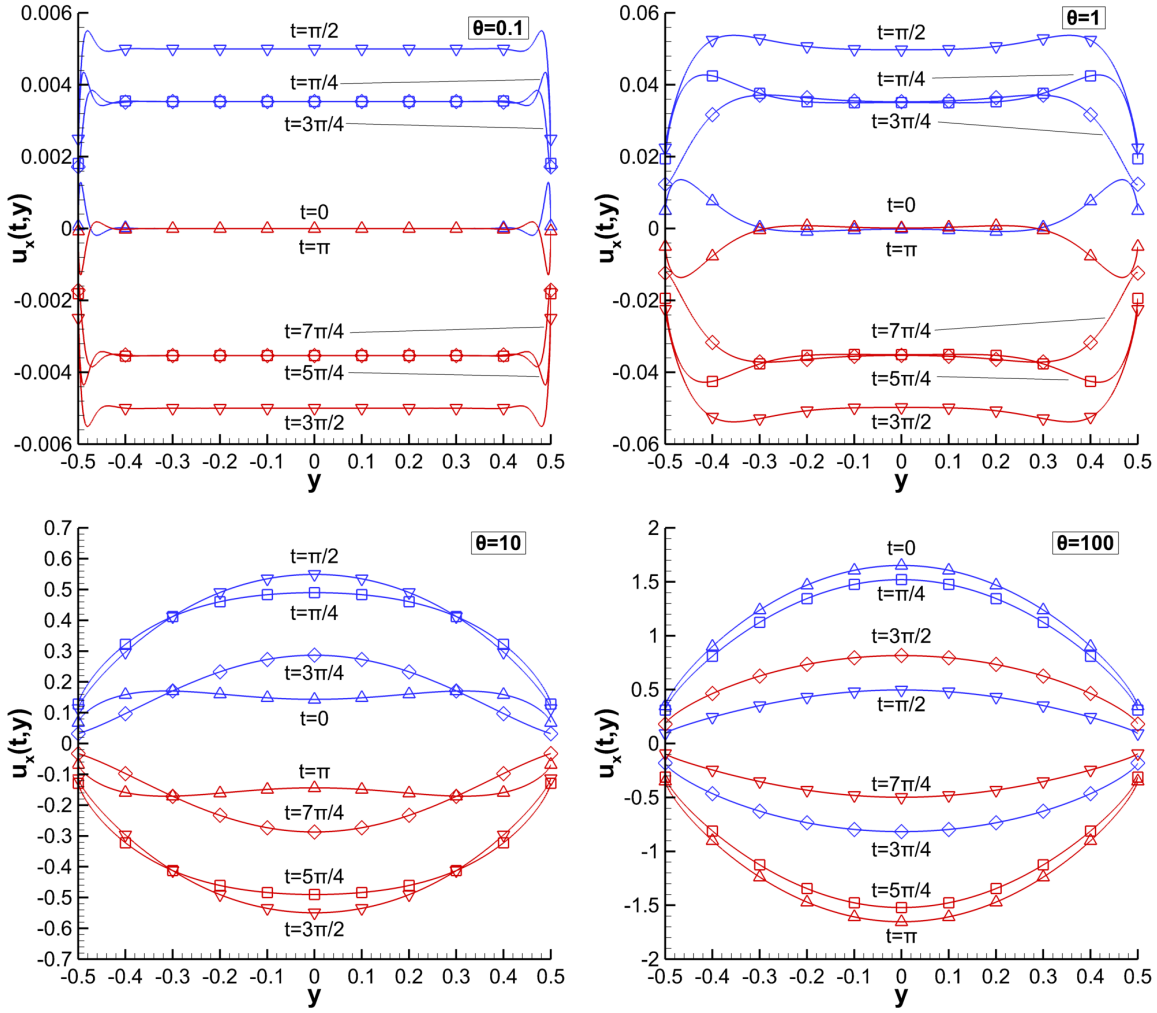

Figure 3.2 Time evolution of velocity distribution $u_x(t, y)$ at specific timeframes over one period of oscillation $t \in [0, 2\pi)$ for $\delta = 10$ and $\theta = [0.1, 1, 10, 10^2]$; blue lines refer to $t < \pi$, while red lines refer to $t \geq \pi$.

Chapter 4

Injection/suction rarefied flows

4.1 Introduction

Injection/suction flows, such as the planar fully-developed Poiseuille flow with uniform injection/suction, as well as, the fully-developed flow over a permeable plate with downward suction, are considered as fundamental flows in fluid mechanics [131, 133]. Pioneering research work related to these flow configurations includes small and large Reynolds number flow between uniformly permeable parallel plates [134–138], pipes [139] and annuli [140]. More recently, the boundary and pressure driven oscillatory flows in a channel with arbitrary wall injection [141, 142] the uniform flow over a downward suction plate [143], the viscous/inertia flow through a channel with wavy permeable walls [144] and the heat transfer in the laminar viscous channel flow with one porous wall [145], have been investigated. Overall, injection/suction flows have attracted considerable attention in the viscous regime due to their theoretical interest, as well as due to their tentative importance in a variety of technological applications, including filtration systems [12], membrane gas permeators [13, 14], detritiation systems [15, 16] and biological applications [17, 18].

However, to the best of the author's knowledge, the planar fully-developed Poiseuille and thermal creep flows with injection/suction, as well as, the asymptotic suction flow under rarefied conditions have not been investigated. In the hydrodynamic regime fully-developed injection/suction flows are characterized by the injection/suction velocity magnitude. The same applies in the slip, transition and free-molecular regimes for the asymptotic suction flow. However, for the planar Poiseuille and thermal creep flows coupled with injection/suction the level of gas rarefaction is also required to fully

characterize the flow. Since this type of rarefied gas flows has not been studied so far, obviously, there is both theoretical and technological interest for their investigation.

In this chapter, kinetic modeling is implemented for the first time in order to simulate injection/suction flows. Thus, the exact Boltzmann equation is also implemented, in order to quantify the discrepancies introduced by the kinetic model equations for the investigated flow configurations.

In Section 4.2, the fully-developed Poiseuille and thermal creep rarefied gas flow between two infinite parallel permeable plates with uniform injection and suction from the bottom and top plate, respectively, is investigated [146]. The driving gradients are assumed to be small and a linearization procedure required for injection/suction flows is proposed and successfully implemented. The flow is investigated by numerically solving both the linearized S model and BE. The full-range acceleration scheme is implemented for the S kinetic model and its efficiency is investigated. Computational results for the macroscopic quantities of interest are presented in a wide range of the gas rarefaction parameter and the injection velocity magnitude. The so-called kinetic coefficients, namely the Poiseuille, mechanocaloric, thermal creep and reduced heat flux coefficients are provided and compared with analytical solutions in the free-molecular and slip regimes. In addition, the macroscopic velocity, heat flux and shear stress distributions are presented for indicative values of the involved parameters.

In Section 4.3, the fully-developed flow over a permeable plate with downward suction, which is also known in the literature as the asymptotic suction flow is investigated. The same linearization procedure described in Section 4.2 is also followed here. The flow is investigated by numerically solving the linearized S model. Computational results based on the S model for the boundary layer thickness with respect to the suction velocity are provided and compared to the analytical results in the slip and hydrodynamic regimes. In addition, kinetic, as well as analytical slip and hydrodynamic results for the macroscopic velocity, heat flux and shear stress distributions are provided.

4.2 Planar pressure and temperature driven fully-developed flow with uniform injection/suction

4.2.1 Flow configuration

Consider a monoatomic single gas confined between two parallel uniformly permeable plates located at $\tilde{y} \in [-H/2, H/2]$. The gas is flowing driven by an externally imposed small pressure and temperature gradient in the longitudinal $\tilde{x}$ direction

$$X_a = \frac{H}{a}\frac{da}{d\tilde{x}} \ll 1, \quad a = P, T, \tag{4.1}$$

where P and T are the local pressure and temperature. In addition to the longitudinal flow, the bottom and top permeable plates inject and remove gas in the $\tilde{y}$ direction respectively with the same constant velocity $\tilde{U}_w$, generating a cross-flow. Since $X_a \ll 1$ and the cross stream velocity is constant, the gas flow may be treated as isothermal and fully-developed [33, 131].

The flow is fully characterized by two parameters, namely, the gas rarefaction parameter δ and the dimensionless injection velocity U_w. The gas rarefaction parameter is given by

$$\delta = \frac{P_0 H}{\tilde{\mu} v_0}, \tag{4.2}$$

where P_0 is the equilibrium pressure, $\tilde{\mu}$ is the gas viscosity at the equilibrium temperature T_0 and $v_0 = \sqrt{2R_g T_0}$ is the most probable molecular speed ($R_g = k_B/m$ is the specific gas constant, with k_B denoting the Boltzmann constant and m the gas molecular mass). The dimensionless injection velocity is defined as

$$U_w = \frac{\tilde{U}_w}{v_0}. \tag{4.3}$$

Next, it is convenient to introduce the dimensionless spatial variables

$$x = \frac{\tilde{x}}{H}, \quad y = \frac{\tilde{y}}{H}. \tag{4.4}$$

The total dimensionless macroscopic quantities of interest in the longitudinal direction, namely the velocity, shear stress and heat flux can be written as a linear superposition of the Poiseuille and thermal creep flow due to the smallness of the driving gradients

as follows [33]:

$$u_x(y) = \frac{\tilde{u}_x(\tilde{y})}{v_0} = u_{x,P}(y) X_P + u_{x,T}(y) X_T \tag{4.5}$$

$$\Pi_{xy}(y) = \frac{P_{xy}(\tilde{y})}{P_0} = \Pi_{xy,P}(y) X_P + \Pi_{xy,T}(y) X_T \tag{4.6}$$

$$q_x(y) = \frac{\tilde{q}_x(\tilde{y})}{v_0 P_0} = q_{x,P}(y) X_P + q_{x,T}(y) X_T \tag{4.7}$$

Here, $\tilde{u}_x$, P_{xy} and $\tilde{q}_x$ are the total dimensional velocity, shear stress and heat flux, respectively. The specific dimensionless macroscopic quantities for the pressure and temperature driven problems in Eqs. (4.5)-(4.7) are given by

$$u_{x,a}(y) = \frac{\tilde{u}_{x,a}(\tilde{y})}{v_0 X_a}, \quad \Pi_{xy,a}(y) = \frac{P_{xy,a}(\tilde{y})}{P_0 X_a}, \quad q_{x,a}(y) = \frac{\tilde{q}_{x,a}(\tilde{y})}{v_0 P_0 X_a}, \quad a = P, T. \tag{4.8}$$

In addition, the overall quantities of the mass and heat flow rates can be computed by introducing the dimensionless kinetic coefficients [67]

$$\begin{aligned} G_P &= -2 \int_{-1/2}^{1/2} u_{x,P} dy, \quad G_T = 2 \int_{-1/2}^{1/2} u_{x,T} dy, \\ Q_P &= 2 \int_{-1/2}^{1/2} q_{x,P} dy, \quad Q_T = -2 \int_{-1/2}^{1/2} q_{x,T} dy. \end{aligned} \tag{4.9}$$

The aforementioned kinetic coefficients G_P, G_T, Q_P and Q_T have been described in Chapter 3 for the classical Poiseuille and thermal creep flows without injection/suction. It has been noted, that in the classical Poiseuille and thermal creep problems, the cross effects G_T and Q_P obey the Onsager-Casimir relation $G_T = Q_P$ [124–127] It turns out that the reciprocity relation $G_T = Q_P$ is also valid in the present fully-developed Poiseuille and thermal creep flows through a channel with permeable walls and its proof is provided in detail in Appendix B. The reciprocity relation is used to validate the accuracy of the computed results.

4.2.2 Analytical solution in the slip and hydrodynamic regimes

At the viscous and slip regimes the fully-developed Poiseuille flow between parallel infinite plates with injection/suction is defined by the x-momentum equation [131]

$$\tilde{\rho}\tilde{U}_w \frac{d\tilde{u}_P^{(j)}}{d\tilde{y}} = -\frac{dP}{d\tilde{x}} + \tilde{\mu}\frac{d^2\tilde{u}_P^{(j)}}{d\tilde{y}^2}, \tag{4.10}$$

where the superscript $j = h, s$ corresponds to the hydrodynamic and slip regimes, respectively. For the thermal creep flow the corresponding equation becomes

$$\tilde{\rho}\tilde{U}_w \frac{d\tilde{u}_T^{(j)}}{d\tilde{y}} = \tilde{\mu}\frac{d^2\tilde{u}_T^{(j)}}{d\tilde{y}^2}. \tag{4.11}$$

Introducing the dimensionless quantities defined in Eqs. (4.1)-(4.4) and (4.8) the governing Eqs. (4.10) and (4.11) can be rewritten in dimensionless form following the present notation as

$$2\delta U_w \frac{du_P^{(j)}}{dy} = -\delta + \frac{d^2u_P^{(j)}}{dy^2}, \tag{4.12}$$

$$2\delta U_w \frac{du_T^{(j)}}{dy} = \frac{d^2u_T^{(j)}}{dy^2}. \tag{4.13}$$

At the hydrodynamic regime ($j = h$), the Poiseuille and thermal creep equations (4.12) and (4.13) are subject to the no-slip boundary conditions at the bottom and top plate, written as

$$u_a^{(h)}(\pm 1/2) = 0, \quad a = P, T. \tag{4.14}$$

For the Poiseuille driven flow, Eq. (4.12), subject to boundary conditions (4.14) is analytically solved to obtain the velocity and shear stress distributions, as well as the Poiseuille coefficient [131]:

$$u_P^{(h)}(y) = \frac{1}{4U_w}\left(2y - 1 + \frac{e^{\delta U_w} - e^{2\delta U_w y}}{\sinh(\delta U_w)}\right) \tag{4.15}$$

$$\Pi_{xy,P}^{(h)}(y) = \frac{1}{2}\left[\frac{e^{2\delta U_w y}}{\sinh(\delta U_w)} - \frac{1}{\delta U_w}\right] \tag{4.16}$$

$$G_P^{(h)} = \frac{\delta U_w \coth(\delta U_w) - 1}{2\delta U_w^2} \tag{4.17}$$

It is noted that, performing a series expansion with respect to $U_w = 0$, Eqs. (4.15)-(4.17) reduce to the hydrodynamic expressions derived for the classical Poiseuille flow without injection/suction [33].

Next, for the thermal creep flow, the trivial solution $u_T^{(h)} = 0$ satisfies the homogenous governing equation (4.13) and the accompanying homogeneous boundary conditions (4.14). Thus, similar to the classical thermal creep flow without injection/suction, thermal creep effects vanish for all values of the injection velocity at the hydrodynamic limit.

At the slip regime ($j = s$), Eq. (4.12) is subject to the viscous slip boundary conditions

$$u_P^{(s)}(\pm 1/2) = \mp \frac{\sigma_P}{\delta} \left. \frac{du_P^{(s)}}{dy} \right|_{\pm 1/2}, \tag{4.18}$$

while Eq. (4.13) is subject to the thermal slip boundary conditions

$$u_T^{(s)}(\pm 1/2) = \frac{\sigma_T}{2\delta}. \tag{4.19}$$

The viscous slip coefficient σ_P and the thermal slip coefficient σ_T are known and are computed by solving the corresponding half-space flow problems [33].

For the pressure driven flow, Eq. (4.12) along with the boundary conditions (4.18) may be solved analytically to yield the velocity and shear stress distributions, as well as, the Poiseuille coefficient

$$u_P^{(s)}(y) = \frac{A\cosh(\delta U_w) + B\sinh(\delta U_w) - (\delta + 2\sigma_P)\left[\cosh(2\delta U_w y) + \sinh(2\delta U_w y)\right]}{4\delta U_w \left[2U_w\sigma_P\cosh(\delta U_w) + \sinh(\delta U_w)\right]}, \tag{4.20}$$

$$\Pi_{xy,P}^{(s)}(y) = -\frac{1}{2\delta U_w} + \frac{\mathrm{e}^{2\delta U_w y}(\delta + 2\sigma_P)}{2\delta\left[2U_w\sigma_P\cosh(\delta U_w) + \sinh(\delta U_w)\right]}, \tag{4.21}$$

$$G_P^{(s)} = \frac{(\delta + 2\sigma_P)\left[2\sigma_P - \delta\left(4U_w^2\sigma_P^2 - 1\right)\right]\cosh(\delta U_w)}{2U_w\delta^2\left[2U_w\sigma_P\cosh(\delta U_w) + \sinh(\delta U_w)\right]} - \frac{1}{2\delta U_w^2} - \frac{\sigma_P}{\delta^2 U_w^2} + \frac{2\sigma_P^2}{\delta} + \sigma_P, \tag{4.22}$$

where $A = \delta + 2\sigma_P + 4\delta U_w\sigma_P y$ and $B = 2\left[\delta y + U_w\sigma_P(\delta + 2\sigma_P)\right]$. For $U_w = 0$ the analytical slip solution reduces to the classical Poiseuille flow slip solution without injection/suction.

Some limiting cases can be derived for validating the kinetic solution at the slip regime. As $\delta \to \infty$ the Poiseuille coefficient tends to

$$\lim_{\delta\to\infty} G_P^{(s)} = \frac{1}{2U_w}. \tag{4.23}$$

Furthermore, as $\delta \to \infty$ and for $U_w > 0$ the velocity and shear stress profiles in the whole flow domain, excluding the suction plate, can be written as

$$\lim_{\delta\to\infty} u_P^{(s)}\left(y < 1/2\right) = \frac{1+2y}{4U_w}, \quad \lim_{\delta\to\infty} \Pi_{xy,P}^{(s)}\left(y < 1/2\right) = 0. \tag{4.24}$$

Exactly at the bottom and top plate they become

$$\lim_{\delta\to\infty} u_P^{(s)}\left(-1/2\right) = 0, \quad \lim_{\delta\to\infty} \Pi_{xy,P}^{(s)}\left(-1/2\right) = 0, \tag{4.25}$$

$$\lim_{\delta\to\infty} u_P^{(s)}\left(1/2\right) = \frac{\sigma_P}{1+2U_w\sigma_P}, \quad \lim_{\delta\to\infty} \Pi_{xy,P}^{(s)}\left(1/2\right) = \frac{1}{1+2U_w\sigma_P}. \tag{4.26}$$

It is worthwhile to note that, as $\delta \to \infty$ in the case without injection/suction ($U_w = 0$) the limiting bottom and top plate velocity and shear stress become $u_P^{(s)}\left(\mp 1/2\right) = \sigma_P/2$ and $\Pi_{xy,P}^{(s)}\left(\mp 1/2\right) = \mp 1/2$, respectively [33]. However, from Eqs. (4.25) and (4.26) it can be clearly seen that, as $U_w \to 0$ the limiting bottom and top plate velocity tends to $u_P^{(s)}\left(-1/2\right) = 0$ and $u_P^{(s)}\left(1/2\right) = \sigma_P$, while the limiting bottom and top plate shear stress tends to $\Pi_{xy,P}^{(s)}\left(-1/2\right) = 0$ and $\Pi_{xy,P}^{(s)}\left(1/2\right) = 1$. This behavior also holds for the kinetic results and will be further addressed in Section 4.2.8.

Next, Eq. (4.13) along with the boundary conditions (4.19) may be solved analytically for the thermal creep flow to yield the velocity and shear stress distributions, as well as, the thermal creep and reduced heat flux coefficients

$$u_T^{(s)}\left(y\right) = \frac{\sigma_T}{2\delta}, \quad \Pi_{xy,T}^{(s)}\left(y\right) = 0, \quad G_T^{(s)} = \frac{\sigma_T}{\delta}, \quad Q_T^{(s)} = \frac{15}{4\delta}. \tag{4.27}$$

It can be validated that, the slip solution for the thermal creep flow with and without injection/suction are identical. Thus, as the flow enters the slip regime the effect of the imposed cross-flow is expected to vanish.

4.2.3 Formulation of the linearized Shakhov model

For arbitrary values of δ and U_w, the Poiseuille ($a = P$) and thermal creep ($a = T$) flows may be modeled at the mesoscale level by the steady-state Shakhov model, which for the investigated setup is given by [33]

$$\boldsymbol{\xi}\frac{\partial f_a}{\partial \tilde{y}} = \frac{P}{\tilde{\mu}}\left[f_a^M\left\{1 + \frac{2m}{15n_a(k_BT_a)^2}\tilde{\boldsymbol{q}}_a\cdot\left(\boldsymbol{\xi}-\tilde{\boldsymbol{u}}_a\right)\left[\frac{m(\boldsymbol{\xi}-\tilde{\boldsymbol{u}}_a)^2}{2k_BT_a} - \frac{5}{2}\right]\right\} - f_a\right], \tag{4.28}$$

where $f = f(\tilde{y}, \boldsymbol{\xi})$ is the unknown distribution function, which depends on the $\tilde{y}$ space variable and the molecular velocity vector $\boldsymbol{\xi} = (\xi_x, \xi_y, \xi_z)$. The quantity $P/\tilde{\mu}$ approximates the collision frequency and

$$f_a^M = n\Big(\frac{m}{2\pi k_B T_a}\Big)^{3/2} \exp\left[-\frac{m(\boldsymbol{\xi} - \tilde{\boldsymbol{u}}_a)^2}{2k_B T_a}\right] \tag{4.29}$$

denotes the local Maxwellian distribution. Since both flow setups are assumed to be isothermal and fully-developed, the temperature T and the number density n are constant along $\tilde{y}$ and may only vary in the $\tilde{x}$ direction. The velocity, shear stress and heat flux introduced in Eq. (4.8), are defined as the first, second and third moments of the unknown distribution function

$$\tilde{\boldsymbol{u}}_a(\tilde{y}) = \frac{1}{n}\int \boldsymbol{\xi} f_a(\tilde{y}, \boldsymbol{\xi})\, d\boldsymbol{\xi}, \tag{4.30}$$

$$\Pi_{xy,a}(\tilde{y}) = m\int \zeta_x \zeta_y f_a(\tilde{y}, \boldsymbol{\xi})\, d\boldsymbol{\xi}, \tag{4.31}$$

$$\tilde{\boldsymbol{q}}_a(\tilde{y}) = \frac{m}{2}\int \boldsymbol{\zeta}^2 \boldsymbol{\zeta} f_a(\tilde{y}, \boldsymbol{\xi})\, d\boldsymbol{\xi}, \tag{4.32}$$

where $\boldsymbol{\zeta} = \boldsymbol{\xi} - \tilde{\boldsymbol{u}}_a$ denotes the peculiar molecular velocity vector. Next, focusing on the boundary conditions the particles incident at the two plates are assumed to be absorbed and are then reemitted following the outgoing distribution

$$f_a^+\left(\pm\frac{H}{2}, \boldsymbol{\xi}\right) = n_{w,a}\Big(\frac{m}{2\pi k_B T_{w,a}}\Big)^{3/2} \exp\left[-\frac{m\left(\boldsymbol{\xi} - \tilde{\boldsymbol{U}}_{\boldsymbol{w}}\right)}{2k_B T_{w,a}}\right], \quad \xi_y \lessgtr 0, \tag{4.33}$$

where the density $n_{w,a}$ is part of the solution and is defined by the penetration condition $\tilde{u}_{y,a}(\pm H/2) = \tilde{U}_w$ at the two plates, while $T_{w,a}$ is the plate temperature. The boundary conditions (4.33) satisfy that the macroscopic velocity $\tilde{y}$-component is equal to $\tilde{U}_w$.

The unknown distribution function can be linearized due to the smallness of the driving gradients as

$$f = f_0^M\left[1 + X_P(h_P + h_{R,P}) + X_T(h_T + h_{R,T})\right], \tag{4.34}$$

where f_0^M is the global Maxwellian defined as

$$f_0^M = \frac{n_0}{\pi^{3/2} v_0^3} e^{-(\boldsymbol{c} - \boldsymbol{U}_w)^2}, \tag{4.35}$$

with $\boldsymbol{c} = \boldsymbol{\xi}/v_0$ being the dimensionless molecular velocity vector and $\boldsymbol{U_w} = (0, U_w, 0)$ denoting the injection velocity in vector form. The quantities h_P and h_T are the unknown perturbed distribution functions, while $h_{R,P}$ and $h_{R,T}$ are the reference perturbations given by

$$h_{R,P} = x, \quad h_{R,T} = x\left[\left(\boldsymbol{c} - \boldsymbol{U_w}\right)^2 - \frac{5}{2}\right]. \tag{4.36}$$

It is noted that, the present linearization differs from the typical linearization procedure of fully developed flows without injection/suction where the global Maxwellian is defined as $f_0^M = n_0 e^{-\boldsymbol{c}^2} \Big/ \left(\pi^{3/2} v_0^3\right)$. If the typical linearization is implemented in this type of flows, the resulting flow in the longitudinal direction is completely decoupled from the cross-flow generated by the injection and suction at the two plates. In addition, it is worthwhile to mention that as a result of the implemented linearization, the reference perturbation $h_{R,T}$, given in Eq. (4.36), differs from the typical one, which is $h_{R,T} = x\left(\boldsymbol{c}^2 - 5/2\right)$.

Substituting Eqs. (4.34)-(4.36) into Eq. (4.28) and introducing the dimensionless quantities, yields the linearized S kinetic model equation

$$c_y \frac{\partial h_a}{\partial y} + \delta h_a = 2\delta u_{x,a} c_x + \frac{4}{15}\delta q_{x,a} c_x \left[\left(\boldsymbol{c} - \boldsymbol{U_w}\right)^2 - \frac{5}{2}\right] + s'_a, \tag{4.37}$$

where s'_a is the source term corresponding to the pressure and temperature driven flow, given by

$$s'_P = -c_x, \quad s'_T = -c_x\left[\left(\boldsymbol{c} - \boldsymbol{U_w}\right)^2 - \frac{5}{2}\right]. \tag{4.38}$$

The linearization and non-dimensionalization is also applied to the velocity and shear stress, as well as to the heat flux given in Eqs. (4.30)-(4.32) to obtain

$$u_{x,a}(y) = \frac{1}{\pi^{3/2}} \int c_x h_a(y, \boldsymbol{c})\, e^{-\left(\boldsymbol{c} - \boldsymbol{U_w}\right)^2} d\boldsymbol{c}, \tag{4.39}$$

$$\Pi_{xy,a}(y) = \frac{2}{\pi^{3/2}} \int c_x \left(c_y - U_w\right) h_a(y, \boldsymbol{c})\, e^{-\left(\boldsymbol{c} - \boldsymbol{U_w}\right)^2} d\boldsymbol{c}, \tag{4.40}$$

$$q_{x,a}(y) = \frac{1}{\pi^{3/2}} \int c_x \left[\left(\boldsymbol{c} - \boldsymbol{U_w}\right)^2 - \frac{5}{2}\right] h_a(y, \boldsymbol{c})\, e^{-\left(\boldsymbol{c} - \boldsymbol{U_w}\right)^2} d\boldsymbol{c}. \tag{4.41}$$

Finally, the linearized boundary conditions become

$$h_a^+(\pm 1/2, \boldsymbol{c}) = 0, \quad c_y \lessgtr 0. \tag{4.42}$$

At this stage the x and z molecular velocity components may be eliminated, in order to significantly reduce the required computational cost, by applying the so-called projection procedure and introducing the following reduced perturbed distribution functions:

$$Y_a\left(y,c_y\right)=\frac{1}{\pi}\int_{-\infty}^{+\infty}\int_{-\infty}^{+\infty}c_x h_a\left(y,\boldsymbol{c}\right)e^{-\left(c_x^2+c_z^2\right)}dc_x dc_z \tag{4.43}$$

$$F_a\left(y,c_y\right)=\frac{1}{\pi}\int_{-\infty}^{+\infty}\int_{-\infty}^{+\infty}c_x\left(c_x^2+c_z^2-2\right)h_a\left(y,\boldsymbol{c}\right)e^{-\left(c_x^2+c_z^2\right)}dc_x dc_z \tag{4.44}$$

Equation (4.37) is multiplied by $(1/\pi)\,c_x e^{-\left(c_x^2+c_z^2\right)}$ and $(1/\pi)\,c_x\left(c_x^2+c_y^2-2\right)e^{-\left(c_x^2+c_z^2\right)}$ successively and the resulting equations are integrated over c_x and c_z to yield

$$c_y\frac{\partial Y_a}{\partial y}+\delta Y_a=\delta u_{x,a}+\frac{2}{15}\delta q_{x,a}\left[\left(c_y-U_w\right)^2-\frac{1}{2}\right]+s_{Y,a}, \tag{4.45}$$

$$c_y\frac{\partial F_a}{\partial y}+\delta F_a=\frac{4}{15}\delta q_{x,a}+s_{F,a}, \tag{4.46}$$

where the reduced source terms $s_{Y,a}$ and $s_{F,a}$ are given by

$$s_{Y,P}=-\frac{1}{2},\quad s_{Y,T}=-\frac{1}{2}\left[\left(c_y-U_w\right)^2-\frac{1}{2}\right],\quad s_{F,P}=0,\quad s_{F,T}=-1. \tag{4.47}$$

Operating in a similar manner on Eqs. (4.39)-(4.41), the macroscopic velocity, shear stress and heat flux are written as

$$u_{x,a}=\frac{1}{\sqrt{\pi}}\int_{-\infty}^{+\infty}Y_a\left(y,c_y\right)e^{-\left(c_y-U_w\right)^2}dc_y, \tag{4.48}$$

$$\Pi_{xy,a}=\frac{2}{\sqrt{\pi}}\int_{-\infty}^{+\infty}\left(c_y-U_w\right)Y_a\left(y,c_y\right)e^{-\left(c_y-U_w\right)^2}dc_y, \tag{4.49}$$

$$q_{x,a}=\frac{1}{\sqrt{\pi}}\int_{-\infty}^{+\infty}\left\{\left[\left(c_y-U_w\right)^2-\frac{1}{2}\right]Y_a\left(y,c_y\right)+F_a\left(y,c_y\right)\right\}e^{-\left(c_y-U_w\right)^2}dc_y. \tag{4.50}$$

The corresponding boundary conditions may be readily deduced:

$$Y_a\left(\pm 1/2,c_y\right)=0,\quad c_y\lessgtr 0,\quad F_a\left(\pm 1/2,c_y\right)=0,\quad c_y\lessgtr 0 \tag{4.51}$$

4.2.4 Synthetic acceleration scheme for the linearized Shakhov model

The discrete velocity method (DVM) that has been thoroughly described and successfully used in Chapter 3 for the solution of the linearized Boltzmann equation may also be implemented here. In this method the continuum molecular velocity space is replaced by a set of discrete velocities and a typical finite difference or control volume scheme is used for the physical space. The macroscopic quantities of interest are computed via numerical integration as moments of the distribution function. In the case of kinetic models, the resulting system of discretized equations is solved in an iterative manner between the kinetic equation and the macroscopic quantities. However, it is well-established that the described iterative scheme suffers from slow convergence at the slip and hydrodynamic regime [50, 51].

In the present work, the solution of the linearized S model is required in the whole range of the rarefaction parameter. Thus, in order to circumvent the aforementioned convergence pitfall, the full-range moment synthetic acceleration scheme described in [50] is implemented. Synthetic acceleration schemes couple the kinetic equation with a system of moment equations. These moment equations are derived by operating on the kinetic equation in a systematic manner that will be thoroughly addressed below. The high order moments needed to close the system of moment equations are computed by numerically integrating the distribution function. The updated values of the accelerated macroscopic quantities are obtained by solving the moment equations and not by directly integrating the distribution function. This advanced iteration scheme shows rapid convergence especially as the rarefaction parameter is increased.

First the discretization used in this work is discussed and then the synthetic acceleration scheme is constructed. The continuum molecular velocity variable c_y is replaced by a set of Nc_y discrete velocities with their own weights Wc_y. The positive part of c_y is replaced by $Nc_y/2$ discrete velocities, which are taken to be the roots of the half-range Hermite polynomials of degree $Nc_y/2$. The negative part is also replaced by $Nc_y/2$ discrete velocities, which are taken to be symmetrical to the positive part with respect to the origin. The discretization of the physical space is based on a second order central difference scheme, where the flow domain $y \in [-1/2, 1/2]$ is divided into Ny evenly distributed segments.

In order to construct the full-range acceleration scheme, the following moments of the reduced distribution functions Y_a and F_a are used:

$$M_{m,a}(y) = \frac{1}{\sqrt{\pi}} \int_{-\infty}^{+\infty} H_m(c_y)\, Y_a(y, c_y)\, e^{-(c_y - U_w)^2} dc_y \tag{4.52}$$

$$N_{m,a}(y) = \frac{1}{\sqrt{\pi}} \int_{-\infty}^{+\infty} H_m(c_y)\, F_a(y, c_y)\, e^{-(c_y - U_w)^2} dc_y \tag{4.53}$$

The quantity $H_m(c_y)$ denotes the full-range Hermite polynomial of order m, satisfying the orthogonality condition

$$\int_{-\infty}^{+\infty} H_m(x)\, H_n(x)\, e^{-x^2} dx = \sqrt{\pi} 2^m m! \delta_{K,mn}, \tag{4.54}$$

where $\delta_{K,mn}$ denotes the Kronecker delta. The first five full-range Hermite polynomials are

$$H_0 = 1, \;\; H_1 = 2x, \;\; H_2 = 4x^2 - 2, \;\; H_3 = 8x^3 - 12x, \;\; H_4 = 16x^4 - 48x^2 + 12. \tag{4.55}$$

Then, the macroscopic velocity and heat flux are obtained from Eqs. (4.48) and (4.50) in terms of the introduced full-range moments:

$$u_{x,a} = M_{0,a} \tag{4.56}$$

$$q_{x,a} = \frac{1}{4} M_{2,a} - U_w M_{1,a} + U_w^2 M_{0,a} + N_{0,a} \tag{4.57}$$

It is noted here that, the shear stress is not accelerated since it does not contribute to the S model collision part and thus, it is directly computed from the reduced distribution functions via Eq. (4.49). Next, the integral operator $\frac{1}{\sqrt{\pi}} \int_{-\infty}^{+\infty} (\cdot)\, c_y^n e^{-(c_y - U_w)^2} dc_y$ is applied on Eq. (4.45) for $n = 0, 1, 2, 3$ and on Eq. (4.46) for $n = 0, 1$. After, some mathematical manipulations the following set of second order ordinary differential equations is derived:

$$\frac{d^2 M_{1,a}}{dy^2} = 0 \tag{4.58}$$

$$\frac{1}{2} \frac{d^2 M_{0,a}}{dy^2} - \delta U_w \frac{dM_{0,a}}{dy} = -\frac{1}{4} \frac{d^2 M_{2,a}}{dy^2} - \delta g_{a,0} \tag{4.59}$$

$$\frac{3}{4}\frac{d^2M_{2,a}}{dy^2}-\frac{\delta U_w}{20}\frac{dM_{2,a}}{dy}-\frac{7\delta^2}{30}M_{2,a}=-\frac{1}{16}\frac{d^2M_{4,a}}{dy^2}-\frac{\delta U_w^2}{5}\frac{dM_{1,a}}{dy}+\frac{\delta^2U_w}{15}M_{1,a}$$
$$-\frac{3}{4}\frac{d^2M_{0,a}}{dy^2}+\delta U_w\left(\frac{6U_w^2}{5}+\frac{3}{2}\right)\frac{dM_{0,a}}{dy}-\frac{16\delta^2U_w^2}{15}M_{0,a} \tag{4.60}$$
$$+\frac{\delta U_w}{5}\frac{dN_{0,a}}{dy}-\frac{\delta^2}{15}N_{0,a}-\delta g_{a,1}$$

$$\frac{1}{2}\frac{d^2N_{0,a}}{dy^2}-\frac{4\delta U_w}{15}\frac{dN_{0,a}}{dy}-\frac{11\delta^2}{15}N_{0,a}=-\frac{1}{4}\frac{d^2N_{2,a}}{d^2y}+\frac{\delta U_w}{15}\frac{dM_{2,a}}{dy}-\frac{\delta^2}{15}M_{2,a}$$
$$-\frac{4\delta U_w^2}{15}\frac{dM_{1,a}}{dy}+\frac{4\delta^2U_w}{15}M_{1,a}+\frac{4\delta U_w^3}{15}\frac{dM_{0,a}}{dy}-\frac{4\delta^2U_w^2}{15}M_{0,a}-\delta g_{a,2} \tag{4.61}$$

The quantities $g_{a,0}$, $g_{a,1}$ and $g_{a,2}$ read as

$$\begin{aligned} g_{P,0}&=\frac{1}{2},\quad g_{P,1}=\frac{1}{4}\left(1+2U_w^2\right),\quad g_{P,2}=0,\\ g_{T,0}&=\frac{1}{8},\quad g_{T,1}=\frac{1}{16}\left(5+2U_w^2\right),\quad g_{T,2}=1. \end{aligned} \tag{4.62}$$

By discretizing Eqs. (4.58)-(4.61) a tridiagonal linear system of algebraic equations is obtained for each one of them, which can be solved by applying the Thomas algorithm. However, since Eqs. (4.59)-(4.61) are coupled, they are iteratively solved until convergence.

The iterative map for the full-range synthetic acceleration scheme is constructed as follows: An initial guess is made for the velocity and heat flux distributions and Eqs. (4.45) and (4.46) are solved for the reduced distribution functions Y_a and F_a, respectively. The reduced distribution functions are then used to provide the boundary conditions and the higher order moments in the right hand side of the ordinary differential equations (4.58)-(4.61). Next, the aforementioned set of equations is solved for the moments $M_{0,a}$, $M_{1,a}$, $M_{2,a}$, $N_{0,a}$ and the accelerated macroscopic velocity and heat flux are computed via Eqs. (4.56) and (4.57). respectively. The updated macroscopic quantities are substituted back into Eqs. (4.45) and (4.46) to continue the iterative procedure, which converges when the following criteria are fulfilled

$$\frac{1}{2}\left(\left|u_{x,a,i}^{(k)}-u_{x,a,i}^{(k-1)}\right|+\left|q_{x,a,i}^{(k)}-q_{x,a,i}^{(k-1)}\right|\right)<\varepsilon,\quad i=1,2,...,Ny+1. \tag{4.63}$$

Here k is the iteration index, i is the physical node index and ε is the tolerance parameter. In addition, when the iterative scheme is completed the shear stress distribution is computed via Eq. (4.49) and the Simpson rule is used to compute the kinetic coefficients G_a and Q_a.

4.2.5 Formulation of the linearized Boltzmann equation

Following the same linearization described in Section 4.2.3 the steady-state linearized Boltzmann equation for the fully-developed Poiseuille and thermal creep flow in a channel with uniform injection/suction through its permeable walls becomes

$$c_y \frac{\partial h_a(y,\boldsymbol{c})}{\partial y} = 2\mu\delta L'_a(h_a) + s'_a(\boldsymbol{c}), \tag{4.64}$$

where $s'_a(\boldsymbol{c})$ denotes the source term for the Poiseuille and thermal creep flow

$$s'_P(\boldsymbol{c}) = -c_x, \quad s'_T(\boldsymbol{c}) = -c_x\left[(\boldsymbol{c}-\boldsymbol{U_w})^2 - \frac{5}{2}\right]. \tag{4.65}$$

It is reminded here that, $\mu = \tilde{\mu}d^2/mv_0$ (d is the molecular diameter) denotes the dimensionless gas viscosity, which for a hard-sphere gas has been computed in Chapter 3. The linearized collision operator $L'_a(h_a)$ reads as

$$L'_a(h_a) = \frac{1}{\pi^{3/2}}\int K'(\boldsymbol{c},\boldsymbol{c}_1)\left[h_a(y,\boldsymbol{c}_1) - \frac{c_{1,y}}{c_y}h_a(y,\boldsymbol{c})\right]e^{-\boldsymbol{c}_1^2}d\boldsymbol{c}_1, \tag{4.66}$$

with

$$K'(\boldsymbol{c},\boldsymbol{c}_1) = \pi g\left\{\frac{2}{g^2}\exp\left[\frac{|(c-\boldsymbol{U_w})\times(c_1-\boldsymbol{U_w})|}{g}\right] - 1\right\}, \tag{4.67}$$

where $\Psi = c_y$ (momentum conservation in the y direction) has been used.

At this stage, in order to reduce the required computational effort for the solution of Eq. (4.64) the number of molecular space velocity components may be reduced, as described in [63], by introducing cylindrical coordinates

$$c_x = c_r\sin\theta, \quad c_y = c_y, \quad c_z = c_r\cos\theta. \tag{4.68}$$

Then, the perturbed distribution function can be written as

$$h_a(y,c_x,c_y,c_z) = \psi_a(y,c_y,c_r)\cos\theta. \tag{4.69}$$

Substituting Eqs. (4.68) and (4.69) in the linearized Boltzmann equation (4.64), yields

$$c_y\frac{\partial\psi_a}{\partial y} = 2\mu\delta L_a(\psi_a) + s_a, \quad s_P = -c_r, \quad s_T = -c_r\left[(c_y-U_w)^2 + c_r^2 - \frac{5}{2}\right], \tag{4.70}$$

where the linearized collision operator becomes

$$L_\alpha\left(\psi_\alpha\right)=\frac{1}{\pi^{3/2}}\int_{-\infty}^{+\infty}\int_{0}^{+\infty}\hat{K}\left(c_y,c_r,c_{1,y},c_{1,r}\right)\times \\ \left[\psi_\alpha\left(y,c_{1,y},c_{1,r}\right)-\frac{c_{1,y}}{c_y}\psi_\alpha\left(y,c_y,c_r\right)\right]c_{1,r}e^{-\left(c_{1,y}^2+c_{1,r}^2\right)}dc_{1,r}dc_{1,y}, \tag{4.71}$$

with

$$\hat{K}\left(c_y,c_r,c_{1,y},c_{1,r}\right)=2\int_0^\pi K\left(c_y,c_r,c_{1,y},c_{1,r},\beta\right)\cos\beta d\beta. \tag{4.72}$$

The kernel $K\left(c_y,c_r,c_{1,y},c_{1,r},\beta\right)$ is given by Eq. (4.67). The corresponding boundary conditions are readily deduced

$$\psi_a\left(\pm 1/2,c_y,c_r\right)=0,\quad c_y\lessgtr 0. \tag{4.73}$$

Performing the corresponding mathematical manipulations on Eqs. (4.39)-(4.41) the velocity, shear stress and heat flux are written as follows:

$$u_{x,a}=\frac{1}{\sqrt{\pi}}\int_{-\infty}^{+\infty}\int_{0}^{+\infty}c_r^2\psi_a(y,c_y,c_r)e^{-\left[(c_y-U_w)^2+c_r^2\right]}dc_rdc_y \tag{4.74}$$

$$\Pi_{xy,a}=\frac{2}{\sqrt{\pi}}\int_{-\infty}^{+\infty}\int_{0}^{+\infty}c_r^2\left(c_y-U_w\right)\psi_a(y,c_y,c_r)e^{-\left[(c_y-U_w)^2+c_y^2\right]}dc_rdc_y \tag{4.75}$$

$$q_{x,a}=\frac{1}{\sqrt{\pi}}\int_{-\infty}^{+\infty}\int_{0}^{+\infty}c_r^2\left\{\left[\left(c_y-U_w\right)^2+c_r^2\right]-\frac{5}{2}\right\}\psi_a(y,c_y,c_r)e^{-\left[(c_y-U_w)^2+c_r^2\right]}dc_rdc_y \tag{4.76}$$

The formulation of the Boltzmann equation is now properly defined by Eq. (4.70) with the corresponding boundary conditions (4.73). The solution of the Boltzmann equation is based on the discrete velocity method that has been described in detail in Chapter 3. The iterative scheme implemented to solve the discretized equations is concluded when the criteria (4.63) are fulfilled.

4.2.6 Analytical solution in the free-molecular regime

At the free-molecular regime analytical expressions can be obtained for the macroscopic quantities and the kinetic coefficients by decomposing the perturbed distribution

function into two parts as

$$h_a\left(y,\boldsymbol{c}\right)=h_{a,0}\left(y,\boldsymbol{c}\right)+h_{a,1}\left(y,\boldsymbol{c}\right). \tag{4.77}$$

Equation (4.77) is substituted in Eq. (4.37) to obtain the two following equations:

$$c_y\frac{\partial h_{a,0}}{\partial y}+\delta h_{a,0}=s_a' \tag{4.78}$$

$$c_y\frac{\partial h_{a,1}}{\partial y}+\delta h_{a,1}=2\delta u_{x,a}c_x+\frac{4}{15}\delta q_{x,a}c_x\left[\left(\boldsymbol{c}-\boldsymbol{U_w}\right)^2-\frac{5}{2}\right] \tag{4.79}$$

As the rarefaction parameter tends to zero, the first term in the decomposition becomes the dominant one, while the second term vanishes. Then, Eq. (4.78) can be solved analytically using the boundary condition (4.42) to derive

$$h_{a,0}\left(y,\boldsymbol{c}\right)=\frac{{s'}_a}{\delta}\left[1-e^{-\frac{\delta(y+1/2)}{c_y}}\right],\ \ c_y>0, \tag{4.80}$$

$$h_{a,0}\left(y,\boldsymbol{c}\right)=\frac{{s'}_a}{\delta}\left[1-e^{-\frac{\delta(y-1/2)}{c_y}}\right],\ \ c_y<0. \tag{4.81}$$

Next, the velocity and heat flux can be obtained analytically by substituting Eqs. (4.80)-(4.81) into Eqs. (4.39) and (4.41):

$$u_{x,P}=-\frac{1}{2\delta}\left(1-\frac{1}{\sqrt{\pi}}I_0\right) \tag{4.82}$$

$$u_{x,\mathrm{T}}=q_{x,P}=\frac{1}{2\sqrt{\pi}\delta}\left(I_2-\frac{1}{2}I_0\right) \tag{4.83}$$

$$q_{x,T}=-\frac{1}{2\delta}\left[\frac{5}{2}-\frac{1}{\sqrt{\pi}}\left(I_4-I_2+\frac{9}{4}I_0\right)\right] \tag{4.84}$$

Here, the functions $I_n=I_n^+ + I_n^-$, $n=0,2,4,...$ are used, where I_n^+ and I_n^- are defined as

$$I_n^+=\int_0^{+\infty}\left(c_y-U_w\right)^n e^{-\frac{\delta(y+1/2)}{c_y}-\left(c_y-U_w\right)^2}dc_y, \tag{4.85}$$

$$I_n^-=\int_{-\infty}^{0}\left(c_y-U_w\right)^n e^{-\frac{\delta(y-1/2)}{c_y}-\left(c_y-U_w\right)^2}dc_y. \tag{4.86}$$

By substituting Eqs. (4.82)-(4.84) to the kinetic coefficient definitions (4.9) the analytical expressions for the kinetic coefficients are deduced in the free-molecular regime:

$$G_P = \frac{1}{\delta}\left(1 - \frac{U_w \mathrm{erf}\left(U_w\right)}{\delta} - \frac{e^{-U_w^2}}{\sqrt{\pi}\delta} - \frac{1}{\sqrt{\pi}}\hat{I}_0\right) \tag{4.87}$$

$$G_T = Q_P = \frac{1}{\sqrt{\pi}\delta}\left(\frac{e^{-U_w^2}}{2\delta} + \hat{I}_2 - \frac{1}{2}\hat{I}_0\right) \tag{4.88}$$

$$Q_T = \frac{1}{\delta}\left[\frac{5}{2} - \frac{5U_w \mathrm{erf}\left(U_w\right)}{2\delta} - \frac{\left(13 + 2U_w^2\right)e^{-U_w^2}}{4\sqrt{\pi}\delta} - \frac{1}{\sqrt{\pi}}\left(\hat{I}_4 - \hat{I}_2 + \frac{9}{4}\hat{I}_0\right)\right] \tag{4.89}$$

where the functions $\hat{I}_n = \hat{I}_n^- - \hat{I}_n^+$, $n = 0, 2, 4, ...$ are used, with $\hat{I}_n^+$ and $\hat{I}_n^-$ defined as

$$\hat{I}_n^+ = \frac{1}{\delta}\int_0^{+\infty} c_y (c_y - U_w)^n e^{-(c_y - U_w)^2 - \frac{\delta}{c_y}} dc_y, \tag{4.90}$$

$$\hat{I}_n^- = \frac{1}{\delta}\int_{-\infty}^{0} c_y (c_y - U_w)^n e^{-(c_y - U_w)^2 + \frac{\delta}{c_y}} dc_y. \tag{4.91}$$

Furthermore, it is important to derive the asymptotic behavior of the kinetic coefficients as $\delta \to 0$. Expanding $\hat{I}_n^+$ and $\hat{I}_n^-$ with respect to U_w and keeping only terms proportional to $\ln\delta$ the asymptotic behavior of the kinetic coefficients becomes:

$$G_P = -\frac{\ln\delta}{\sqrt{\pi}} e^{-U_w^2} \tag{4.92}$$

$$G_T = Q_P = -\frac{\ln\delta}{2\sqrt{\pi}}\left(1 - 2U_w^2\right)e^{-U_w^2} \tag{4.93}$$

$$Q_T = -\frac{\ln\delta}{\sqrt{\pi}}\left(U_w^4 - U_w^2 + \frac{9}{4}\right)e^{-U_w^2} \tag{4.94}$$

4.2.7 Computational efficiency of the acceleration scheme

The fully-developed Poiseuille and thermal creep flows between infinite parallel permeable plates with injection/suction are simulated via both the S model and BE in a wide range of the gas rarefaction parameter and injection velocity. The full-range synthetic acceleration scheme is implemented for the S model in order to reduce the computational cost and also to obtain results for large values of δ. In this section, the

computational effort of the full-range acceleration (FRA) scheme for rarefied gas flows coupled with injection and suction is compared to the non-accelerated (NA) scheme.

In Tables 4.1 and 4.2 the number of iterations and the computational time in seconds for the pressure driven case with the NA and FRA schemes are presented for $\delta \in [10^{-3}, 10^{2}]$ and $U_w = [0, 0.1, 0.3, 0.5]$. The presented results have been obtained for $Nc_y = 160$ discrete velocities and $Ny = 2 \times 10^4$ discrete segments, while the corresponding simulations have been performed on an Intel i5-3570 processor. The number of iterations required for the convergence of the NA scheme is significantly increased as δ is increased and as U_w is decreased. On the other hand, the required iterations for the FRA scheme are slightly increased as δ is increased, while for $\delta \geq 10$ they remain almost constant. In addition, the required iterations for the FRA scheme are only slightly increased for intermediate values of U_w. In addition, the required computational time per iteration for the FRA scheme is only slightly increased compared to the NA one. Thus, the remarks made for the number of iterations also apply to the computational time. It is evident that, the FRA scheme is far superior for $\delta \geq 10$, since both the number of iterations and computational time required, are at least one order of magnitude smaller compared to the NA scheme.

In Tables 4.3 and 4.4 the number of iterations and the computational time in seconds for the temperature driven case with the NA and FRA schemes are presented for $\delta \in [10^{-3}, 10^{2}]$ and $U_w = [0, 0.1, 0.3, 0.5]$. The required number of iterations and computational time for both the NA and FRA schemes for $\delta \geq 1$ is reduced in the temperature driven case compared to the pressure driven one. Furthermore, the remarks made above with regard to the required computational cost for the pressure driven case also apply here. Thus, the FRA scheme is also superior to the NA scheme in the case of the thermal creep flow.

4.2.8 Kinetic coefficients

In this section, the kinetic coefficients are provided based on the S model and the BE for the pressure and temperature driven flows. In addition, a comparison between the kinetic and the analytical results in the slip and free-molecular regimes is provided for all coefficients. However, since the solution of the BE requires significantly higher computational effort than the linearized S model, most of the presented results have been obtained by the S model, while the BE results are mostly used for benchmarking purposes. It is reminded here that, the results for the Poiseuille and thermal creep flows without injection/suction ($U_w = 0$) are not novel and have been obtained in

various previous works [60–66]. However, they are included here for completeness and comparison purposes. The presented results have been obtained by the linearized S model based on $Nc_y = 160$ discrete velocities and $Ny = 2 \times 10^4$, 2×10^5 and 2×10^6 segments for $\delta \leq 10^2$, $10^2 < \delta \leq 10^3$ and $10^3 < \delta \leq 10^4$, respectively. The results obtained by the BE are limited to $\delta \leq 10$ and are based on a set of $Nc_y = 2Nc_r = 160$ discrete velocities and $Ny = 5 \times 10^3$ segments.

In Fig. 4.1, the Poiseuille coefficient G_P, computed via the S model and the BE is presented in terms of $\delta \in [10^{-3}, 10^2]$ for $U_w = [0, 0.1, 0.3, 0.5]$. As the injection velocity is increased (cross-flow becomes more significant), G_P is monotonically decreased (bulk flow rate is reduced). For $U_w = 0$ the classical Poiseuille flow results without injection/suction are recovered. In this case, as it is well-known, when the flow is in the slip and hydrodynamic regimes ($\delta > 10$), G_P is proportional to δ. However, for $U_w > 0$ as δ is increased, G_P tends to the constant limit $1/(2U_w)$ (Eq. (4.23)). It is noted that, this behavior holds for all $U_w > 0$. Thus, even for negligible values of the injection velocity, the Poiseuille coefficient will tend to a constant value at adequately high values of the gas rarefaction parameter. Furthermore, as U_w increases, the well-known Knudsen minimum becomes gradually shallower. Finally, for $U_w = 0.5$ the Knudsen minimum vanishes and the Poiseuille coefficient tends monotonically to the viscous limit value as δ is increased. In the cases where the Knudsen minimum can be observed ($U_w \leq 0.3$), it appears at $\delta \sim 1$, similar to the classical Poiseuille flow without injection/suction. As expected from the asymptotic behavior (Eq. (4.92)) in the free-molecular limit ($\delta < 0.1$) it can be observed that the Poiseuille coefficient is proportional to $\ln \delta$ in the whole range of the injection velocity. Furthermore, for $\delta = 10^{-3}$ the S model and BE results deviate from the analytical ones (Eq. (4.87)) by less than 0.5% and 4% respectively. Comparing the linearized S model with the corresponding BE results, an excellent agreement is observed. The relative deviations are of the same order in the whole spectrum of U_w with the highest one reaching 4.8%.

In Table 4.5, the Poiseuille coefficient G_P obtained by the linearized S model is provided in the slip and hydrodynamic regimes $\delta \in [10, 10^4]$ for $U_w = [0, 0.1, 0.3, 0.5]$. In addition, the Poiseuille coefficient $G_P^{(s)}$ calculated by the analytical slip solution (4.22) is presented. Comparing G_P with the corresponding $G_P^{(s)}$, very good agreement can be observed for all injection velocities and the comparison between the kinetic and slip results improves as δ is increased. This comparison demonstrates the efficiency of the kinetic results to capture the analytical slip results for the Poiseuille coefficient, as well as, the range of validity of the slip solution depending on the required accuracy.

In Fig. 4.2, the reduced heat flux coefficient Q_T, computed via the linearized S model and BE is provided in terms of $\delta \in [10^{-3}, 10^2]$ for $U_w = [0, 0.1, 0.3, 0.5]$. It is observed that Q_T follows the same trend with respect to the rarefaction parameter for all values of the injection velocity. As δ is increased the heat flux is decreased monotonically and asymptotically tends to zero at the viscous regime. In addition, as δ is increased the effect of the injection velocity is drastically decreased. Furthermore, as U_w is increased, the reduced heat flux is monotonically decreased. Hence, it is noted that as the injection/suction cross flow becomes more significant heat transfer phenomena are hindered. The reduced heat flux coefficient is also proportional to $\ln \delta$ in the free-molecular limit ($\delta < 0.1$) in the whole spectrum of injection velocity and for $\delta = 10^{-3}$ the linearized S model and BE results deviate less than 0.7% and 5.6% from the analytical ones (Eq. (4.89)), respectively. As shown in Fig. 4.2, the corresponding linearized S model and BE results for the reduced heat flux coefficient Q_T are in excellent agreement. The relative deviation between the two approaches is of the same order for all investigated injection velocity values with the highest deviation reaching up to 6.4%.

In Table 4.6 the reduced heat flux coefficient Q_T obtained by the S model is tabulated in the slip and hydrodynamic regimes $\delta \in [10, 10^4]$ for $U_w = [0, 0.1, 0.3, 0.5]$. In addition, $Q_T^{(s)}$ calculated by the analytical slip solution (4.27) is provided. As discussed in Section 4.2.2, the analytical slip solution is independent from the injection velocity. More specifically, the analytical solution for the thermal creep flow with injection/suction ($U_w > 0$) reduces to the analytical solution without injection/suction ($U_w = 0$). In Table 4.6, the same behavior is observed for the kinetic results. As δ is increased the kinetic results do not depend on the injection velocity and tend to the results obtained for $U_w = 0$. In this latter case a great agreement between Q_T and $Q_T^{(s)}$ is observed. Moreover, the agreement between the kinetic and slip results is further improved as the rarefaction parameter is increased. This comparison demonstrates the accuracy of the kinetic results in the slip and hydrodynamic regimes for the temperature driven flow, as well as, the range of validity of the analytical slip solution.

Next, the so-called cross effects for the Poiseuille and thermal creep flows, namely the mechanocaloric Q_P and thermal creep G_T coefficients, are investigated. In Appendix B it has been proven that the Onsager-Casimir reciprocity relation $G_T = Q_P$ holds for arbitrary values of the injection velocity. The results presented for the thermal creep coefficient G_T are equal to the corresponding results for the mechanocaloric coefficient Q_P to at least six significant digits.

In Fig. 4.3, the thermal creep coefficient G_T computed by the linearized S model and the BE is presented with respect to $\delta \in [10^{-3}, 10^2]$ for $U_w = [0, 0.1, 0.3, 0.5, 0.7, 0.8]$. It is noted here that, additional results for $U_w > 0.5$ have been included to showcase the peculiar behavior observed for G_T, although the flow may not be isothermal for such high values of the injection velocity. More specifically, the thermal creep coefficient G_T is positive (gas flows from cold to hot regions) for $U_w \leq 0.7$ in the whole range of δ, while for $U_w > 0.7$ it becomes negative (gas flows from hot to cold regions) for small values of δ and becomes positive again as δ is increased. In both cases, G_T tends to zero at the slip and hydrodynamic regimes. This behavior is also validated from the asymptotic behavior of the thermal creep coefficient. It is readily seen that Eq. (4.93) provides a positive G_T for $U_w < \sqrt{1/2}$ and a negative one for $U_w > \sqrt{1/2}$. As the injection velocity is further increased the thermal creep coefficient is not decreased indefinitely, on the contrary it is decreased to a minimum and then it is increased again, tending to zero as $U_w \to \infty$. This behavior is to be expected, since as $U_w \to \infty$ flow phenomena in the longitudinal direction are expected to vanish. In addition, in the free-molecular regime and for $\delta = 10^{-3}$ the linearized S model and BE results deviate from analytical ones (Eq. (4.88)) by less than 0.8% and 13% respectively. The relative deviation between the linearized S model and BE results is increased with U_w and in this case the discrepancies are more significant with a highest relative deviation of about 20% for $U_w \leq 0.5$.

In Table 4.7, the thermal creep coefficient G_T obtained by the S model is presented in the slip and hydrodynamic regimes $\delta \in [10, 10^4]$ for $U_w = [0, 0.1, 0.3, 0.5]$. In addition, $G_T^{(s)}$ calculated by the analytical slip solution in Eq. (4.27) is provided. As already pointed out the analytical slip solution is independent from the injection velocity and reduces to the classical thermal creep solution without injection/suction. By comparing G_T and $G_T^{(s)}$, a good agreement can be observed for $U_w = 0$ and in this case, the agreement is improved as the rarefaction parameter is increased. However, as the injection velocity is increased the agreement between the kinetic and analytical slip results deteriorates. More specifically, as the rarefaction parameter is increased the kinetic and analytical slip results are inversely proportional to δ and the relative deviation between the two approaches tends to a constant value. This comparison demonstrates the accuracy of the kinetic results and the inefficiency of the analytical slip solution to accurately capture the cross effects G_T and Q_P.

4.2.9 Macroscopic distributions

In this section, the velocity, heat flux and shear stress distributions, computed by the S model are provided for the planar Poiseuille and thermal creep flows with injection/suction. In Fig. 4.4, the velocity distribution $u_{x,P}(y)$ is plotted in terms of y for $\delta = [10^{-2}, 0.1, 1, 10]$ and $U_w = [0, 0.1, 0.3, 0.5]$. In the case of $U_w = 0$, the velocity distribution takes the typical parabolic profile (symmetric about $y = 0.$), which becomes more acute as the rarefaction parameter is increased. As the injection velocity increases the parabolic profile changes and the velocity maximum shifts from the center of the flow domain towards the suction plate at $y = 1/2$. It is noted that, as δ increases the velocity maximum moves closer to the suction plate. In addition, for $U_w > 0$ and as δ increases the velocity profile tends to become linear near the injection plate and in the bulk of the flow ($y < 1/2$), while it suddenly drops close to the suction plate. It is noted that, the same behavior can be observed in the analytical slip solution from the velocity distribution limiting solutions (Eqs. (4.24) and (4.26)).

The heat flux distribution $q_{x,P}(y)$ is plotted in Fig. 4.5 with respect to y for $\delta = [10^{-2}, 0.1, 1, 10]$ and $U_w = [0, 0.1, 0.3, 0.5]$. For $U_w = 0$ the heat flux profile is parabolic and as δ increases the heat flux distribution becomes flatter. For $U_w \leq 0.3$, in the free-molecular and early transition regimes ($\delta \leq 1$) the heat flux profile is slightly altered and the minimum heat flux shifts towards the suction plate. As U_w is further increased the heat flux profile changes considerably and tends to become linear at the bulk of the flow with a shallow minimum inside the viscous layer close to the suction plate. In the late transition and slip regimes ($\delta > 1$) the heat flux distribution is drastically changed. More specifically, the profile curvature is significantly changed and a deep minimum is formed towards the suction plate. As U_w is increased the heat flux minimum becomes more acute and moves closer to the plate. Also, for $\delta \geq 0.1$ when the injection velocity is increased the heat flux changes sign and becomes positive near the injection plate.

The shear stress distribution $\Pi_{xy,P}(y)$ is presented in Fig. 4.6 in terms of y for $\delta = [10^{-2}, 0.1, 1, 10]$ and $U_w = [0, 0.1, 0.3, 0.5]$. For $U_w = 0$ the well-known shear stress profile, varying linearly between the limiting values of $-1/2$ and $1/2$ at the bottom and top plate is recovered. For $U_w > 0$ and small values of the rarefaction parameter ($\delta \leq 0.1$) the shear stress is monotonically decreased as the injection velocity is increased, while as the gas rarefaction parameter is further increased ($\delta \geq 1$) the shear stress is not monotonically decreased in the whole flow domain. More specifically,

for $U_w > 0$ and $\delta \geq 1$, the shear stress gradually tends to zero near the injection plate and in the bulk of the flow, while it rises rapidly towards the suction plate. This trend can also be verified from the analytical slip solutions for the shear stress distribution (Eqs. (4.24) and (4.26)).

In Fig. 4.7, the velocities $u_{x,P}(\mp 1/2)$ at the injection and suction plates are plotted with respect to $\delta \in [10^{-3}, 10^{4}]$ for $U_w = [0, 10^{-2}, 0.1, 0.3, 0.5]$. It can be seen that as U_w is increased, the velocity $u_{x,P}(-1/2)$ at the injection plate is monotonically decreased in the whole range of the rarefaction parameter, while the velocity $u_{x,P}(1/2)$ at the suction plate does not follow any particular trend. Furthermore, for high values of δ the velocity $u_{x,P}(-1/2)$ tends to zero for all $U_w > 0$, while the velocity $u_{x,P}(1/2)$ tends to different limiting values depending on U_w. One remark that can be made is that for very small values of U_w (i.e. $U_w = 10^{-2}$) at adequately high values of δ the velocity at the two boundaries does not tend to the same limit for $U_w = 0$. A similar observation has already been made in Section 4.2.2 for the analytical slip velocity (Eqs. (4.25) and (4.26)). In the case of $U_w = 0$, the analytical slip velocity at the bottom and top plate $u_P^{(s)}(\mp 1/2)$ tends to the same value of $\sigma_P/2$ for high values of δ, while it is clearly seen from the limiting slip solutions that, for U_w very close to zero, $u_P^{(s)}(-1/2)$ and $u_P^{(s)}(1/2)$ tend to zero and σ_P, respectively. All these observations are confirmed by the kinetic solution at high values of the gas rarefaction parameter.

The shear stresses $\Pi_{xy,P}(\mp 1/2)$ at the injection and suction plates are plotted in Fig. 4.8 in terms of $\delta \in [10^{-3}, 10^{4}]$ for $U_w = [0, 10^{-2}, 0.1, 0.3, 0.5]$. No monotonic trend can be observed for the shear stress at the two boundaries in the whole range of the rarefaction parameter. However, as δ is increased the shear stress $\Pi_{xy,P}(-1/2)$ at the injection plate always tends to zero, while the shear stress $\Pi_{xy,P}(1/2)$ at the suction plate tends to different limiting values based on the injection velocity. Similar to the velocity at the boundaries, it is also seen here that, for U_w very close to zero (i.e. $U_w = 10^{-2}$) the shear stress at the boundaries does not tend to the corresponding values for $U_w = 0$, which is also consistent to the behavior of the limiting cases for the analytical shear stress in the slip solution (Eqs. (4.25) and (4.26)). As pointed out in Section 4.2.2, for very small values of U_w the analytical shear stress at the injection plate $\Pi_{xy,P}^{(s)}(-1/2)$ tends to zero, instead of the typical value of $-1/2$ and at the suction plate $\Pi_{xy,P}^{(s)}(1/2)$ tends to one, instead of the typical value of $1/2$. Again these findings are in agreement with the kinetic results.

Moving on to the thermal creep flow, the velocity distribution $u_{x,T}(y)$ is plotted in Fig. 4.9 versus y for $\delta = [10^{-2}, 0.1, 1, 10]$ and $U_w = [0, 0.1, 0.3, 0.5]$. For $U_w = 0$, the

velocity distribution has a parabolic profile that becomes more acute as δ is increased. As U_w is increased, in the free-molecular and early transition regimes ($\delta \leq 1$), the macroscopic velocity is decreased near the injection plate and the bulk of the flow, while the velocity maximum moves from the flow center towards the suction plate. For high values of the injection velocity ($U_w > 0.3$) the macroscopic velocity is monotonically increased moving from the injection towards the suction plate for small values of the rarefaction parameter (i.e. for $\delta = 10^{-2}$), while as the rarefaction parameter is increased a velocity maximum can be observed inside the flow domain. In the late transition and slip regimes ($\delta > 1$), the velocity profile is significantly altered. More specifically, the velocity profile curvature changes and a velocity maximum, that becomes more acute as U_w is increased, is formed towards the suction plate.

In Fig. 4.10, the heat flux distribution $q_{x,T}(y)$ is presented in terms of y for $\delta = [10^{-2}, 0.1, 1, 10]$ and $U_w = [0, 0.1, 0.3, 0.5]$. In the case without injection/suction ($U_w = 0$), the heat flux distribution is parabolic. As U_w is increased, the heat flux is increased close to the injection plate and the minimum shifts close to the suction plate. As the gas rarefaction parameter is increased the injection velocity has a weaker effect on the heat flux distribution. This is also confirmed by the analytical slip solution (Eq. (4.27)) for the reduced heat flux, which is independent of the injection/suction velocity as already pointed out in Section 4.2.2.

In Fig. 4.11, the shear stress distribution $\Pi_{xy,T}(y)$ is plotted with respect to y for $\delta = [10^{-2}, 0.1, 1, 10]$ and $U_w = [0, 0.1, 0.3, 0.5]$. In the case without injection/suction ($U_w = 0$), the shear stress is zero in the whole flow domain. However, as the injection velocity is increased viscous forces start to appear. It can be observed that, in the free-molecular regime ($\delta \leq 10^{-2}$) the shear stress is negative in the whole flow domain for small and medium values of the injection velocity ($U_w \leq 0.3$). As both the rarefaction parameter and injection velocity are increased, the shear stress becomes positive close to the injection plate, while it either remains negative or also becomes positive close to the suction plate depending on the specific values of δ and U_w. In the late transition and slip regimes ($\delta \geq 10$), the shear stress profile is considerably changed. More specifically, the profile curvature is changed with a minimum appearing close to the suction plate.

4.3 Asymptotic suction flow

4.3.1 Flow configuration

Consider a monoatomic gas stream with velocity $\tilde{U}_\infty$ flowing over an infinite permeable plate located at $\tilde{y} = 0$. The bulk of the flow moves in the longitudinal $\tilde{x}$ direction, while the permeable plate produces a uniform downward suction with a constant suction velocity $\tilde{U}_w$. The flow may be fully characterized by the dimensionless suction velocity defined as

$$U_w = \frac{\tilde{U}_w}{v_0}. \tag{4.95}$$

Here, $v_0 = \sqrt{2R_g T_0}$ is the most probable velocity, where T_0 is the equilibrium temperature and $R_g = k_B/m$ is the specific gas constant, with k_B denoting the Boltzmann constant and m the gas molecular mass. The free stream velocity $\tilde{U}_\infty$ is assumed to be small compared the most probable velocity

$$X_U = \frac{\tilde{U}_\infty}{v_0} \ll 1 \tag{4.96}$$

and since the cross-flow stream velocity is constant, the gas flow may be treated as isothermal and fully-developed [33, 131, 133].

It is convenient to introduce the dimensionless spatial variables

$$x = \frac{\tilde{x}}{l_0}, \quad y = \frac{\tilde{y}}{l_0}, \tag{4.97}$$

where $l_0 = \tilde{\mu} v_0 / P_0$ is the equivalent free path, with $\tilde{\mu}$ denoting the gas viscosity and P_0 the equilibrium pressure. Moreover, the dimensionless macroscopic quantities of interest, namely the velocity, shear stress and heat flux are introduced

$$u_x(y) = \frac{\tilde{u}_x(\tilde{y})}{v_0 X_U}, \;\; \Pi_{xy}(y) = \frac{P_{xy}(\tilde{y})}{P_0 X_U}, \;\; q_x(y) = \frac{\tilde{q}_x(\tilde{y})}{v_0 P_0 X_U}. \tag{4.98}$$

The main quantity of interest for the investigated flow is the boundary layer thickness, which is defined by $\tilde{u}_x\left(\tilde{\delta}_L\right) = 0.99\tilde{U}_\infty$ and is written in dimensionless form as

$$\delta_L = \frac{\tilde{\delta}_L}{l_0}. \tag{4.99}$$

It is also useful to define the Knudsen number by taking the boundary layer thickness as the reference length of the flow

$$Kn = \frac{\sqrt{\pi}}{2\delta_L}. \tag{4.100}$$

4.3.2 Analytical solution in the slip and hydrodynamic regimes

At the hydrodynamic and slip regimes the asymptotic suction flow is governed by the x-momentum equation [131, 133]

$$-\tilde{\rho}\tilde{U}_w \frac{d\tilde{u}_x^{(j)}}{d\tilde{y}} = \tilde{\mu}\frac{d^2\tilde{u}_x^{(j)}}{d\tilde{y}^2}, \tag{4.101}$$

where $\tilde{\rho}$ is the gas density and the superscript $j = h,\ s$ denotes the hydrodynamic and slip regimes respectively. It is noted that, in the present notation $\tilde{U}_w$ is assumed positive or negative when suction or injection occurs at the plate, respectively. Introducing the dimensionless quantities defined in Eqs. (4.95)-(4.98) the x-momentum Eq. (4.101) may be given in dimensionless form

$$-2U_w \frac{du_x^{(j)}}{dy} = \frac{d^2u_x^{(j)}}{dy^2}. \tag{4.102}$$

In the hydrodynamic regime ($j = h$), Eq. (4.102) subject to the no-slip boundary condition at the permeable plate and the free stream boundary condition far away from the plate

$$u_x^{(h)}(0) = 0, \quad \lim_{y\to\infty} u_x^{(h)}(y) = 1, \tag{4.103}$$

may be solved analytically for $U_w > 0$ to obtain the velocity and shear stress distributions:

$$u_x^{(h)}(y) = 1 - e^{-2U_w y} \tag{4.104}$$

$$\Pi_{xy}^{(h)}(y) = -2U_w e^{-2U_w y} \tag{4.105}$$

It is evident from Eq. (4.104) that, U_w must be positive (wall suction), otherwise $u_x^{(h)}$ would be unbounded far away from the permeable plate [131]. In addition, the boundary layer thickness can be obtained by setting $u_x^{(h)} = 0.99$:

$$\delta_L^{(h)} = \frac{2.30259}{U_w} \tag{4.106}$$

In the slip regime ($j = s$), the slip boundary condition is applied at the permeable plate and the free stream boundary condition far away from the plate

$$u_x^{(s)}(0) = \sigma_P \frac{du_x^{(s)}}{dy}\bigg|_0, \quad \lim_{y\to\infty} u_x^{(s)}(y) = 1, \tag{4.107}$$

where the viscous slip coefficient σ_P is known and computed by solving the corresponding half-space flow problem [33]. Then, Eq. (4.102) subject to the boundary conditions (4.107) may be solved to provide the velocity and shear stress:

$$u_x^{(s)}(y) = 1 - \frac{e^{-2U_w y}}{1 + 2U_w\sigma_P} \tag{4.108}$$

$$\Pi_{xy}^{(s)}(y) = -\frac{2U_w e^{-2U_w y}}{1 + 2U_w\sigma_P} \tag{4.109}$$

Furthermore, the boundary layer thickness in the slip regime may be obtained:

$$\delta_L^{(s)} = \delta_L^{(h)} - \frac{\ln(1 + 2U_w\sigma_P)}{2U_w} \tag{4.110}$$

It is noted here that, since $U_w > 0$, the boundary layer thickness in the slip regime will always be smaller compared to the hydrodynamic one.

4.3.3 Formulation of the linearized Shakhov model

The Shakhov model equation for the aforementioned flow setup is written as

$$\boldsymbol{\xi}\frac{\partial f}{\partial \tilde{y}} = \frac{P}{\tilde{\mu}}\left[f^M\left\{1 + \frac{2m}{15n(k_BT)^2}\tilde{\boldsymbol{q}}\cdot(\boldsymbol{\xi}-\tilde{\boldsymbol{u}})\left[\frac{m(\boldsymbol{\xi}-\tilde{\boldsymbol{u}})^2}{2k_BT} - \frac{5}{2}\right]\right\} - f\right], \tag{4.111}$$

where $f = f(\tilde{y}, \boldsymbol{\xi})$ is the unknown distribution function, depending on the $\tilde{y}$ space variable and the molecular velocity vector $\boldsymbol{\xi} = (\xi_x, \xi_y, \xi_z)$. The quantity f^M denotes the local Maxwellian distribution defined as

$$f^M = n\left(\frac{m}{2\pi k_BT}\right)^{3/2}\exp\left[-\frac{m(\boldsymbol{\xi}-\tilde{\boldsymbol{u}})^2}{2k_BT}\right] \tag{4.112}$$

and $P/\tilde{\mu}$ approximates the collision frequency. The macroscopic quantities of interest, namely the velocity, shear stress and heat flux are defined as the first, second and third

moments of the unknown distribution function as

$$\tilde{\boldsymbol{u}}\left(\tilde{y}\right)=\frac{1}{n}\int\boldsymbol{\xi}f\left(\tilde{y},\boldsymbol{\xi}\right)d\boldsymbol{\xi}, \tag{4.113}$$

$$\Pi_{xy}\left(\tilde{y}\right)=m\int\zeta_x\zeta_y f\left(\tilde{y},\boldsymbol{\xi}\right)d\boldsymbol{\xi}, \tag{4.114}$$

$$\tilde{\boldsymbol{q}}\left(\tilde{y}\right)=\frac{m}{2}\int\boldsymbol{\zeta}^2\boldsymbol{\zeta}f\left(\tilde{y},\boldsymbol{\xi}\right)d\boldsymbol{\xi}, \tag{4.115}$$

where $\boldsymbol{\zeta}=\boldsymbol{\xi}-\tilde{\boldsymbol{u}}$ denotes the peculiar molecular velocity vector. The boundary condition on the suction plate is given by

$$f^{+}\left(0,\boldsymbol{\xi}\right)=n_w\Big(\frac{m}{2\pi k_B T_w}\Big)^{3/2}\exp\left[-\frac{m\left(\boldsymbol{\xi}-\tilde{\boldsymbol{U}}_{\boldsymbol{w}}\right)}{2k_B T_w}\right],\ \ \xi_y>0, \tag{4.116}$$

where the density n_w is part of the solution and is defined by the penetration condition $\tilde{u}_y\left(0\right)=-\tilde{U}_w$, while T_w is the plate temperature. The quantity $\tilde{\boldsymbol{U}}_{\boldsymbol{w}}=\left(0,-\tilde{U}_w,0\right)$ denotes the suction velocity in vector form. Far away from the suction plate the boundary condition is given by

$$\lim_{\tilde{y}\to\infty}f^{+}\left(\tilde{y},\boldsymbol{\xi}\right)=n_\infty\Big(\frac{m}{2\pi k_B T_\infty}\Big)^{3/2}\exp\left[-\frac{m\left(\boldsymbol{\xi}-\tilde{\boldsymbol{U}}_{\infty}\right)}{2k_B T_\infty}\right],\ \ \xi_y<0, \tag{4.117}$$

where n_∞, T_∞ and $\tilde{\boldsymbol{U}}_{\infty}=\left(\tilde{U}_\infty,0,0\right)$ denote the free stream number density, temperature and velocity vector, respectively.

The unknown distribution function can be linearized due to the smallness of the driving free stream velocity

$$f=f_0^M\left[1+X_U h\right], \tag{4.118}$$

where f_0^M denotes the global Maxwellian

$$f_0^M=\frac{n_0}{\pi^{3/2}v_0^3}e^{-(\boldsymbol{c}-\boldsymbol{U}_{\boldsymbol{w}})^2}, \tag{4.119}$$

with $\boldsymbol{c}=\boldsymbol{\xi}/v_0$ being the dimensionless molecular velocity vector and $\boldsymbol{U}_{\boldsymbol{w}}=(0,-U_w,0)$ denoting the dimensionless suction velocity in vector form. Substituting Eqs. (4.118) and (4.119) in Eq. (4.111) and introducing the dimensionless quantities in Eqs. (4.95)-

(4.98), yields the linearized S kinetic model equation

$$c_y \frac{\partial h}{\partial y} + h = 2u_x c_x + \frac{4}{15} q_x c_x \left[\left(\boldsymbol{c} - \boldsymbol{U_w} \right)^2 - \frac{5}{2} \right]. \tag{4.120}$$

In the same manner the dimensionless velocity, shear stress and heat flux are obtained:

$$u_x \left(y \right) = \frac{1}{\pi^{3/2}} \int c_x h e^{-\left(\boldsymbol{c} - \boldsymbol{U_w} \right)^2} d\mathbf{c} \tag{4.121}$$

$$\Pi_{xy} \left(y \right) = \frac{2}{\pi^{3/2}} \int c_x \left(c_y + U_w \right) h e^{-\left(\boldsymbol{c} - \boldsymbol{U_w} \right)^2} d\mathbf{c} \tag{4.122}$$

$$q_x \left(y \right) = \frac{1}{\pi^{3/2}} \int c_x \left[\left(\boldsymbol{c} - \boldsymbol{U_w} \right)^2 - \frac{5}{2} \right] h e^{-\left(\boldsymbol{c} - \boldsymbol{U_w} \right)^2} d\mathbf{c} \tag{4.123}$$

Finally, the linearized boundary conditions at the permeable plate and far away from the plate become

$$h^+ \left(0, \boldsymbol{c} \right) = 0, \quad c_y > 0, \tag{4.124}$$

$$\lim_{y \to \infty} h^+ \left(y, \boldsymbol{c} \right) = 0, \quad c_y < 0. \tag{4.125}$$

At this stage by introducing the following reduced perturbed distribution functions

$$Y \left(y, c_y \right) = \frac{1}{\pi} \int_{-\infty}^{+\infty} \int_{-\infty}^{+\infty} c_x h \left(y, \boldsymbol{c} \right) e^{-\left(c_x^2 + c_z^2 \right)} dc_x dc_z, \tag{4.126}$$

$$F \left(y, c_y \right) = \frac{1}{\pi} \int_{-\infty}^{+\infty} \int_{-\infty}^{+\infty} c_x \left(c_x^2 + c_z^2 - 2 \right) h \left(y, \boldsymbol{c} \right) e^{-\left(c_x^2 + c_z^2 \right)} dc_x dc_z, \tag{4.127}$$

the x and z molecular velocity components can be eliminated, in order to significantly reduce the required computational cost. Equation (4.120) is multiplied by $\left(1/\pi \right) c_x e^{-\left(c_x^2 + c_z^2 \right)}$ and $\left(1/\pi \right) c_x \left(c_x^2 + c_y^2 - 2 \right) e^{-\left(c_x^2 + c_z^2 \right)}$ successively and the resulting equations are integrated over c_x and c_z to yield

$$c_y \frac{\partial Y}{\partial y} + Y = u_x + \frac{2}{15} q_x \left[\left(c_y + U_w \right)^2 - \frac{1}{2} \right], \tag{4.128}$$

$$c_y \frac{\partial F}{\partial y} + F = \frac{4}{15} q_x. \tag{4.129}$$

Operating in a similar manner on Eqs. (4.121)-(4.123), the macroscopic velocity, shear stress and heat flux become

$$u_x(y) = \frac{1}{\sqrt{\pi}} \int_{-\infty}^{+\infty} Y(y, c_y)\, e^{-(c_y+U_w)^2} dc_y, \tag{4.130}$$

$$\Pi_{xy}(y) = \frac{2}{\sqrt{\pi}} \int_{-\infty}^{+\infty} (c_y + U_w)\, Y(y, c_y)\, e^{-(c_y+U_w)^2} dc_y, \tag{4.131}$$

$$q_x(y) = \frac{1}{\sqrt{\pi}} \int_{-\infty}^{+\infty} \left\{ \left[(c_y + U_w)^2 - \frac{1}{2} \right] Y(y, c_y) + F(y, c_y) \right\} e^{-(c_y+U_w)^2} dc_y. \tag{4.132}$$

The corresponding boundary conditions may be readily deduced

$$\begin{aligned} &Y(0, c_y > 0) = 0, \quad \lim_{y\to\infty} Y(y, c_y < 0) = 1, \\ &F(0, c_y > 0) = 0, \quad \lim_{y\to\infty} F(y, c_y < 0) = 0. \end{aligned} \tag{4.133}$$

At this point, the formulation of the S model is properly defined by Eqs. (4.128)-(4.129), with the associated Eqs. (4.130)-(4.132) and the corresponding boundary conditions (4.133). The deterministic numerical solution is based on the discrete velocity method. The continuum molecular velocity variable c_y is replaced by a set of Nc_y discrete velocities with their own weights Wc_y. The positive part of c_y is replaced by $Nc_y/2$ discrete velocities, which are taken to be the roots of the half-range Hermite polynomials of degree $Nc_y/2$. The negative part is also replaced by $Nc_y/2$ discrete velocities, which are taken to be symmetrical to the positive part with respect to the origin. The discretization of the physical space is based on a second order central difference scheme, where the flow domain $y \in [-1/2, 1/2]$ is divided into Ny evenly distributed segments. An iterative scheme is implemented to solve the discretized equations. The iteration map is concluded when the following criteria are fulfilled

$$\frac{1}{2}\left(\left| u_{x,a,i}^{(k)} - u_{x,a,i}^{(k-1)} \right| + \left| q_{x,a,i}^{(k)} - q_{x,a,i}^{(k-1)} \right| \right) < \varepsilon, \quad i = 1, 2, ..., Ny + 1. \tag{4.134}$$

Here k is the iteration index, i is the physical node index and ε is the tolerance parameter. The computational effort for the proposed scheme is increased as the suction velocity U_w is decreased. This is due to the fact that, as U_w is decreased a larger flow domain (i.e. high number of physical space segments) is required in order to satisfy the free steam boundary condition.

4.3.4 Boundary layer thickness and macroscopic distributions

The asymptotic suction flow is simulated via the linearized S kinetic model. The boundary layer thickness, along with the macroscopic quantities are provided in a wide range of the suction velocity. In addition, the corresponding results calculated via the analytical solutions provided in Section 4.3.2 for the slip and hydrodynamic regimes are also presented. The S model results have been obtained based on $Nc_y = 160$ discrete velocities. In the physical space $Ny = 10^5$ and $Ny = 10^4$ segments have been used for $U_w < 0.1$ and $U_w \geq 0.1$, respectively

In Table 4.8 the boundary layer thickness is provided based on the kinetic, slip and hydrodynamic approaches with respect to the suction velocity U_w. It is evident that, the boundary layer thickness is increased as the suction velocity U_w is decreased. This can be rationalized by considering that, the viscous layer ends when the suction velocity is balanced by the viscous diffusion velocity, which is inversely proportional to the boundary layer thickness [133]. A great agreement is observed between the kinetic and slip solution (4.110) for $U_w \leq 0.1$ ($Kn < 0.1$), while a good agreement between the kinetic and hydrodynamic solution (4.106) can only be observed for $U_w \leq 2 \times 10^{-2}$ ($Kn < 10^{-2}$). As expected, the agreement deteriorates in both cases as the suction velocity is increased i.e. as the boundary layer thickness is decreased. In addition, in the whole investigated suction velocity spectrum the slip solution underestimates, while the hydrodynamic solution overestimates the boundary layer thickness.

Next, the macroscopic quantities of interest, such as the velocity, shear stress and heat flux are provided. In Fig. 4.12, the macroscopic velocity computed via the S model, as well as, via the analytical slip and hydrodynamic velocity analytical expressions (4.104) and (4.108) are plotted with respect to the dimensionless spatial variable y for $U_w = [10^{-2}, 0.1, 0.3, 0.5]$. As expected, the macroscopic velocity tends to one far away from the suction plate and is monotonically decreased when approaching the suction plate. In addition, it is seen that, the velocity slip at the plate is increased as the suction velocity is increased. An excellent agreement between the kinetic, slip and hydrodynamic approaches can be observed for $U_w = 10^{-2}$, which deteriorates as the suction velocity is increased.

In Fig. 4.13, the shear stress distribution computed based on the S model, as well as, from the analytical slip and hydrodynamic velocity expressions (4.105) and (4.109) is presented in terms of y for $U_w = [10^{-2}, 0.1, 0.3, 0.5]$. As expected, the macroscopic shear stress is zero (macroscopic velocity is constant) outside of the boundary layer,

while inside the boundary layer viscous forces start to appear, becoming more significant closer to the suction plate. It is noted that, the shear stress acting on the plate is increased as the suction velocity is increased. The excellent agreement between the three approaches can also be observed for the shear stress in the case of $U_w = 10^{-2}$.

The heat flux distribution computed based on the S model is presented in terms of y for $U_w = [10^{-2}, 0.1, 0.3, 0.5]$ in Fig. 4.14. As expected, outside of the boundary layer the heat flux tends to zero, since, the flow is isothermal and the macroscopic velocity is constant. However, inside the boundary layer heat transfer phenomena start to appear. For small values of the suction velocity ($U_w < 0.1$) the heat flux at the plate is positive, while as the suction velocity is increased it becomes negative. In addition, moving away from the plate the heat flux distribution is initially decreased to a minimum and then it is increased tending to zero far away from the plate. It is also noted that, the heat flux minimum is inside the boundary layer and moves closer to the suction plate as the suction velocity is increased. These remarks hold even for $U_w = 10^{-2}$, although they are not clearly seen in Fig 4.14.

4.4 Concluding remarks

Overall, injection/suction flows have attracted considerable attention in the viscous regime due to their theoretical interest, as well as, due to their tentative importance in various technological applications. Here, fundamental injection/suction flow configurations, namely the planar fully-developed Poiseuille and thermal creep flow coupled with uniform injection/suction and the asymptotic suction flow are investigated in the whole range of rarefaction via deterministic kinetic modeling based on the S model and the BE.

In Section 4.2, the fully-developed Poiseuille and thermal creep rarefied gas flow between parallel permeable plates, with uniform gas injection and suction from the bottom and top plate, respectively, is investigated based on the linearized S model and BE. Both flows are characterized by the gas rarefaction parameter and injection velocity magnitude. First, the analytical slip and hydrodynamic solutions are provided and then, the linearization procedure required to tackle these flows is introduced and implemented to the S model and BE. In addition, a synthetic acceleration scheme is constructed for the solution of the S kinetic model. Furthermore, the analytical solution in the free-molecular regime is provided. The full-range acceleration scheme is found to be far superior to the non-accelerated scheme for large values of the

rarefaction parameter, while for small values of the rarefaction parameter they are similar in terms of computational effort. The analytical free-molecular and slip results for the kinetic coefficients are properly recovered by the kinetic solution at small and large values of the gas rarefaction parameter, respectively. The Poiseuille coefficient monotonically decreases when the injection velocity increases and tends to a constant value at dense atmospheres. Also, as the injection velocity increases, the well-known Knudsen minimum becomes gradually shallower and finally vanishes. The reduced heat flux, mechanocaloric and thermal creep coefficients are also decreased value as the injection velocity is increased. It has been found that, for adequately large values of the injection velocity the mechanocaloric and thermal creep coefficients change sign. Furthermore, the Onsager-Casimir reciprocity relation for the mechanocaloric and thermal creep coefficients has been proven and implemented to validate the accuracy of the presented results. Comparing the S model to the BE a great agreement has been observed for the Poiseuille and reduced heat flux coefficient and an adequate agreement for the mechanocaloric and thermal creep coefficients. In both flow setups, as the injection velocity is increased the velocity and heat flux distributions are significantly affected. The profiles are becoming non-symmetric and the velocity maximum and heat flux minimum are shifted from the flow domain center towards the suction plate. Furthermore, as the injection velocity is increased the shear stress distribution significantly deviates from the typical linear profile in the Poiseuille flow and the constant zero profile in the thermal creep flow.

In Section 4.3, the fully-developed rarefied gas flow over a permeable plate with uniform suction is investigated in a wide range of the suction velocity based on the S kinetic model. First, the analytical solutions in the slip and hydrodynamic regimes are provided and then, the S model is formulated based on the linearization procedure described in Section 4.2. The boundary layer thickness, as well as, the macroscopic velocity, shear stress and heat flux are provided based on the kinetic and viscous approaches. The boundary layer thickness is found to be inversely proportional to the suction velocity, as expected. The velocity and shear stress are one and zero outside of the boundary layer, respectively and are decreased close to the suction plate. On the other hand, a more complex behavior is obtained for the heat flux, which moving away from the suction plate is initially decreased to a minimum inside the boundary layer and then it is increased tending to zero far away from the suction plate.

Table 4.1 Number of iterations for the Poiseuille flow through a permeable channel with the NA and FRA schemes.

δ	NA				FRA			
	$U_w = 0$	$U_w = 0.1$	$U_w = 0.3$	$U_w = 0.5$	$U_w = 0$	$U_w = 0.1$	$U_w = 0.3$	$U_w = 0.5$
0.001	5	5	5	5	5	5	5	5
0.01	7	7	7	7	7	7	7	7
0.1	12	12	12	11	12	12	12	11
1	38	38	34	29	28	28	27	25
10	494	427	212	114	32	33	32	31
100	28304	3369	740	387	32	33	33	31

Table 4.2 Computational time [s] for the Poiseuille flow through a permeable channel with the NA and FRA schemes.

δ	NA				FRA			
	$U_w = 0$	$U_w = 0.1$	$U_w = 0.3$	$U_w = 0.5$	$U_w = 0$	$U_w = 0.1$	$U_w = 0.3$	$U_w = 0.5$
0.001	8.01(-1)	8.50(-1)	8.53(-1)	8.70(-1)	9.54(-1)	9.06(-1)	9.57(-1)	9.56(-1)
0.01	1.13	1.15	1.18	1.21	1.23	1.24	1.29	1.34
0.1	1.92	1.97	2.08	1.92	2.19	2.25	2.29	2.11
1	7.94	6.30	5.85	5.02	5.31	5.53	5.31	4.90
10	8.73(1)	7.01(1)	3.75(1)	2.03(1)	6.35	6.58	6.32	6.10
100	4.83(3)	5.61(2)	1.31(2)	6.83(1)	7.64	6.63	6.80	6.52

Table 4.3 Number of iterations for the thermal creep flow through a permeable channel with the NA and FRA schemes.

δ	NA				FRA			
	$U_w = 0$	$U_w = 0.1$	$U_w = 0.3$	$U_w = 0.5$	$U_w = 0$	$U_w = 0.1$	$U_w = 0.3$	$U_w = 0.5$
0.001	5	5	5	5	5	5	5	5
0.01	7	7	7	6	7	7	7	6
0.1	12	12	11	10	12	12	11	11
1	36	35	31	26	26	26	25	23
10	389	339	171	91	27	28	27	25
100	12469	2371	632	342	23	24	23	22

Table 4.4 Computational time [s] for the thermal creep flow through a permeable channel with the NA and FRA schemes.

δ	NA				FRA			
	$U_w = 0$	$U_w = 0.1$	$U_w = 0.3$	$U_w = 0.5$	$U_w = 0$	$U_w = 0.1$	$U_w = 0.3$	$U_w = 0.5$
0.001	8.29(-1)	8.36(-1)	8.30(-1)	8.91(-1)	9.68(-1)	9.52(-1)	9.58(-1)	9.85(-1)
0.01	1.13	1.17	1.28	1.01	1.39	1.30	1.33	1.11
0.1	1.98	1.96	1.96	1.71	2.36	2.32	2.11	2.10
1	5.86	5.75	5.49	4.46	5.06	5.08	4.87	4.48
10	6.35(1)	5.66(1)	2.94(1)	1.56(1)	5.23	5.45	5.25	4.85
100	2.03(3)	3.89(2)	1.10(2)	5.83(1)	4.42	4.85	4.57	4.26

Table 4.5 Kinetic and slip Poiseuille coefficients G_P and $G_P^{(s)}$ respectively, in terms of δ and U_w in the slip and hydrodynamic regimes.

δ	G_P				$G_P^{(s)}$			
	$U_w = 0$	$U_w = 0.1$	$U_w = 0.3$	$U_w = 0.5$	$U_w = 0$	$U_w = 0.1$	$U_w = 0.3$	$U_w = 0.5$
10	2.780	2.506	1.569	1.044	2.685	2.453	1.594	1.084
20	4.405	3.378	1.630	1.027	4.351	3.370	1.646	1.047
50	9.375	4.336	1.656	1.012	9.351	4.339	1.663	1.020
10^2	1.770(1)	4.676	1.662	1.006	1.768(1)	4.678	1.665	1.010
10^3	1.677(2)	4.968	1.666	1.001	1.677(2)	4.969	1.667	1.001
10^4	1.668(3)	4.997	1.667	1.000	1.668(3)	4.997	1.667	1.000

Table 4.6 Kinetic and slip reduced heat flux coefficients Q_T and $Q_T^{(s)}$ respectively, in terms of δ and U_w in the slip and hydrodynamic regimes.

δ	Q_T				$Q_T^{(s)}$)
	$U_w = 0$	$U_w = 0.1$	$U_w = 0.3$	$U_w = 0.5$	
10	3.406(-1)	3.400(-1)	3.360(-1)	3.305(-1)	3.750(-1)
20	1.789(-1)	1.787(-1)	1.777(-1)	1.763(-1)	1.875(-1)
50	7.362(-2)	7.359(-2)	7.343(-2)	7.321(-2)	7.500(-2)
10^2	3.716(-2)	3.715(-2)	3.711(-2)	3.705(-2)	3.750(-2)
10^3	3.747(-3)	3.746(-3)	3.746(-3)	3.746(-3)	3.750(-3)
10^4	3.750(-4)	3.750(-4)	3.750(-4)	3.750(-4)	3.750(-4)

Table 4.7 Kinetic and slip thermal creep coefficients G_T and $G_T^{(s)}$ respectively, in terms of δ and U_w in the slip and hydrodynamic regimes.

δ	$G_T = Q_P$				$G_T^{(s)} = Q_P^{(s)}$
	$U_w = 0$	$U_w = 0.1$	$U_w = 0.3$	$U_w = 0.5$	
10	9.815(-2)	8.873(-2)	5.256(-2)	2.779(-2)	1.175(-1)
20	5.385(-2)	4.586(-2)	2.591(-2)	1.421(-2)	5.875(-2)
50	2.271(-2)	1.800(-2)	1.022(-2)	5.758(-3)	2.350(-2)
10^2	1.155(-2)	8.906(-3)	5.087(-3)	2.891(-3)	1.175(-2)
10^3	1.173(-3)	8.823(-4)	5.065(-4)	2.903(-4)	1.175(-3)
10^4	1.175(-4)	8.814(-5)	5.063(-5)	2.904(-5)	1.175(-4)

Table 4.8 Asymptotic suction flow: Boundary layer thickness δ_L based on the kinetic, slip and hydrodynamic approaches in terms of the suction velocity U_w.

U_w	δ_L	$\delta_L^{(s)}$	$\delta_L^{(h)}$
0.01	2.293(2)	2.293(2)	2.303(2)
0.02	1.141(2)	1.141(2)	1.151(2)
0.05	4.508(1)	4.508(1)	4.605(1)
0.1	2.221(1)	2.210(1)	2.303(1)
0.2	1.095(1)	1.066(1)	1.151(1)
0.3	7.182	6.881	7.675
0.4	5.239	5.012	5.756
0.5	4.014	3.903	4.605

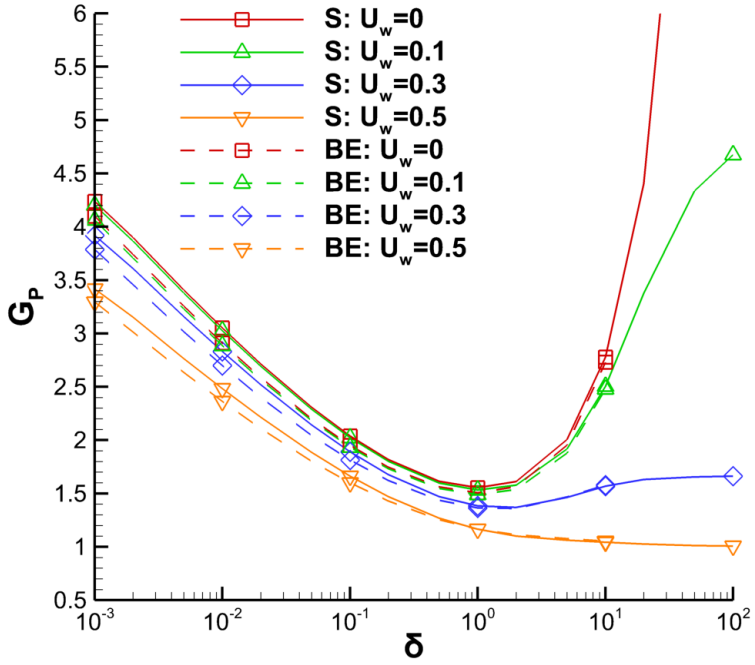

Figure 4.1 Poiseuille coefficient G_P in terms of the rarefaction parameter δ and injection velocity U_w; comparison between S and BE results.

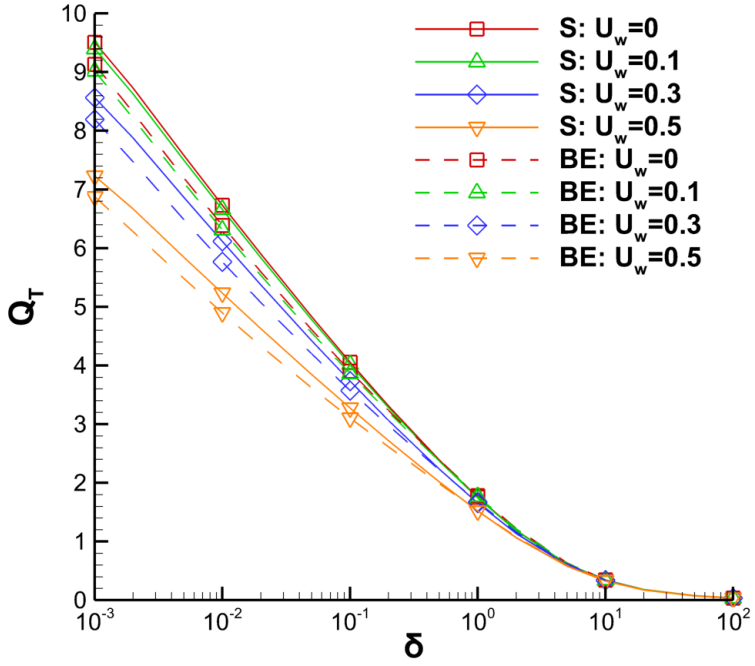

Figure 4.2 Heat flux coefficient Q_T in terms of the rarefaction parameter δ and injection velocity U_w; comparison between S and BE results.

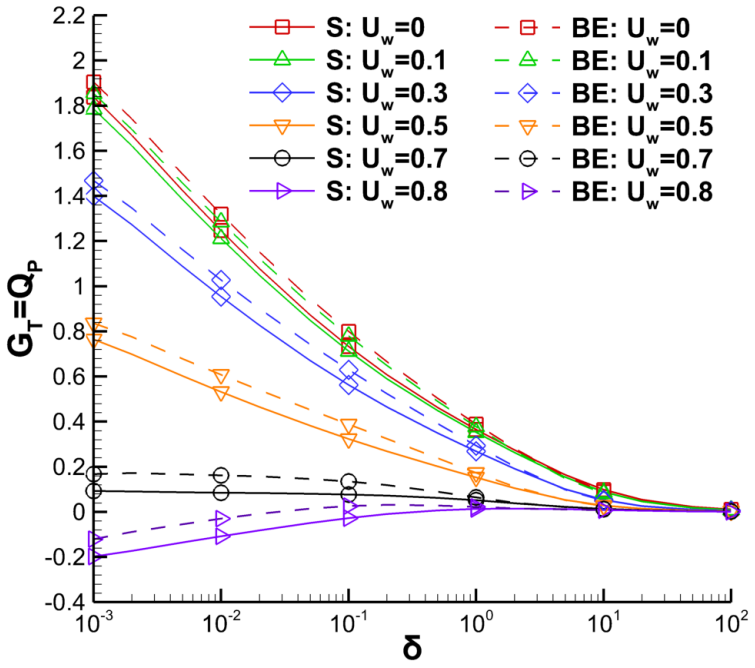

Figure 4.3 Thermal creep G_T and mechanocaloric Q_P coefficients ($G_T = Q_P$) in terms of the rarefaction parameter δ and injection velocity U_w; comparison between S and BE results.

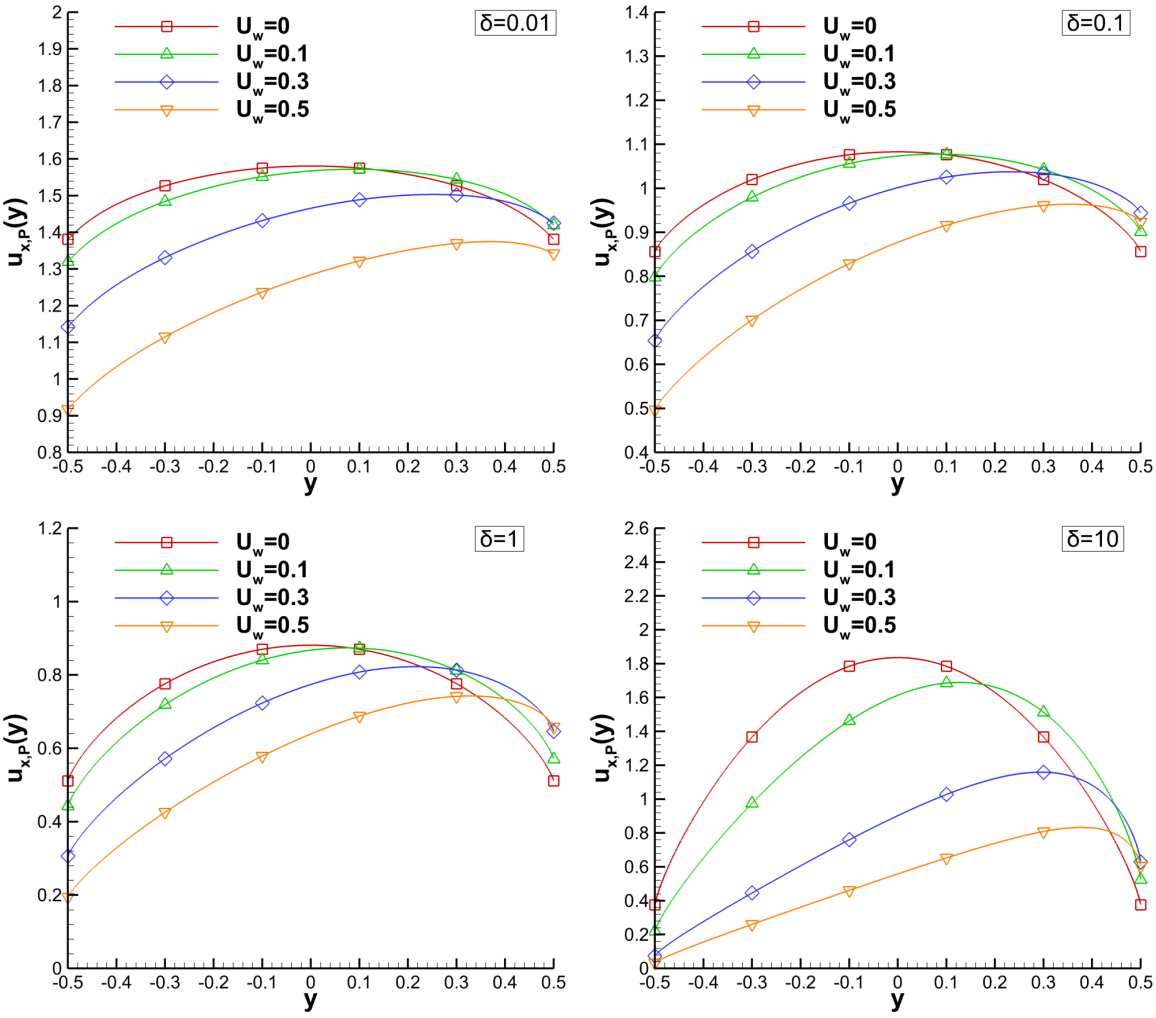

Figure 4.4 Velocity $u_{x,P}\,(y)$ for $\delta = [10^{-2}, 0.1, 1, 10]$ and $U_w = [0, 0.1, 0.3, 0.5]$.

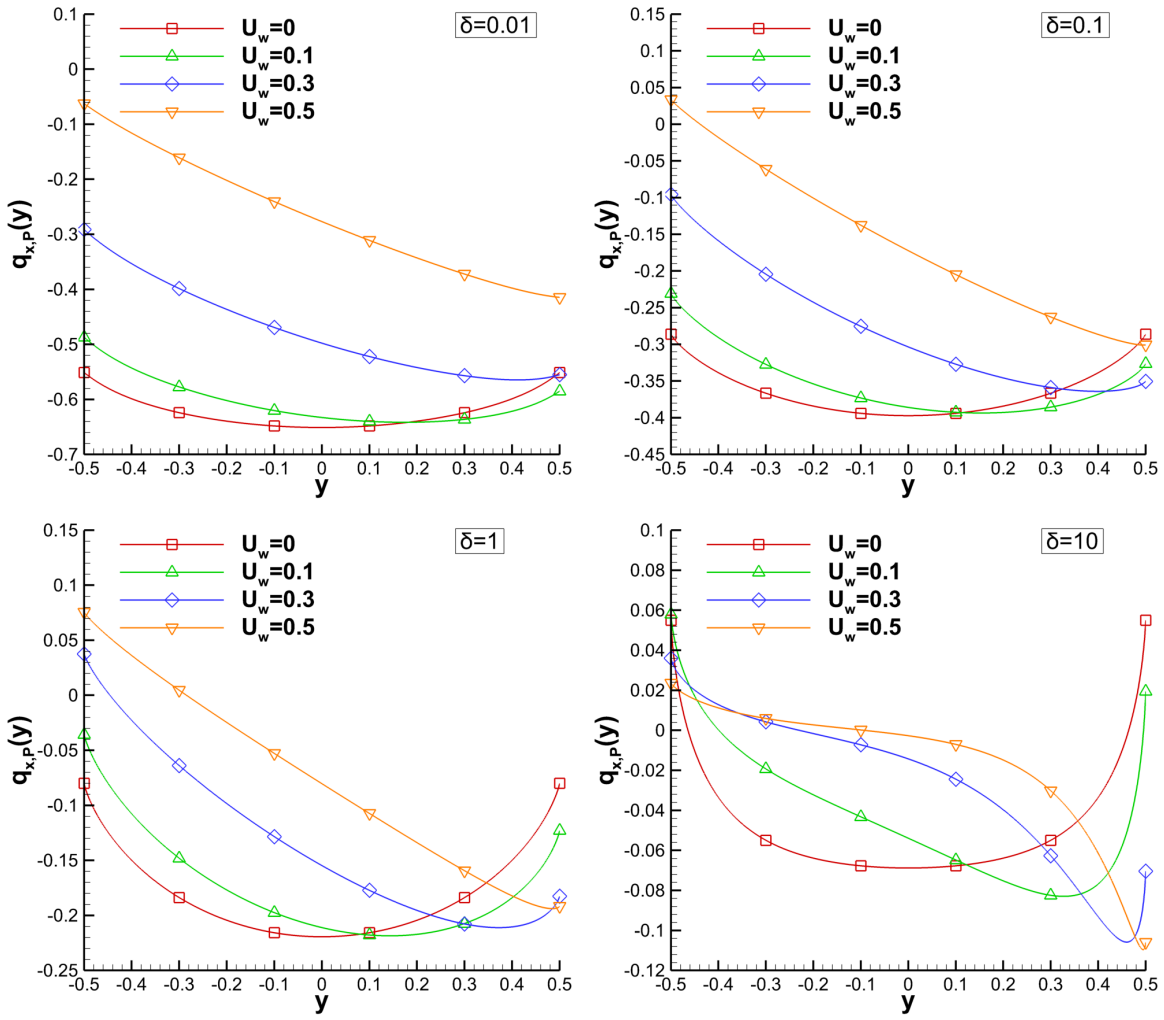

Figure 4.5 Heat flux $q_{x,P}(y)$ for $\delta = [10^{-2}, 0.1, 1, 10]$ and $U_w = [0, 0.1, 0.3, 0.5]$.

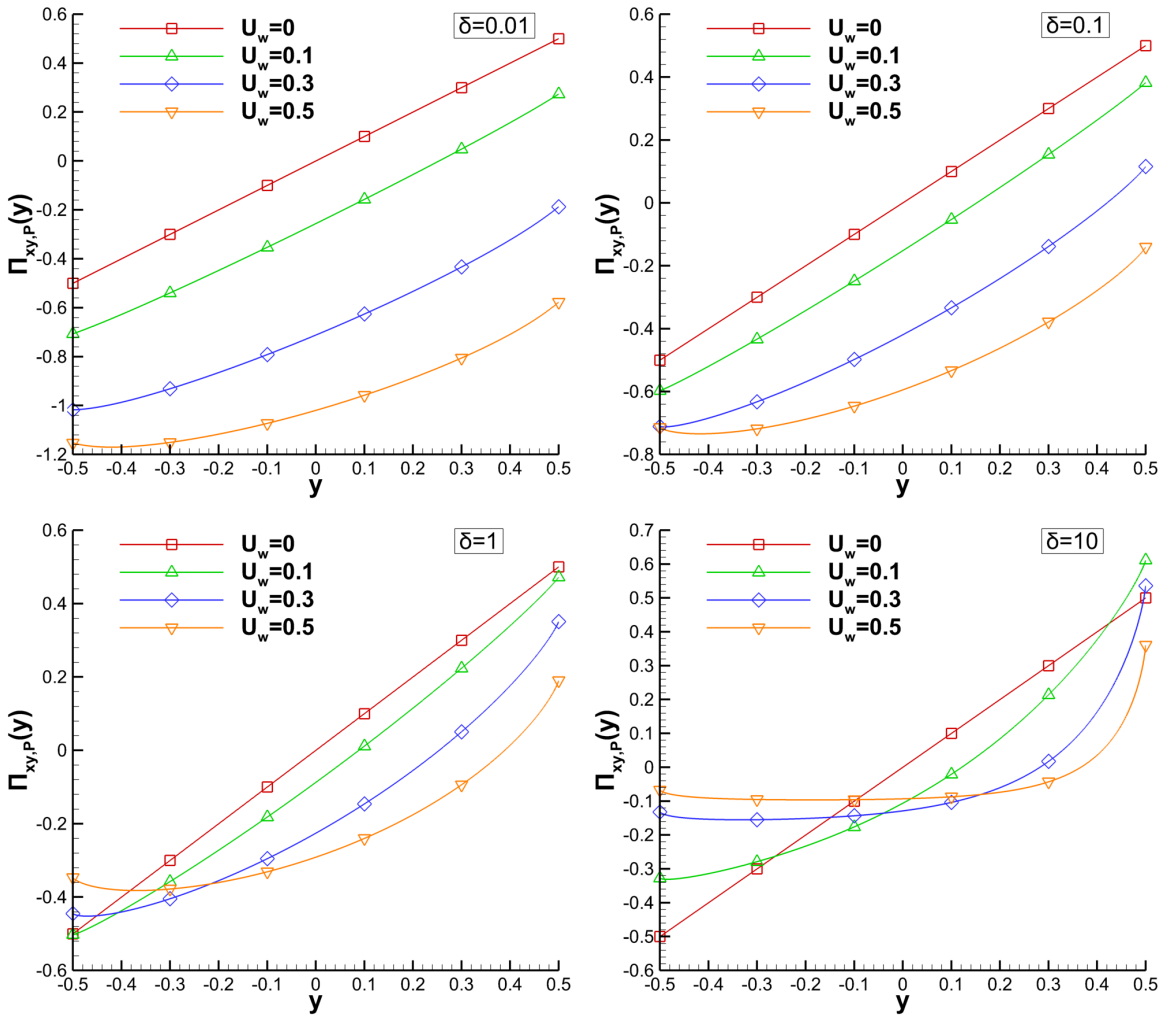

Figure 4.6 Shear stress $\Pi_{xy,P}(y)$ for $\delta = [10^{-2}, 0.1, 1, 10]$ and $U_w = [0, 0.1, 0.3, 0.5]$.

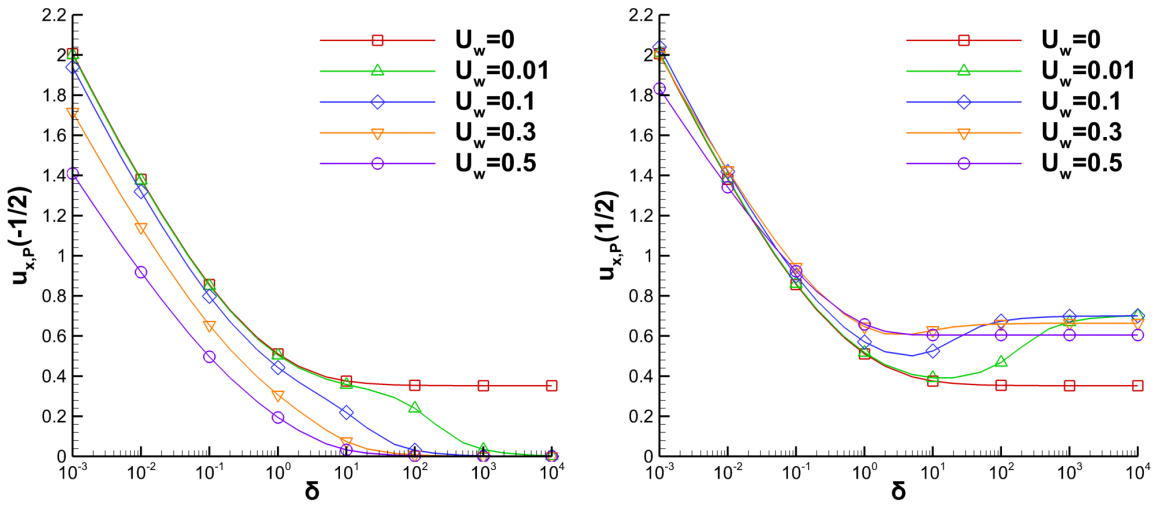

Figure 4.7 Velocities $u_{x,P}\,(\mp 1/2)$ at the injection (left) and suction (right) plates in terms of gas rarefaction parameter δ for $U_w = [0, 10^{-2}, 0.1, 0.3, 0.5]$.

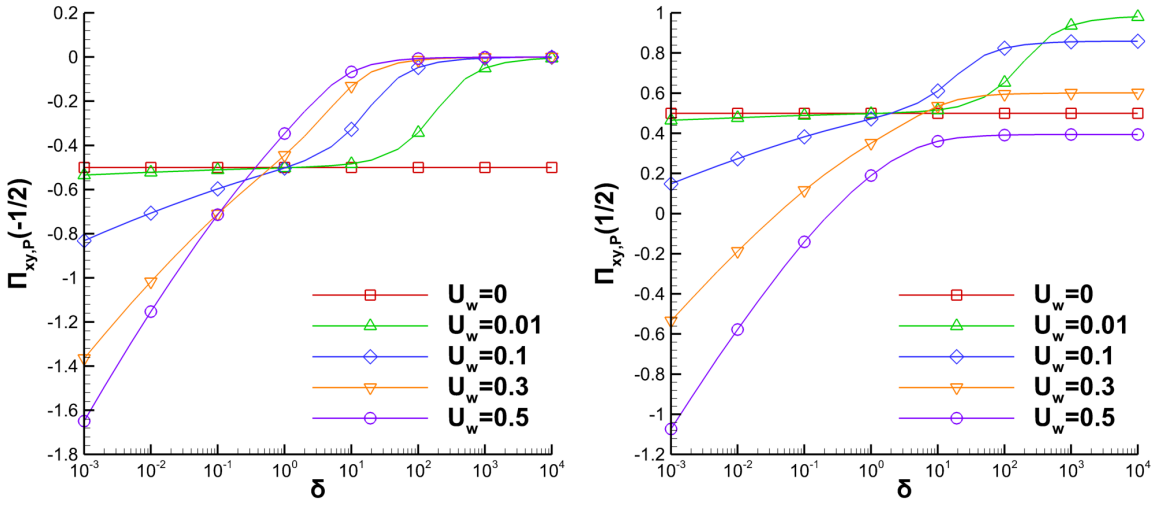

Figure 4.8 Shear stresses $\Pi_{xy,P}\,(\mp 1/2)$ at the injection (left) and suction (right) plates in terms of gas rarefaction parameter δ for $U_w = [0, 10^{-2}, 0.1, 0.3, 0.5]$.

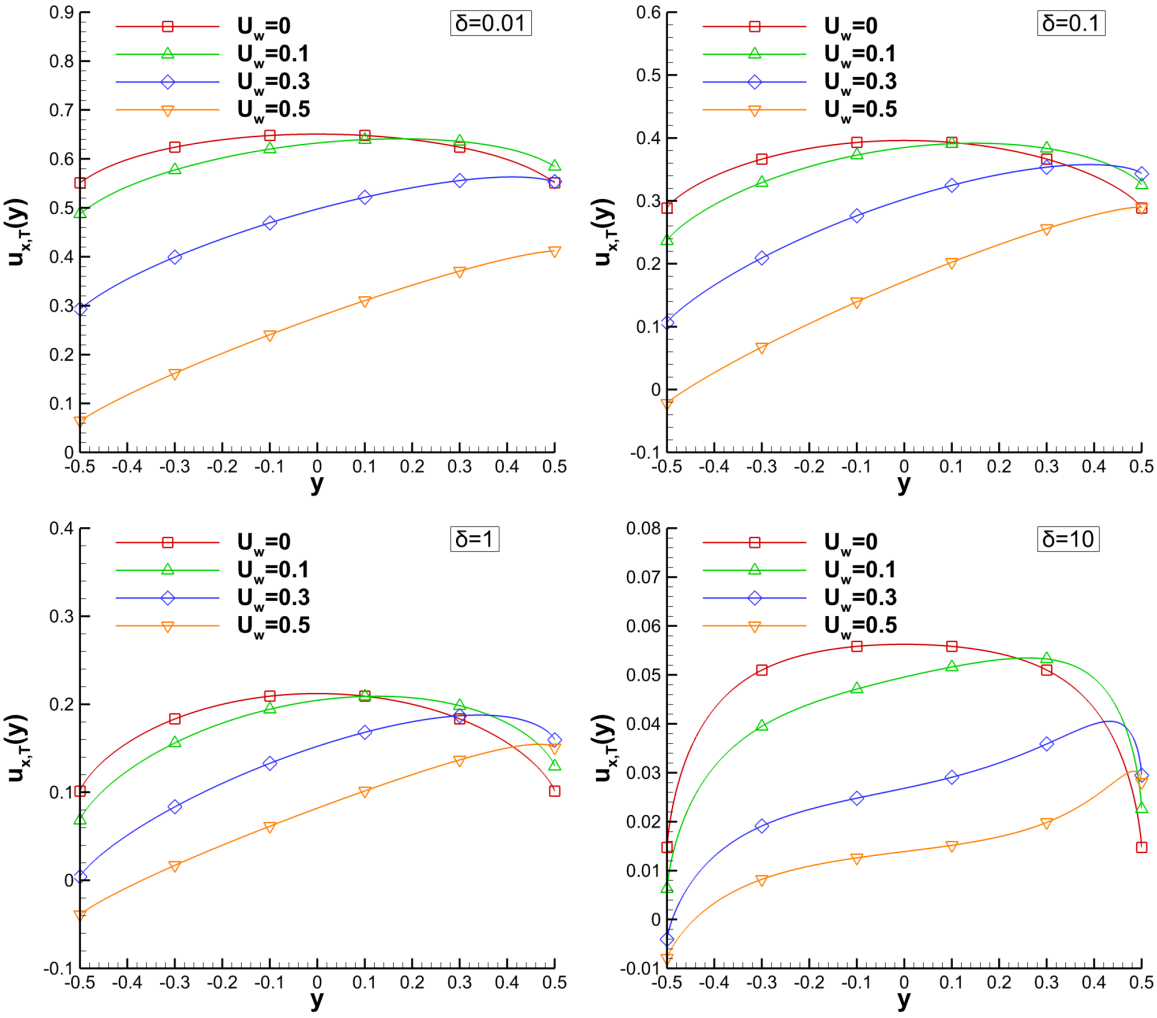

Figure 4.9 Velocity $u_{x,T}\,(y)$ for $\delta = [10^{-2}, 0.1, 1, 10]$ and $U_w = [0, 0.1, 0.3, 0.5]$.

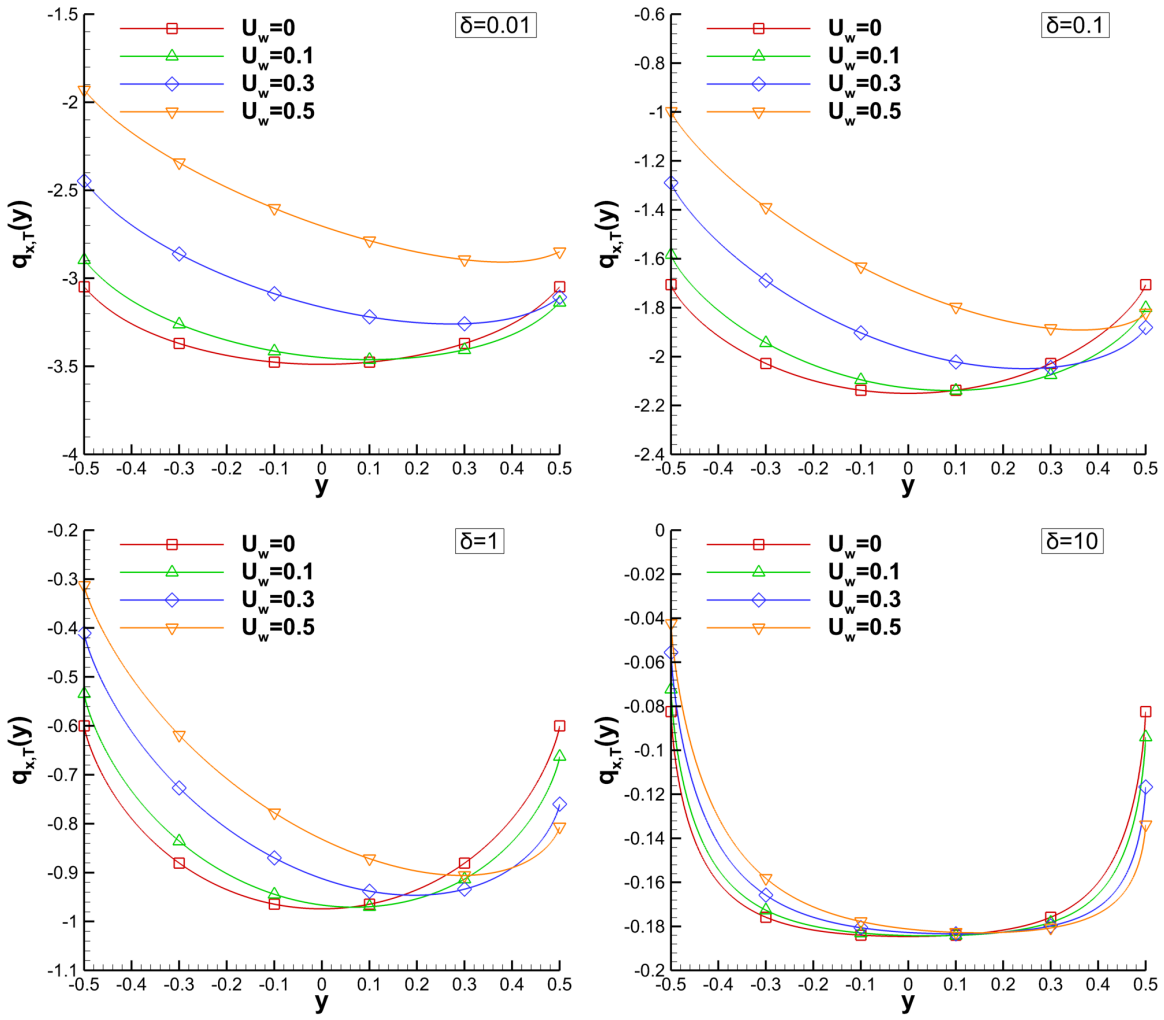

Figure 4.10 Heat flux $q_{x,T}\,(y)$ for $\delta = [10^{-2}, 0.1, 1, 10]$ and $U_w = [0, 0.1, 0.3, 0.5]$.

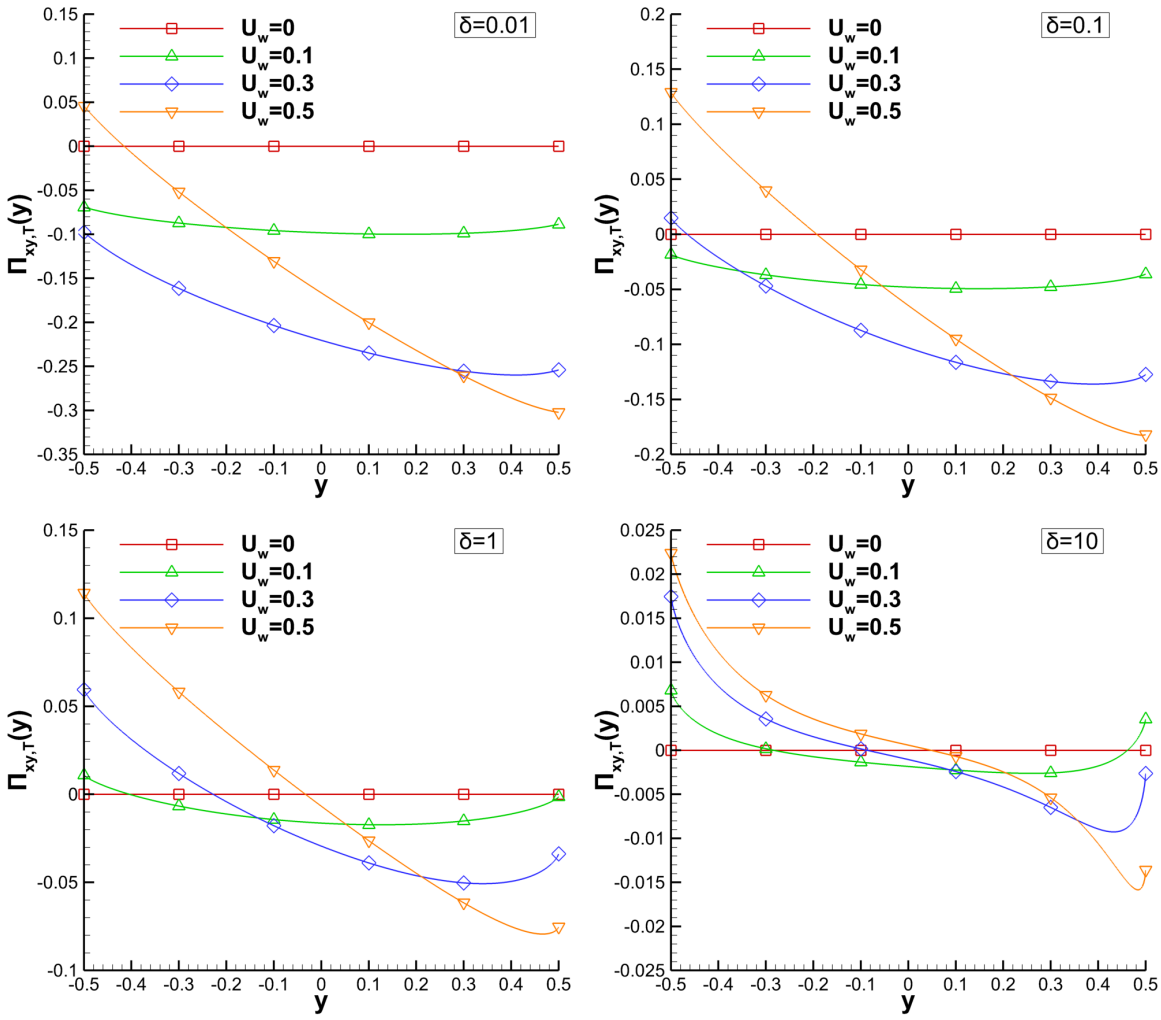

Figure 4.11 Shear stress $\Pi_{xy,T}(y)$ for $\delta = [10^{-2}, 0.1, 1, 10]$ and $U_w = [0, 0.1, 0.3, 0.5]$.

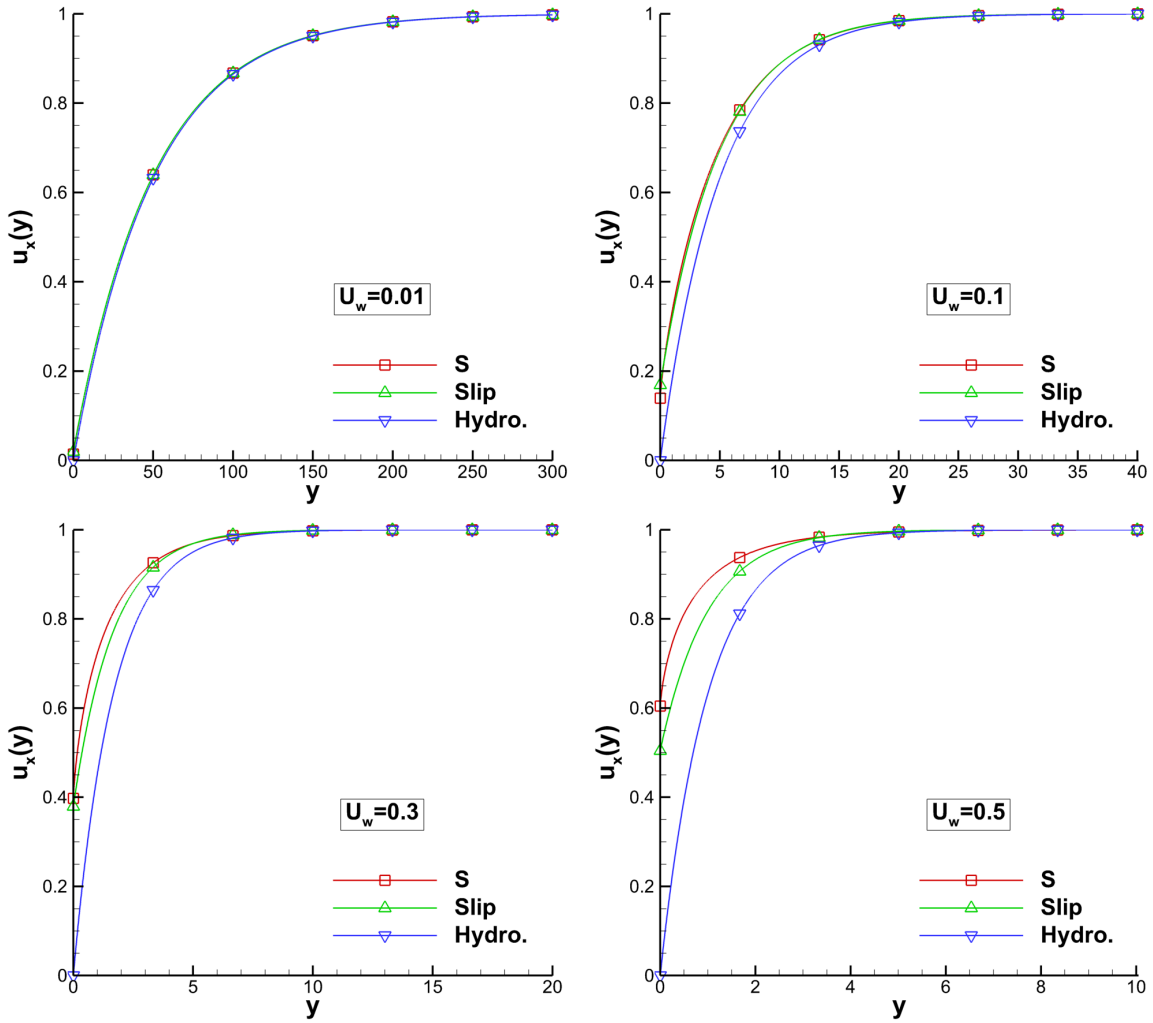

Figure 4.12 Asymptotic suction flow: Velocity $u_x\,(y)$ based on the S model and analytical expressions in the slip and hydrodynamic regimes for $U_w = [10^{-2}, 0.1, 0.3, 0.5]$.

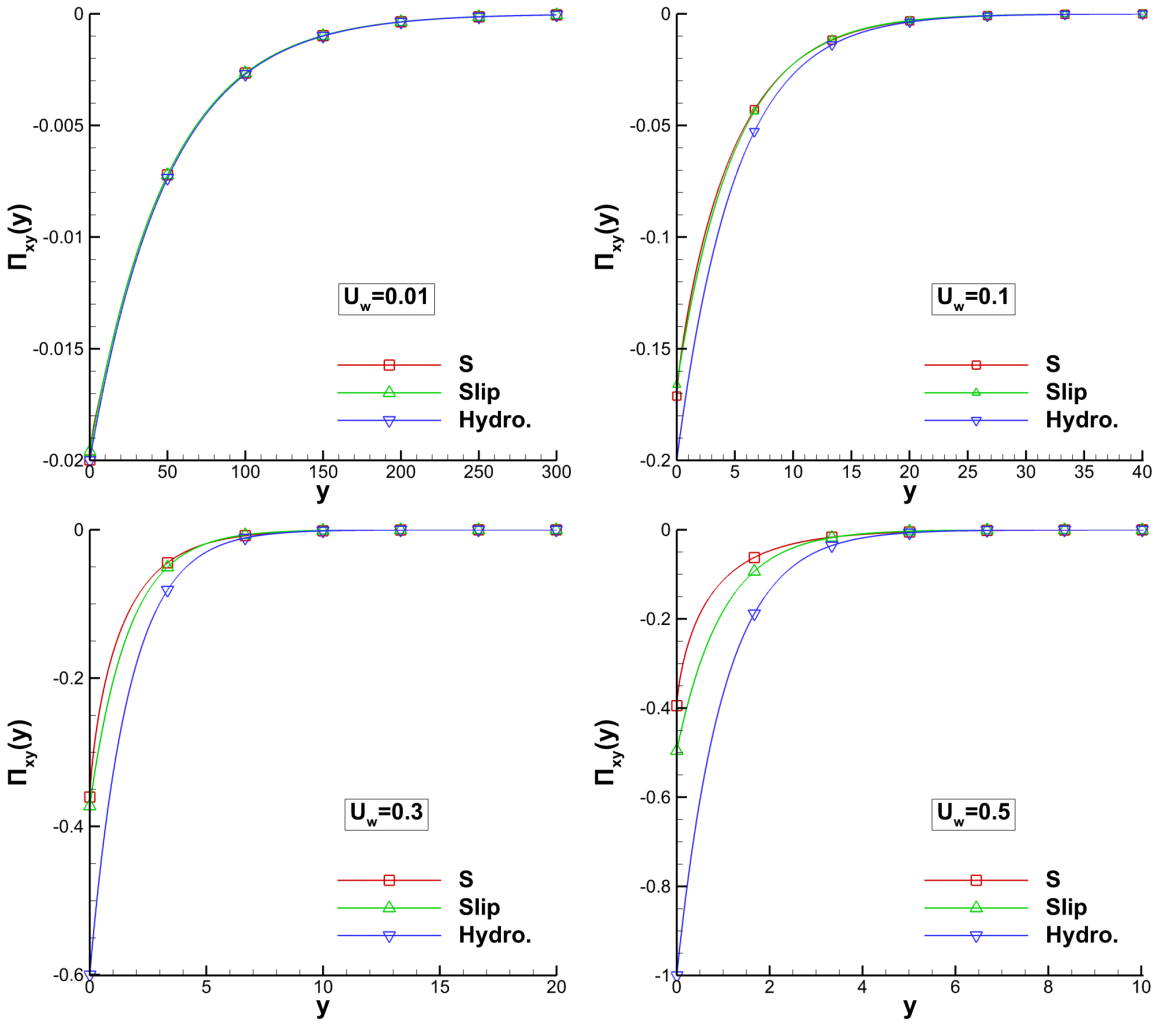

Figure 4.13 Asymptotic suction flow: Shear stress $\Pi_{xy}(y)$ based on the S model and analytical expressions in the slip and hydrodynamic regimes for $U_w = [10^{-2}, 0.1, 0.3, 0.5]$.

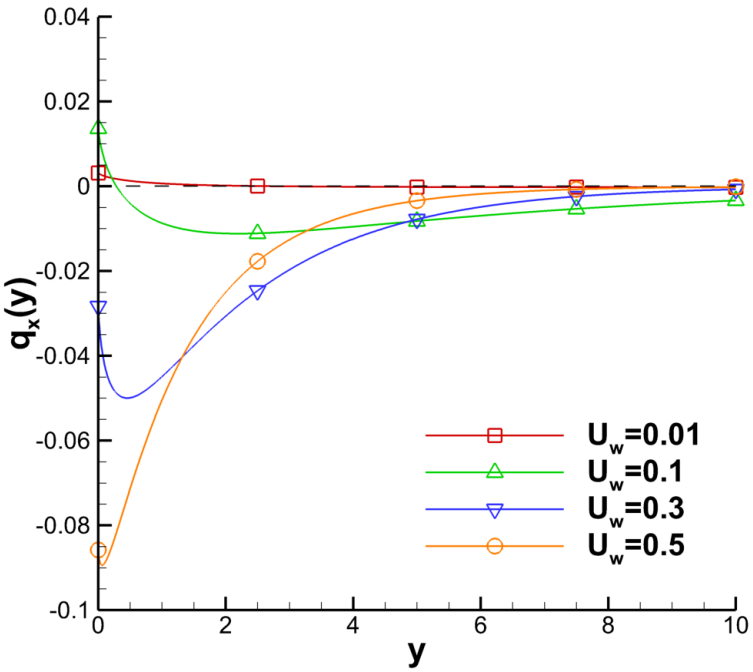

Figure 4.14 Asymptotic suction flow: Heat flux $q_x\,(y)$ based on the S model for $U_w = [10^{-2}, 0.1, 0.3, 0.5]$.

Chapter 5

Simulation of gas distribution systems

5.1 Introduction

Large gas pumping systems operating in a wide range of the Knudsen number play a significant role in particle accelerators [9] and fusion reactors [10, 11]. In addition, vacuum gas distribution systems may be found in many industrial processes and technological fields including semiconductor technologies, material deposition, vacuum metallurgy, food packaging and metrology [3–5]. Since these systems operate from very low pressures ($\sim 10^{-10}$ Pa) up to atmospheric pressure, the gas flow may be from the free-molecular regime up to the transition or even the slip and viscous flow regimes. To accurately simulate gas flows in the whole range of gas rarefaction, mesoscale kinetic modeling, as described by the Boltzmann equation is required [33]. However, in gas distribution networks with hundreds or thousands of piping elements, as the ones in large fusion reactors (e.g. in ITER), applying directly stochastic or deterministic kinetic modeling is a formidable or even prohibitive task.

To circumvent this pitfall, at the University of Thessaly (UTH) in-house codes have been developed for simulating gas pumping distribution systems of arbitrary size and complexity in the whole range of rarefaction (free-molecular, transition and viscous regimes) under steady-state [96, 97, 147] and time-dependent conditions [148]. This is achieved by integrating a dense kinetic database providing the flow rates through pipe elements of various geometries subject to any pressure difference into a typical gas network solver. The aforementioned flow rates have been computed via kinetic modeling and are considered very accurate since they are based on theoretical principles.

In the first part of this chapter an overview of the in-house developed codes for simulating gas networks is provided. More specifically in Section 5.2 the kinetic pressure drop relations implemented in the present work are briefly reviewed and indicative results for the dimensionless flowrates are provided. Then, in Section 5.3 the input data, namely the geometrical and operational data required for the simulations of a gas network are introduced. In Section 5.4 the UTH steady-state code is briefly reviewed and in Section 5.5 the advancements made in the upgraded UTH steady-state code ARIADNE, such as the ability to simulate multiple pumps with an arbitrary pressure - pumping speed characteristic curve, are described. In Section 5.6 the proposed hybrid time-dependent algorithm, which takes advantage of the time scale separation commonly found in gas distribution systems and implements ARIADNE in each time step, is reviewed.

In the second part of this chapter the developed time-dependent algorithm is validated and an uncertainty analysis method is implemented in a steady-state network. More specifically, in Section 5.7 two benchmarks are performed. The first one is related to gas expansion into vacuum and the second one to a distribution system with two vacuum vessels and one pump. The temporal evolution of the network pressures are compared in the former case with DSMC results available in the literature [149, 150] and in the latter case with results obtained by the Test particle Monte Carlo (TPMC) code Molflow+ [151]. In Section 5.8, the implementation of the Monte Carlo (MC) [152] uncertainty analysis method to gas distribution systems is demonstrated for the second benchmark network of Section 5.7. The network is assumed to be operating under steady-state conditions and the uncertainty of the pumped throughput with respect to the pipe radius, pipe length, vessel pressure and pump pumping speed uncertainties is computed.

5.2 Flow rates through tubes based on kinetic theory

The proposed methodology for simulating gas distribution systems operating under rarefied conditions includes the computed dimensionless flow rates through single pipe elements of arbitrary length, radius and pressure difference via kinetic theory, which are stored in a database for the needs of the network algorithm. An overview of the pursued approaches in reproducing the flow rates from the free-molecular to the viscous

regime is presented. The rarefied gas flow through tubes of arbitrary length over radius ratio and pressure difference is a fundamental problem in rarefied gas dynamics and has been (and still is) the subject of many theoretical, computational and experimental investigations.

Consider the pressure driven flow of a rarefied gas through a tube of length L and radius R with the tube inlet and outlet pressures maintained at P_1 and P_2, respectively ($P_1 > P_2$). In general, the flow is fully characterized by three dimensionless parameters, namely (a) the dimensionless length L/R, (b) the pressure ratio P_2/P_1 and c) the reference rarefaction parameter δ which is defined as

$$\delta = \frac{P_0 R}{\tilde{\mu} v_0}. \tag{5.1}$$

Here, P_0 is the equilibrium pressure, $\tilde{\mu}$ is the gas viscosity at the equilibrium temperature T_0 and $v_0 = \sqrt{2R_g T_0}$ is the most probable molecular speed ($R_g = k_B/m$ is the specific gas constant, with k_B denoting the Boltzmann constant and m the gas molecular mass).

The case of a tube much longer than its radius ($L/R \gg 1$) driven by a small pressure gradient is the most widely considered. It is tackled by the infinite capillary theory, where the flow is considered as fully-developed, the pressure varies only in the flow direction and end effects are neglected. Once the Poiseuille coefficient $G(\delta)$, also known as the reduced flow rate, which is a function only of δ at each cross-section, is known, the tube mass flow rate is obtained by [40]

$$\dot{M}_{FD} = G^* \frac{\pi R^3}{v_0} \frac{P_1 - P_2}{L}, \tag{5.2}$$

where

$$G^* = \frac{1}{\delta_1 - \delta_2} \int_{\delta_1}^{\delta_2} G(\delta)\, d\delta, \tag{5.3}$$

is computed by integrating $G(\delta)$ between the inlet and outlet rarefaction parameters δ_1 and δ_2, corresponding to the inlet and outlet pressures P_1 and P_2, respectively. The reduced flow rate $G(\delta)$ may be calculated from the following expression, which interpolates the numerical data based on the linearized BGK kinetic model within 0.2% uncertainty in the whole range of the rarefaction parameter [153]:

$$G(\delta) = \frac{1.505 + 0.0524\delta^{0.75} \ln \delta}{1 + 0.738\delta^{0.78}} + \left(\frac{\delta}{4} + 1.018\right) \frac{\delta}{1.073 + \delta} \tag{5.4}$$

In order to extend the range of applicability of the infinite capillary theory, which is computationally very efficient, from very long channels to channels of moderate length, the end effect correction concept may be introduced. Following the end effect theory the overall reduced flow rate G^*, given by Eq. (5.3), is revised according to [79]

$$G^*_{EE} = \frac{1}{(\delta_1 - \delta_2)\,(1 + \Delta L_1/L + \Delta L_2/L)} \int_{\delta_1}^{\delta_2} G\,(\delta)\, d\delta, \tag{5.5}$$

where $\Delta L_1/L$ and $\Delta L_2/L$ are the additional lengths at the inlet and outlet of the channel correcting the real length of the channel by taking into account the end effects. The corrective lengths are provided in Table 5.1. As pointed out in [154], the consideration of the end effect correction will always improve the accuracy of the simulations and therefore, it is always applied in the network algorithm. The values of G^*_{EE}, according to Eq. (5.5) are introduced into Eq. (5.2) to deduce by taking into consideration the end effects the corrected values of the mass flow rate $\dot{M}_{EE}$.

The great advantage of the infinite capillary and end effect theories is that the dimensionless solutions solely depend on the gas rarefaction parameter (they do not depend on L/R and P_2/P_1). However, they are both based on linear kinetic theory and are valid when the Mach number of the flow is sufficiently small [155].

In the case of $L/R \leq 10$ and $P_2/P_1 \geq 0.9$, i.e., the pressure difference is small, the flow is linear even in short tubes and the solution is obtained by solving the linearized BGK equation in the whole flow field (not just in a cross-section as before) [80]. The mass flow rate is obtained by

$$\dot{M}_{LIN} = W_{LIN} \frac{\sqrt{\pi} R^2\,(P_1 - P_2)}{v_0}, \tag{5.6}$$

where the dimensionless flow rate W_{LIN} is computed in terms of L/R and the reference rarefaction parameter δ (W_{LIN} is independent of P_2/P_1). Indicative results for W_{LIN} are given in Table 5.2.

Otherwise, in the case of $L/R \leq 10$ and $P_2/P_1 < 0.9$, the flow is considered as nonlinear and it is tackled based on the DSMC method [89, 156] and nonlinear kinetic model equations [81, 86, 157–159] solved via the discrete velocity method. The mass flow rate in this case is obtained by

$$\dot{M}_{NL} = W_{NL} \frac{\sqrt{\pi} R^2 P_1}{v_0}, \tag{5.7}$$

where W_{NL} is the dimensionless nonlinear flow rate and depends on all three parameters (δ, L/R and P_2/P_1). The pressure difference between the inlet and the outlet of the tube is given by

$$P_1 - P_2 = \frac{v_0}{\sqrt{\pi}R^2}\frac{\dot{M}_{NL}}{W_{NL}}\left(1 - \frac{P_2}{P_1}\right). \tag{5.8}$$

This case is the most computationally demanding one and extensive computations have been performed to prepare an adequate data base in a wide range of the involved parameters. Indicative results of W_{NL} are reported in Table 5.3 based on the ES kinetic model.

5.3 Definition of gas distribution system components and algorithm input data

In general, a gas distribution system may be modeled by a pipe network represented by an undirected graph [160]. The graph vertices and edges correspond to the gas network n nodes and the p piping elements acting as the connections between two nodes, respectively. A variety of node types may be used to represent the different components of a gas pipe network. More specifically, pipe junctions and pipe end caps are represented by the inner nodes n_i, vessels by the vessel nodes n_v, pumps by the pump nodes n_p, while constant pressure regions are represented by the so-called fixed pressure nodes n_f. The total number of nodes is $n = n_i + n_f + n_v + n_p$. Furthermore, closed paths formed by connecting adjacent nodes and open paths formed by connecting two non-inner nodes (fixed pressure, vessel and pump nodes) are named loops and pseudoloops, respectively. Both of them are involved in the formulation of the equations modeling the network. The number of loops and pseudoloops, in a well-defined network, are given by $l = p - n + 1$ and $l_p = (n_f + n_v + n_p) - 1$ respectively.

A schematic representation of a sample network for demonstration and clarity purposes is shown in Fig. 5.1. It consists of $n = 9$ nodes and $p = 10$ pipes. The total number of nodes includes $n_i = 6$ inner nodes (circles), $n_f = 1$ fixed pressure node (square), $n_v = 1$ vessel node (pentagon) and $n_p = 1$ pump node (triangle). Also, there is a set of $l = 2$ independent loops and $l_p = 2$ pseudoloops denoted by l_1, l_2 and pl_1, pl_2, respectively.

To complete the description of the network configuration, additional geometrical data are required. It is very important to properly specify the node ($i = 1, ..., n$) and pipe ($j = 1, ..., p$) indexing, the type of each node and the connectivity matrix

defining the connections between the nodes of the network. Also, the length L_j and the hydraulic radius $R_{h,j}$ for each piping element $j = 1, ..., p$, as well as the volume V of the vessel at each vessel node are specified.

Next, the operational input data of the gas distribution system are provided. They commonly include the molar mass and the viscosity of the pumped gas species, as well as the network temperature T. In addition, the operational input data include the pressure values P_i for the fixed pressure nodes, the initial pressure $P_i(t_0)$ at some initial time t_0 and the outgassing or gas injection data $Q_{in,i}(t)$ for the vessel nodes, the flow demand W_i at the inner nodes and the characteristic pumping speed - inlet pressure curve $S_i^*(P_i)$ for the pump nodes. In the sample network of Fig. 5.1 some of the required operational data are shown for demonstration purposes. At the fixed pressure node 1 the pressure is P_1, at the inner node 3 the gas flow demand is W_3 , at the vessel node 4 the initial pressure is $P_4(t_0)$ and the outgassing data are given by some $Q_{in,4}(t)$ and at the pump node 9 the characteristic curve is $S_9^*(P_9)$.

All aforementioned geometrical and operational data must be provided in order to advance in the steady-state or time-dependent simulation of the gas distribution network. It is noted that unless otherwise stated, all piping elements are considered as circular tubes and the hydraulic radius concept is applied in the case of non-circular piping elements. Furthermore, in the case of no flow demand or outgassing the corresponding quantities are set equal to zero.

5.4 The UTH steady-state network code

In this section, the algorithm of the UTH steady-state network code that has been described in detail in [96, 97, 147] is briefly reviewed mainly for completeness and clarity purposes. The flowchart of this code is shown in Fig. 5.2. It is seen that, initially the input data described in Section 5.3 are defined and then the loops and pseudoloops of the network are determined. The solution of the pipe network is obtained in an iterative manner making an initial assumption for the pressure at all inner nodes. In each iteration, the following linear algebraic system, consisting of the mass conservation equations at the inner nodes

$$\sum_j \left(\pm \dot{M}_{ij}\right) - W_i = 0, \quad i = 1, ..., n_i \tag{5.9}$$

and the energy conservation equations along the loops

$$\sum_j \left[\pm \Delta P_{kj}\left(\dot{M}_{kj}\right)\right] = 0, \quad k = 1, ..., l \tag{5.10}$$

and pseudoloops

$$\sum_j \left[\pm \Delta P_{mj}\left(\dot{M}_{mj}\right)\right] = \Delta P_m, \quad m = 1, ..., l_p \tag{5.11}$$

is solved for the unknown pipe mass flow rates. In this notation, the summation index j refers, in Eq. (5.9) to the pipes that are connected to node i, while in Eqs. (5.10) and (5.11) it refers to the pipes included in loop k and pseudoloop m, respectively. In Eq. (5.9), the unknown quantities $\dot{M}_{ij}$ are the mass flow rates at node i from pipe j. The plus or minus sign correspond to gas flow into or out of node i, respectively. The quantity W_i denotes the mass flow demand at the node i and is taken to be positive or negative when gas is exiting or entering the system, respectively. In Eqs. (5.10) and (5.11), the quantities ΔP_{kj} and ΔP_{mj} denote the pressure difference between the inlet and outlet nodes of pipe j and depend on the respective flow rates $\dot{M}_{kj}$ and $\dot{M}_{mj}$, respectively. The plus or minus sign is used if the definition of pipe j is in the same or opposite direction as the definition of loop or the pseudoloop. In Eq. (5.11), ΔP_m is the pressure difference between the first and the last pseudoloop nodes. Depending on the specific geometrical and operational data for each pipe element, the pressure differences in the energy balance equations (5.10) and (5.11) are substituted by the kinetic theory pressure drop expressions provided in Section 5.2.

Once the linear system is solved and the mass flow rates of all piping elements are computed, all inner node pressures are updated based on the kinetic pressure drop relations and are compared to the previous ones. The iterative procedure is continued until the relative pressure difference between two successive iterations at all inner nodes is smaller than a specified value.

In addition to the node pressures and the pipe mass flow rates the network solution also provides the pipe throughput [Pam^3/s]

$$Q_j = \dot{M}_j R_g T_r, \quad j = 1, ..., p \tag{5.12}$$

and the node pumping speed [m^3/s]

$$S_i = \frac{Q_i}{P_i} = \frac{\dot{M}_i R_g T_r}{P_i}, \quad i = 1, ..., n, \tag{5.13}$$

where T_r is some reference temperature, commonly taken to be 273.15 K. The quantity $Q_i = \dot{M}_i R_g T_r$ denotes the total gas throughput that passes through node i and is calculated as the sum of all the pipe throughputs that are connected to node i. Both the pipe throughput and node pumping speed are of major practical importance in vacuum gas dynamics.

5.5 The UTH upgraded steady-state network code ARIADNE

In this section, certain code advancements, which have been performed in the present work and are integrated in the steady-state code, are presented. The acronym given to the upgraded steady-state algorithm is "**ARIADNE**", which stands for **A**lgorithm for **R**aref**i**ed gas flow in **A**rbitrary **D**istribution **Ne**tworks. The acronyn of the upgraded steady-state network code has been proposed and adapted by S. Misdanitis.

The flowchart of the upgraded steady-state network code ARIADNE is shown in Fig. 5.3. In the present work, the main advancement refers to the simulation of pipe networks with an arbitrary number pumps. In this case, an additional iterative procedure is required, in order to meet the pumping speed restrictions, i.e. to satisfy the pumping speed - inlet pressure $S_i^*(P_i)$ at each pump node. Following an initial assumption for the pump pressures, the network solver, as described in Section 5.4, is applied to compute the pipe mass flow rates and the node pressures of the network, including the pumping speeds at the pump nodes. The pumping speed differences between the obtained solution $S_{i,0}(P_{i,0})$ and the given pumping speed curve $S_i^*(P_i)$, defined as $\Delta S_{i,0} = \left[S_i^*(P_{i,0}) - S_{i,0}(P_{i,0})\right] / S_i^*(P_{i,0})$, is computed and stored for all pumps $i = 1, ..., n_p$.

Next, all pump pressures are set to the initial pressure assumption except for a specific pump pressure P_j, which is changed by a small amount ε_j. The network is solved again and the pumping speed differences $\Delta S_{i,j} = \left[S_i^*(P_{i,j}) - S_{i,j}(P_{i,j})\right] / S_i^*(P_{i,j})$ are computed and stored for all pump nodes $i = 1, ..., n_p$. This computation is performed for all pumps $j = 1, ..., n_p$ and when it is completed, the Jacobian $J_{i,j} = (\Delta S_{i,j} - \Delta S_{i,0}) / \varepsilon_i$, $i, j = 1, ..., n_p$ is constructed.

Then, the linear system of equations $J_{i,j} \times \Delta P_i = -\Delta S_{i,0}$ is solved and all pump pressures are updated as $P_i = P_i + \Delta P_i$. The procedure is repeated until the network solution fulfills the convergence criterion imposed on $\Delta S_{i,0}$. The applied methodology

is Newton's iterative method, where the partial derivatives are numerically computed and its convergence close to the solution is superlinear.

It is important to note that in the aforementioned iterative method, the main computational effort is due to the initial network solution to compute $\Delta S_{i,0}$. The subsequent solutions of the network for each pump $j = 1, ..., n_p$ in order to compute $\Delta S_{i,j}$ converge much faster than the initial one (generally in one or two iterations). This is achieved by taking the inner node pressures of the previous network solution as the initial assumption for the inner node pressures for the current network solution. Thus, the involved computational effort is not dramatically increased by increasing the number of pumps in the network.

In addition to the above, a robust and computationally efficient algorithm for extracting the loops and pseudoloops has been implemented. The implemented algorithm utilizes the well-known depth-first-search algorithm (DFS) [161], which is a traversing procedure which starts at an arbitrary node and explores the graph as far as possible before backtracking. Furthermore, the involved kinetic data bases, needed in the implementation of the steady-state network code, have been accordingly enriched with more dense flow rate results in terms of the operating conditions and geometrical data. Also, efficient interpolating algorithms have been integrated in the code to improve its accuracy. The steady-state code has been restructured based on object-oriented programming to facilitate its accessibility, adaptation and implementation in various technological applications.

All these advancements significantly increase the robustness and the efficiency of the steady-state network code. It is noted that, the hybrid time-dependent simulation of gas distribution systems, described in the next section, involves the solution of a steady-state network configuration in each time step.

5.6 Hybrid methodology for time-dependent gas distribution systems

The direct simulation of time-dependent gas pumping scenarios can be computationally very expensive, even in comparatively small or moderate size vacuum systems. Particularly, in large size vacuum systems, such as the ITER divertor pumping system, the computational cost of a direct time-dependent approach is prohibitive. In cases where a time scale separation is applicable the hybrid time-dependent approach pro-

posed in [162], explicitly coupling a macro model for the vessels of the gas distribution system with a micro model for the piping elements, may be implemented to significantly reduce the required computational effort.

The characteristic time defining the flow inside the piping elements is defined as the time needed to cross a characteristic length with the most probable molecular speed v_0 of the conveying gas and is given by

$$t_m = R_h / v_0, \tag{5.14}$$

while, the corresponding characteristic time inside a vessel of volume V is

$$t_M = V \Big/ \left(v_0 R_h^2\right). \tag{5.15}$$

Since in many cases, the macroscopic quantities in the vessels vary in a much slower pace than those in the pipes it is readily seen that $t_M \gg t_m$ (e.g. the instantaneous variation of the mass flow rate in the piping elements modifies the vessel pressure in a quasi-steady manner). Therefore, it is reasonable to exploit the time scale separation and investigate separately the network vessels and pipes by the corresponding micro and macro models, which are explicitly coupled in sequence (not simultaneously). The micro model consists of the upgraded UTH steady-state ARIADNE code described in the previous section.

The macro model describing the temporal evolution of pressure $P_i(t)$ in some vacuum vessel i can be derived by considering the mass balance in the vessel and the equation of state. It is easily deduced that

$$V_i \frac{dP_i(t)}{dt} = Q_{in,i}(t) + \dot{M}_i(t) R_g T, \tag{5.16}$$

where the throughput $Q_{in,i}(t)$ is entering the vacuum vessel at some time t due to either outgassing or direct gas injection inside the vacuum vessel and the mass flow rate $\dot{M}_i(t)$ is entering (positive) or exiting (negative) the vacuum vessel through the piping elements connected to the vessel. Equation (5.16) can also be written in terms of the effective vacuum vessel pumping speed $S_{eff,i}(t)$ in the equivalent form

$$V_i \frac{dP_i(t)}{dt} = Q_{in,i}(t) - P_i(t) S_{eff,i}(t). \tag{5.17}$$

It is noted that, in the present notation $S_{eff,i}(t)$ is considered as positive when gas is pumped out of the vessel i. The ordinary differential equation (5.16) or (5.17), defining the macro model, subject to the corresponding initial condition $P_i(t_0)$, may be numerically solved by typical integration schemes (e.g. Runge-Kutta methods) once the macroscale time integration step Δt is specified.

The coupling between the macro and micro models is rather simple and it is shown in the flowchart of Fig. 5.4. At each macroscale time step the gas distribution system is solved via ARIADNE, which includes a micro model computing the dimensionless flow rates at each pipe of the network in the whole range of rarefaction. Thus, at some time t, based on the current input conditions, the mass flow rates and the pressures of the network are computed. The output data are written to respective output files. The vessel node pressures are updated via Eq. (5.16) or (5.17) (macro model) and the algorithm can move to the next time $t + \Delta t$. The evolution in time proceeds until a specified final time t_f or until an equilibrium state is reached.

5.7 Benchmarking of the time-dependent algorithm

In this section, the time-dependent algorithm implementing the ARIADNE code at each time step is validated by solving two benchmark prototype problems.

The first prototype problem involves gas expansion into vacuum. More specifically, the dynamic standard apparatus for the measurement of the response and relaxation times of vacuum gauges developed at Physikalische-Technische Bundesanstalt (PTB) is considered [149]. In Fig. 5.5, the schematic representation of the flow setup of prototype problem 1 is provided. Two vessels, namely the upstream and downstream vessels with volumes $V_1 = 3.1$ L and $V_2 = 185$ L, respectively, are interconnected via a circular tube with length $L = 0.492$ mm and radius $R_h = 0.50565$ mm. The valve between the two vessels is closed. The upstream vessel is filled with a monatomic gas up to an initial pressure of $P_1(t_0 = 0) = 1000$ Pa, while the downstream vessel is evacuated via a turbomolecular pump. Next, the valve rapidly opens and time-dependent gas expansion between the two vessels occurs. The turbomolecular pump keeps running during the whole experiment in order to maintain high vacuum at the downstream vessel ($P_2 \sim 0$ Pa). This flow setup has been considered in [150] and the temporal evolution of the upstream pressure vessel $P_1(t)$ for the monatomic gases of He, Ne, Ar and Kr has been obtained both computationally and experimentally indicating very good comparison between the corresponding results. The computational work in

[150] is based on the same hybrid scheme implemented here. However, in [150] the steady-state solution at each time step is obtained by the DSMC method.

In the ARIADNE code the above configuration is represented as a vessel node (upstream vessel) connected with a fixed pressure node (downstream vessel) via a single piping element. The input data include the temperature $T = 295$ K, the vessel volume V_1, the length L and radius R_h of the tube, the initial upstream pressure $P_1(t_0 = 0)$, the fixed pressure $P_2 = 10^{-20}$ Pa and the time step $\Delta t = 10^{-4}$ s. In addition, the required gas properties of He, Ne, Ar and Kr at $T = 295$ K are provided in Table 5.4.

In Fig. 5.6 the temporal evolution of the upstream vessel pressure $P_1(t)$ computed by the hybrid time-dependent algorithm is plotted for the four monatomic gases. The experimental and computational results of [150] are also provided for comparison purposes. An excellent agreement is observed for all investigated gases. It is noted that, the agreement between the present computational results and experimental results of [150] is improved compared to the agreement reported in [150]. This is mainly contributed to the more dense kinetic database and interpolation algorithms implemented in ARIADNE. Based on this comparison, the proper implementation of the ARIADNE code in the hybrid time-dependent scheme is demonstrated.

The second prototype problem involves the transient response of a pipe network in the free-molecular regime and its comparison with the well-established TPMC code Molflow+ [151]. In Fig. 5.7, the schematic representation of the second prototype problem network is provided. It consists of two vacuum vessels, with equal volumes $V_1 = V_2 = 8$ L, one pump, with sticking coefficient 0.8, running at all times and five piping elements. The nodes 1 and 2 are vessel nodes, the nodes 3, 4 and 5 are inner nodes and node 6 is a pump node. A sample material inside the first vessel is outgassing helium at a rate of $Q_1(t) = 2.5 \times 10^{-3} e^{-2t}$ Pam^3/s, while in the second vessel no outgassing occurs $Q_2(t) = 0$ Pam^3/s. The pipe lengths and the radii are provided in Fig. 5.7. On purpose, the pipe dimensionless lengths L/R are in a wide range, varying from 7.87 up to 30.5, in order to have a more complete comparison.

In the TPMC time-dependent simulation the above network has been designed in the open source software Salome [163] and has been imported into Molflow+, along with all the required input data. The network has been simulated for 10 s by Molflow+ and the computed temporal pressure evolution at the six network nodes $i = 1, ..., 6$, is shown in Fig. 5.8. In addition, from the Molflow+ simulation the pumping speed at the pump node is found to be constant throughout the simulation and equal to 4.8×10^{-2} m^3/s. This constant pumping speed value (instead of the sticking coefficient)

has been imported as input data in the ARIADNE code, since the pumping speed - inlet pressure curve must be defined for all pumps. Having properly defined all input data, the present time-dependent algorithm is implemented. The deduced temporal pressure evolution at the six nodes of the network, are also plotted in Fig. 5.8. In all cases an excellent agreement between corresponding results is observed, with the average relative deviation at each node ranging from 0.7% up to 4.4%. The smallest deviation is observed at node 1 corresponding to the outgassing vessel, while the largest one is observed at node 5 corresponding to the elbow before the pump.

From the qualitative point of view the reported transient response of the system is well expected. At vessel node 1, the pressure P_1, is initially increased, due to the initially high outgassing up to some maximum value and then, as the outgassing is decreased, the pressure is monotonically decreased due to the presence of the continuously running pump. At the inner nodes 2-5 and the pump node 6 the pressure evolution follows a similar trend, obtaining however smaller maximum values.

5.8 Uncertainty propagation in gas distribution systems

Uncertainties are very important in gas distribution systems, since they can significantly affect their performance [3]. These uncertainties originate from various sources, including the uncertainty of the measurement instruments, the changing environmental conditions and the flaws in the vacuum system setup. The introduced uncertainties reflect to the operation of the gas distribution system and deviations from the expected performance may be observed. Thus, in many cases the investigation of the uncertainty propagation through the gas distribution system is required.

One of the most versatile methods for uncertainty propagation is the Monte Carlo (MC) method [152]. In the MC method, a large number of trials $i = 1, 2, ..., N_t$ is conducted. In each trial the values of the input quantities are sampled from their respective distributions and the output quantities are computed. Then, the distribution functions of the output quantities are constructed and the uncertainties are computed from these distributions.

The input quantities x_m are usually known with respect to their nominal value $x_{m,n}$ and their uncertainty $u(x_m)$ as

$$x_m = x_{m,n} \pm u(x_m), \tag{5.18}$$

while their distribution is not always known. In the case where the distributions of the input quantities are not known, they are sampled from a uniform distribution between $x_m \in [x_{m,n} - u(x_m), x_{m,n} + u(x_m)]$.

The output quantities are presented in terms of the mean value and the associated uncertainty as

$$y_l = \bar{y}_l \pm u(y_l), \tag{5.19}$$

where the mean value is calculated as

$$\bar{y}_l = \frac{1}{N_t} \sum_{i=1}^{N_t} y_{l,i}, \tag{5.20}$$

with $y_{l,i}$ denoting the output quantity l in the ith trial. The associated uncertainty is given by

$$u(y_l) = k\sigma(y_l), \tag{5.21}$$

where $\sigma(y_l)$ denotes the standard deviation calculated as

$$\sigma(y_l) = \sqrt{\frac{1}{N_t - 1} \sum_{i=1}^{N_t} (y_{l,i} - \bar{y}_l)^2}. \tag{5.22}$$

The coefficient k in Eq. (5.21) is the coverage factor and when a large number of trials are performed ($N_t > 10^3$) the values $k = 2$ and $k = 3$ are used for a 95% and 99% coverage interval, respectively [164].

In this section, the implementation of the MC method is demonstrated for the gas network shown in Fig 5.7. It is reminded that, this gas network has been used in Section 5.7 to validate the developed hybrid time-dependent gas network algorithm. Here, the network is assumed to operate under steady-state conditions and thus the pressure at the two vessels is constant and has been taken to be $P_1 = [0.2, 2, 20, 200]$ Pa and $P_2 = 0.2$ Pa. The pressure range has been specifically chosen in order to investigate the uncertainty propagation through the network from the free-molecular to the slip regime. The pump is assumed to have a constant pumping speed of 4.8×10^{-2} m^3/s, while the geometrical data remain the same and can be seen in Fig 5.7. The investigated input quantities include the pipe radii, pipe lengths, vessel pressures and pump pumping speed, while the pumped throughput is the output quantity of interest. In each trial, one of the aforementioned input quantities is sampled from a uniform distribution, while the remaining input quantities are set to their nominal values. The ARIADNE code is implemented to simulate the resulting gas network and the pumped

throughput is stored. For each one of the investigated input quantities a total of trials $N_t = 10^3$ are performed and the pumped throughput uncertainty is obtained.

In Fig 5.9 the uncertainty of the pumped throughput with respect to the uncertainty of the input quantities, namely the pipe radii, pipe lengths, vessel pressures and pump pumping speed to the pumped throughput is presented for $P_1 = [0.2, 2, 20, 200]$ Pa. It is clearly seen that, in the whole investigated pressure range the pumped throughput uncertainty is linearly increased as the uncertainty of the input quantities is increased. This linear trend has also been observed for the mass flow rate uncertainty due to the pipe radius, pipe length and pressure uncertainty in the case of the pressure driven flow through a single circular tube [165]. In addition, it is observed that, in all cases the pumped throughput uncertainty is smaller than the input uncertainties. Moreover, the pipe radius uncertainty is the most impactful one, followed by the pressure, pipe length and pumping speed uncertainties. Furthermore, the pumped throughput uncertainty due to the pipe radius, pipe length, pressure and pumping speed uncertainties is monotonically increased as the gas rarefaction is decreased.

It is noted here that, the findings of the performed uncertainty analysis are not general and only apply for the investigated network. Thus, in each gas network a separate uncertainty propagation analysis is required in order to investigate the impact of the input uncertainties to the uncertainty of the output quantities of interest.

5.9 Concluding remarks

The simulation of gas pumping systems operating in a wide range of the Knudsen number has attracted considerable attention over the last years, due to their importance in many technological applications, as well as, in particle accelerators and fusion reactors. In many cases, the direct simulation of such systems via kinetic theory is prohibitive due to the involved computational effort. To circumvent this, an in-house code has been developed for simulating gas pumping distribution systems of arbitrary size and complexity in the whole range of the Knudsen number, by integrating a kinetic database in a typical gas network solver.

In this chapter the proposed methodologies, as well as their implementation in the UTH upgraded steady-state gas network code ARIADNE have been thoroughly described. In addition, a hybrid algorithm for simulating the transient response of gas networks, implementing ARIADNE at each time step has been presented. Moreover, the time-dependent code has been validated to some extend via two benchmark problems.

The first one involved the dynamic standard apparatus for the measurement of the response and relaxation times of vacuum gauges developed at PTB. The presented results showed an excellent agreement with the corresponding experimental and computational results provided in the literature. The second benchmark problem involved a gas network operating in the free-molecular regime. The benchmark network is simulated via both the proposed time-dependent algorithm and the well-established TPMC code Molflow+. Also, here an excellent qualitative and quantitative agreement has been observed between the two approaches. Furthermore, the implementation of the MC uncertainty analysis method to gas distribution systems has been demonstrated for the second benchmark network. The network was assumed to operate under steady-state conditions and the uncertainty of the pumped throughput with respect to the pipe radius, pipe length, vessel pressure and pump pumping speed uncertainties has been presented. In general, the qualitative behavior of the throughput uncertainty has been in agreement with the one observed for the mass flow rate uncertainty in the case of the pressure driven flow through a single circular tube.

Having established confidence in the proposed methodologies, the capabilities of the ARIADNE code and the time-dependent algorithm will be demonstrated in Chapter 6 by simulating the burn and dwell phases of the ITER primary exhaust system.

Table 5.1 Length increment $\Delta L/R$ in terms of the rarefaction parameter δ.

δ	0.005	0.05	0.1	0.2	0.4	0.6	0.8
$\Delta L/R$	2.22	1.72	1.52	1.33	1.16	1.07	1.01
δ	1	2	4	6	8	10	∞
$\Delta L/R$	0.964	0.841	0.735	0.704	0.688	0.682	0.680

Table 5.2 Dimensionless flow rate W_{LIN} through a tube for indicative values of the rarefaction parameter δ and dimensionless length L/R, based on the BGK model [80].

L/R	δ					
	0	0.1	1	2	5	10
0	9.99(-1)	1.04	1.37	1.72	2.77	4.35
1	6.72(-1)	6.96(-1)	8.92(-1)	1.10	1.70	2.63
5	3.11(-1)	3.16(-1)	3.73(-1)	4.40(-1)	6.42(-1)	9.88(-1)
10	1.91(-1)	1.92(-1)	2.17(-1)	2.51(-1)	3.62(-1)	5.54(-1)

Table 5.3 Dimensionless flow rate W_{NL} through a tube for indicative values of the rarefaction parameter δ, dimensionless length L/R and pressure ratio P_2/P_1 based on the ES model [157].

L/R	P_2/P_1	δ						
		0	0.01	0.1	1	2	5	10
0	0.1	9.00(-1)	9.03(-1)	9.23(-1)	1.07	1.18	1.35	1.45
	0.5	5.00(-1)	5.02(-1)	5.18(-1)	6.53(-1)	7.78(-1)	1.04	1.22
	0.9	1.00(-1)	1.00(-1)	1.05(-1)	1.40(-1)	1.76(-1)	2.80(-1)	4.32(-1)
1	0.1	6.05(-1)	6.06(-1)	6.19(-1)	7.13(-1)	7.88(-1)	9.31(-1)	1.06
	0.5	3.36(-1)	3.37(-1)	3.45(-1)	4.28(-1)	5.05(-1)	6.92(-1)	8.88(-1)
	0.9	6.72(-2)	6.75(-2)	7.00(-2)	9.08(-2)	1.12(-1)	1.70(-1)	2.64(-1)
5	0.1	2.79(-1)	2.80(-1)	2.83(-1)	3.12(-1)	3.41(-1)	4.23(-1)	5.37(-1)
	0.5	1.55(-1)	1.56(-1)	1.58(-1)	1.82(-1)	2.07(-1)	2.80(-1)	3.98(-1)
	0.9	3.10(-2)	3.11(-2)	3.18(-2)	3.78(-2)	4.44(-2)	6.41(-2)	9.76(-2)
10	0.1	1.71(-1)	1.72(-1)	1.73(-1)	1.85(-1)	2.00(-1)	2.49(-1)	3.28(-1)
	0.5	9.54(-2)	9.55(-2)	9.63(-2)	1.06(-1)	1.19(-1)	1.60(-1)	2.29(-1)
	0.9	1.90(-2)	1.91(-2)	1.93(-2)	2.19(-2)	2.53(-2)	3.59(-2)	5.43(-2)

Table 5.4 Gas properties of He, Ne, Ar and Kr at 295 K.

Gas	He	Ne	Ar	Kr
Molar mass [kg/kmol]	4.003	20.18	39.95	83.80
Viscosity $\tilde{\mu}$ [μPas]	19.70	30.89	22.80	24.86

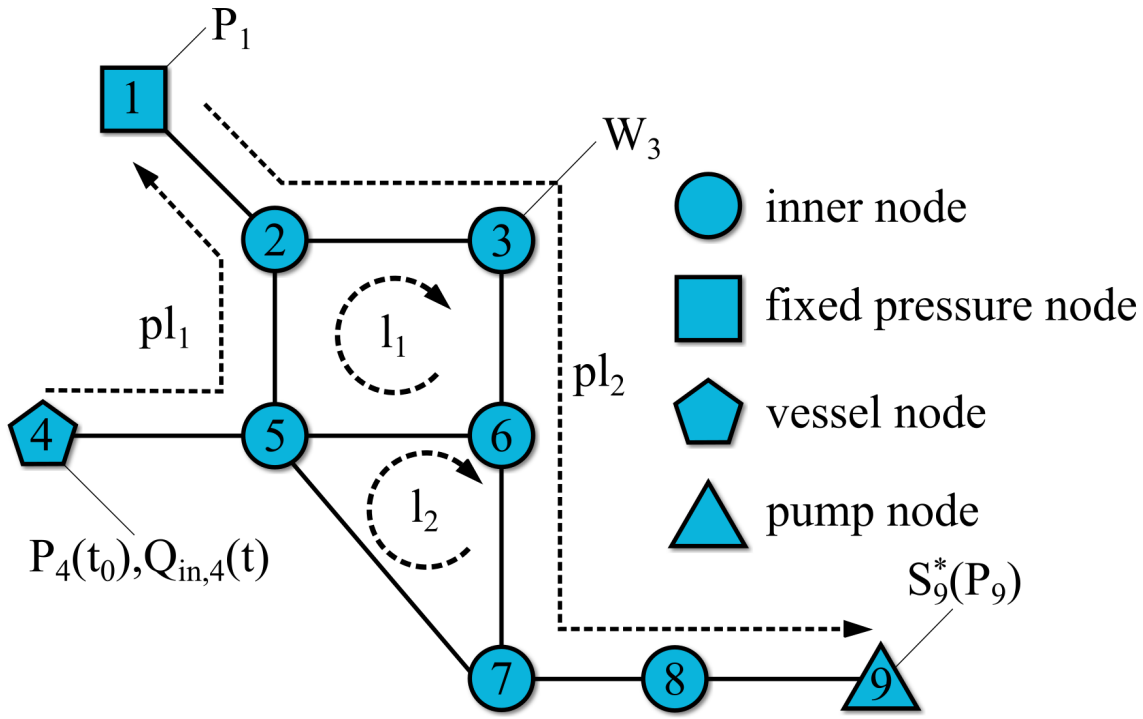

Figure 5.1 Schematic representation of a sample network with indicative geometrical and operational data.

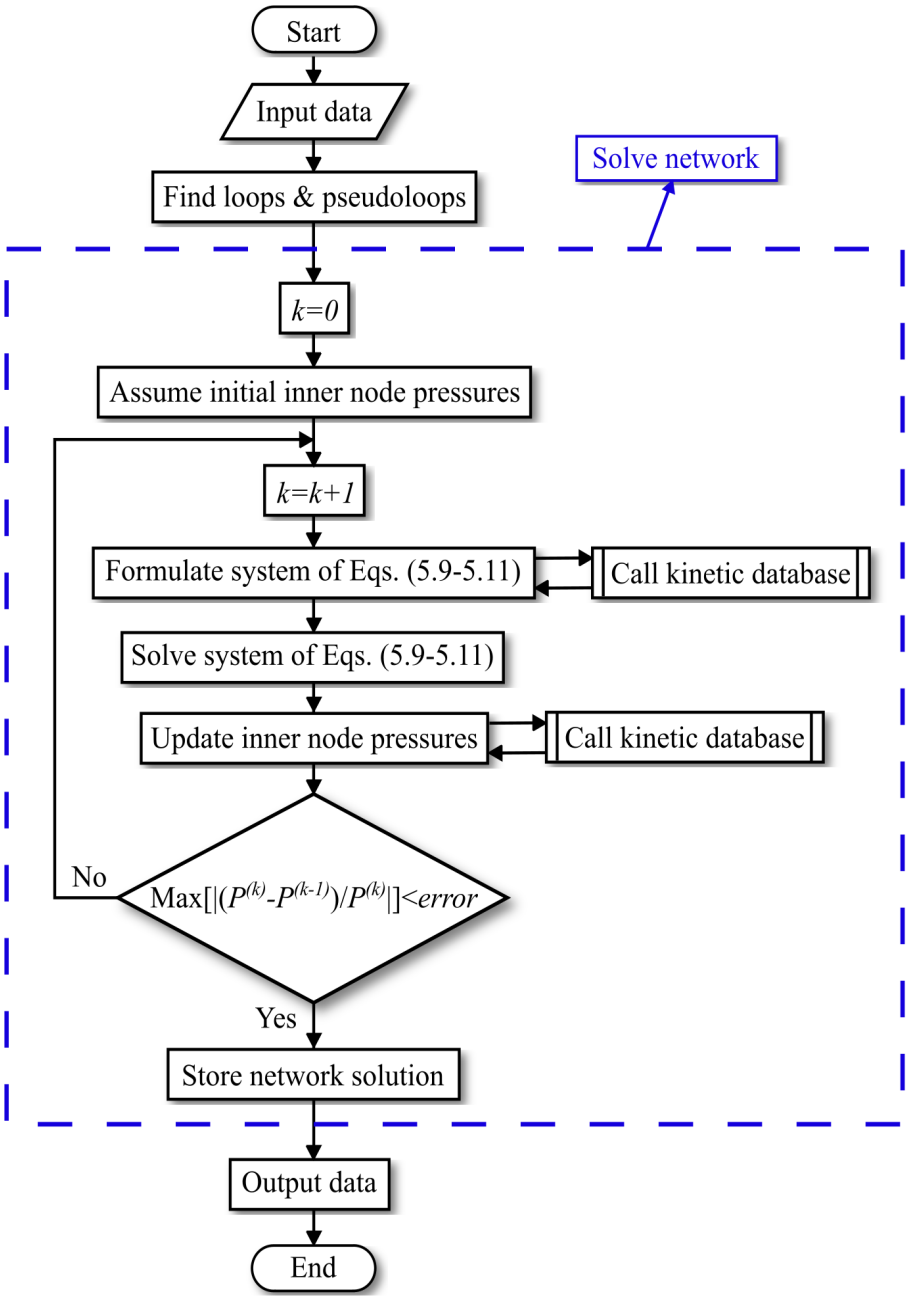

Figure 5.2 Flowchart of the UTH steady-state code.

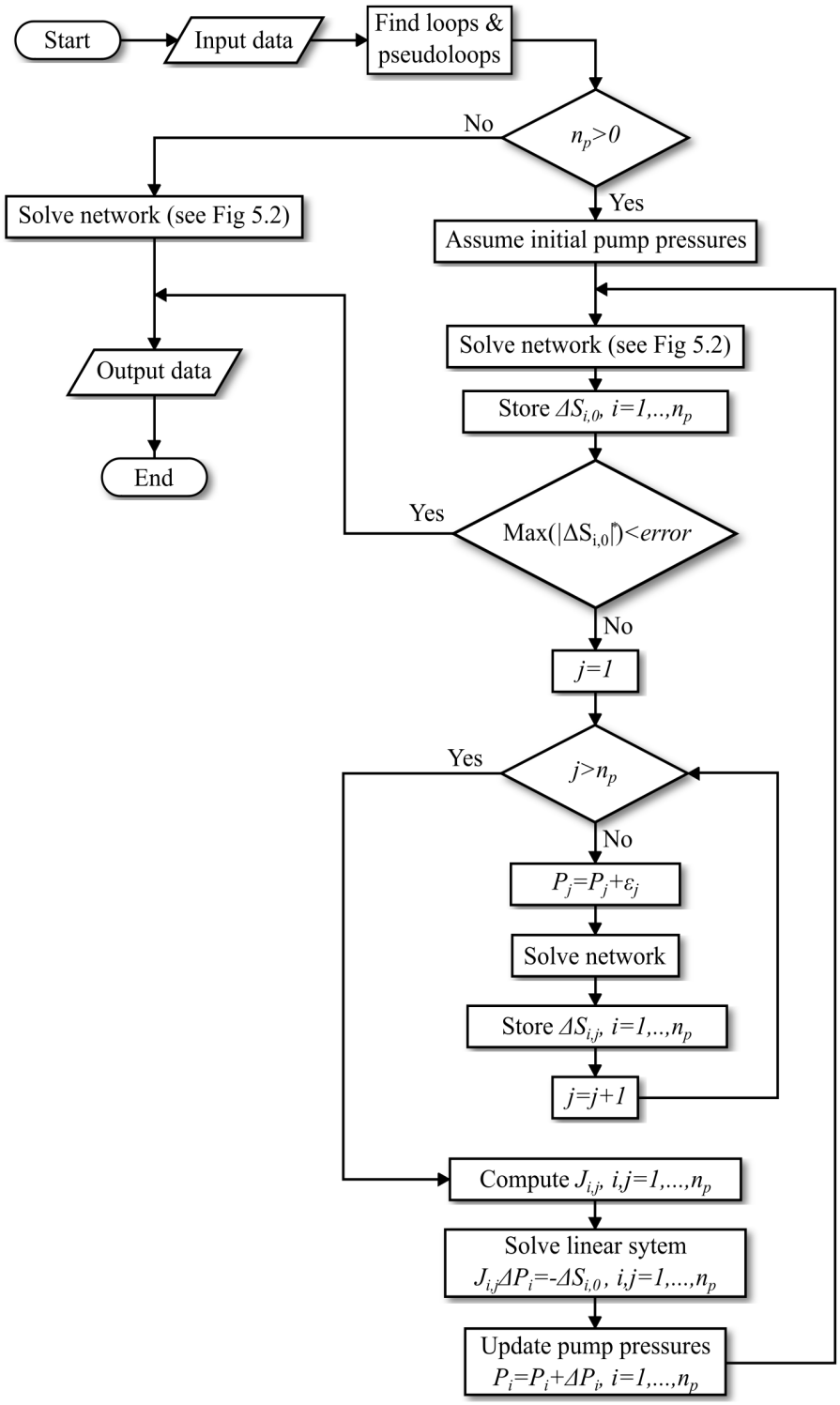

Figure 5.3 Flowchart of the UTH upgraded steady-state code ARIADNE.

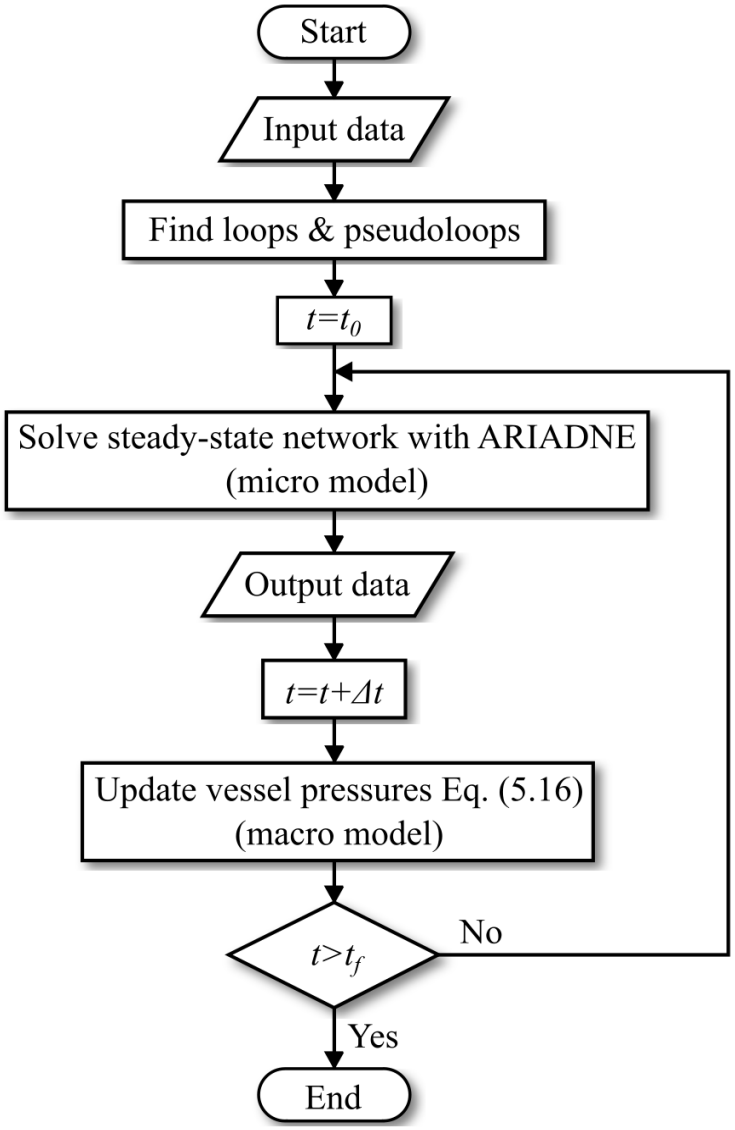

Figure 5.4 Flowchart of the hybrid time-dependent algorithm.

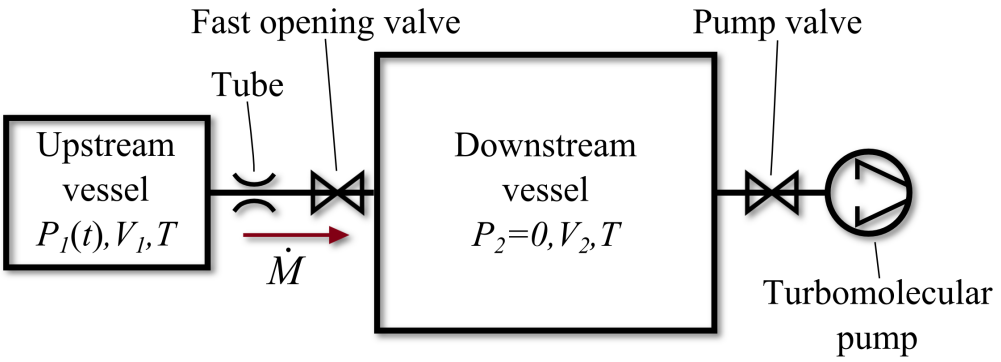

Figure 5.5 Schematic of the gas expansion apparatus (prototype problem 1).

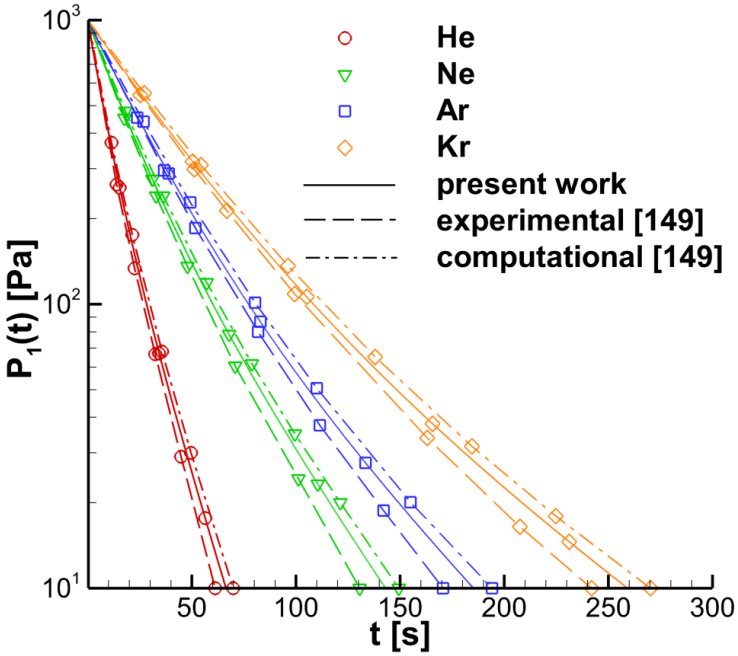

Figure 5.6 Temporal evolution of the upstream vessel pressure for He, Ne, Ar and Kr in prototype problem 1; comparison between the present time-dependent algorithm and [150].

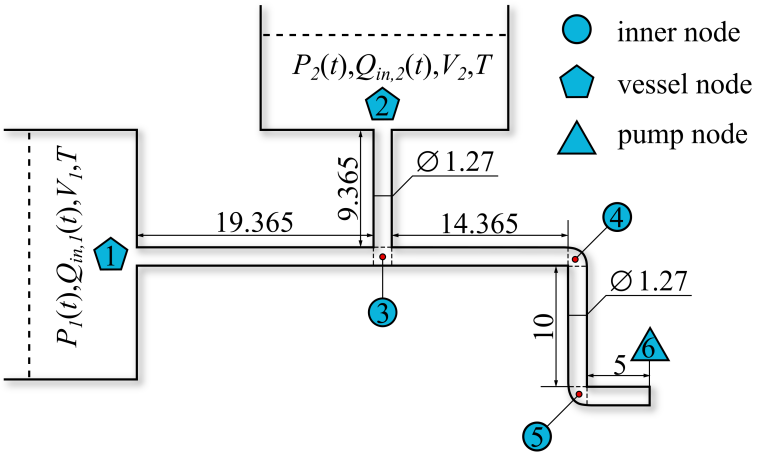

Figure 5.7 Schematic of the Molflow+ pipe network (prototype problem 2).

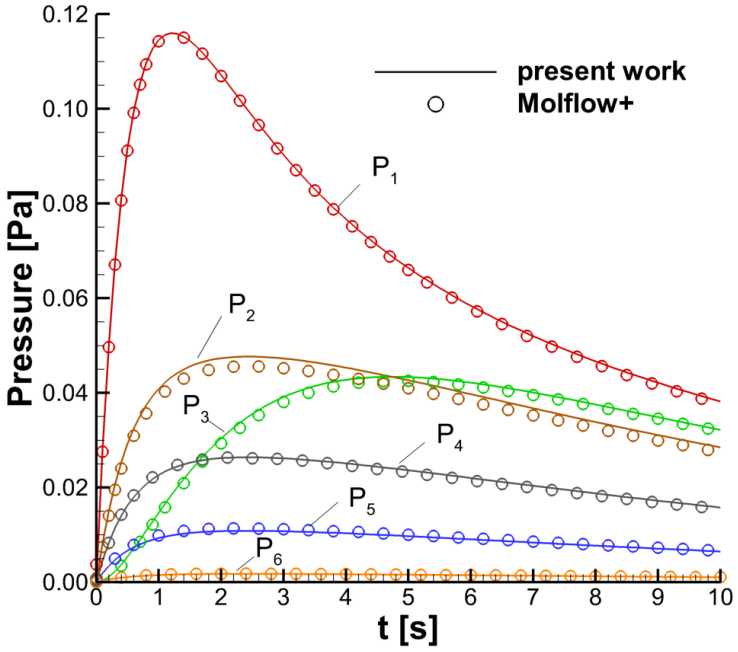

Figure 5.8 Temporal evolution of pressure $P_i\,(t)$ at the six nodes $i = 1, ..., 6$ of prototype problem 2; comparison between present time-dependent algorithm and Molflow+.

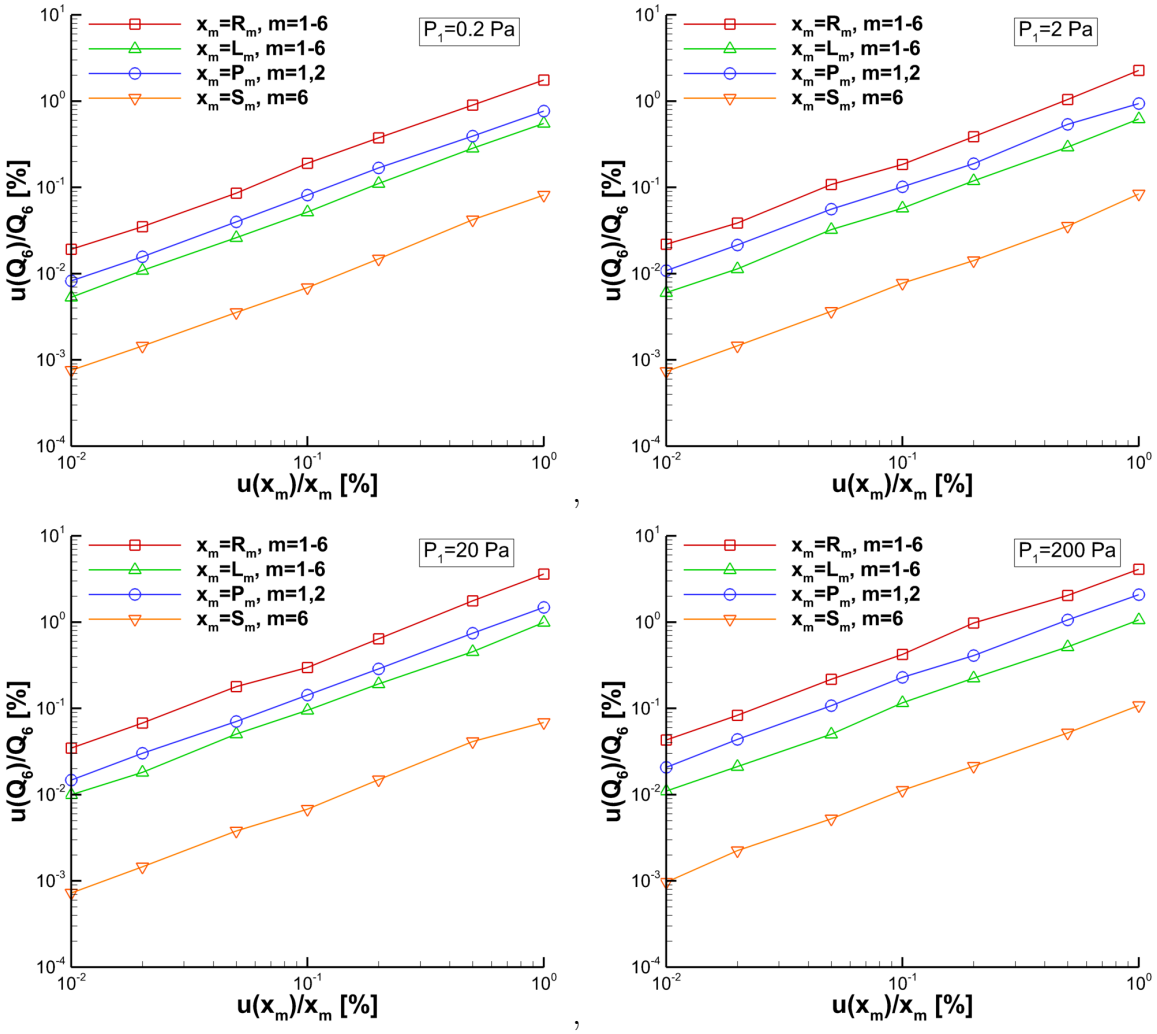

Figure 5.9 Pumped throughput uncertainty in terms of the pipe radius, pipe length, vessel pressure and pump pumping speed uncertainties for the network of Fig. 5.7 with $P_1 = [0.2, 2, 20, 200]$ Pa, $P_2 = 0.2$ Pa, $S_6 = 5 \times 10^{-2}$ m^3/s.

Chapter 6

Simulation of the ITER primary pumping system

6.1 Introduction

The International Thermonuclear Experimental Reactor (ITER) is the key facility on the European roadmap to the realization of fusion electricity, as it is expected to achieve most of the important milestones [166]. In addition, the successful operation of ITER requires the largest, complex vacuum systems yet to be built [10]. One of these vacuum systems is the primary pumping system, which is used for conditioning the vacuum vessel, maintaining the required neutral particle pressure during the burn phase and evacuating the vacuum vessel between the plasma pulses in a limited time frame during the dwell phase.

In this framework, the ARIADNE code and time-dependent algorithm discussed in Chapter 5 are implemented to simulate the ITER primary pumping system during the burn and dwell phases.

In Section 6.2, the geometrical data of the ITER primary pumping system are provided. Three distinct pipe network segments are constructed in order approximate the actual gas flow through the different divertor parts. The first network segment approximates the actual gas flow along one of the 54 divertor cassettes and consists of 43 nodes and 43 pipes, while the second segment approximates each one of the 6 pumping ducts and consists of 7 nodes and 7 pipes. The third network segment approximates the actual gas flow inside the 54 divertor gaps between adjacent cassettes and consists of 15 nodes and 41 pipes. These three networks are interconnected to construct the gas network model that approximates the actual gas flow through the

whole ITER divertor and consists of 3174 nodes and 4578 pipes. This gas network model is used in Sections 6.3 and 6.4 to simulate the burn and dwell phases of the ITER primary pumping system.

In Section 6.3, the ARIADNE code is implemented to simulate the ITER burn phase under steady-state conditions. Three pressure scenarios are investigated corresponding to low, medium and high torus pressure during burn [167]. In addition, three pump setups with 2, 4 and 6 pumps operating are investigated. Both qualitative and quantitative results are provided. The former ones include the typical gas flow direction in a cassette connected to a pump, as well as, in the open gaps between adjacent cassettes. The latter ones include the computed throughputs towards the pumps and the plasma for the different pressure scenarios and pump setups. Furthermore, the cyclic pumping/regeneration mode with 4 pumps running and 2 pumps in regeneration is considered by simulating the 4 unique possible pump setups [11].

In Section 6.4, the time-dependent algorithm is implemented to simulate the transient response of the ITER primary pumping system during the dwell pump-down of the ITER vacuum vessel. The required ITER outgassing data are extrapolated from the Joint European Torus (JET) and three different temperatures and different pump setups with 2, 4 and 6 pumps operating are investigated. First, assuming a constant torus effective pumping speed an analytical solution is provided for the temporal evolution of the torus pressure. In addition, steady-state torus effective pumping speed results based on the ARIADNE code are presented for the dwell phase in order to facilitate the discussion for the time-dependent problem. The temporal evolution of the torus pressure based on the time-dependent algorithm and the analytical solution is presented and interesting findings are reported. Furthermore, a parametric study of the involved input parameters for the torus pressure after the end of the dwell phase is provided.

6.2 Geometrical data of the ITER primary pumping system

The latest design of the ITER divertor consists of 54 cassettes with a 20 mm gap between adjacent cassettes, while the pumping load of the vacuum vessel is managed by 6 cryopumps located at the direct lower ports 4, 6, 10, 12, 16 and 18 as shown in Fig. 6.1. The most recent geometric configuration of the ITER divertor is visualized

in the 2012 drawings, which provide detailed geometrical data of the divertor ring with the 54 cassettes and interconnecting paths, as well as, of the pumping ducts and ports. A recent modification to this configuration is the neutron shielding added to the lower port ducts [168].

In Fig. 6.2 a view of the cross-section along a cassette connected to a pump and the corresponding pipe network approximating the actual gas flow path along the cassette cross-section, is shown. The regions of the dome, the inlet and outlet divertor arm gaps, as well as, the inlet and the outlet slots are indicated. The channel flow configurations of the upper and lower parts of the cassette are approximated by 25 and 16 channels of various lengths and diameters, respectively. The upper part consists of nodes 1 to 26 and the lower part of nodes 27 to 43. They are interconnected with 2 pipes resulting to a total of 43 channels and 43 nodes per cassette. The 6 nodes {1,10,14,18,26,43}, where the pressure must be specified are provided. Through these nodes the pipe network representing the flow along a cassette is open to the torus. The 11 nodes {6,9,13,17,21,28,31,33,35,38,40} connecting this cassette to its adjacent cassette in the toroidal direction, defined as toroidal connection nodes, are also presented in Fig. 6.2. Six out of the 54 cassettes and more specifically cassettes 11, 17, 29, 35, 47 and 53, corresponding to the lower ports 4, 6, 10, 12, 16 and 18 are connected to the six cryopumps. The pumping duct network consisting of 7 nodes (not numbered) and 7 pipes used to approximate the gas flow from a divertor cassette towards a direct cryopump is also shown in Fig. 6.2.

In Fig. 6.3 the pipe network simulating the geometry of the actual gas flow path between adjacent cassettes is shown. The 11 connection pipes between two cassettes (5 for the upper part and 6 for the lower part) originate from the corresponding toroidal connection nodes, mentioned in the description of Fig. 6.2. These pipes create the segment of the network representing the gas flow in the toroidal direction along the divertor ring. In addition, the middle points of these 11 pipes are interconnected, as demonstrated in Fig. 6.3, in order to produce the segment of the pipe network representing the gas flow through the cassette gap between the lower and the upper part. It consists from 19 pipes defined by the so-called 15 gap nodes including the 4 nodes {45,48,53,56}, that are open to the torus and where the pressure must be specified. Thus, the gap pipe network in Fig. 6.3 consists of 15 nodes and $2 \times 11 + 19 = 41$ pipes.

In total, the resulting pipe network approximating the gas flow through the ITER divertor gas system, consists of $54 \times (43 + 15) + 6 \times 7 = 3174$ nodes and $54 \times (43 + 41) + 6 \times 7 = 4578$ pipes.

6.3 Steady-state simulation of the ITER burn phase

The UTH upgraded steady-state network code ARIADNE is implemented to simulate the ITER burn phase for three pressure scenarios. The input parameters are the ones described in [167]. They have been obtained from the B2-EIRENE code modeling an ITER scenario where the plasma consists mainly from deuterium with the ratio of the fusion over the input power to be equal to $Q_{DT} = 10$ and the power entering the scrape-off layer equal to 100MW. These input parameters have been also used in [169]. Following [167], three different burn phase pressure scenarios, corresponding to the total pressures of 2.6 Pa, 4.1 Pa and 9.9 Pa are simulated. They are related to low, medium and high dome pressure scenarios. Since only the dominant deuterium gas fraction is considered the resulting partial pressures at the 10 fixed pressure nodes are given in Table 6.1 and they are the same with the data of Table 1 in [167]. The same pressure values are given to the fixed pressure nodes in all 54 cassettes and the associated gaps between the cassettes. The operating temperature is 420 K and the conveying gas is pure deuterium (D_2) with molar mass 4.028 kg/kmol and viscosity 15.90 μPas. The limiting pumping speed of the cryopumps is considered to be constant and equal to 55 m^3/s at the reference temperature of 273.15 K.

In Fig. 6.4 the gas flow path in the cross-section along a cassette, as described in Fig. 6.2, is shown. This flow pattern is qualitatively the same in all three pressure scenarios investigated in the burn phase and applies to all 54 cassettes. The gas enters from the vacuum vessel into each cassette via the outer slot (node 10). One part of the gas remains in the upper part of the cassette and flows in opposite directions returning finally back into the plasma from the fixed pressure nodes at the dome, the inner slot and the inner and outer divertor arm gaps, defined by the nodes 14, 18, 26 and 1, respectively. Another part of the gas reaches the lower part of the cassette and then is separated with one fraction flowing towards the cryopump and the remaining one returning to the plasma via the outer and inner divertor arm gap nodes 1 and 43, respectively.

In Fig. 6.5 the gas flow path along the divertor ring and in the open gaps between the cassettes, as described in Fig. 6.3, is shown. It is clearly seen that, gas is entering the gap network from the high pressure gap nodes 48 and 53 and is returning back to the plasma from the low pressure gap nodes 45 and 56 in the upper part. This recirculation flow pattern is the same in all 54 cassettes. The gas which remains in the gap network flows toward the inner or outer targets and then it is conveyed to the

adjacent cassettes via the 11 toroidal connections. The direction of the gas flow in the toroidal direction depends on the location of the toroidal connection (if it is in the inner or outer part of the gap), as well as, on the cassette position with regard to the operating pumps.

The flow back into the vacuum vessel observed in Figs. 6.4 and 6.5 is known as backflow and has been also observed in previous studies [167, 169, 170]. As it is discussed later depending upon the pressure scenario and the number of pumps operating, only 3–8% of the gas throughput entering the divertor is pumped toward the pumping ports, while the remaining amount is flowing back into the plasma. From that amount, about 40% is returning from the dome fixed pressure node 14 and about 23% from the gap fixed pressure nodes 45 and 56, while the remaining gas escapes from the rest of the fixed pressure nodes that face the vacuum vessel. These percentages are approximately the same in all three pressure scenarios and pump setups. Concerning the percentage break down of the throughput entering the divertor it is noted that, about 3%, 7% and 12% is entering from the outer slot node 10 in the low, medium and high pressure scenarios. The remaining 97%, 93% and 88% is entering from the gap nodes 48 and 53 in the low, medium and high pressure scenarios, respectively.

In Fig. 6.6 the computed throughputs in the burn phase toward the pumps and plasma are plotted in terms of the dome pressure with 2, 4 and 6 pumps operating. It is noted that, these pumps are planned to operate in a cyclic pumping/regeneration mode with 4 pumps running and 2 pumps in regeneration [11]. However, the case of 2 and 6 pumps operating is included here, for completeness purposes. In the case of 2 pumps they are assumed to be located at the lower ports 4 and 6, while in the case of four pumps they located at the lower ports 4, 6, 10 and 12. As expected, as the dome pressure is increased the throughput towards both the pumps and the plasma is increased. Furthermore, with the 4 and 6 pumps setup the pumped throughput is about 2 and 3 times higher than the corresponding one with the 2 pumps, respectively. This behavior indicates that, in both the 4 and 6 pumps scenarios the flow is not limited by the divertor and each cryopump added to the system, pumps about the same amount of gas as the other ones. As mentioned in the previous paragraph, only a small fraction of the gas entering the divertor is pumped out of the system. More specifically, in the case of 2 pumps only 2.7% of the total inlet gas throughput is pumped out, while in the case of 4 and 6 pumps, this percentage is increased to 5.3% and 7.8%, respectively. In addition, the backflow to the plasma is decreased by about 2.2% and 4.4%, with respect to the 2 pump scenario, when 4 and 6 pumps are employed.

Since the 6 cryopumps are planned to operate in a cyclic pumping/regeneration mode with 4 pumps running and 2 pumps in regeneration, it is important to investigate the pumped throughputs for each possible pump setup. From the latest pump placement shown in Fig. 6.1 with 4 pumps operating 15 possible pump setups can be identified. However, due to the symmetries present in the pump port locations these 15 setups can be reduced to 4 unique ones.

In Table 6.2 the pumped throughputs for each pump, as well as, the total pumped throughputs are presented for the 4 unique pump setups in the low and high pressure burn phase scenarios. In all the investigated setups the total throughput is very close to each other with the highest deviation between different setups reaching 2.4% and 1.8% in the low and high pressure scenarios, respectively. In addition, in each setup the individual pump throughputs are well balanced. These remarks are in favor of the cyclic pumping/regeneration mode, moving smoothly from one operating pump setup to the next.

6.4 Transient simulation of the ITER dwell phase

In this section, the hybrid time-dependent algorithm is implemented to simulate the transient response of the ITER dwell phase. During the dwell phase the ITER vacuum vessel, having a volume of about 1400 m^3, must be pumped down to the threshold pressure of 5×10^{-4} Pa in order to start the next plasma shot [171]. The main impediment to the torus evacuation is the outgassing of hydrogen isotopes and helium implanted on the vacuum vessel walls during the plasma discharge.

It is evident that, the outgassing data of the ITER torus during the dwell phase are of major importance for the time-dependent simulations and are obtained following [171], where a realistic estimation of the ITER outgassing rate is given by considering corresponding data from JET. The outgassing rate from the ITER-like beryllium wall of JET follows an inverse power law, written as [172]

$$Q_{in}(t) = K_1 t^{-n}, \tag{6.1}$$

where K_1 is the initial outgassing rate, t is the dwell phase elapsed time and n is the decay index. Substituting Eq. (6.1) into Eq. (5.16) and (5.17) yields the macro model

describing the temporal evolution of the ITER torus pressure $P(t)$ as

$$V\frac{dP(t)}{dt} = K_1 t^{-n} + \dot{M}(t) R_g T = K_1 t^{-n} - P(t) S_{eff}(t), \tag{6.2}$$

where V is the torus volume and $S_{eff}(t)$ the torus effective pumping speed. For constant effective pumping speed at the torus, Eq. (6.2) may be solved analytically to deduce the closed form expression

$$P(t) = \frac{1}{e^{\frac{S_{eff}}{V}t}} \left(P(t_0) e^{\frac{S_{eff}}{V}t_0} + \frac{K_1}{V} \int_{t_0}^{t} x^{-n} e^{\frac{S_{eff}}{V}x} dx \right), \tag{6.3}$$

where $P(t_0)$ is the initial torus pressure at time t_0. The analytical solution (6.3), subject to the assumption of constant pumping speed, will be implemented later in this section for comparing and physically justifying some of the computational results.

It is noted that Eqs. (6.1)-(6.3) hold for $t > 0$ and thus, following [171], the dwell phase is assumed to start at $t_0 = 1$ s, where by setting $dP/dt = 0$, according to Eq. (6.2), yields $Q_{in}(t_0) = K_1 = P(t_0) S_{eff}(t_0)$. Based on the experimental data from six consecutive JET pulses #70530 - #70535 [173] and the JET torus effective pumping speed of $S_{eff,JET} \sim 200$ m^3/s, the initial outgassing rate of the vacuum vessel is estimated between 1.2-1.5 Pam^3/s. Thus, assuming the active vessel areas of JET and ITER being 144 m^2 [174] and 700 m^2 respectively [171], the initial outgassing rate of the ITER vessel is estimated between 5.8-7.2 Pam3/s. The decay index n has been repeatedly reported in the literature to be 0.75±0.1 [172, 174, 175].

Three pumping scenarios are investigated with 2, 4 and 6 pumps operating. In the first one the 2 pumps located at lower ports 4 and 6 are operating and the remaining 4 pumps are regenerating, while in the second one the 4 pumps located at lower ports 4, 6, 10 and 12 are running and the remaining 2 pumps are regenerating. As it was discussed in Section 6.3 the chosen 2 and 4 pump setups correspond to the worst case scenario i.e. the minimum torus effective pumping speed of all possible pump setups. The limiting pumping speed of the cryopumps is considered to be 55 m^3/s at the reference temperature of 273.15 K. Since the ITER torus and divertor system temperature may vary, the temperatures of 400, 600 and 800 K are considered. The conveying gas is D_2 (molar mass 4.028 kg/kmol, viscosity of 15.4, 20.3, 24.8 μPas at 400, 600 and 800K) as the main outgassing hydrogen isotope [174].

Before proceeding with the transient response of the ITER torus primary pumping system, some steady-state results of the ITER torus effective pumping speed in terms

of the torus pressure are provided. The pressure at the torus pressure nodes (red nodes in Figs. 6.2 and 6.3), is specified, along with the other required input data to the ARIADNE code, which is implemented to compute the torus effective pumping speed.

In Table 6.3, the torus effective pumping speed for torus node pressures equal to $[10^{-5}, 10^{-4}, 10^{-3}, 10^{-2}, 10^{-1}, 1]$ Pa is tabulated based on the 2, 4 and 6 running pump scenarios at temperatures 400, 600 and 800 K. It is observed that, when the torus node pressure is less than or equal to $\sim 10^{-3}$ Pa, i.e., when the flow is in the free molecular regime, the torus pumping speed is almost constant and thus, the pumped throughput is linear with respect to pressure. On the contrary, when the torus node pressure is higher than $\sim 10^{-3}$ Pa, i.e., when the flow is in the transition regime, the torus pumping speed increases monotonically with the torus pressure. These remarks are valid for all three pump setups. Furthermore, with 4 and 6 pumps operating the torus effective pumping speed is about 2 and 3 times higher than the corresponding one with the 2 pumps. As discussed in Section 6.3 this behavior indicates that, in both the 4 and 6 pumps scenarios the flow is not limited by the divertor and each cryopump added to the system, pumps about the same amount of gas as the other ones.

Moving to the transient response of the ITER dwell phase, in Fig. 6.7, the temporal evolution of the ITER torus pressure during the 1400 s dwell phase, computed based on the time-dependent algorithm is compared with the corresponding one, based on the analytical solution (6.3) subject to the constant torus effective pumping speed assumption. The comparison is made for the three pumping scenarios at $T = 400$K, with initial torus pressure equal to 1 Pa, average initial outgassing rate $K_1 = 6.5$ Pam^3/s and $n = 0.65$ and 0.85, which are the lowest and highest decay index values found in the literature. Furthermore, the constant pumping speed in Eq. (6.3) is taken from Table 6.3 for torus pressure 10^{-5} Pa, and is equal to 39.16 m^3/s, 77.22 m^3/s and 114.2 m^3/s for the 2, 4 and 6 running pumps, respectively. The specific values have been chosen since, based on the results of Table 6.3, the assumption of the constant pumping speed is justified in the low pressure regime.

As it is seen in Fig. 6.7, the results are in good qualitative agreement in the whole dwell phase. However, for $t \leq 300$ s, $t \leq 200$ s and $t \leq 100$ s in the cases of 2, 4 and 6 pumps respectively, there are significant quantitative deviations, with the present time-dependent algorithm considered as the accurate prediction. These discrepancies are justified, since for all above specified times the torus pressure is above 10^{-3} Pa (i.e. the gas flow in the transition regime) and the torus effective pumping speed in all three pumping scenarios is not constant as clearly seen in Table 6.3, which makes

the analytical solution of Eq. (6.3) invalid. On the contrary, for $t > 300$ s, $t > 200$ s and $t > 100$ s in the cases of 2, 4 and 6 pumps respectively, with the torus pressure below $\sim 10^{-3}$ Pa and the whole pumping system in the free-molecular regime the two approaches show an excellent quantitative agreement. The observations with regard to the validity of the two approaches are important for the following reasons: a) The effectiveness of the present time-dependent algorithm in modeling the transient response of large size pipe networks is validated; b) When the torus pressure at the end of the 1400 s dwell phase is the only quantity of interest, it can be accurately predicted directly from Eq. (6.3), based on the constant torus pumping speed in the free-molecular regime computed by ARIADNE, without implementing the hybrid time-dependent algorithm; c) The physical behavior of the torus pressure temporal evolution including the final torus pressure at the end of the 1400 s dwell phase can be qualitatively explained based on the simple form of Eq. (6.3).

The temporal evolution of the torus pressure during the dwell phase for initial torus pressures equal to 1, 10^{-1} and 10^{-2} Pa is plotted in Fig. 6.8. The other data are as before (three pumping scenarios, $T = 400$K, $K_1 = 6.5$ Pam^3/s, $n = 0.65$ and 0.85). Starting with the 2 pumps scenario, it is seen that the torus pressure evolution depends on the initial torus pressure when $t \leq 300$ s, while it becomes identical for all initial pressure conditions when $t > 300$s. The observed behavior also holds with the 4 or 6 pumps scenarios, with the corresponding times, where the merging of the torus pressure temporal evolution curves takes place, at approximately $t = 200$ s and $t = 100$ s, respectively. These remarks are valid for both investigated values of the decay index. Thus, it may be concluded that in the range of the investigated parameters the torus pressure after the 1400 s dwell phase is independent from the initial pressure conditions of the torus. The above remark is easily justified by examining the right hand side of the analytical solution (6.3), where the first term inside the parenthesis, related to the initial pressure is constant, while the second term, related to outgassing, grows with time. Therefore, at adequately large times the temporal pressure evolution will be independent of the initial pressure conditions and will only depend on the outgassing term.

Many of the required ITER dwell phase input data have been either extrapolated from corresponding JET data or have been assumed. Thus, a parametric study is performed in order to deduce some useful information on the importance of the involved input data on the final torus pressure. In Fig. 6.9 the final torus pressure after the 1400 s dwell phase is presented in terms of the initial outgassing rates K_1, for the decay

indices $n = 0.65$ and 0.85, the system temperatures $T = 400$, 600 and 800 K with 2, 4 and 6 pumps operating.

It is readily seen that, in all cases the final torus pressure grows linearly with the initial outgassing rate. This trend is justified by Eq. (6.3), where K_1 multiplies the integral term, which is the one, affecting the final torus pressure. Furthermore, the final torus pressure with the 4 and 6 pumps is always reduced about 2 and 3 times respectively, compared to the corresponding one with the 2 pumps scenario. It is reminded here that, the torus effective pumping speed is increased by about 2 and 3 times when 4 and 6 cryopumps are employed. It is also seen that the final torus pressure is reduced as the torus temperature is increased. More specifically, when the torus temperature is increased from 400 K to 600 K the final torus pressure is always decreased by about 22%, while when the torus temperature is doubled from 400 K to 800 K the torus pressure reduction is about 34%. In addition, for $n = 0.85$, corresponding to the lowest outgassing scenario, after the 1400 s dwell pumping the target torus pressure of 5×10^{-4} Pa can be always achieved in the cases of 4 and 6 operating pumps, while in the case of 2 operating pumps it can only be achieved in a certain range of the investigated parameters. However, for $n = 0.65$, which corresponds to the highest outgassing, the required threshold pressure is marginally achieved in the expected range of initial outgassing rates (5.8-7.2 Pam^3/s) only when all 6 cryopumps are employed. Actually, even with the utilization of all 6 cryopumps, considering the uncertainty of the initial outgassing rate estimation (extrapolated from JET), it cannot be stated with absolute certainty, that the target pressure of 5×10^{-4} Pa can be achieved when $n = 0.65$.

6.5 Concluding remarks

The capabilities of the UTH steady-state code ARIADNE and the proposed hybrid time-dependent algorithm have been demonstrated by successfully simulating the burn and dwell phases of the ITER primary pumping system.

The UTH steady-state code ARIADNE has been implemented to simulate the ITER burn phase under steady conditions for several operating scenarios and both qualitative and quantitative results have been provided. Regarding the qualitative results, the gas flow direction through a cassette connected to a pump port, as well as, inside a typical gap between adjacent cassettes has been provided. Regarding the quantitative results for the pumped throughput and the backflow into the plasma, it

has been found that they are both increased moving from the low, to the medium and to the high pressure scenarios. In addition, the pumped throughput in the 4 and 6 pump scenarios is increased by about 2 and 3 times compared to the 2 pump scenario. Moreover, concerning the cyclic pumping/regeneration mode it has been found that the total throughput is very close for all unique pump setups and the individual pump throughputs are well balanced.

The proposed time-dependent algorithm has been implemented to simulate the ITER 1400 s dwell phase for various operating scenarios and several interesting findings have been reported. Regarding the torus pressure at the end of the dwell phase, which is of major importance, it has been found that it is independent of the initial torus pressure conditions, it increases linearly with the initial outgassing rate and it decreases as the network temperature increases. It is also seen that, the final torus pressure in the 4 and 6 pump scenario is reduced about 2 and 3 times compared to the corresponding one in the 2 pump scenario. Concerning the specified target pressure of 5×10^{-4} Pa at the end of the dwell phase, based on the present simulations subject to the introduced operational and geometrical data, it is concluded that in the lowest outgassing scenario it can be achieved in a wide range of the investigated parameters, while on the contrary in the highest outgassing scenario it is marginally achieved only in the expected range of initial outgassing rates when all 6 cryopumps are employed.

Table 6.1 Partial pressure [Pa] of deuterium (D_2) at the fixed pressure nodes for three pressure scenarios during the burn phase [167].

Node number	Corresponding location in [167]	Low-p	Mid-p	High-p
1	E	8.2×10^{-4}	1.0×10^{-3}	8.1×10^{-4}
10	D	3.65	7.20	15.0
14	C	1.85	3.10	7.82
18	B	10.4	12.5	23.6
26	A	6.7×10^{-5}	2.6×10^{-4}	8.8×10^{-4}
43	A	6.7×10^{-5}	2.6×10^{-4}	8.8×10^{-4}
45	Upper gap part, outer target	0.20	0.30	0.30
48	Lower gap part, inner target	8.30	18.5	33.7
53	Lower gap part, outer target	32.3	42.7	70.1
56	Upper gap part, inner target	0.08	0.20	0.60

Table 6.2 Pumped throughput [Pam^3/s] in the low and high pressure burn phase scenarios for the four unique pump setups; R denotes regeneration.

Pump port	Low-p				High-p			
4	98.0	96.1	97.5	97.9	367.7	363.2	366.4	364.2
6	96.2	96.1	96.5	97.9	363.2	363.2	364.2	364.2
10	96.2	101.3	100.8	R	363.2	376.7	375.5	R
12	98.0	R	R	101.2	367.7	R	R	379.8
16	R	R	102.5	101.2	R	R	379.8	379.8
18	R	101.3	R	R	R	376.7	R	R
Total	388.4	394.8	397.3	398.1	1461.9	1479.7	1486.0	1488.0

Table 6.3 Torus effective pumping speed (m^3/s) of D_2 with respect to the torus pressure with two, four and six pumps operating at 400, 600 and 800 K.

Pumping scenario	2 pumps			4 pumps			6 pumps		
Torus pressure [Pa]	400 K	600 K	800 K	400 K	600 K	800 K	400 K	600 K	800 K
10^{-5}	39.16	50.20	59.63	77.22	98.94	117.5	114.2	146.3	173.6
10^{-4}	39.17	50.21	59.64	77.25	98.95	117.5	114.3	146.3	173.6
10^{-3}	39.28	50.30	59.71	77.46	99.12	117.6	114.5	146.5	173.8
10^{-2}	40.33	51.18	60.48	79.47	100.8	119.1	117.2	148.7	175.7
10^{-1}	48.61	58.58	67.16	95.01	114.8	131.7	138.4	167.7	192.8
1	79.10	96.07	107.0	152.6	184.0	204.6	225.3	267.7	295.9

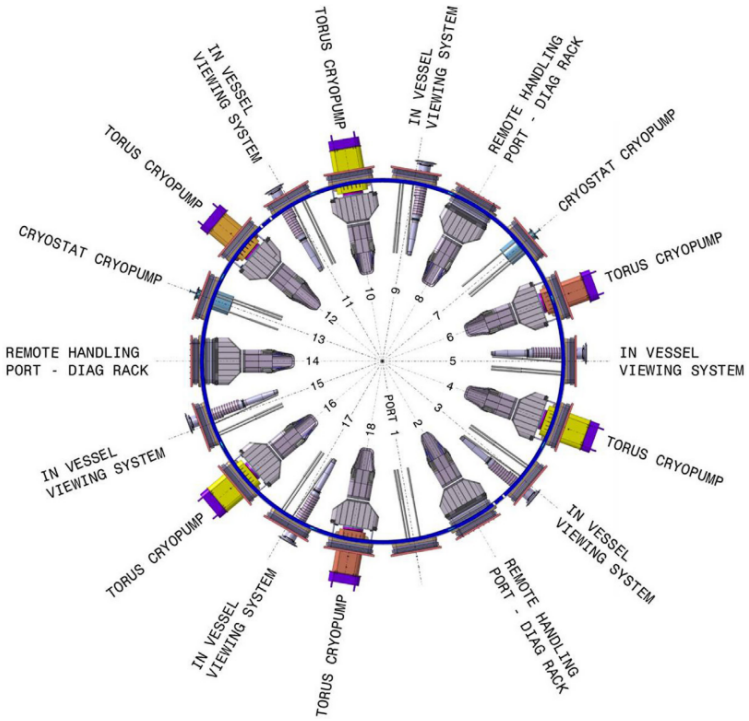

Figure 6.1 View of the cryopump positions [11].

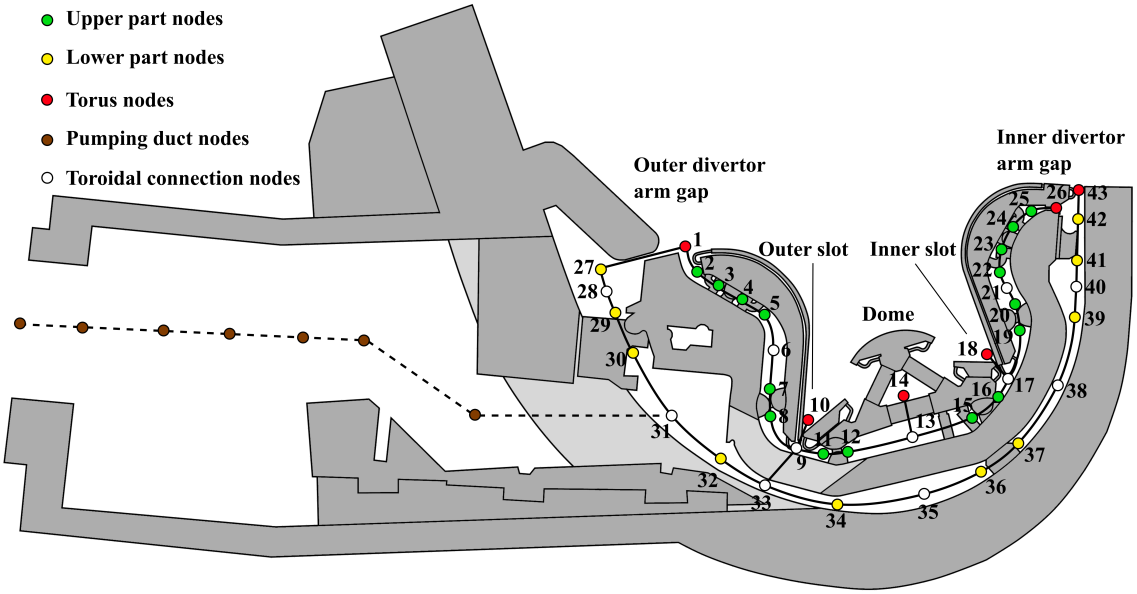

Figure 6.2 Cross-section view of a cassette connected to a pump along with the pipe network approximating the gas flow path.

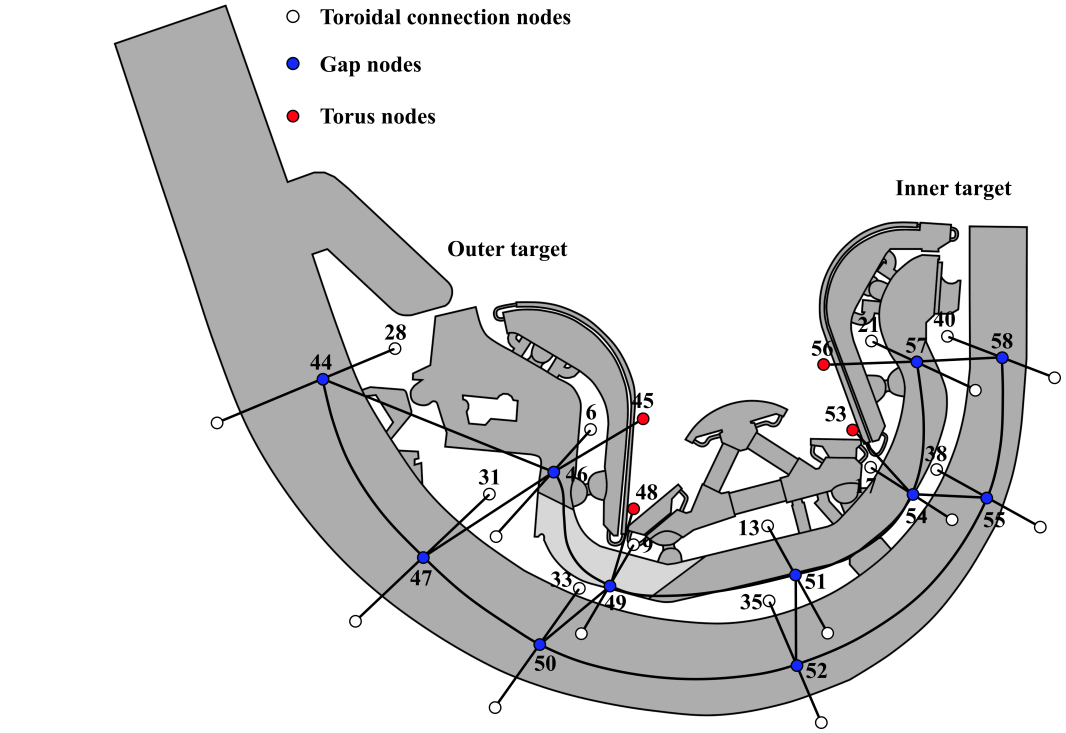

Figure 6.3 Cross-section view of a gap between adjacent cassettes along with the pipe network approximating the gas flow path.

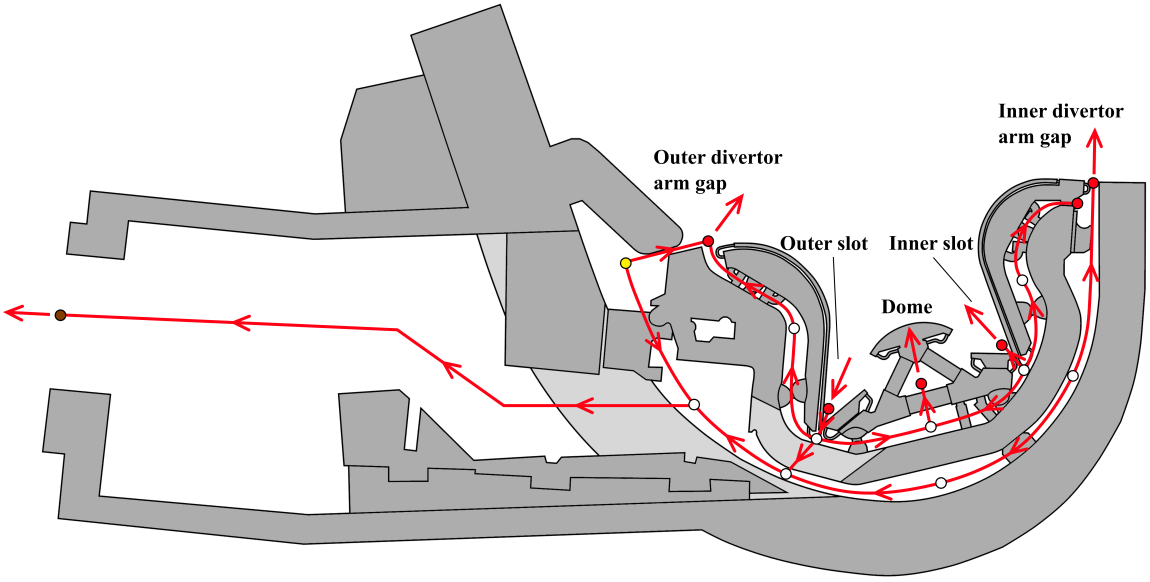

Figure 6.4 Direction of gas flow through the pipe network approximating a cassette connected to a pump.

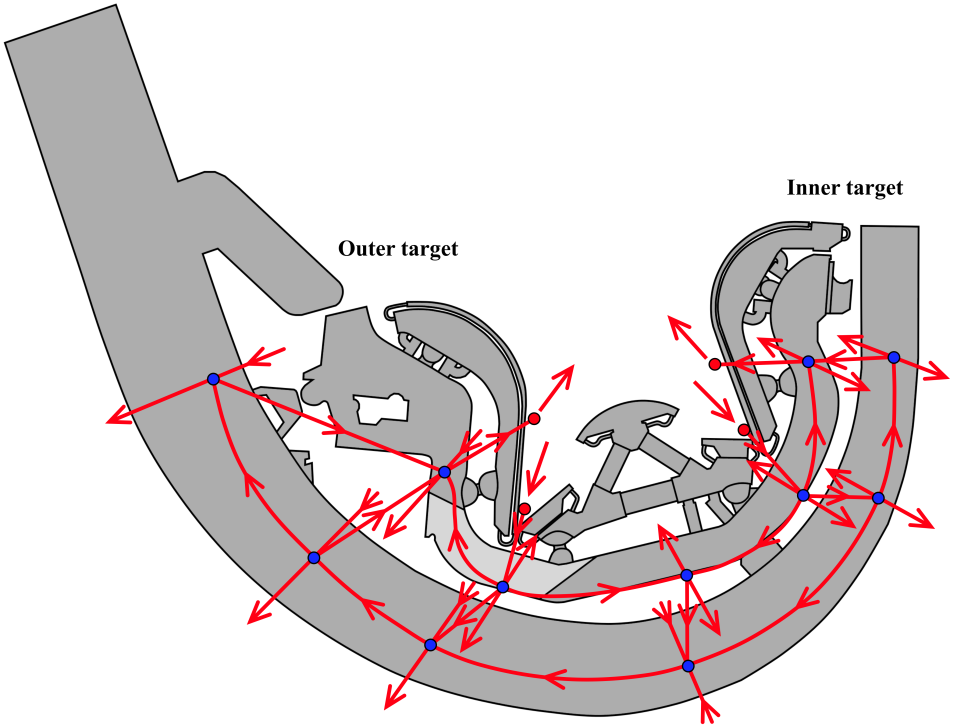

Figure 6.5 Direction of gas flow through the pipe network approximating the gap between adjacent cassettes.

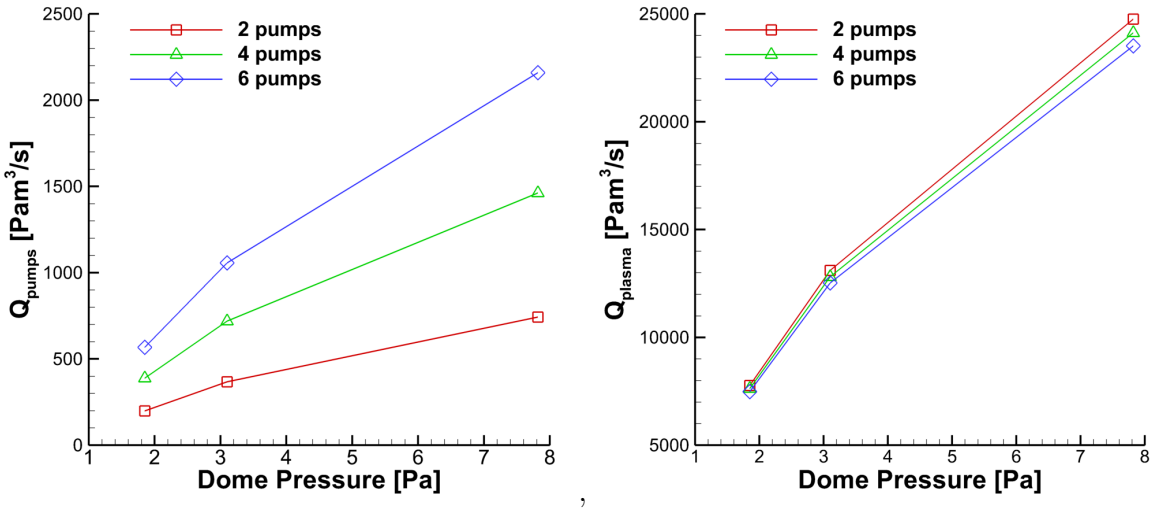

Figure 6.6 Computed throughput towards the pumps (left) and the plasma (right) in the low, medium and high pressure burn phase scenarios with respect to the dome pressure with two, four and six pumps operating.

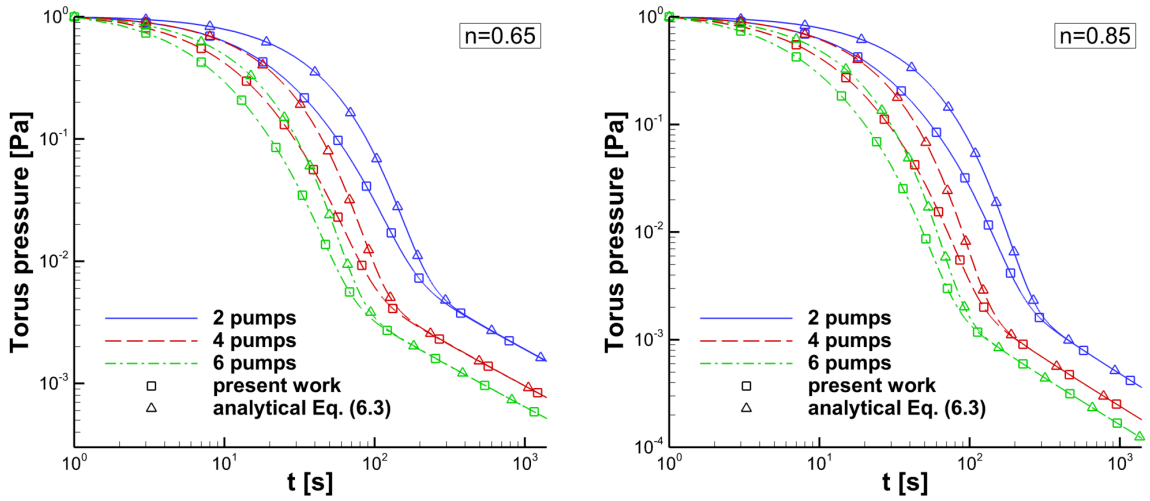

Figure 6.7 Temporal evolution of the ITER torus pressure, based on the time-dependent algorithm and analytical Eq. (6.3), with two, four and six pumps operating, initial torus pressure 1 Pa, initial outgassing rate $K_1 = 6.5\text{Pam}^3/\text{s}$, temperature $T = 400$ K and decay indices $n = 0.65$ (left) and $n = 0.85$ (right).

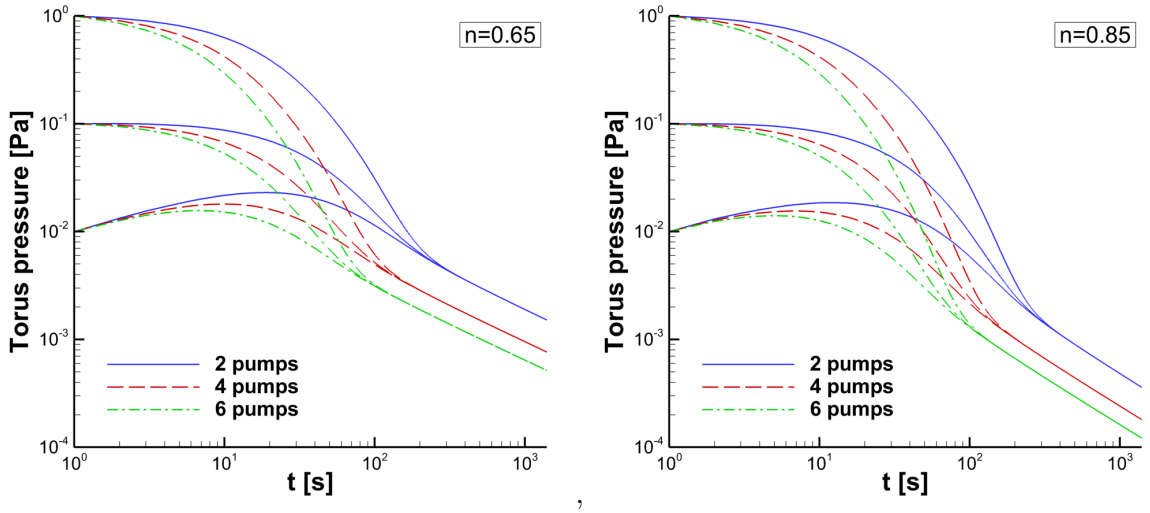

Figure 6.8 Temporal evolution of the ITER torus pressure for initial torus pressures $P(t_0 = 1) = [10^{-2}, 10^{-1}, 1]$ Pa, with two, four and six pumps operating, initial outgassing rate $K_1 = 6.5$ Pam^3/s, temperature $T = 400$ K and decay indices $n = 0.65$ (left) and $n = 0.85$ (right).

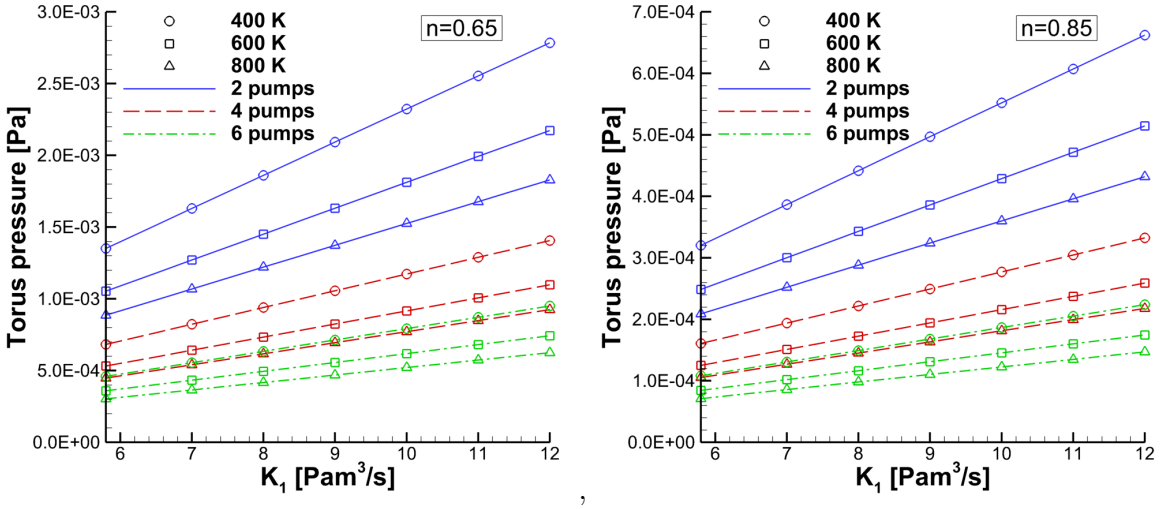

Figure 6.9 Torus pressure after the 1400 s dwell phase in terms of the initial outgassing rate K_1 with two, four and six pumps operating, temperature $T = 400$, 600 and 800 K and decay indices $n = 0.65$ (left) and $n = 0.85$ (right).

Chapter 7

Aerosol flows via stochastic modeling

7.1 Introduction

Recently the simulation of aerosol flows under rarefied conditions has attracted considerable attention due to their significant role in the semiconductor and MEMS manufacturing industry [19–21], as well as due to their tentative importance in fusion reactor plasma and tritiated dust control [22–25].

At the Laboratory of Transport Phenomena and Process Equipment at the University of Thessaly the 3D DSMC code "PROGRESS", which stands for **Pr**ediction **o**f **G**as **R**arefaction **E**ffects through **S**tochastic **S**imulations, has been developed by Dr. S. Pantazis, based on the DSMC method proposed by Bird [30]. In the present work, PROGRESS has been appropriately modified in order to simulate the transport of a single rigid spherical particle inside a rarefied gas.

In the first part of this chapter, an overview of the DSMC method proposed by Bird [30] is described in order to facilitate the discussion for the developed aerosol code. Next, the structure of the developed aerosol code is provided in detail. In the developed code a two-way coupling is implemented [109]. The force and torque exerted on the solid particle are computed based on the gas-solid particle collisions. The gas-solid particle collision detection is perfomed in a deterministic manner, while the gas particles are reflected from the solid particle surface stochastically. The computed force and torque are then used to determine the translational and rotational motion of the solid particle deterministically based on the Newton-Euler equations. The DSMC aerosol code has been developed based on object-oriented programming in order to be

easily accessible, adaptable and to facilitate the addition of new features in the future, such as the transport of multiple solid particles. In addition, several advancements have been made to the code, such as the implementation of the Variable Soft Sphere (VSS) intemolecular potential, as well as, the implementation of the so-called subcell and tetrahedron meshes. Furthermore, the developed code has been parallelized using the MPI communication protocol in order to be able to tackle computationally intensive simulations.

In the second part of this chapter, the developed DSMC code is validated based on three benchmark cases. In the first benchmark case the thermophoresis of a solid particle suspended in a rarefied gas between two infinite parallel plates kept at slightly unequal temperatures is investigated via the proposed aerosol code. The purpose of this benchmark is to validate the force computation, as well as the computation of the gas macroscopic quantities. The obtained results for the heat flux between the plates and the thermophoretic force exerted on the particle are benchmarked with the ones reported in [20], where the typical DSMC method is used and a force Green's function is implemented for the computation of the thermophoretic force. In addition, the computed results are compared with the approximate closed form expressions for the heat flux and the thermophoretic force proposed in [20, 176]. In the second and third benchmark cases the translational and rotational Brownian motion respectively, of a solid particle suspended in a rarefied gas bath at rest is investigated. The purpose of these two benchmarks is the validation of the force and torque computation, as well as the translational and rotational movement of the rigid particle. The translational and rotational diffusion coefficients are computed based on the translational and angular position variance of the particle and they are compared with their theoretical values in the free-molecular regime [100, 177]

7.2 The direct simulation Monte Carlo method

The DSMC method proposed by Bird [30] emulates the physics of the Boltzmann equation by following the motion and collisions of a large number of simulator particles. Each simulator particle represents a large number of real gas particles F_n and possesses molecular information such as the position vector $\boldsymbol{r}$, molecular velocity vector $\boldsymbol{\xi}$, molecular mass m and diameter d. The particle motion and collisions are decoupled over a small time step Δt. The free motion part is purely deterministic and the simulator particle travels a distance proportional to its velocity, when no external forces act on

the gas. In addition, during the movement of the gas simulator particles, boundary conditions such as the reflection from a solid surface are applied in a stochastic manner, where the reflected particle velocity is sampled from a scattering distribution. The particle collisions are also simulated stochastically. The most widely employed collision technique is the No Time Counter (NTC) scheme suggested by Bird [30]. In this scheme, a number of particle pairs is chosen regardless of their position and molecular velocity and a collision probability for the specific gas particle pair is calculated based on the product of the collision cross-section and relative velocity. The collision between the two particles occurs when a random number $r_f \in [0, 1]$ is smaller than the collision probability. A variety of intermolecular potentials have been developed for DSMC simulations, with the Hard Sphere (HS), Variable Hard Sphere (VHS) and Variable Soft Sphere (VSS) being the most widely used ones [30, 178]. The flow domain is usually discretized by either a structured or unstructured mesh of cells. The mesh cells are used for the collision particle pair selection and for sampling the macroscopic quantities, such as the density, velocity vector, temperature, stress tensor and heat flux vector. Furthermore, the mesh cells may be split into subcells in order to improve the particle collision computations. In this case, the subcells are employed for the collision sampling, while the cells are employed for the macroscopic quantities sampling.

In general, a DSMC simulation starts from an initial time and ends after a predetermined number of time steps. The typical steps in each DSMC time step are: (1) Move the particles over the time step Δt; (2) Index the particles into the cells and subcells; (3) Collide the particles in each cell or subcell; (4) Sample the macroscopic quantities. These steps are also present in the developed DSMC aerosol code, with some modifications required for the simulation of the solid particle.

7.3 Structure of the 3D DSMC aerosol code

The flowchart of the developed 3D DSMC aerosol code is provided in Fig. 7.1. As it is seen, the first task is to provide the required simulation data as input to the developed code. These data include a variety of information, such as the nominal time step Δt_0, the total simulation time t_f, the number of simulator particles, the gas properties and intermolecular model, the solid particle properties, as well as the boundary and initial conditions. Furthermore, the cell mesh discretizing the flow domain, which is used to sample, average and output the macroscopic quantities, can be designed in any suitable 3D CAD software and must be provided as a Universal

Format file (UNV). In its current state, the developed code supports hexahedral and tetrahedral cells.

In addition to the cell mesh, two more meshes are constructed in the proposed algorithm as shown in Fig 7.1. The first is the subcell mesh, which is implemented for the gas particle collisions and is created by splitting the initial mesh cells into subcells. The method used here to create the subcells for each cell is to use the cell center and faces. In Fig. 7.2 an example of the proposed subcell creation method is shown for a hexahedron cell. It is evident that, in the case of a hexahedral cell six pyramid subcells are created, while in the case of a tetrahedral cell four tetrahedral subcells are created. The second mesh is the tetrahedral mesh, which is used in the gas and solid particle initialization, as well as, in order to compute the cell and subcell volume occupied by the solid particle. The tetrahedral mesh, as the name suggests, only consists of tetrahedrons and is created by splitting the subcell mesh. In Fig. 7.3 an example of the proposed tetrahedron mesh creation method is shown for a pyramid subcell. As it can be seen, in the case of a pyramid subcell two tetrahedron cells are created by splitting the quadrilateral face in two triangular ones, while in the case of a tetrahedron subcell no further splitting is required. Each cell in the initial mesh contains the subcells and each subcell contains the tetrahedron cells. Thus, computations performed for the tetrahedron mesh are easily translated to the subcell and cell mesh.

After the creation of the subcell and tetrahedron mesh the spherical solid particle with a predetermined radius R_s is initialized. The user may specify an initial center of mass position and an initial translational velocity $\boldsymbol{v}_{s,0}$ and angular velocity $\boldsymbol{\omega}_{s,0}$ in the input files. Otherwise, the solid particle is assumed to be at rest ($\boldsymbol{v}_{s,0} = \boldsymbol{\omega}_{s,0} = 0$) and is generated in a random position inside the flow domain (confirming that it does not intersect any of the flow domain boundaries).

Then, given the initial translational velocity any possible collision between the solid particle and the flow domain boundaries within the nominal time step Δt_0 is examined [179]. In the case where, a collision occurs in time $\Delta t_{coll} < \Delta t_0$ the time step Δt becomes Δt_{coll}, otherwise the nominal time step Δt_0 is maintained. This time step modification is performed to ensure that, in each iteration the solid particle performs a single linear movement. This modification significantly reduces the computational effort required for the gas-solid particle collision detection and most importantly it facilitates the simulation of multiple solid particles in the future.

The gas solid particle is indexed by detecting which cells are partially or fully occupied by the solid particle [179]. Furthermore, the volume occupied by the solid

particle in each cell and subcell is computed analytically by computing the overlap volume between the spherical solid particle and the tetrahedron mesh following [180]. However, the methodology proposed in [180] only considers a stationary sphere. Thus, the suggested computations are performed for 10 time increments during the solid particle motion and the average overlapping volumes are computed for all the mesh cells and subcells.

Next, the gas particles are initialized at uniformly distributed random points inside each cell and the molecular velocity vector $\boldsymbol{\xi}$ is sampled from the Maxwellian distribution

$$f(\boldsymbol{\xi}) = \frac{1}{\pi^{3/2} v_0^3} e^{-\left(\frac{\xi}{v_0}\right)^2}, \tag{7.1}$$

where $v_0 = \sqrt{2R_g T_0}$ is the most probable molecular velocity speed, T_0 is the initial cell temperature, while $R_g = k_B/m$ denotes the specific gas constant (k_B is the Boltzmann constant and m is the molecular mass). The number of particles initialized in each cell is proportional to the cell free volume (i.e. the cell volume that is not occupied by the solid particle) over the total mesh free volume. Next, the gas particles initialized in each cell are sorted to the corresponding subcells.

The initialization phase is now complete and the DSMC code can move on to the flow simulation. In each time step the following steps are identified: (1) Compute the first solid particle collision; (2) Index the solid particle; (3) Move the gas particles; (4) Index the gas particles; (5) Collide the gas particles; (6) Move the solid particle; (7) Update the solid particle velocity; (8) Sample the gas macroscopic quantities and solid particle properties; (9) Average the sampled quantities; (10) Output the averaged quantities.

The first two steps, namely the computation of the first solid particle collision with a boundary and the indexing of the solid particle, have been described above and are omitted in the first time step since they have been already performed during the initialization of the code.

Similar to the free streaming of the gas paticles in the typical DSMC method, in the developed code the free motion of the gas particles is purely deterministic following the Newton-Euler equation, which for a monoatomic gas where no external forces are applied, reads

$$\frac{d\boldsymbol{r}}{dt} = \boldsymbol{\xi}, \quad \frac{d\boldsymbol{\xi}}{dt} = 0, \tag{7.2}$$

where $\boldsymbol{r}$ and $\boldsymbol{\xi}$ denote the simulator gas particle position and velocity, respectively. During the free motion step a gas particle may impinge on any of the cell faces or on

the solid particle. In the former case, if the cell face is "inner" (not on the flow domain boundary) the gas particle crosses to a new cell, which is registered to the memory, and continues to move freely. Otherwise, in the case where the gas particle impinges on a boundary face with incident velocity $\boldsymbol{\xi}'$, diffuse-specular interaction is assumed and the reflected velocity $\boldsymbol{\xi}$ is sampled from the scattering distribution

$$R_d^{(w)}\left(\boldsymbol{\xi}', \boldsymbol{\xi}\right) = \frac{2\boldsymbol{\xi}\cdot\boldsymbol{n}}{\pi(2R_gT_w)^2} e^{-\frac{\boldsymbol{\xi}^2}{2R_gT_w}}, \tag{7.3}$$

with probability a or it is computed by

$$\boldsymbol{\xi} = \boldsymbol{\xi}' - 2\left[\boldsymbol{\xi}'\cdot\boldsymbol{n}\right]\boldsymbol{n}, \tag{7.4}$$

with probability $1-a$. The quantity a denotes the accommodation coefficient of the boundary face, which represents the fraction of particles that are reflected diffusively, while $1-a$ represents the fraction of the particles that are reflected specularly, T_w is the boundary face temperature and $\boldsymbol{n}$ denotes the unit vector normal to the boundary face towards the flow domain. In the case where the gas particle impinges on the solid item with incident velocity $\boldsymbol{\xi}'$, purely diffuse interaction is assumed and the reflected velocity $\boldsymbol{\xi}$ is sampled from the scattering distribution

$$R_d^{(s)}\left(\boldsymbol{\xi}', \boldsymbol{\xi}\right) = \frac{2\left(\boldsymbol{\xi}-\boldsymbol{u}_s\right)\cdot\boldsymbol{n}}{\pi(2R_gT_s)^2} e^{-\frac{(\boldsymbol{\xi}-\boldsymbol{u}_s)^2}{2R_gT}}, \tag{7.5}$$

where $\boldsymbol{u}_s = \boldsymbol{v}_s + R_s\left(\boldsymbol{\omega}_s\times\boldsymbol{n}\right)$ is the solid particle impact point velocity, with $\boldsymbol{v}_s$ and $\boldsymbol{\omega}_s$ denoting the translational and angular velocity, respectively, while T_s is the particle temperature and $\boldsymbol{n}$ is the unit vector normal to the solid particle surface towards the flow domain. The force and torque exerted on the solid particle are computed based on the pre- and post-collision gas particle velocities that collide with the solid item as

$$\boldsymbol{F}_s = \frac{mF_n}{\Delta t}\sum_i\left(\boldsymbol{\xi}'_i - \boldsymbol{\xi}_i\right), \tag{7.6}$$

$$\boldsymbol{\tau}_s = \frac{mF_nR_s}{\Delta t}\sum_i \boldsymbol{n}_i\times\left(\boldsymbol{\xi}'_i - \boldsymbol{\xi}_i\right). \tag{7.7}$$

Here, the index i refers to all the gas particles that impinge on the solid particle during the time step Δt.

Next, after the completion of the free motion step the gas particles are indexed. The typical indexing method is to search for all particles inside all the cells and subcells of the mesh. However, as mentioned above in the developed code the current gas particle cell is stored during the move step. Thus, the gas particle is only searched in the subcells of its current cell. This indexing method has been found to be more computationally efficient than the typical indexing method.

The NTC collision technique suggested by Bird [30] is implemented here. A slight modification proposed in [181] is introduced in the calculation of the maximum number of collision pairs N_{coll} in each subcell, which is calculated as

$$N_{coll} = \frac{1}{2}\frac{N_{sc}(N_{sc}-1)F_n(\sigma_t\left|\boldsymbol{\xi}_r\right|)_{\max}\Delta t}{V_{sc,f}}. \tag{7.8}$$

Here N_{sc} is the actual number of simulator gas particles in the subcell, $(\sigma_t\left|\boldsymbol{\xi}_r\right|)_{\max}$ is the maximum value of the product of the collision cross-section σ_t and the relative velocity magnitude $|\boldsymbol{\xi}_r|$ of the particles in the collision and is updated throughout the simulation. The quantity $V_{sc,f}$ denotes the subcell free volume (i.e. the subcell volume that is not occupied by the solid particle). The collision cross-section and the post-collision velocities of the gas particle pair depend on the intermolecular potential. Currently in the developed code the HS, VHS and VSS potentials have been implemented. A detailed description for the implementation of these intermolecular potentials is given in [30].

At this stage the free motion and collision part for the gas particles is complete and the code can move to the solid particle movement step. The free motion step of the solid particle is also purely deterministic following the Newton-Euler equations, which for a rigid spherical particle read as

$$\frac{d\boldsymbol{r}_s}{dt} = \boldsymbol{v}_s, \tag{7.9}$$

$$m_s\frac{d\boldsymbol{v}_s}{dt} = \boldsymbol{F}_s, \quad I_s\frac{d\boldsymbol{\omega}_s}{dt} = \boldsymbol{\tau}_s, \tag{7.10}$$

where $\boldsymbol{r}_s$ denotes the center of mass position and $I_s = (2/5)\,m_sR_s^2$ is the solid particle moment of inertia. It is noted that, since the solid paricle is spherical its orientation is not required and thus, it is not computed in order to reduce the required computational time.

Next, the solid particle translational and rotational velocities are updated. Two distinct cases are identified. In the first case, the solid particle does not collide with a flow domain boundary and the translational and angular velocities are updated via Eq. (7.10) based on the updated values of the force $\boldsymbol{F}_s$ and torque $\boldsymbol{\tau}_s$ computed via Eq. (7.6) and (7.7), respectively. In the second case, the solid particle at the end of the free motion step impinges on a flow domain boundary, as shown in Fig 7.4 and the translational and angular velocities must be updated based on the solid particle-wall interaction model. In the present work, the hard-sphere model proposed by Crowe et al. [182], is considered. In the suggested model the collision process is divided into two periods, namely the compression period, where the material of the particle is deformed and the recovery period, where the elastic deformation force is released. The fact that the particle may slide along the surface for some or all the collision period is also taken into account. The model distinguishes between three cases: (1) The particle stops sliding during the compression period; (2) The particle stops sliding during the recovery period; (3) The particle slides throughout the entire collision. A detailed description of the impulse equations involved in order to determine the post-collision velocities $\boldsymbol{v}_s$ and $\boldsymbol{\omega}_s$ with respect to the pre-collision velocities $\boldsymbol{v}'_s$ and $\boldsymbol{\omega}'_s$ is given in [182]. It is noted that, although the impulse equations are different for the first two cases, where the solid particle stops sliding in the compression period or the recovery period, they produce the same expressions for the post-collision velocities:

$$v_{s,n} = -\varepsilon v'_{s,n}, \quad \omega_{s,n} = \omega'_{s,n} \tag{7.11}$$

$$v_{s,t_1} = \frac{5v'_{s,t_1} - 2R_s\omega'_{t_2}}{7}, \quad \omega_{s,t_1} = \frac{5v'_{s,t_2} + 2R_s\omega'_{t_1}}{7R_s} \tag{7.12}$$

$$v_{s,t_2} = \frac{5v'_{s,t_2} + 2R_s\omega'_{t_1}}{7}, \quad \omega_{s,t_2} = \frac{5v'_{s,t_1} + 2R_s\omega'_{t_2}}{7R_s} \tag{7.13}$$

Here the quantity $\varepsilon \in [0, 1]$ is the restitution coefficient, which is defined as the ratio of the normal impulse during the recovery period over the normal impulse during the compression period. The restitution coefficient is a property of the solid particle and wall materials, with $\varepsilon = 1$ corresponding to a perfectly elastic collision, while $\varepsilon = 0$ corresponding to a perfectly inelastic one.

In the third case, where the solid particle continues to slide throughout the collision, the impulse equations yield:

$$v_{s,n} = -\varepsilon v'_{s,n}, \quad \omega_{s,n} = \omega'_{s,n} \tag{7.14}$$

$$v_{s,t_1} = v'_{s,t_1} + (1+\varepsilon)e_{t_1}\mu_f v'_{s,n}, \;\; \omega_{s,t_1} = \omega'_{s,t_1} - \frac{5}{2R_s}(1+\varepsilon)\, e_{t_2}\mu_f v'_{s,n} \tag{7.15}$$

$$v_{s,t_2} = v'_{s,t_2} + (1+\varepsilon)e_{t_2}\mu_f v'_{s,n}, \;\; \omega_{s,t_2} = \omega'_{s,t_2} + \frac{5}{2R_s}(1+\varepsilon)\, e_{t_1}\mu_f v'_{s,n} \tag{7.16}$$

Here, μ_f denotes the Coulomb dynamic friction coefficient, while e_{t_1} and e_{t_2} are the direction cosines of the pre-collision velocity with respect to the boundary plane given by

$$e_{t_1} = -\frac{v'_{s,t_1} + R\omega'_{s,t_2}}{\sqrt{\left(v'_{s,t_1} + R\omega'_{s,t_2}\right)^2 + \left(v'_{s,t_2} - R\omega'_{s,t_1}\right)^2}}, \tag{7.17}$$

$$e_{t_2} = \frac{v'_{s,t_2} - R\omega'_{s,t_1}}{\sqrt{\left(v'_{s,t_1} + R\omega'_{s,t_2}\right)^2 + \left(v'_{s,t_2} - R\omega'_{s,t_1}\right)^2}}. \tag{7.18}$$

In order to determine whether the solid particle stops or continues sliding throughout the collision the total normal impulse J_n computed as

$$J_n = -(1+\varepsilon)m_s v'_{s,n}, \tag{7.19}$$

is compared to the total tangential impulse J_t, which is computed as

$$J_t = \frac{2}{7}m_s\sqrt{\left(v'_{s,t_1} + R\omega'_{s,t_2}\right)^2 + \left(v'_{s,t_2} - R\omega'_{s,t_1}\right)^2}. \tag{7.20}$$

It is easily deduced from Coulomb's friction law that the solid particle will stop sliding during the collision if the following criterion holds:

$$J_t \leq J_n\mu_f \tag{7.21}$$

In this case, the solid particle post-collision velocities are computed based on Eqs. (7.11)-(7.13), otherwise they are computed via Eqs. (7.14)-(7.16).

Similar to the typical DSMC method, in each iteration the sums of certain useful quantities, such as the molecular velocity moments for all gas particles in each cell are computed and stored. In the present work, the sums of the solid particle properties, such as the center of mass position, the translational and rotational velocities, the force and the torque, are also calculated and stored during the sample step.

After a predetermined number of time steps S the code output data, which consists of the gas macroscopic quantities in each cell, as well as, the solid particle properties

are exported to respective output files. The gas macroscopic quantities in each cell are given as time averages of the sums computed in the sampling step:

- Number density

$$n = \frac{F_n}{V_{c,f}} \frac{\sum_{k=1}^{S} N\left(t_k\right) \Delta t_k}{\sum_{k=1}^{S} \Delta t_k} \tag{7.22}$$

- Velocity

$$u_i = \frac{F_n}{n V_{c,f}} \frac{\sum_{k=1}^{S} \sum_{m=1}^{N(t_k)} \xi_{m,i}(t_k) \Delta t_k}{\sum_{k=1}^{S} \Delta t_k}, \quad i = x, y, z \tag{7.23}$$

- Temperature

$$T = \frac{F_n m}{3 n k_B V_{c,f}} \frac{\sum_{k=1}^{S} \sum_{m=1}^{N(t_k)} \left[\xi_{m,x}^2\left(t_k\right) + \xi_{m,y}^2\left(t_k\right) + \xi_{m,z}^2\left(t_k\right)\right] \Delta t_k}{\sum_{k=1}^{S} \Delta t_k} - \frac{m}{3 k_B}\left(u_x^2 + u_y^2 + u_z^2\right) \tag{7.24}$$

- Stress

$$\sigma_{ij} = \frac{F_n m}{V_{c,f}} \frac{\sum_{k=1}^{S} \sum_{m=1}^{N(t_k)} \xi_{m,i}\left(t_k\right) \xi_{m,j}\left(t_k\right) \Delta t_k}{\sum_{k=1}^{S} \Delta t_k} - m n u_i u_j, \quad i, j = x, y, z \tag{7.25}$$

- Heat flux

$$q_i = \frac{F_n m_g}{2 V_{c,f}} \frac{\sum_{k=1}^{S} \sum_{m=1}^{N(t_k)} \xi_{m,i}\left(t_k\right) \left[\xi_{m,x}^2\left(t_k\right) + \xi_{m,y}^2\left(t_k\right) + \xi_{m,z}^2\left(t_k\right)\right] \Delta t_k}{\sum_{k=1}^{S} \Delta t_k} - \left(u_x \sigma_{ix} + u_y \sigma_{iy} + u_z \sigma_{iz}\right) - \frac{m_g n}{2} u_i \left(u_x^2 + u_y^2 + u_z^2\right) - \frac{3}{2} n k_B T u_i, \quad i = x, y, z \tag{7.26}$$

In this notation, k denotes the time step index, $V_{c,f}$ is the cell free volume and $N\left(t_k\right)$ is the number of particles inside the cell at time step k. In the same manner, the

solid particle properties are also given as time averages of the sums computed in the sampling step

$$\varphi_s = \frac{\sum_{k=1}^{S} \varphi_s\left(t_k\right) \Delta t_k}{\sum_{k=1}^{S} \Delta t_k}, \tag{7.27}$$

where φ_s denotes any of the solid particle properties of interest, namely the center of mass position vector $\boldsymbol{r}_s$, the translational velocity $\boldsymbol{v}_s$, rotational velocity $\boldsymbol{\omega}_s$, the force $\boldsymbol{F}_s$ and the torque $\boldsymbol{\tau}_s$. The aforementioned steps are repeated until the simulation is complete i.e. when the predetermined time t_f is reached.

The 3D DSMC aerosol code is based on object-oriented programming to facilitate its accessibility, adaptation and enhancement in the future. In addition, the code has been parallelized implementing the MPI communication protocol. In the implemented parallelization each processor core runs an independent instance of the DSMC simulation (trajectory). Communication between the different processor cores is only required to ensemble average the macroscopic quantities of interest over all trajectories during the averaging step. Thus, a satisfactory efficiency is maintained even with a high number of processors.

7.4 Test Case I: Thermophoretic effect on a spherical particle

Consider a monoatomic rarefied gas, which is confined between two infinite parallel plates of slightly unequal temperature located at $\pm H/2$. The hot top plate is kept at a constant temperature T_h, while the cold bottom plate is kept at a constant temperature T_c with $\left(T_h - T_c\right)/T_c \ll 1$. In addition, a rigid spherical particle with radius $R_s \ll H$ is suspended in the gas. In this configuration the rigid particle experiences a force called the thermophoretic force due to momentum being transferred to the solid particle by the thermal motion of the surrounding gas molecules. The thermophoretic force is pushing the solid particle away from the warmer top plate towards the colder bottom plate. A schematic representation of the described flow configuration is presented in Fig 7.5

The level of gas rarefaction is indicated by the rarefaction parameter δ_H, which is defined by taking the plate separation distance as the reference length:

$$\delta_H = \frac{PH}{\tilde{\mu} v_0} \tag{7.28}$$

Here P is the gas pressure, $\tilde{\mu}$ is the gas viscosity at temperature $T_0 = (T_h + T_c)/2$ and $v_0 = \sqrt{2R_g T_0}$ is the most probable molecular velocity speed. The secondary reference length which is required to fully define the flow is the particle radius R_s [102]. The corresponding rarefaction parameter is defined as

$$\delta_{R_s} = \frac{PR_s}{\tilde{\mu} v_0}. \tag{7.29}$$

In the present work it is assumed that $R_s \ll H$ and thus $\delta_{R_s} \ll \delta_H$. Consequently, when the gas is exhibiting noncontinuum behavior, the free-molecular limit is assumed to apply on the particle length scale.

In the hydrodynamic regime ($\delta_H \gg 1$) the gas acts as a continuum and the heat flux between the two plates is simply derived by Fourier's law

$$q^{(h)} = -\tilde{\kappa} \frac{dT}{dz}, \tag{7.30}$$

where $\tilde{\kappa}$ is the gas thermal conductivity. In the case of small temperature differences the temperature dependence of the thermal conductivity can be neglected and Eq. (7.30) is integrated analytically to obtain the heat flux between the two plates:

$$q^{(h)} = -\tilde{\kappa} \frac{T_h - T_c}{H} \tag{7.31}$$

In the hydrodynamic regime, a closed form expression has been derived for the thermophoretic force in [183] written as

$$F_{th}^{(h)} = \left(\frac{32}{15\pi} \right) \left(\frac{\pi R_s^2}{\bar{v}} \right) q^{(h)}, \tag{7.32}$$

where $\bar{v} = \sqrt{8k_B T/(\pi m)}$ is the gas mean thermal speed.

In the free-molecular regime the heat flux between the two plates for a monoatomic gas has been derived by Bird [30] for an arbitrary temperature difference

$$q^{(fm)} = -P\left(\frac{8k_B}{\pi m}\right)^{1/2}\left(T_h^{1/2} - T_c^{1/2}\right). \tag{7.33}$$

An expression for the thermophoretic force exerted on the solid particle in the free-molecular regime has been obtained in [19]

$$F_{th}^{(fm)} = -\frac{3}{2}\pi R_s^2 P\left(\frac{T_h^{1/2} - T_c^{1/2}}{T_h^{1/2} + T_c^{1/2}}\right), \tag{7.34}$$

which in the case of a small temperature difference can be written as [184]

$$F_{th}^{(fm)} = \left(\frac{3}{4}\right)\left(\frac{\pi R_s^2}{\bar{v}}\right) q^{(fm)}. \tag{7.35}$$

Comparison of Eqs. (7.32) and (7.35) showed that the thermophoretic force expressions in both the free-molecular and hydrodynamic limits are identical within a numerical constant [184]. More specifically, both expressions are proportional to the particle cross-sectional area and the heat flux, while they are inversely proportional to the mean thermal speed.

In the transition regime, the calculation of the heat flux between the two plates requires the solution of the Boltzmann equation. In [176] a simple interpolation formula has been suggested for the heat flux:

$$q = \frac{q^{(fm)}}{1 + q^{(fm)}\Big/q^{(h)}} \tag{7.36}$$

It can be easily seen that, the above expression tends to $q^{(fm)}$ and $q^{(h)}$ in the free-molecular and hydrodynamic regimes, respectively. In addition, Eq. (7.36) has been reported to agree well with the limited experimental data [185].

As mentioned above the thermophoretic force depends on the heat flux in the same manner in both the hydrodynamic and free-molecular regime. This fact is used in [19, 186], where the following closed form expression for the thermophoretic force in the whole transition regime was proposed

$$F_{th} = \zeta_{th}\left(\frac{\pi R_s^2}{\bar{v}}\right) q, \tag{7.37}$$

where ζ_{th} is the so-called thermophoresis parameter. The thermophoresis parameter depends on the local molecular velocity distribution but in a very weak manner [19]. A simple approximation expression for the thermophoretic parameter, which tends to the correct values in the free-molecular and hydrodynamic regimes is provided in the present work

$$\zeta_{th} = \zeta_{th}^{(fm)} + \frac{\delta_H}{1+\delta_H}\left(\zeta_{th}^{(h)} - \zeta_{th}^{(fm)}\right), \;\; \zeta_{th}^{(fm)} = \frac{3}{4}, \;\; \zeta_{th}^{(h)} = \frac{32}{15\pi}. \tag{7.38}$$

Substituting Eqs. (7.36) and (7.38) in Eq. (7.37) the thermophoretic force can be easily calculated in the whole range of gas rarefaction, from the hydrodynamic to the free-molecular regime as

$$F_{th} = \left[\frac{3}{4} + \frac{\delta_H}{1+\delta_H}\left(\frac{32}{15\pi} - \frac{3}{4}\right)\right]\left(\frac{\pi R_s^2}{\bar{v}}\right)\frac{q^{(fm)}}{1+q^{(fm)}\Big/q^{(h)}}. \tag{7.39}$$

The closed form expression (7.39) can approximate the thermophoretic force in the whole range of gas rarefaction with an approximation error less than 10%.

The developed 3D DSMC aerosol code is implemented to compute the thermophoretic force exerted on a rigid spherical particle suspended in a rarefied gas between two infinite parallel plates of slightly unequal temperatures, as well as the heat flux exchanged between the two plates. The flow configuration investigated here, is the one reported in [20], where the 2D DSMC Icarus code is implemented and the force Green's function is used for the thermophoretic force computation. The heat flux and thermophoretic force computed via the developed code are compared with the ones reported in [20], as well as, with the results produced by the approximate closed form expressions (7.36), (7.39).

The plate separation is taken to be $H = 10^{-2}$ m, the top plate is kept at $T_h = 283$ K, while the bottom plate is kept at $T_c = 263$ K. Purely diffuse accommodation is considered at the two plates, while the boundaries perpendicular to the plates are considered to be purely specular due to symmetry. The solid particle has a radius $R_s = 5 \times 10^{-6}$ and is fixed in the flow domain center. The particle is kept at $T_s = 273$ K and is not allowed to move either translationally or rotationally in order to have a valid comparison with [20]. The investigated gas pressure ranged between 0.1 and 100 mTorr i.e. from the free-molecular up to the transition and slip regime. In total 800 cube cells are used with 200 cells in the z direction perpendicular to the plates and 2 cells in the x and y directions. In each cell 100 gas simulator particles are

initialized, resulting in a total of 8×10^4 simulator gas particles. Two monoatomic gases are considered, namely Argon and Helium and the VSS model is implemented. The required gas properties are shown in Table 7.1. The time step is taken as $\sim 1/3$ of the mean cell transversal time, which corresponds to $\Delta t = 5 \times 10^{-8}$ s for Argon and $\Delta t = 1.5 \times 10^{-8}$ s for Helium and the simulation ends after 8×10^4 time steps. The presented results are based on simulations performed on 20 Intel Xeon 8160 (SkyLake) nodes resulting to a total of 2400 independent trajectories.

In Table 7.2 the heat flux q [W/m^2] based on the developed DSMC code, the 2D DSMC Icarus code implemented in [20], as well as, based on the approximate expression (7.36) are presented with respect to the pressure $P = [0.1, 0.3, 1, 10, 30, 10^2]$ mTorr. As expected, the heat flux is proportional to the gas pressure in the free-molecular regime. As the gas pressure is increased the heat flux is also increased and tends to a constant value at the hydrodynamic limit. An excellent agreement is observed between the present heat flux results and the ones reported in [20] for both Ar and He with the highest relative deviation reaching 1%. In addition, as reported in [20] the closed form expression (7.36) successfully approximates the numerical heat flux results with the highest relative deviation being below 10% in the transition regime.

In Table 7.3 the thermophoretic force exerted on the solid particle over the particle cross-sectional area $F_{th}/(\pi R_s^2)$ [N/m^2] based on the developed DSMC code, the 2D DSMC Icarus code and force Green's function implemented in [20], as well as, based on the closed form expression (7.39) are presented with respect to the gas pressure $P = [0.1, 0.3, 1, 10, 30, 10^2]$ mTorr. As already mentioned, the thermophoretic force is proportional to the heat flux and thus, in the free-molecular regime it is found to be proportional to the gas pressure. As the gas pressure is increased the thermophoretic force exerted on the particle is also increased and tends to its limiting value in the viscous regime. The presented results for the thermophoretic force show an excellent agreement with the ones reported in [20] with the relative deviations being below 1% in the whole investigated pressure range for both Argon and Helium. Moreover, the closed form expression (7.39) successfully predicts the thermophoretic force. The highest relative deviation between the present results and Eq. (7.39) appears in the transition regime and has been found to be below 10%.

7.5 Test Case II: Translational Brownian motion of a spherical particle

Consider a rigid spherical particle with radius R_s suspended in a monoatomic gas, which is at rest occupying a volume V, having a constant temperature T. The particle exhibits a random motion due to the gas particles impinging on its surface. The theory of Brownian motion states that the translational velocity of the particle follows the Maxwellian distribution [187]

$$f\left(\boldsymbol{v}_s\right)=\left(\frac{m_s}{2\pi k_B T}\right)^{3/2} e^{-\frac{m_s \boldsymbol{v}_s^2}{2k_B T}}. \tag{7.40}$$

It is easily seen that, the translational velocity has expectation and variance equal to

$$<\boldsymbol{v}_s>=0,\ \ <\boldsymbol{v}_s^2>=\frac{3k_B T}{m_s}. \tag{7.41}$$

The translational Brownian motion of a rigid particle may be modeled by the phenomenological stochastic Langevin equation [187, 188]

$$m_s\frac{d^2\boldsymbol{r}_s\left(t\right)}{dt^2}=-\gamma_T\frac{d\boldsymbol{r}_s\left(t\right)}{dt}+\boldsymbol{F}_s\left(t\right), \tag{7.42}$$

where γ_T is the translational friction coefficient, which is assumed to be independent of the particle velocity. The second right hand side term $\boldsymbol{F}_s\left(t\right)$ is the random force exerted on the particle, which is usually assumed to be a Gaussian process with infinitely small correlation time [187, 188].

In the case where the observation time is much larger than the translational correlation time $t\gg\tau_T=m_s/\gamma_T$, the particle center of mass displacement $\Delta\boldsymbol{r}_s\left(t\right)=\boldsymbol{r}_s\left(t\right)-\boldsymbol{r}_s\left(0\right)$, is given by the following distribution [189]

$$f\left(\Delta\boldsymbol{r}_s\right)=\frac{1}{\left(4\pi D_T t\right)^{3/2}}e^{-\frac{\Delta\boldsymbol{r}_s{}^2}{4D_T t}},\ \ D_T=\frac{k_B T}{\gamma_T}, \tag{7.43}$$

where D_T denotes the translational diffusion coefficient. From Eq. (7.43) it is easily seen that, the particle displacement has expectation and variance equal to

$$<\Delta\boldsymbol{r}_s>=0,\ \ <\Delta\boldsymbol{r}_s^2>=6D_T t. \tag{7.44}$$

The translational Brownian motion of a solid particle suspended in a gas bath is characterized by the gas rarefaction parameter

$$\delta = \frac{PR_s}{\tilde{\mu} v_0}, \tag{7.45}$$

where P is the gas pressure, $\tilde{\mu}$ is the gas viscosity at the temperature T and $v_0 = \sqrt{2R_g T}$ is the most probable molecular speed.

In the free-molecular regime, the friction coefficient for a purely diffuse rigid spherical particle has been derived in [100]

$$\gamma_T = \frac{8}{3} R_s^2 \rho \sqrt{\frac{2\pi k_B T}{m}} \left(1 + \frac{\pi}{8}\right), \tag{7.46}$$

where ρ denotes the gas density. Substituting Eq. (7.46) in Eq. (7.43) the free-molecular translational diffusion coefficient is obtained:

$$D_T = \frac{3}{8} \sqrt{\frac{m k_B T}{2\pi}} \frac{1}{\left(1 + \frac{\pi}{8}\right) \rho R_s^2} \tag{7.47}$$

The developed 3D DSMC code is implemented to simulate the translational Brownian motion of a rigid spherical particle suspended in a rarefied gas in the free-molecular regime. The developed code is validated by comparing the numerical results of the translational diffusion coefficients with the analytical expressions given above. It is noted that, in this particular case the fluctuations inherent in the DSMC method determine the Brownian motion [109]. These fluctuations have the correct value and thus yield the correct translational diffusion coefficient when the statistical weight of the DSMC molecules is equal to $F_n = 1$.

The computational domain is a cube cell with edges $L = 10^{-6}$ m and purely diffuse accommodation is assumed at the domain boundary. The background gas is Argon having a constant density $\rho = 5.645 \times 10^{-2}$ kg/m^3 and temperature $T = 300$ K. Based on the gas density and temperature and taking into account $F_n = 1$ a total of 8.47×10^5 gas particles are initialized inside the cell. Initially, the spherical particle is assumed to be at rest ($\boldsymbol{v}_{s,0} = 0$) at the cell center $\boldsymbol{r}_s = 5 \times 10^{-7}$ m and has a constant temperature $T_s = 300$ K. The investigated particle radius is taken to be $R_s \leqslant 10^{-7}$ m in order to be in the free-molecular regime $\delta \leqslant 0.05$. In addition, the rigid particle is not allowed to rotate ($\boldsymbol{\omega}_s = 0$) and can only move translationally inside the flow domain. The numerical time step is taken to be $\Delta t = 5.66 \times 10^{-12}$ s and the final simulation time is

$t_f = 1.415 \times 10^{-7}$ s. In order to determine the translational diffusion coefficient the above simulation is performed on 25 Intel Xeon 8160 (SkyLake) nodes. A total of 15000 independent simulations are performed and the particle translational displacement $\Delta \boldsymbol{r}_s(t_f)$ and translational velocity $\boldsymbol{v}_s(t_f)$ at the end of each simulation are sampled. The translational diffusion coefficient is then derived from Eq. (7.44) based on the computed displacement variance.

In Fig. 7.6 the particle translational velocity and displacement distributions based on the developed DSMC aerosol code and on the analytical expressions (7.40) and (7.43) for $R_s = 10^{-7}$ m, $m_s = 2.09 \times 10^{-22}$ kg and $t = 1.415 \times 10^{-7}$ s are presented. It is seen that the displacement in the x, y and z directions follows a Gaussian distribution with expectation equal to zero and variance equal to $2D_T t$. Similarly, the translational velocity in each direction also follows a Gaussian distribution with expectation zero and variance equal to $k_B m_s/T$. In all cases, an excellent agreement between the computed distributions and the analytical distributions (7.40) and (7.43) is observed.

In Fig. 7.7 the translational diffusion coefficient D_T based on the developed DSMC aerosol code and the analytical expression (7.47) is plotted with respect to the particle radius R_s. As predicted by (7.47) the translational diffusion coefficient is inversely proportional to the square of the particle radius. In addition, an excellent agreement is observed between the computational and analytical results for the translational diffusion coefficient D_T with the highest relative deviation reaching 1.2%.

7.6 Test Case III: Rotational Brownian motion of a spherical particle

Consider a rigid spherical particle suspended in a monoatomic gas, which is at rest occupying a volume V, having temperature T. The particle is only allowed to rotate around the x-axis and thus, it rotates randomly due to the gas particles impinging on its surface. The theory of Brownian motion states that the rotational velocity of the particle follows the Maxwellian distribution [190]

$$f(\omega_{s,x}) = \left(\frac{I_s}{2\pi k_B T}\right)^{1/2} e^{-\frac{I_s \omega_{s,x}^2}{2k_B T}}. \tag{7.48}$$

It is easily seen that, the rotational velocity has expectation and variance equal to

$$< \omega_{s,x} >= 0, \;\; < \omega_{s,x}^2 >= \frac{k_B T}{I_s}. \tag{7.49}$$

The model describing the rotational Brownian motion of a rigid particle around a fixed axis is derived from the rotational analog of the Langevin equation [190]

$$I_s \frac{d^2 \theta_{s,x}(t)}{dt^2} = -\gamma_R \frac{d\theta_{s,x}(t)}{dt} + \tau_{s,x}(t), \;\; \frac{d\theta_{s,x}}{dt} = \omega_{s,x}, \tag{7.50}$$

where $\theta_{s,x}$ is the rotationa angle around the x-axis and γ_R is the rotational friction coefficient, which is assumed to be independent of the particle angular velocity. The second right hand side term $\tau_{s,x}(t)$ is the random torque exerted on the particle, which is usually assumed to be a Gaussian process with infinitely small correlation time [190].

In the case where the observation time is much larger than the rotational correlation time $t \gg \tau_R = I_s/\gamma_R$, the particle angular displacement around the x-axis $\Delta\theta_{s,x}(t) = \theta_{s,x}(t) - \theta_{s,x}(0)$, is given by

$$f(\Delta\theta_{s,x}) = \frac{1}{(4\pi D_R t)^{1/2}} e^{-\frac{\Delta\theta_{s,x}{}^2}{4D_R t}}, \;\; D_R = \frac{k_B T}{\gamma_R} \tag{7.51}$$

where D_R denotes the rotational diffusion coefficient. From Eq. (7.51) it is easily deduced that, the angular displacement of the particle has expectation and variance equal to

$$< \Delta\theta_{s,x} >= 0, \;\; < \Delta\theta_{s,x}^2 >= 2D_R t. \tag{7.52}$$

The rotational Brownian motion of a solid particle suspended in a gas bath is characterized by the gas rarefaction parameter

$$\delta = \frac{P R_s}{\tilde{\mu} v_0}, \tag{7.53}$$

where P is the gas pressure, $\tilde{\mu}$ is the gas viscosity at the temperature T and $v_0 = \sqrt{2R_g T}$ is the most probable molecular speed.

In the free-molecular regime, the rotational friction coefficient for a purely diffuse rigid spherical particle has been derived in [100, 177]

$$\gamma_R = \frac{2\pi}{3} \sqrt{\frac{8k_B T}{\pi m}} \rho R_s^4, \tag{7.54}$$

where ρ denotes the gas density. Substituting Eq. (7.54) in Eq. (7.51) the rotational diffusion coefficient in the free-molecular regime is obtained:

$$D_R = \frac{3}{4\pi}\sqrt{\frac{\pi m k_B T}{2}}\frac{1}{\rho R_s^4} \tag{7.55}$$

The developed 3D DSMC aerosol code is implemented to simulate the rotational Brownian motion of a rigid spherical particle suspended in a rarefied gas in the free-molecular regime and is validated by comparing the obtained numerical results for the rotational diffusion coefficient with the analytical ones. Similar to the translational Brownian motion the statistical weight of the DSMC molecules is also taken here to be equal to $F_n = 1$ in order to obtain the correct value for the rotational diffusion coefficient.

The computational domain is a cube cell with edges $L = 10^{-6}$ m and purely diffuse accommodation is assumed at the domain boundary. The background gas is Argon having a constant density $\rho = 5.645 \times 10^{-2}$ kg/m^3 and temperature $T = 300$ K. Based on the gas density and temperature and taking into account $F_n = 1$ a total of 8.47×10^5 gas particles are generated inside the cell. Initially, the spherical particle is assumed to be at rest ($\omega_{s,x,0} = 0$) and has a constant temperature $T_s = 300$ K. The investigated particle radius is taken to be $R_s \leqslant 10^{-7}$ m in order to be in the free-molecular regime $\delta \leqslant 0.05$. In addition, the rigid particle center of mass is fixed at the cell center $\boldsymbol{r}_s = 5 \times 10^{-7}$ m and is only allowed to rotate around the x-axis ($\boldsymbol{v}_s = \omega_{s,y} = \omega_{s,z} = 0$). The numerical time step is taken to be $\Delta t = 5.66 \times 10^{-12}$ s and the simulation ends at $t_f = 1.415 \times 10^{-7}$ s. In order to determine the rotational diffusion coefficient the above simulation is performed on 25 Intel Xeon 8160 (SkyLake) nodes. A total of 15000 independent simulations are performed and the particle angular displacement $\Delta\theta_{s,x}(t_f)$ and angular velocity $\omega_{s,x}(t_f)$ at the end of each simulation are sampled. The rotational diffusion coefficient is then derived from Eq. (7.52) based on the computed angular displacement variance.

In Fig. 7.8 the particle angular velocity and displacement distributions based on the developed DSMC aerosol code and the analytical expressions (7.48) and (7.51) for $R_s = 10^{-7}$ m, $m_s = 2.09 \times 10^{-22}$ kg and $t = 1.415 \times 10^{-7}$ s are presented. It is seen that the angular displacement follows a Gaussian distribution with mean zero and variance $2D_R t$. Similarly, the angular velocity follows a Gaussian distribution with mean zero and variance $k_B I_s / T$. An excellent agreement between the computed distributions and the analytical distributions (7.48) and (7.51) is observed in all cases.

In Fig. 7.9 the rotational diffusion coefficient D_R based on the developed DSMC aerosol code and the analytical expression (7.55) is plotted with respect to the particle radius R_s. As predicted by (7.55) the rotational diffusion coefficient is inversely proportional to the fourth power of the particle radius R_s. Moreover, an excellent agreement is observed between the computational and analytical results for the rotational diffusion coefficient D_R with the highest relative deviation reaching 0.8%.

7.7 Concluding remarks

A 3D DSMC aerosol code has been developed for simulating the transport of a solid spherical particle through a rarefied gas. The presented aerosol code has been based on the 3D DSMC code PROGRESS, which has been developed at the Laboratory of Transport Phenomena and Process Equipment at University of Thessaly by Dr. S. Pantazis. The structure of the aerosol code and the required modifications with respect to the typical DSMC method have been described in detail.

The developed aerosol code has been validated for three benchmark cases. In the first benchmark case the thermophoretic effect on a solid particle suspended in a rarefied gas between two infinite parallel plates kept at slightly different temperatures is investigated. The computed heat flux and thermophoretic force exerted on the solid particle showed an excellent agreement with the ones reported in the literature [20]. In addition, the approximate closed form expressions proposed for the heat flux and the thermophoretic force [20, 176] provide a satisfactory comparison with the DSMC results. These simple expressions can be used to provide the heat flux and thermophoretic force in the whole range of rarefaction when 10% error is acceptable. In the second and third benchmark cases the translational and rotational Brownian motion of a solid particle suspended in a rarefied gas at rest is investigated in the free-molecular regime. The velocity and displacement distributions of the particle have been computed and a great agreement is provided with the distributions predicted by Brownian theory. In addition, the translational and rotational diffusion coefficients have been computed with respect to the particle radius and have shown an excellent agreement with the theoretical values.

It is believed that the presented code has a lot of potential and of course it may be further advanced to simulate multiple solid particles, as well as more complex processes involving absorption, desorption, agglomeration and deposition.

Table 7.1 Molecular properties at standard conditions: $P = 1$ atm, $T = 273$ K [30].

Gas	ω	a	$\tilde{\mu}$ [Pas]	m [kg]	d [m]
Argon	0.81	1.40	2.117(-5)	6.63(-26)	4.11(-10)
Helium	0.66	1.26	1.865(-5)	6.65(-27)	2.30(-10)

Table 7.2 Heat flux q [W/m^2] between parallel plates with respect to the gas pressure; comparison between the present DSMC aerosol code, Ref. [20] and Eq. (7.36).

P [mTorr]	Argon				Helium			
	δ_H	Present work	Ref. [20]	Eq. (7.36)	δ_H	Present work	Ref. [20]	Eq. (7.36)
0.1	1.87(-2)	1.82(-1)	1.83(-1)	1.85(-1)	6.71(-3)	5.79(-1)	5.84(-1)	5.85(-1)
0.3	5.60(-2)	5.35(-1)	5.40(-1)	5.48(-1)	2.01(-2)	1.73	1.73	1.75
1	1.87(-1)	1.68	1.69	1.76	6.71(-2)	5.60	5.66	5.75
3	5.60(-1)	4.43	4.45	4.77	2.01(-1)	1.58(1)	1.60(1)	1.66(1)
10	1.87	1.09(1)	1.09(1)	1.19(1)	6.71(-1)	4.56(1)	4.58(1)	4.89(1)
30	5.60	1.96(1)	1.96(1)	2.07(1)	2.01	1.01(2)	1.02(2)	1.10(2)
100	1.87(1)	2.74(1)	2.77(1)	2.80(1)	6.71	1.86(2)	1.87(2)	1.96(2)

Table 7.3 Thermophoretic force over the particle cross-sectional area $F_{th}/\left(\pi R_s^2\right)$ [N/m^2] with respect to the gas pressure; comparison between the present DSMC aerosol code, Ref. [20] and Eq. (7.39).

P [mTorr]	Argon				Helium			
	δ_H	Present work	Ref. [20]	Eq. (7.39)	δ_H	Present work	Ref. [20]	Eq. (7.39)
0.1	1.87(-2)	3.60(-4)	3.61(-4)	3.64(-4)	6.71(-3)	3.63(-4)	3.64(-4)	3.65(-4)
0.3	5.60(-2)	1.06(-3)	1.06(-3)	1.08(-3)	2.01(-2)	1.07(-3)	1.08(-3)	1.09(-3)
1	1.87(-1)	3.30(-3)	3.30(-3)	3.42(-3)	6.71(-2)	3.51(-3)	3.52(-3)	3.53(-3)
3	5.60(-1)	8.57(-3)	8.53(-3)	9.08(-3)	2.01(-1)	9.83(-3)	9.86(-3)	9.99(-3)
10	1.87	2.06(-2)	2.05(-3)	2.20(-2)	6.71(-1)	2.78(-2)	2.78(-2)	2.86(-2)
30	5.60	3.57(-2)	3.57(-2)	3.76(-2)	2.01	6.06(-2)	6.07(-2)	6.32(-2)
100	1.87(1)	4.91(-2)	4.89(-2)	5.04(-2))	6.71	1.07(-1)	1.08(-1)	1.12(-1)

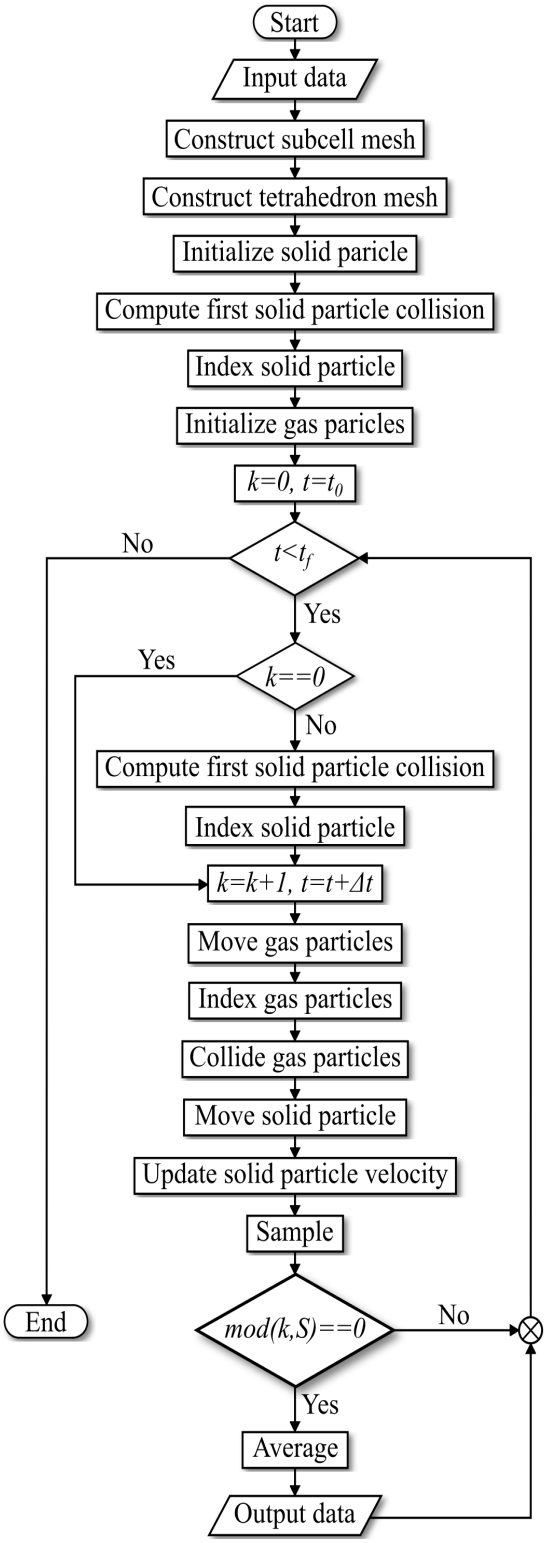

Figure 7.1 Flowchart of the developed 3D DSMC aerosol code.

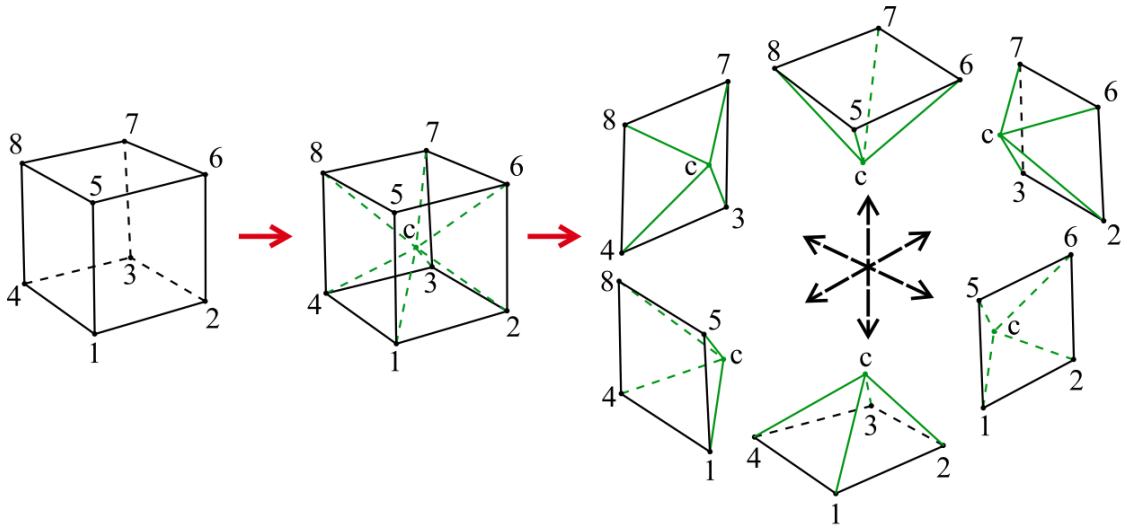

Figure 7.2 Schematic example of a hexahedron cell split into six pyramid subcells.

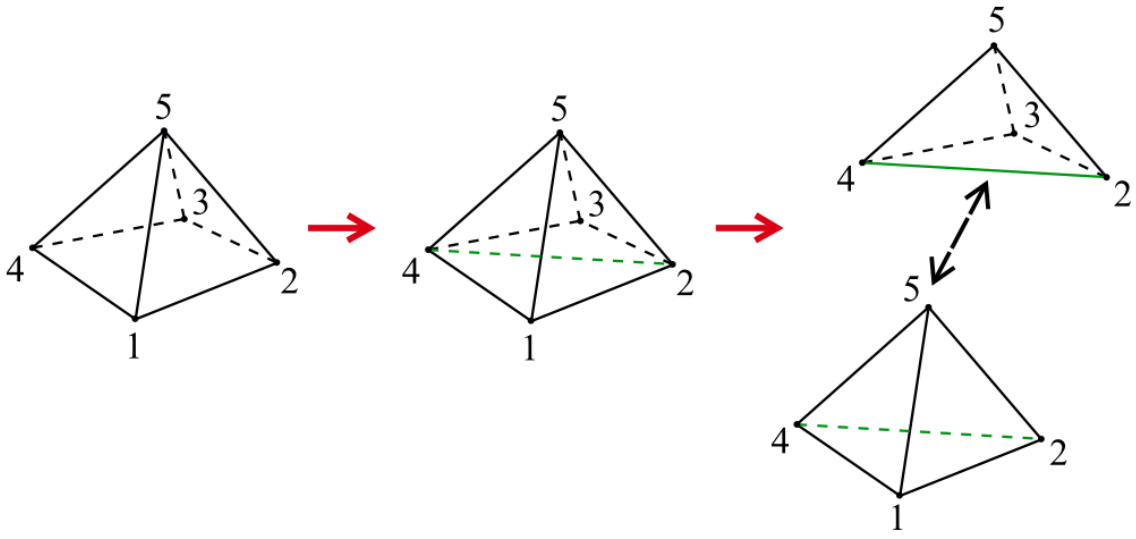

Figure 7.3 Schematic example of a pyramid subcell split into 2 tetrahedrons.

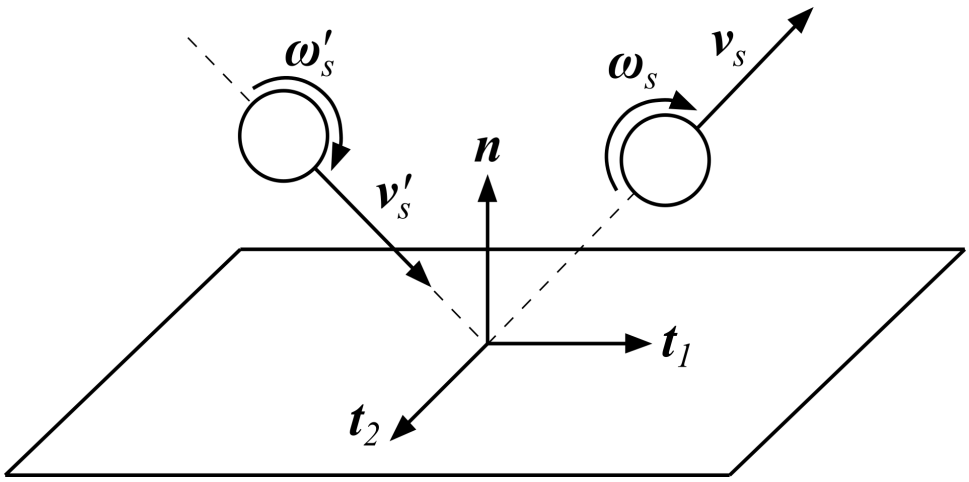

Figure 7.4 Schematic representation of a solid particle collision with a boundary.

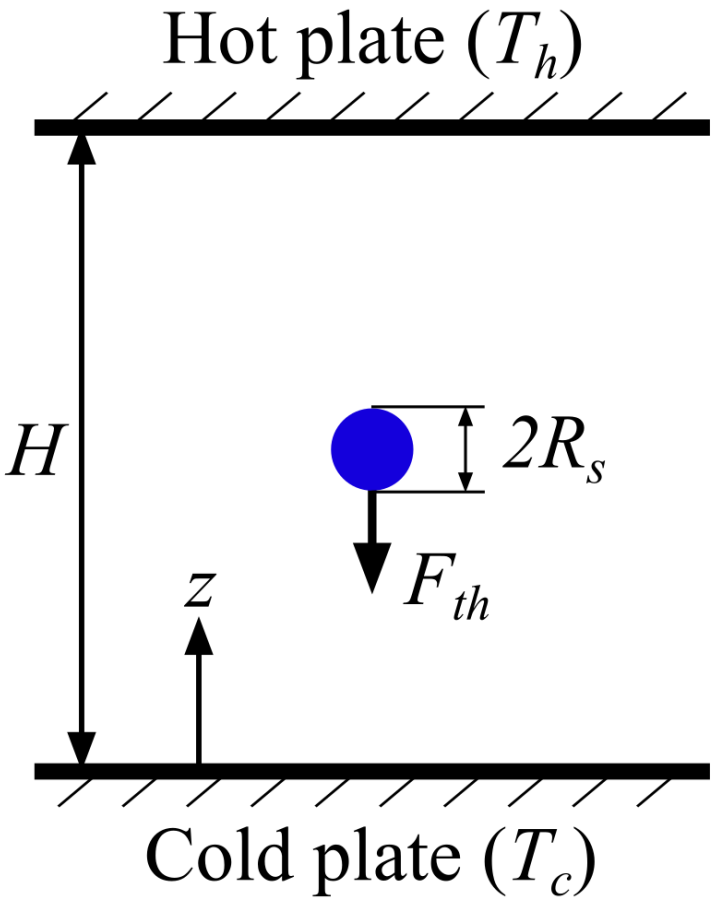

Figure 7.5 Schematic representation of the thermophoresis of a solid particle suspended between two parallel plates.

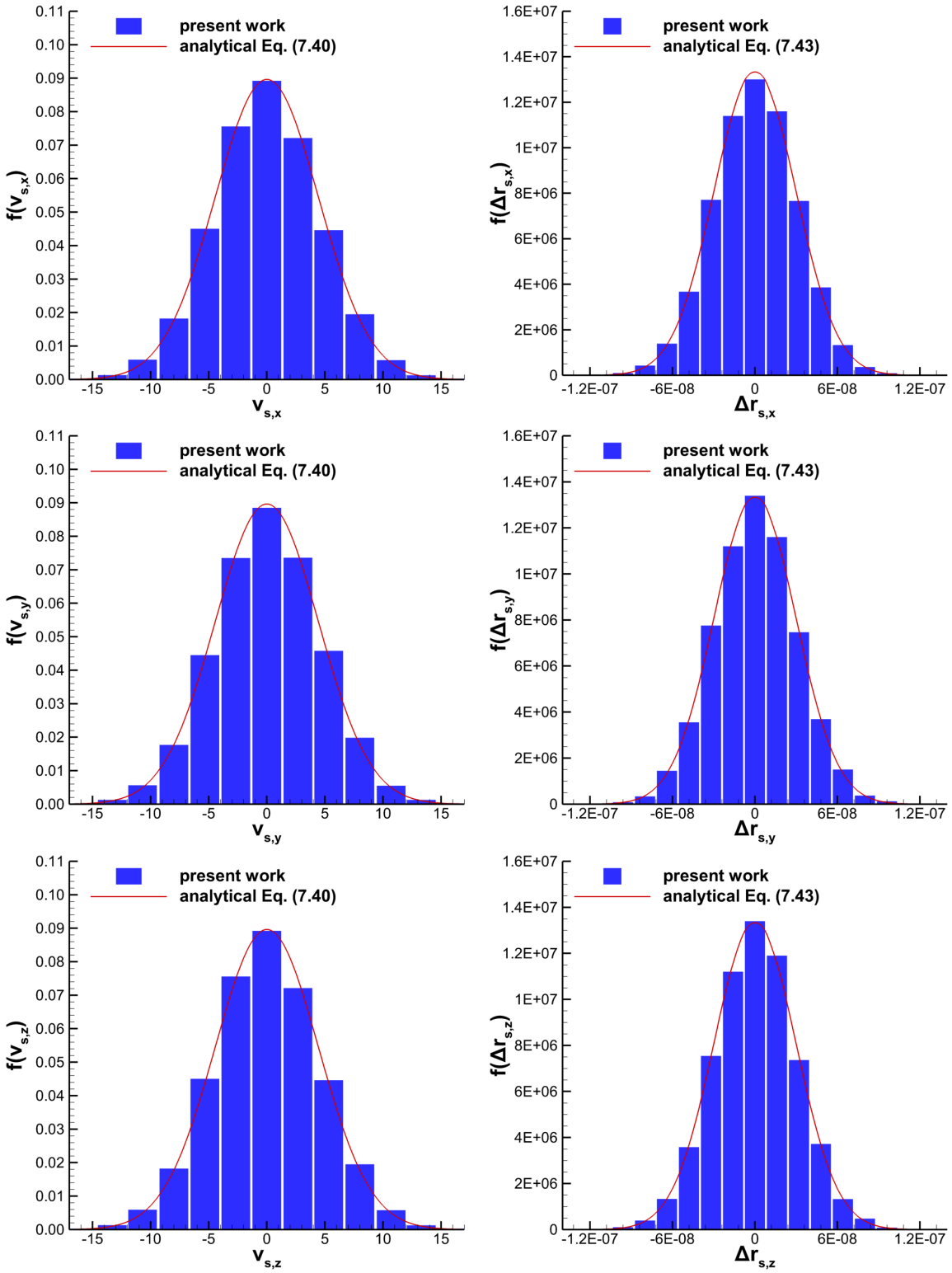

Figure 7.6 Particle translational velocity distribution (left) and translational displacement distribution (right) for $R_s = 10^{-7}$ m, $m_s = 2.09 \times 10^{-22}$ kg and $t = 1.415 \times 10^{-7}$ s; comparison between developed DSMC aerosol code and analytical expressions (7.40) and (7.43).

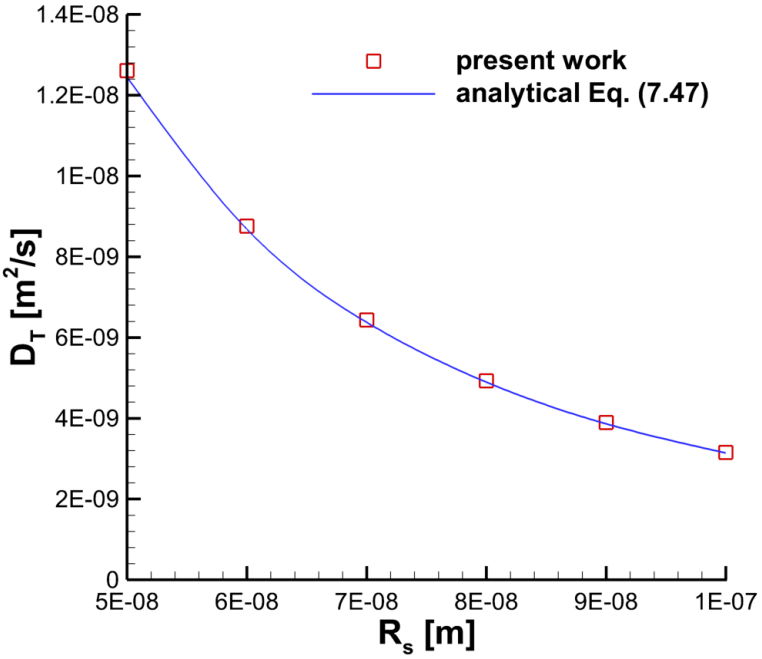

Figure 7.7 Translational diffusion coefficient D_T in terms of the particle radius R_s; comparison between developed DSMC aerosol code and analytical expression (7.47).

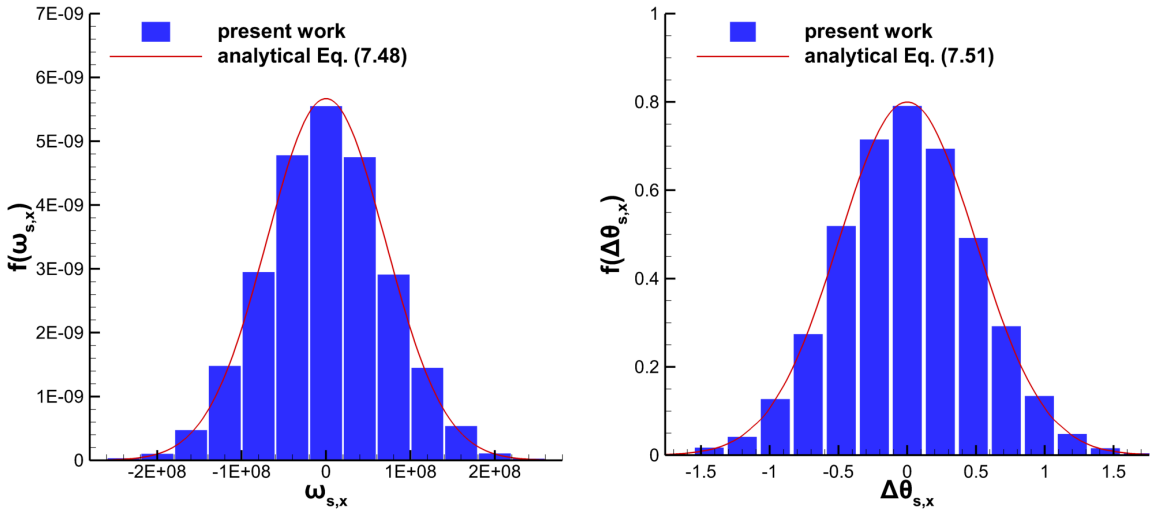

Figure 7.8 Particle angular velocity distribution (left) and angular displacement distribution (right) for $R_s = 10^{-7}$ m, $m_s = 2.09 \times 10^{-22}$ kg and $t = 1.415 \times 10^{-7}$ s; comparison between developed DSMC aerosol code and analytical expressions (7.48) and (7.51).

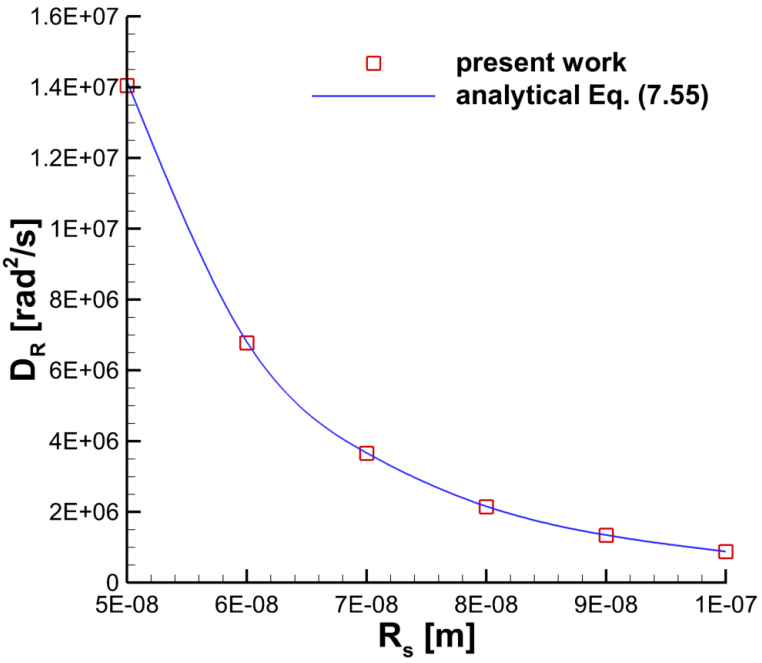

Figure 7.9 Rotational diffusion coefficient D_R in terms of the particle radius R_s; comparison between developed DSMC aerosol code and analytical expression (7.55).

Chapter 8

Concluding remarks

8.1 Summary and contributions

The present dissertation is focused on the computational solution of novel rarefied gas flow configurations, as well as, the development and implementation of advanced kinetic codes. The validity and effectiveness of the developed codes have been demonstrated by solving several prototype problems, as well as complex rarefied gas flow configurations. A brief review of the subjects investigated in Chapters 3-7 along with the main contributions of the present work is provided.

In Chapter 3, the linearized Boltzmann equation for the hard-sphere intermolecular potential has been computationally solved. This task is tackled for the first time at the Laboratory of Transport Phenomena and Process Equipment. The integration of the Boltzmann collision operator has been validated by computing the heat conductivity and dynamic viscosity coefficients for a hard-sphere gas. In addition, the computational solution of the linearized Boltzmann equation has been validated based on two prototype rarefied gas flow configurations, namely the planar fully-developed Poiseuille and thermal creep flows. In all cases, an excellent agreement has been observed between the present work and the literature. Then, the Boltzmann equation has been implemented to simulate the planar fully-developed rarefied gas flow due to a harmonically oscillating pressure gradient in the whole range of gas rarefaction and arbitrary oscillation frequency. In addition, the BGK numerical solution, as well as, analytical solutions in the slip and hydrodynamic regimes have been provided for comparison purposes. The quantities of interest, namely the complex Poiseuille coefficient and the macroscopic velocity distribution have been presented in tabulated and graphical form. It has been observed that, the Boltzmann equation results are in good agreement with the BGK ones in

the whole range of investigated parameters justifying the use of kinetic models for simulating pressure driven oscillatory rarefied gas flows. In addition, the analytical slip solution and the steady-state solution are properly recovered. The Poiseuille coefficient and velocity distribution have been found to be in phase with the pressure gradient for low oscillation frequencies, while as the oscillation frequency is increased the macroscopic quantities phase lag is increased and amplitude is decreased. For the Poiseuille coefficient a non-monotonic behavior has been observed with respect to the gas rarefaction parameter and a local maximum may be observed for some intermediate value of the gas rarefaction depending on the oscillation parameter value. Furthermore, at high frequencies, the plug-flow mode in the channel center and the velocity overshoot near the two plates, that has been well-established in the viscous regime and more recently under rarefied conditions based on the BGK model, has also been observed based on the Boltzmann equation.

In Chapter 4, rarefied gas flows coupled with gas injection and suction through permeable surfaces, have been investigated. These flows have been well-established in the viscous regime, however they have not been investigated in rarefied conditions. The fully-developed Poiseuille and thermal creep rarefied gas flow between parallel permeable plates, with uniform gas injection and suction from the bottom and top plate, respectively, has been investigated based on the linearized Shakhov (S) model and Boltzmann equation, in the whole range of the gas rarefaction parameter and in a wide range of the injection velocity. The full-range synthetic acceleration scheme has been implemented for the S model and has been compared to the non accelerated scheme. As expected, the accelerated scheme has been found to be far superior to the non accelerated one for large values of the rarefaction parameter, while for small values of the rarefaction parameter they are very similar in terms of the required computational effort. The Poiseuille, mechanocaloric, thermal creep and reduced heat flux coefficients, as well as the velocity, shear stress and heat flux distributions have been provided. Excellent agreement has been observed between the Boltzmann and S model equations justifying the use of kinetic models for the simulation of rarefied gas flows coupled with injection and suction. In addition, the analytical solutions derived in the free-molecular and slip regimes are properly recovered. The Poiseuille coefficient has been found to monotonically decrease when the injection velocity is increased, tending to a constant value at the viscous regime. In addition, as the injection velocity is increased, the well-known Knudsen minimum for the Poiseuille coefficient becomes gradually shallower and finally vanishes. It has been observed that, the reduced heat flux, mechanocaloric and

thermal creep coefficients are also decreased as the injection velocity is increased and for high injection velocity values the mechanocaloric and thermal creep coefficients change sign. In addition, the Onsager-Casimir reciprocity relation for the mechanocaloric and thermal creep coefficients has been proven theoretically for arbitrary injection velocity and has been implemented to validate the accuracy of the obtained results. Both in the pressure and temperature driven flow configurations the velocity and heat flux distributions become non-symmetric and their extrema are shifted from the channel center towards the suction plate as the injection velocity is increased. Furthermore, as the injection velocity is increased the shear stress distribution significantly deviates from the typical linear profile in the Poiseuille flow and the constant zero profile in the thermal creep flow. The fully-developed rarefied gas flow over a permeable plate with uniform downward suction has also been investigated based on the S kinetic model equation in a wide range of the suction velocity. The boundary layer thickness, as well as, the macroscopic velocity, shear stress and heat flux distributions have been provided based on the kinetic, slip and hydrodynamic approaches. The boundary layer thickness has been found to be inversely proportional to the suction velocity as predicted by the analytical viscous solution. The kinetic, slip and hydrodynamic macroscopic quantities are in excellent agreement outside of the Knudsen layer. However, inside the Knudsen layer only the kinetic approach may be considered as valid.

In Chapter 5, the developed codes for simulating steady-state and time-dependent arbitrary gas distribution systems under any vacuum conditions have been presented. The structure of the developed steady-state gas network code ARIADNE and the hybrid time-dependent gas network code, which implements the ARIADNE code in each time step, have been described in detail. In addition, the hybrid time-dependent code has been validated based on two benchmark gas networks. The first benchmark problem involved the dynamic standard apparatus for the measurement of the response and relaxation times of vacuum gauges developed by Physikalische-Technische Bundesanstalt. The temporal evolution of the upstream vessel pressure has been presented and has provided an excellent agreement with both experimental and numerical results reported in the literature. The second benchmark problem involved a gas network operating in the free-molecular regime. The temporal evolution of the gas network vessels, pipe junctions and pump has been provided and has been found to be in excellent agreement with results obtained via the well-established TPMC code Molflow+. Furthermore, the ARIADNE code has been used to demonstrate the implementation of the MC uncertainty propagation analysis method to gas distribution systems. The

aforementioned second benchmark network was assumed to operate under steady-state conditions and the uncertainty of the pumped throughput with respect to the pipe radius, pipe length, vessel pressure and pump pumping speed uncertainties has been presented in the whole range of gas rarefaction. In general, the qualitative behavior of the throughput uncertainty has been in agreement with the one observed for the mass flow rate uncertainty in the case of the pressure driven flow through a single circular tube. However, these results cannot be generalized and a separate uncertainty propagation analysis is required for each specific vacuum system.

In Chapter 6, the capabilities of the aforementioned developed gas network codes have been demonstrated by simulating the ITER primary pumping system during the burn and dwell phases. The steady-state code ARIADNE has been implemented to simulate the ITER burn phase under steady conditions for several operating scenarios and both qualitative and quantitative results, including the gas flow paths through the divertor, as well as the backflow and pumped throughputs, have been provided. The pumped and backflow throughputs have been found to increase moving from the low, to the medium and to the high pressure burn phase scenarios. In addition, an almost linear relation has been established between the pumped throughput and the number of operating cryopumps. Concerning the burn phase cyclic pumping/regeneration mode it has been found that the total pumped throughput is very close in all possible pump setups and the individual pump throughputs are well balanced. The time-dependent gas network code has been implemented to simulate the ITER dwell phase for various operating scenarios and the temporal evolution of the torus pressure has been presented. It has been established that, the torus pressure at the end of the dwell phase, which is of major importance from the engineering point of view, is independent of the initial torus pressure conditions, while it linearly depends on the initial outgassing rate. In addition, it has been established that, the torus pressure at the end of the dwell phase is inversely proportional to the number of operating pumps in an almost linear manner. Moreover, it has been observed that the required target pressure after the end of the dwell phase is achieved in a wide range of the investigated parameters for the lowest outgassing case. On the contrary, for the highest outgassing case it is only marginally achieved when all six available cryopumps are employed.

In Chapter 7, the developed stochastic 3D aerosol code is presented in detail and validated. The presented code has been based on the well-established DSMC method and in its present state is capable to simulate the transport of a single spherical solid particle suspended in a rarefied gas. The capabilities of the developed code have been

demonstrated and validated via three benchmark prototype flow configurations. In the first benchmark, a solid particle suspended in a rarefied gas confined between two parallel plates with slightly unequal temperatures has been considered. The heat flux between the two plates, as well as the thermophoretic force exerted on the particle due to the imposed temperature gradient have been provided. In addition, a simple approximate expression for the thermophoretic parameter, which tends to the correct analytical values in the free-molecular and viscous regimes has been proposed. The obtained results have shown an excellent agreement with the ones reported in the literature, as well as, with the closed form approximate expressions proposed in the literature and in the present work. In the second and third benchmarks, the translational and rotational Brownian motion of a spherical solid particle suspended in a rarefied gas in the free-molecular regime have been considered, respectively. The translational velocity and displacement distributions, as well as the rotational ones have been presented and have been found to be in excellent agreement with the analytical free-molecular solution. In addition, the translational and rotational diffusion coefficients have been computed with respect to the particle radius and excellent agreement has been observed with the analytical free-molecular expressions.

Overall, certain advancements in kinetic modeling have been made and advanced software tools to model and simulate several diverse subjects related to gaseous transport phenomena in rarefied conditions have been developed. It is hoped that, the present work will prove to be useful, at some extend, to the scientific rarefied gas community and also support the design and optimization of several applications, devices and systems in gaseous microsystems, vacuum engineering and fusion technology.

8.2 Future work

The work of the present Ph.D. dissertation covers a broad range of gaseous transport phenomena far from local equilibrium and may be further extended in several directions outlined here.

The solution of the Boltzmann equation may be extended to more complex pressure and temperature driven flow configurations, such as in circular tubes and rectangular ducts. In addition, in these configurations the Cercignani-Lampis reflection law, which describes the gas-surface interaction via two accommodation coefficients, may be applied along with the Boltzmann equation in order to investigate more accurately the impact of gas-surface interaction on the quantities of interest, such as the mass

and heat flow rates. In addition, the solution of the Boltzmann equation may be advanced to more realistic intermolecular potentials, such as the Lennard-Jones and ab initio potentials. Moreover, the simulation of binary gas mixtures via the exact Boltzmann equation may be of interest since recently high discrepancies have been reported between the linearized Boltzmann equation and the McCormack model, which is one of the most widely used kinetic models for gas mixtures.

The investigation of rarefied gas flows through channels with permeable walls may be extended to simulate the planar force driven fully-developed flow between two infinite parallel permeable plates via nonlinear kinetic modeling. This flow configuration is particularly interesting since an arbitrary injection/suction velocity magnitude can be investigated and may be used to validate the peculiar behavior of the mechanocaloric and thermal creep coefficients in the linear case that has been examined in the present work. In addition, nonlinear modeling of rarefied gas flows coupled with injection and suction will allow the simulation of more complex flow configurations, such as circular tubes and ducts where the cross-flow velocity is not constant.

Currently, the steady-state gas distribution system code ARIADNE and the hybrid time-dependent code constitute fully integrated software tools, which in principal can be applied for the simulation, design and optimization of any vacuum system. The modeling and simulation of the exhaust system of operating fusion reactor facilities, such as JET and comparison of the obtained numerical results with in-situ measurements is of interest and will fully demonstrate the capabilities of the presented codes. The developed codes may be further extended to tackle non-isothermal gas networks, by taking into consideration the gas transport that occurs in the network due to temperature gradients. Another possible code advancement is the addition of non-constant cross-section piping elements in the code, such as bellows, which are very common in many vacuum systems. The existing codes may be further advanced with the implementation of optimization subroutines for optimal sensor placement and leak detection. In addition, the developed gas network codes may be parallelized in order to be able to tackle even larger gas distribution systems.

In its current state, the developed 3D DSMC aerosol code may be used to simulate any flow configuration involving the transport of a single spherical solid particle suspended in a rarefied gas. The investigation of the inverse Magnus effect that has been observed under rarefied conditions for a rotating cylinder may also be investigated with the presented code for a rotating sphere. In addition, the present aerosol code may be implemented in complex thermophoretic trapping contraptions, where a solid

particle levitates due to the imposed temperature fields. The developed code may be further extended to simulate the transport of a solid particle suspended in polyatomic gases and gas mixtures. In addition, the simulation of multiple solid particles that interact with the background gas and with each other through gas-solid and solid-solid collisions may be added in the future. Furthermore, more complex processes, such as the absorption and desorption of gas from the solid particle surface, as well as, the agglomeration and deposition of solid particles may be implemented.

Appendix A

Analytical hydrodynamic and slip solution for the oscillatory planar Poiseuille flow

At the viscous and slip regimes ($\delta \gg 1$ and $\theta \gg 1$) the oscillatory planar fully-developed Poiseuille flow is governed by the x-momentum equation [128]:

$$\tilde{\rho}\frac{\partial \tilde{u}^{(j)}\left(\tilde{t},\tilde{y}\right)}{\partial \tilde{t}} = -\frac{dP\left(\tilde{x}\right)}{d\tilde{x}}e^{-i\omega\tilde{t}} + \tilde{\mu}\frac{\partial^2 \tilde{u}^{(j)}\left(\tilde{t},\tilde{y}\right)}{\partial \tilde{y}^2} \tag{A.1}$$

The quantities $\tilde{\rho}$ and $\tilde{\mu}$ are the gas density and viscosity, $\tilde{u}\left(\tilde{t},\tilde{y}\right)$ denotes the macroscopic velocity, while the superscript $j = h, s$ denotes the hydrodynamic and slip regimes, respectively. Applying the complex notation in Eq. (3.75) for the velocity and the dimensionless quantities defined in Eqs. (3.71)-(3.74), the x-momentum equation yields

$$\frac{\partial^2 u^{(j)}\left(y\right)}{\partial y^2} + 2\frac{\delta^2}{\theta}u^{(j)}\left(y\right)i = -\delta. \tag{A.2}$$

In the hydrodynamic regime ($j = h$) the no-slip boundary conditions apply at the two infinite plates

$$u^{(h)}\left(\pm\frac{1}{2}\right) = 0. \tag{A.3}$$

Then, Eq. (A.2) subject to (A.3) can be solved analytically to provide the velocity and shear stress distributions, as well as, the Poiseuille coefficient given by

$$u^{(h)}(y) = i\frac{\theta}{2\delta}\left[1 - \frac{\cos(Ay)}{\cos(A/2)}\right], \tag{A.4}$$

$$\Pi_{xy}{}^{(h)}(y) = -i\frac{\theta A}{2\delta^2}\frac{\sin(Ay)}{\cos(A/2)}, \tag{A.5}$$

$$G^{(h)}(\delta,\theta) = i\frac{\theta}{\delta}\left[\frac{2\tan(A/2)}{A} - 1\right], \tag{A.6}$$

respectively, where $A = (1+i)\delta\big/\sqrt{\theta}$. It can be easily verified that the above expressions tend to the steady-state ones as the oscillation parameter $\theta \to \infty$:

$$u^{(h)}(y) = \frac{\delta}{8}\left(4y^2 - 1\right), \quad \Pi_{xy}^{(h)}(y) = y, \quad G(\delta,\theta) = \frac{\delta}{6} \tag{A.7}$$

In the slip regime Eq. (A.2) is subject to the slip boundary condition

$$u^{(s)}\left(\pm\frac{1}{2}\right) = \mp\frac{\sigma_P}{\delta}\left.\frac{du^{(s)}}{dy}\right|_{\pm\frac{1}{2}}, \tag{A.8}$$

where σ_P is the viscous slip coefficient. Equation (A.2) subject to the boundary conditions (A.8) is then solved analytically to obtain the velocity and shear stress distributions and the Poiseuille coefficient:

$$u^{(s)}(y) = i\frac{\theta}{2\delta}\left[1 - \frac{\cos(Ay)}{\cos(A/2) - \frac{\sigma_P}{\delta}A\sin(A/2)}\right] \tag{A.9}$$

$$\Pi_{xy}{}^{(s)}(y) = i\frac{\theta A}{2\delta^2}\left[\frac{\sin(Ay)}{\cos(A/2) - \frac{\sigma_P}{\delta}A\sin(A/2)}\right] \tag{A.10}$$

$$G^{(s)}(\delta,\theta) = i\frac{\theta}{\delta}\left[\frac{2}{\cot(A/2) - \frac{\sigma_P}{\delta}A} - 1\right] \tag{A.11}$$

It is readily deduced that, the above expressions tend to the steady-state ones as $\theta \to \infty$:

$$u^{(h)}(y) = \frac{\delta}{8}\left(4y^2 - 1\right) + \frac{\sigma_P}{2}, \quad \Pi_{xy}^{(h)}(y) = y, \quad G(\delta,\theta) = \frac{\delta}{6} + \sigma_P \tag{A.12}$$

Appendix B

Onsager-Casimir reciprocity relation for the thermal creep and mechanocaloric coefficients for arbitrary injection velocity

In order to derive the Onsager-Casimir reciprocity relations the formalism in [33, 191] is followed. The linearized Boltzmann equation is given in the form

$$\boldsymbol{\xi} \cdot \frac{\partial h\left(\tilde{\boldsymbol{r}}, \boldsymbol{\xi}\right)}{\partial \tilde{\boldsymbol{r}}} = \hat{L}\left(h\right) + g\left(\tilde{\boldsymbol{r}}, \boldsymbol{\xi}\right), \tag{B.1}$$

where $\tilde{\boldsymbol{r}}$ is the spatial vector, h is the perturbation from the Maxwellian distribution, $\hat{L}$ is the linearized collision operator and g is the source function. On a solid surface restricting the flow the boundary condition in the general form is written as

$$h^{+} = \hat{A}h^{-} + h_w + \hat{A}h_w. \tag{B.2}$$

Here, the plus and minus signs denote quantities arriving and departing from the solid surface, respectively, h_w is the perturbation from the surface Maxwellian and $\hat{A}$ is the scattering operator defined as

$$\hat{A}h = \frac{1}{\left|\boldsymbol{\xi}^{+} \cdot \boldsymbol{n}\right|} \int \left|\boldsymbol{\xi}^{-} \cdot \boldsymbol{n}\right| \tilde{f}_0^M\left(\boldsymbol{\xi}^{-}\right) R_0\left(\boldsymbol{\xi}^{-}, \boldsymbol{\xi}^{+}\right) d\boldsymbol{\xi}^{-}, \tag{B.3}$$

where the quantity $R_0\left(\boldsymbol{\xi}^-, \boldsymbol{\xi}^+\right)$ is the linearized scattering kernel. It is noted here that, the global Maxwellian is written as

$$\tilde{f}_0^M = \frac{n_0}{\pi^{3/2} v_0^3} \exp\left[-\left(\frac{\boldsymbol{\xi} - \tilde{\boldsymbol{U}}_w}{v_0}\right)^2\right], \quad \tilde{\boldsymbol{U}}_w = (U_{w,n}, 0, 0)\,. \tag{B.4}$$

In the case of a stationary permeable wall where the gas has a fixed macroscopic velocity $\tilde{U}_{w,n}$ normal to the wall the linearized scattering kernel reads as

$$R_0\left(\boldsymbol{\xi}^-, \boldsymbol{\xi}^+\right) = \frac{2\left|\boldsymbol{\xi}^+ \cdot \boldsymbol{n}\right| \mathrm{e}^{-\frac{\left(\xi^+ - \tilde{U}_w\right)^2}{v_0^2}}}{\pi v_0^4 \left\{ e^{-\left(\frac{\tilde{U}_{w,n}}{v_0}\right)^2} + \tilde{U}_{w,n} \frac{\sqrt{\pi}}{v_0} \left[1 + \operatorname{erf}\left(\frac{\tilde{U}_{w,n}}{v_0}\right)\right] \right\}}. \tag{B.5}$$

Then, the useful scalar products

$$(\varphi, \psi) = \int \varphi\left(\boldsymbol{\xi}\right) \tilde{f}_0^M\left(\boldsymbol{\xi}\right) \psi\left(\boldsymbol{\xi}\right) d\boldsymbol{\xi}, \tag{B.6}$$

$$((\varphi, \psi)) = \int_\Omega (\varphi, \psi)\, d\Omega, \tag{B.7}$$

$$(\varphi, \psi)_B = \int\limits_{|\boldsymbol{\xi}\cdot\boldsymbol{n}| \geqslant 0} |\boldsymbol{\xi} \cdot \boldsymbol{n}|\, \varphi\left(\boldsymbol{\xi}\right) \tilde{f}_0^M\left(\boldsymbol{\xi}\right) \psi\left(\boldsymbol{\xi}\right) d\boldsymbol{\xi}, \tag{B.8}$$

with Ω denoting the gas domain, are introduced.

When a set of small parameters X_k is used for linearization the functions g, h_w and h may be written as

$$g = \sum_{k=1}^{N} g_k X_k, \quad h_w = \sum_{k=1}^{N} h_{w,k} X_k, \quad h = \sum_{k=1}^{N} h_k X_k \tag{B.9}$$

and the Boltzmann equation reads as

$$\boldsymbol{\xi} \cdot \frac{\partial h_k}{\partial \tilde{\boldsymbol{r}}} = \hat{L} h_k + g_k, \quad g_k = -\boldsymbol{\xi} \cdot \frac{\partial h_{R,k}}{\partial \tilde{\boldsymbol{r}}}. \tag{B.10}$$

The linearized Boltzmann collision operator is defined as

$$\hat{L}h = \iiint \tilde{f}_0^M\left(\boldsymbol{\xi}_1\right) \left[h\left(\boldsymbol{\xi'}_1\right) + h\left(\boldsymbol{\xi'}\right) - h\left(\boldsymbol{\xi}_1\right) - h\left(\boldsymbol{\xi}\right)\right] w\left(\boldsymbol{\xi'}, \boldsymbol{\xi'}_1; \boldsymbol{\xi}, \boldsymbol{\xi}_1\right) d\boldsymbol{\xi'} \boldsymbol{\xi'}_1 d\boldsymbol{\xi}_1, \tag{B.11}$$

where $w\left(\boldsymbol{\xi}', \boldsymbol{\xi}'_1; \boldsymbol{\xi}, \boldsymbol{\xi}_1\right)$ is the probability density of a transition from pre-collision velocities $\boldsymbol{\xi}, \boldsymbol{\xi}_1$ to post-collision velocities $\boldsymbol{\xi}', \boldsymbol{\xi}'_1$ in a binary collision. Introduce the time-reverse operator $\hat{T}$, which in the case of a monatomic gas particle just changes the sign of the molecular velocity. It can be shown that the operator $\hat{T}\hat{L}$ is self-adjoint

$$\left(\hat{T}\hat{L}\varphi, \psi\right) = \left(\hat{T}\hat{L}\psi, \varphi\right) \tag{B.12}$$

and that the linearized scattering kernel satisfies the reciprocal relation

$$-\left|\boldsymbol{\xi}^- \cdot \boldsymbol{n}\right| \tilde{f}_0^M\left(\boldsymbol{\xi}^-\right) R_0\left(\boldsymbol{\xi}^-, \boldsymbol{\xi}^+\right) = \left|\boldsymbol{\xi}^+ \cdot \boldsymbol{n}\right| \tilde{f}_0^M\left(\boldsymbol{\xi}^+\right) R_0\left(-\boldsymbol{\xi}^+, -\boldsymbol{\xi}^-\right). \tag{B.13}$$

Then, using Eq. (B.13) it can be shown that the scattering operator $\hat{A}$ satisfies:

$$\left(\hat{T}\varphi, \hat{A}\psi\right)_B = \left(\hat{T}\psi, \hat{A}\varphi\right)_B \tag{B.14}$$

The kinetic coefficients and the time-reverse ones are introduced:

$$\Lambda_{kn} = \left(\left(g_k, h_k\right)\right) + \int\limits_{\Sigma_w} \left(\left|\boldsymbol{\xi} \cdot \boldsymbol{n}\right| h_{w,k}, h_n\right) d\Sigma + \frac{1}{2} \int\limits_{\Sigma_g} \left(\left|\boldsymbol{\xi} \cdot \boldsymbol{n}\right| h_k, h_n\right) d\Sigma \tag{B.15}$$

$$\Lambda^t_{kn} = \left(\left(\hat{T} g_k, h_k\right)\right) + \int\limits_{\Sigma_w} \left(\hat{T}\left|\boldsymbol{\xi} \cdot \boldsymbol{n}\right| h_{w,k}, h_n\right) d\Sigma + \frac{1}{2} \int\limits_{\Sigma_g} \left(\hat{T}\left|\boldsymbol{\xi} \cdot \boldsymbol{n}\right| h_k, h_n\right) d\Sigma \tag{B.16}$$

Here Σ_W and Σ_g denote the solid and imaginary boundaries confining the gas. The properties (B.12) and (B.14) are necessary and sufficient to prove the Onsager-Casimir reciprocity relations in the form:

$$\Lambda^t_{kn} = \Lambda^t_{nk} \tag{B.17}$$

In the planar Poiseuille and thermal creep flows with injection/suction, the surface Maxwellian perturbations and the source functions are defined as

$$h_{w,P} = 0, \;\; h_{w,T} = 0, \;\; g_P = -\frac{\xi_x}{H}, \;\; g_T = -\frac{\xi_x}{H}\left[\frac{m\left(\boldsymbol{\xi} - \tilde{\boldsymbol{U}}_w\right)^2}{2k_B T_0} - \frac{5}{2}\right]. \tag{B.18}$$

In this particular case the kinetic coefficients can be written as

$$\Lambda_{PT} = -\Lambda^t_{PT} = -\frac{n_0 v_0}{2} G_T, \;\; \Lambda_{TP} = -\Lambda^t_{TP} = -\frac{n_0 v_0}{2} Q_P. \tag{B.19}$$

Thus, using Eqs. (B.17) and (B.19) it is readily seen that $G_T = Q_P$.

Bibliography

[1] K. Moe, M. M. Moe, and S. D. Wallace. Improved Satellite Drag Coefficient Calculations from Orbital Measurements of Energy Accommodation. *Journal of Spacecraft and Rockets*, 35(3), 266–272, 1998.

[2] P. A. Gnoffo. Planetary-entry Gas Dynamics. *Annual Review of Fluid Mechanics*, 31(1), 459–494, 1999.

[3] K. Jousten, editor. *Handbook of Vacuum Technology*. Wiley-VCH Verlag GmbH Co. KGaA, Weinheim, Germany, 2016.

[4] F. Sharipov, Y. Yang, J. E. Ricker, and J. H. Hendricks. Primary pressure standard based on piston-cylinder assemblies. Calculation of effective cross sectional area based on rarefied gas dynamics. *Metrologia*, 53(5), 1177–1184, 2016.

[5] S. Naris, N. Vasileiadis, D. Valougeorgis, A. S. Hashad, and W. Sabuga. Computation of the effective area and associated uncertainties of non-rotating piston gauges FPG and FRS. *Metrologia*, 56(1), 015004, 2019.

[6] F. Sharipov. Numerical simulation of turbomolecular pump over a wide range of gas rarefaction. *Journal of Vacuum Science Technology A: Vacuum, Surfaces, and Films*, 28(6), 1312–1315, 2010.

[7] S. Giors, L. Campagna, and E. Emelli. New spiral molecular drag stage design for high compression ratio, compact turbomolecular-drag pumps. *Journal of Vacuum Science Technology A: Vacuum, Surfaces, and Films*, 28(4), 931–936, 2010.

[8] S. Naris, C. Tantos, and D. Valougeorgis. Kinetic modeling of a tapered Holweck pump. *Vacuum*, 109, 341–348, 2014.

[9] J. Jimenez. LHC: The world's largest vacuum systems being operated at CERN. *Vacuum*, 84(1), 2–7, 2009.

[10] R. J. Pearce, A. Antipenkov, J. L. Bersier, B. Boussier, S. Bryan, M. Dremel, S. Hughes, I. Sekachev, L. Worth, L. Baylor, W. Gardner, S. Meitner, P. Wikus, R. Laesser, and S. Papastergiou. Gas species, their evolution and segregation through the ITER vacuum systems. *Vacuum*, 86(11), 1725–1730, 2012.

[11] R. J. Pearce, A. Antipenkov, B. Boussier, S. Bryan, M. Dremel, B. Levesy, C. Mayaux, and M. Wykes. The ITER divertor pumping system, design evolution, simplification and performance. *Fusion Engineering and Design*, 88(6-8), 809–813, 2013.

[12] M. Rebaï, M. Prat, M. Meireles, P. Schmitz, and R. Baclet. A semi-analytical model for gas flow in pleated filters. *Chemical Engineering Science*, 65(9), 2835–2846, 2010.

[13] A. S. Kovvali, S. Vemury, K. R. Krovvidi, and A. A. Khan. Models and analyses of membrane gas permeators. *Journal of Membrane Science*, 73(1), 1–23, 1992.

[14] S. P. Lim, X. Tan, and K. Li. Gas/vapour separation using membranes: Effect of pressure drop in lumen of hollow fibres. *Chemical Engineering Science*, 55(14), 2641–2652, 2000.

[15] M. Le Digabel, D. Ducret, C. Laquerbe, P. Perriat, and J. C. Niepce. Application of gas separation membranes to detritiation systems. *Desalination*, 148(1-3), 297–302, 2002.

[16] M. Le Digabel, P. Truan, D. Ducret, C. Laquerbe, P. Perriat, J. Niepce, and T. Pelletier. Glovebox atmosphere detritiation process using gas separation membranes. *Fusion Engineering and Design*, 69(1-4), 61–65, 2003.

[17] C. Pozrikidis. Stokes flow through a permeable tube. *Archive of Applied Mechanics*, 80(4), 323–333, 2010.

[18] M. Kahshan, D. Lu, and M. Rahimi-Gorji. Hydrodynamical study of flow in a permeable channel: Application to flat plate dialyzer. *International Journal of Hydrogen Energy*, 44(31), 17041–17047, 2019.

[19] M. A. Gallis, J. R. Torczynski, and D. J. Rader. An approach for simulating the transport of spherical particles in a rarefied gas flow via the direct simulation Monte Carlo method. *Physics of Fluids*, 13(11), 3482–3492, 2001.

[20] M. A. Gallis, D. J. Rader, and J. R. Torczynski. Thermophoresis in Rarefied Gas Flows. *Aerosol Science and Technology*, 36(12), 1099–1117, 2002.

[21] M. A. Gallis, D. J. Rader, and J. R. Torczynski. A generalized approximation for the thermophoretic force on a free-molecular particle. *Aerosol Science and Technology*, 38(7), 692–706, 2004.

[22] D. K. Mansfield, D. W. Johnson, B. Grek, H. W. Kugel, M. G. Bell, R. E. Bell, R. V. Budny, C. E. Bush, E. D. Fredrickson, K. W. Hill, D. L. Jassby, R. J. Maqueda, H. K. Park, A. T. Ramsey, E. J. Synakowski, G. Taylor, and G. A. Wurden. Observations concerning the injection of a lithium aerosol into the edge of TFTR discharges. *Nuclear Fusion*, 41(12), 1823–1834, 2001.

[23] A. Y. Pigarov, S. I. Krasheninnikov, T. K. Soboleva, and T. D. Rognlien. Dust-particle transport in tokamak edge plasmas. *Physics of Plasmas*, 12(12), 122508, 2005.

[24] N. Taylor, B. Merrill, L. Cadwallader, L. Di Pace, L. El-Guebaly, P. Humrickhouse, D. Panayotov, T. Pinna, M. T. Porfiri, S. Reyes, M. Shimada, and S. Willms. Materials-related issues in the safety and licensing of nuclear fusion facilities. *Nuclear Fusion*, 57(9), 2017.

[25] C. Grisolia, F. Gensdarmes, S. Peillon, G. Dougniaux, E. Bernard, A. Autricque, G. Pieters, B. Rousseau, S. Feuillastre, S. Garcia-Argote, O. Carvalho, V. Malard, I. George, L. Lebaron-Jacobs, T. Orsiere, C. Uboldi, J. Rose, M. Sanles Sobrido, D. Lambertin, D. Vrel, C. Decanis, K. Liger, T. Acsente, and G. Dinescu. Current investigations on tritiated dust and its impact on tokamak safety. *Nuclear Fusion*, 59(8), 086061, 2019.

[26] P. L. Bhatnagar, E. P. Gross, and M. Krook. A Model for Collision Processes in Gases. I. Small Amplitude Processes in Charged and Neutral One-Component Systems. *Physical Review*, 94(3), 511–525, 1954.

[27] E. M. Shakhov. Generalization of the Krook kinetic relaxation equation. *Fluid Dynamics*, 3(5), 95–96, 1972.

[28] L. H. Holway. New Statistical Models for Kinetic Theory: Methods of Construction. *Physics of Fluids*, 9(9), 1658, 1966.

[29] A. B. Huang. Nonlinear Rarefied Couette Flow with Heat Transfer. *Physics of Fluids*, 11(6), 1321, 1968.

[30] G. A. Bird. *Molecular Gas Dynamics and the Direct Simulation of Gas Flows*. Clarendon, Oxford, 1994.

[31] M. Knudsen. Die Molekularströmung der Gase durch Offnungen und die Effusion. *Annalen der Physik*, 333(5), 999–1016, 1909.

[32] J. H. Ferziger and H. G. Kaper. *Mathematical Theory of Transport Processes in Gases*. North-Holland Publishing Company, Amsterdam, 1972.

[33] F. Sharipov. *Rarefied Gas Dynamics*. Wiley-VCH Verlag GmbH Co. KGaA, Weinheim, 2016.

[34] G. Karniadakis, A. Beskok, and N. Aluru. *Microflows and Nanoflows - Fundamentals and Simulation*. Springer-Verlag, New York, 2005.

[35] J. C. Maxwell. *The Scientific Papers of James Clerk Maxwell*. Cambridge University Press, Cambridge, 2011.

[36] J. C. Maxwell. V. Illustrations of the dynamical theory of gases. —Part I. On the motions and collisions of perfectly elastic spheres. *The London, Edinburgh, and Dublin Philosophical Magazine and Journal of Science*, 19(124), 19–32, 1860.

[37] L. Boltzmann. Weitere Studien über das Wärmegleichgewicht unter Gasmolekülen. In *Kinetische Theorie II*. Vieweg+Teubner Verlag, Wiesbaden, 1970.

[38] C. Shen. *Rarefied Gas Dynamics*. Heat and Mass Transfer. Springer Berlin Heidelberg, Berlin, Heidelberg, 2005.

[39] P. Welander. On The Temperature jump in a rarefied gas. *Ark. Fys.*, 7, 1954.

[40] F. Sharipov and V. Seleznev. Data on internal rarefied gas flows. *Journal of Physical and Chemical Reference Data*, 27(3), 657–706, 1998.

[41] V. A. Rykov. A model kinetic equation for a gas with rotational degrees of freedom. *Fluid Dynamics*, 10(6), 959–966, 1976.

[42] P. Andries, P. Le Tallec, J. P. Perlat, and B. Perthame. The Gaussian-BGK model of Boltzmann equation with small Prandtl number. *European Journal of Mechanics - B/Fluids*, 19(6), 813–830, 2000.

[43] T. F. Morse. Kinetic Model Equations for a Gas Mixture. *Physics of Fluids*, 7(12), 2012, 1964.

[44] B. B. Hamel. Kinetic Model for Binary Gas Mixtures. *Physics of Fluids*, 8(3), 418, 1965.

[45] F. J. McCormack. Construction of linearized kinetic models for gaseous mixtures and molecular gases. *Physics of Fluids*, 16(12), 2095, 1973.

[46] M. Epstein. A model of the wall boundary condition in kinetic theory. *AIAA Journal*, 5(10), 1797–1800, 1967.

[47] C. Cercignani and M. Lampis. Kinetic models for gas-surface interactions. *Transport Theory and Statistical Physics*, 1(2), 101–114, 1971.

[48] R. G. Lord. Some extensions to the Cercignani–Lampis gas–surface scattering kernel. *Physics of Fluids A: Fluid Dynamics*, 3(4), 706–710, 1991.

[49] R. G. Lord. Some further extensions of the Cercignani–Lampis gas–surface interaction model. *Physics of Fluids*, 7(5), 1159–1161, 1995.

[50] D. Valougeorgis and S. Naris. Acceleration Schemes of the Discrete Velocity Method: Gaseous Flows in Rectangular Microchannels. *SIAM Journal on Scientific Computing*, 25(2), 534–552, 2003.

[51] J. Lihnaropoulos, S. Naris, and D. Valougeorgis. Formulation and stability analysis of rapidly convergent iteration schemes for the 2-D linearized BGK equation. *Transport Theory and Statistical Physics*, 36(4-6), 513–528, 2007.

[52] W. Wagner. A convergence proof for Bird's direct simulation Monte Carlo method for the Boltzmann equation. *Journal of Statistical Physics*, 66(3-4), 1011–1044, 1992.

[53] M. Knudsen. Die Gesetze der Molekularströmung und der inneren Reibungsströmung der Gase durch Röhren. *Annalen der Physik*, 333(1), 75–130, 1909.

[54] M. V. Smoluchowski. Zur kinetischen Theorie der Transpiration und Diffusion verdünnter Gase. *Annalen der Physik*, 338(16), 1559–1570, 1910.

[55] P. Clausing. Über die Strömung sehr verdünnter Gase durch Röhren von beliebiger Länge. *Annalen der Physik*, 404(8), 961–989, 1932.

[56] W. C. DeMarcus and E. H. Hopper. Knudsen Flow through a Circular Capillary. *The Journal of Chemical Physics*, 23(7), 1344–1344, 1955.

[57] D. H. Davis. Monte Carlo Calculation of Molecular Flow Rates through a Cylindrical Elbow and Pipes of Other Shapes. *Journal of Applied Physics*, 31(7), 1169–1176, 1960.

[58] D. H. Davis, L. L. Levenson, and N. Milleron. Effect of "Rougher-than-Rough" Surfaces on Molecular Flow through Short Ducts. *Journal of Applied Physics*, 35(3), 529–532, 1964.

[59] W. Steckelmacher. Knudsen flow 75 years on: the current state of the art for flow of rarefied gases in tubes and systems. *Reports on Progress in Physics*, 49(10), 1083–1107, 1986.

[60] C. Cercignani and A. Daneri. Flow of a Rarefied Gas between Two Parallel Plates. *Journal of Applied Physics*, 34(12), 3509–3513, 1963.

[61] S. K. Loyalka, N. Petrellis, and T. S. Storvick. Some exact numerical results for the BGK model: Couette, Poiseuille and thermal creep flow between parallel plates. *Zeitschrift für angewandte Mathematik und Physik ZAMP*, 30(3), 514–521, 1979.

[62] V. G. Chernyak, V. V. Kalinin, and P. E. Suetin. On theory of non-sothermal flow of gas in plane channel. *Inzh.-Fiz. Zh.*, 36(6), 1059–1065, 1979.

[63] T. Ohwada, Y. Sone, and K. Aoki. Numerical analysis of the Poiseuille and thermal transpiration flows between two parallel plates on the basis of the Boltzmann equation for hard-sphere molecules. *Physics of Fluids A*, 1(12), 2042–2049, 1989.

[64] K. A. Hickey and S. K. Loyalka. Plane Poiseuille flow: Rigid sphere gas. *Journal of Vacuum Science Technology A: Vacuum, Surfaces, and Films*, 8(2), 957–960, 1990.

[65] S. K. Loyalka and K. A. Hickey. Kinetic theory of thermal transpiration and the mechanocaloric effect: Planar flow of a rigid sphere gas with arbitrary accommodation at the surface. *Journal of Vacuum Science Technology A: Vacuum, Surfaces, and Films*, 9(1), 158–163, 1991.

[66] C. E. Siewert. The linearized Boltzmann equation: Concise and accurate solutions to basic flow problems. *Zeitschrift fur Angewandte Mathematik und Physik*, 54(2), 273–303, 2003.

[67] F. Sharipov and G. Bertoldo. Poiseuille flow and thermal creep based on the Boltzmann equation with the Lennard-Jones potential over a wide range of the Knudsen number. *Physics of Fluids*, 21(6), 067101, 2009.

[68] C. Cercignani and F. Sernagiotto. Cylindrical Poiseuille Flow of a Rarefied Gas. *Physics of Fluids*, 9(1), 40, 1966.

[69] S. S. Lo and S. K. Loyalka. An efficient computation of near-continuum rarefied gas flows. *ZAMP Zeitschrift fur angewandte Mathematik und Physik*, 33(3), 419–424, 1982.

[70] S. K. Loyalka and S. A. Hamoodi. Poiseuille flow of a rarefied gas in a cylindrical tube: Solution of linearized Boltzmann equation. *Physics of Fluids A*, 2(11), 2061–2065, 1990.

[71] F. Sharipov. Rarefied gas flow through a long tube at any temperature ratio. *Journal of Vacuum Science Technology A: Vacuum, Surfaces, and Films*, 14(4), 2627–2635, 1996.

[72] S. Varoutis, S. Naris, V. Hauer, C. Day, and D. Valougeorgis. Computational and experimental study of gas flows through long channels of various cross sections in the whole range of the Knudsen number. *Journal of Vacuum Science Technology A: Vacuum, Surfaces, and Films*, 27(1), 89–100, 2009.

[73] F. Sharipov. Rarefied gas flow through a long rectangular channel. *Journal of Vacuum Science Technology A: Vacuum, Surfaces, and Films*, 17(5), 3062–3066, 1999.

[74] F. Sharipov. Non-isothermal gas flow through rectangular microchannels. *Journal of Micromechanics and Microengineering*, 9(4), 394–401, 1999.

[75] I. Graur and F. Sharipov. Gas flow through an elliptical tube over the whole range of the gas rarefaction. *European Journal of Mechanics - B/Fluids*, 27(3), 335–345, 2008.

[76] S. Naris and D. Valougeorgis. Rarefied gas flow in a triangular duct based on a boundary fitted lattice. *European Journal of Mechanics - B/Fluids*, 27(6), 810–822, 2008.

[77] L. Szalmás and D. Valougeorgis. A fast iterative model for discrete velocity calculations on triangular grids. *Journal of Computational Physics*, 229(11), 4315–4326, 2010.

[78] S. Pantazis, D. Valougeorgis, and F. Sharipov. End corrections for rarefied gas flows through capillaries of finite length. *Vacuum*, 97, 26–29, 2013.

[79] S. Pantazis, D. Valougeorgis, and F. Sharipov. End corrections for rarefied gas flows through circular tubes of finite length. *Vacuum*, 101, 306–312, 2014.

[80] S. Pantazis and D. Valougeorgis. Rarefied gas flow through a cylindrical tube due to a small pressure difference. *European Journal of Mechanics - B/Fluids*, 38, 114–127, 2013.

[81] V. Titarev. Rarefied gas flow in a circular pipe of finite length. *Vacuum*, 94, 92–103, 2013.

[82] E. Shakhov. Solution of axisymmetric problems of rarefied gas theory by a finite-difference method. *USSR Computational Mathematics and Mathematical Physics*, 14(4), 147–157, 1974.

[83] H. Taniguchi, M. Ota, and M. Aritomi. Effects of surface boundary conditions on transmission probabilities through circular tubes. *Vacuum*, 47(6-8), 787–790, 1996.

[84] A. Alexeenko, D. Levin, S. Gimelshein, M. Ivanov, and A. Ketsdever. Numerical and experimental study of orifice flow in the transitional regime. In *35th AIAA Thermophysics Conference*, Reston, Virigina, 2001.

[85] F. Sharipov. Numerical simulation of rarefied gas flow through a thin orifice. *Journal of Fluid Mechanics*, 518, 35–60, 2004.

[86] S. Misdanitis, S. Pantazis, and D. Valougeorgis. Pressure driven rarefied gas flow through a slit and an orifice. *Vacuum*, 86(11), 1701–1708, 2012.

[87] O. Sazhin. Gas molecule-molecule interaction and the gas-surface scattering effect on the rarefied gas flow through a slit into a vacuum. *Journal of Experimental and Theoretical Physics*, 108(5), 874–879, 2009.

[88] T. C. Lilly, S. F. Gimelshein, A. D. Ketsdever, and G. N. Markelov. Measurements and computations of mass flow and momentum flux through short tubes in rarefied gases. *Physics of Fluids*, 18(9), 093601, 2006.

[89] S. Varoutis, D. Valougeorgis, and F. Sharipov. Simulation of gas flow through tubes of finite length over the whole range of rarefaction for various pressure drop ratios. *Journal of Vacuum Science Technology A: Vacuum, Surfaces, and Films*, 27(6), 1377–1391, 2009.

[90] J. C. Schönfeld. Analogy of hydraulic, mechanical, acoustic and electric systems. *Applied Scientific Research, Section B*, 3(1), 417–450, 1954.

[91] C. Day, V. Hauer, G. Class, D. Valougeorgis, and M. Wykes. Development of a simulation code for ITER vacuum flows. *IAEA Fusion Energy Conference*, 2006.

[92] C. Day, A. Antipenkov, M. Dremel, H. Haas, V. Hauer, A. Mack, D. Murdoch, and M. Wykes. RD and design for the cryogenic and mechanical vacuum pumping systems of ITER. *Vacuum*, 81(6), 738–747, 2007.

[93] D. Stephenson, D. A. Lockerby, M. K. Borg, and J. M. Reese. Multiscale simulation of nanofluidic networks of arbitrary complexity. *Microfluidics and Nanofluidics*, 18(5-6), 841–858, 2015.

[94] M. K. Borg, D. A. Lockerby, and J. M. Reese. A hybrid molecular-continuum simulation method for incompressible flows in micro/nanofluidic networks. *Microfluidics and Nanofluidics*, 15(4), 541–557, 2013.

[95] M. K. Borg, D. A. Lockerby, and J. M. Reese. A multiscale method for micro/nano flows of high aspect ratio. *Journal of Computational Physics*, 233, 400–413, 2013.

[96] S. Misdanitis and D. Valougeorgis. Design of steady-state isothermal gas distribution systems consisting of long tubes in the whole range of the Knudsen number.

Journal of Vacuum Science Technology A: Vacuum, Surfaces, and Films, 29(6), 061602, 2011.

[97] S. Misdanitis and D. Valougeorgis. Modeling of ITER related vacuum gas pumping distribution systems. *Fusion Engineering and Design*, 88(9-10), 2352–2356, 2013.

[98] C. T. Crowe. *Multiphase Flow Handbook*. CRC Press, Boca Raton, 2005.

[99] E. Cunningham. On the velocity of steady fall of spherical particles through fluid medium. *Proc. R. Soc. Lond.*, 83(563), 357–365, 1910.

[100] P. S. Epstein. On the Resistance Experienced by Spheres in their Motion through Gases. *Physical Review*, 23(6), 710–733, 1924.

[101] M. J. Baines, I. P. Williams, A. S. Asebiomo, and R. L. Agacy. Resistance to the Motion of a Small Sphere Moving Through a Gas. *Monthly Notices of the Royal Astronomical Society*, 130(1), 63–74, 1965.

[102] J. R. Brock. On radiometer forces. *Journal of Colloid and Interface Science*, 25(4), 564–567, 1967.

[103] K. Yamamoto and Y. Ishihara. Thermophoresis of a spherical particle in a rarefied gas of a transition regime. *Physics of Fluids*, 31(12), 3618, 1988.

[104] S. Loyalka. Thermophoretic force on a single particle—I. Numerical solution of the linearized Boltzmann equation. *Journal of Aerosol Science*, 23(3), 291–300, 1992.

[105] S. Beresnev and V. Chernyak. Thermophoresis of a spherical particle in a rarefied gas: Numerical analysis based on the model kinetic equations. *Physics of Fluids*, 7(7), 1743–1756, 1995.

[106] S. Takata and Y. Sone. Flow induced around a sphere with a non-uniform surface temperature in a rarefied gas, with application to the drag and thermal force problem of a spherical particle with an arbitrary thermal conductivity. *European Journal of Mechanics - B/Fluids*, 14((4)), 487–518, 1995.

[107] V. Chernyak and T. Sograbi. The role of molecule-surface interaction in thermophoresis of an aerosol particle. *Journal of Aerosol Science*, 128, 62–71, 2019.

[108] D. Kalempa and F. Sharipov. Drag and thermophoresis on a sphere in a rarefied gas based on the Cercignani–Lampis model of gas–surface interaction. *Journal of Fluid Mechanics*, 900, A37, 2020.

[109] S. Shrestha, S. Tiwari, A. Klar, and S. Hardt. Numerical simulation of a moving rigid body in a rarefied gas. *Journal of Computational Physics*, 292, 239–252, 2015.

[110] S. Chapman and T. Cowling. *The Mathematical Theory of Non-Uniform Gases*. University Press, Cambridge, 1952.

[111] C. Cercignani. *The Boltzmann Equation and Its Applications*. Springer New York, New York, 1988.

[112] C. L. Pekeris and Z. Alterman. Solution of the Boltzmann-Hilbert Integral Equation Ii. the Coefficients of Viscosity and Heat Conduction. *Proceedings of the National Academy of Sciences*, 43(11), 998–1007, 1957.

[113] C. E. Siewert. On computing the Chapman-Enskog functions for viscosity and heat transfer and the Burnett functions. *Journal of Quantitative Spectroscopy and Radiative Transfer*, 74(6), 789–796, 2002.

[114] L. B. Barichello, P. Rodrigues, and C. E. Siewert. On computing the Chapman-Enskog and Burnett functions. *Journal of Quantitative Spectroscopy and Radiative Transfer*, 86(1), 109–114, 2004.

[115] A. Mohan, R. V. Tompson, K. A. Hickey, and S. K. Loyalka. Chapman-Enskog and Burnett solutions for a simple, rigid-sphere gas: Numerical solutions using a subtraction technique. *Journal of Quantitative Spectroscopy and Radiative Transfer*, 109(5), 741–751, 2008.

[116] F. Sharipov and G. Bertoldo. Numerical solution of the linearized Boltzmann equation for an arbitrary intermolecular potential. *Journal of Computational Physics*, 228(9), 3345–3357, 2009.

[117] A. Tsimpoukis and D. Valougeorgis. Rarefied isothermal gas flow in a long circular tube due to oscillating pressure gradient. *Microfluidics and Nanofluidics*, 22(1), 5, 2018.

[118] A. Tsimpoukis and D. Valougeorgis. Pulsatile pressure driven rarefied gas flow in long rectangular ducts. *Physics of Fluids*, 30(4), 047104, 2018.

[119] T. Doi. Numerical analysis of oscillatory Couette flow of a rarefied gas on the basis of the linearized Boltzmann equation. *Vacuum*, 84(5), 734–737, 2009.

[120] J. Hirschfelder, C. Curtiss, and R. Bird. *The Molecular Theory of Gases and Liquids*. Wiley, New York, 1954.

[121] Y. Sone, T. Ohwada, and K. Aoki. Temperature jump and Knudsen layer in a rarefied gas over a plane wall: Numerical analysis of the linearized Boltzmann equation for hard-sphere molecules. *Physics of Fluids A: Fluid Dynamics*, 1(2), 363–370, 1989.

[122] B. Shizgal. A Gaussian quadrature procedure for use in the solution of the Boltzmann equation and related problems. *Journal of Computational Physics*, 41(2), 309–328, 1981.

[123] W. H. Press, S. A. Teukolsky, T. W. Vetterling, and B. P. Flannery. *Numerical Recipes in FORTRAN: The Art of Scientific Computing*. Cambridge University Press, New York, 1993.

[124] L. Onsager. Reciprocal Relations in Irreversible Processes. I. *Physical Review*, 37(4), 405–426, 1931.

[125] L. Onsager. Reciprocal Relations in Irreversible Processes. II. *Physical Review*, 37(12), 2265–2279, 1931.

[126] H. B. G. Casimir. On Onsager's Principle of Microscopic Reversibility. *Reviews of Modern Physics*, 17(2-3), 343–350, 1945.

[127] S. K. Loyalka. Kinetic theory of thermal transpiration and mechanocaloric effect. I. *The Journal of Chemical Physics*, 55(9), 4497–4503, 1971.

[128] H. Schlichting and K. Gersten. *Boundary-Layer Theory*. Springer Berlin Heidelberg, Berlin, Heidelberg, 2017.

[129] F. Sharipov and D. Kalempa. Oscillatory Couette flow at arbitrary oscillation frequency over the whole range of the Knudsen number. *Microfluidics and Nanofluidics*, 4(5), 363–374, 2008.

[130] A. Tsimpoukis, N. Vasileiadis, G. Tatsios, and D. Valougeorgis. Nonlinear oscillatory fully-developed rarefied gas flow in plane geometry. *Physics of Fluids*, 31(6), 067108, 2019.

[131] F. M. White. *Viscous Fluid Flow*. McGraw-Hill, New York, 1991.

[132] M. Zamir. *The Physics of Pulsatile Flow*. Springer New York, New York, 2000.

[133] R. L. Panton. *Incompressible Flow*. John Wiley Sons, Inc., Hoboken, NJ, USA, 2013.

[134] A. S. Berman. Laminar flow in channels with porous walls. *Journal of Applied Physics*, 24(9), 1232–1235, 1953.

[135] J. R. Sellars. Laminar Flow in Channels with Porous Walls at High Suction Reynolds Numbers. *Journal of Applied Physics*, 26(4), 489–490, 1955.

[136] S. W. Yuan. Further investigation of laminar flow in channels with porous walls. *Journal of Applied Physics*, 27(3), 267–269, 1956.

[137] T. Wah. Laminar Flow in a Uniformly Porous Channel. *Aeronautical Quarterly*, 15(3), 299–310, 1964.

[138] R. M. Terrill. Laminar Flow in a Uniformly Porous Channel with Large Injection. *Aeronautical Quarterly*, 16(4), 323–332, 1965.

[139] R. M. Terrill and P. W. Thomas. On laminar flow through a uniformly porous pipe. *Applied Scientific Research*, 21(1), 37–67, 1969.

[140] A. S. Berman. Laminar flow in an annulus with porous walls. *Journal of Applied Physics*, 29(1), 71–75, 1958.

[141] J. Majdalani. A hybrid multiple scale procedure for boundary layers involving several dissimilar scales. *Zeitschrift für angewandte Mathematik und Physik*, 49(6), 849–868, 1998.

[142] J. Majdalani. The oscillatory channel flow with arbitrary wall injection. *Zeitschrift für angewandte Mathematik und Physik*, 52(1), 33–61, 2001.

[143] P. C. Hsieh, P. Y. Hsu, and Y. T. Lin. Analytical Solution to Uniform Flow over a Porous Plane with Downward Suction. *Journal of Engineering Mechanics*, 142(9), 04016061, 2016.

[144] M. Rasoulzadeh and M. Panfilov. Asymptotic solution to the viscous/inertial flow in wavy channels with permeable walls. *Physics of Fluids*, 30(10), 106604, 2018.

[145] M. Rashevski and S. Slavtchev. Heat transfer in laminar viscous flow in a channel with one porous wall. *European Journal of Mechanics - B/Fluids*, 82, 11–20, 2020.

[146] N. Vasileiadis, G. Tatsios, and D. Valougeorgis. Pressure and temperature driven fully-developed rarefied gas flow in a channel with uniform injection/suction through its permeable walls. *Vacuum*, 188, 110155, 2021.

[147] N. Vasileiadis, G. Tatsios, S. Misdanitis, and D. Valougeorgis. Modeling of complex gas distribution systems operating under any vacuum conditions: Simulations of the ITER divertor pumping system. *Fusion Engineering and Design*, 103, 125–135, 2016.

[148] N. Vasileiadis and D. Valougeorgis. Modeling of time-dependent gas pumping networks in the whole range of the Knudsen number: Simulation of the ITER dwell phase. *Fusion Engineering and Design*, 151, 111383, 2020.

[149] K. Jousten, S. Pantazis, J. Buthig, R. Model, M. Wüest, and J. Iwicki. A standard to test the dynamics of vacuum gauges in the millisecond range. *Vacuum*, 100, 14–17, 2014.

[150] M. Vargas, S. Naris, D. Valougeorgis, S. Pantazis, and K. Jousten. Time-dependent rarefied gas flow of single gases and binary gas mixtures into vacuum. *Vacuum*, 109, 385–396, 2014.

[151] R. Kersevan and J. L. Pons. Introduction to MOLFLOW+ : New graphical processing unit-based Monte Carlo code for simulating molecular flows and for calculating angular coefficients in the compute unified device architecture environment. *Journal of Vacuum Science Technology A: Vacuum, Surfaces, and Films*, 27(4), 1017–1023, 2009.

[152] J. M. Hammersley and D. C. Handscomb. Monte Carlo Methods. In *Methuen's monographs on applied probability and statistics*. Menthuen Co, London, 1964.

[153] F. Sharipov and I. Graur. General approach to transient flows of rarefied gases through long capillaries. *Vacuum*, 100, 22–25, 2014.

[154] D. Valougeorgis, N. Vasileiadis, and V. Titarev. Validity range of linear kinetic modeling in rarefied pressure driven single gas flows through circular capillaries. *European Journal of Mechanics - B/Fluids*, 64, 2–7, 2017.

[155] F. Sharipov and V. Seleznev. Rarefied gas flow through a long tube at any pressure ratio. *Journal of Vacuum Science Technology A: Vacuum, Surfaces, and Films*, 12(5), 2933–2935, 1994.

[156] S. Varoutis, D. Valougeorgis, O. Sazhin, and F. Sharipov. Rarefied gas flow through short tubes into vacuum. *Journal of Vacuum Science Technology A: Vacuum, Surfaces, and Films*, 26(2), 228–238, 2008.

[157] S. Pantazis. *Simulation of Transport Phenomena*. Ph.d. dissertation, University of Thessaly, Volos, 2011.

[158] V. Titarev and E. Shakhov. Computational study of a rarefied gas flow through a long circular pipe into vacuum. *Vacuum*, 86(11), 1709–1716, 2012.

[159] S. Pantazis, S. Naris, C. Tantos, D. Valougeorgis, J. André, F. Millet, and J. P. Perin. Nonlinear vacuum gas flow through a short tube due to pressure and temperature gradients. *Fusion Engineering and Design*, 88(9-10), 2384–2387, 2013.

[160] J. Xu, P. S. Fischbeck, M. J. Small, J. M. VanBriesen, and E. Casman. Identifying Sets of Key Nodes for Placing Sensors in Dynamic Water Distribution Networks. *Journal of Water Resources Planning and Management*, 134(4), 378–385, 2008.

[161] N. Deo. Graph Theory with Applications to Engineering and Computer Science. *Networks*, 5(3), 299–300, 1975.

[162] M. Vargas, S. Naris, D. Valougeorgis, S. Pantazis, and K. Jousten. Hybrid modeling of time-dependent rarefied gas expansion. *Journal of Vacuum Science Technology A: Vacuum, Surfaces, and Films*, 32(2), 021602, 2014.

[163] A. Ribes and C. Caremoli. Salome platform component model for numerical simulation. In *31st Annual International Computer Software and Applications Conference*. IEEE, 2007.

[164] ISO, IEC, BIPM, and OIML. Guide to the Expression of Uncertainty in Measurement, 1995.

[165] G. Tatsios and D. Valougeorgis. Uncertainty analysis of computed flow rates and pressure differences in rarefied pressure and temperature driven gas flows through long capillaries. *European Journal of Mechanics - B/Fluids*, 79, 190–201, 2020.

[166] A. J. H. Donné. The European roadmap towards fusion electricity. *Philosophical Transactions of the Royal Society A: Mathematical, Physical and Engineering Sciences*, 377(2141), 20170432, 2019.

[167] V. Hauer and C. Day. ITER divertor gas flow modelling. *Fusion Engineering and Design*, 98-99, 1775–1778, 2015.

[168] G. Pedroche, A. Lopez-Revelles, A. Kolsek, M. Dremel, G. Bansal, R. Pearce, J. Sanz, and R. Juarez. Nuclear analysis of the ITER torus cryopumps. *Nuclear Fusion*, 59(10), 106045, 2019.

[169] C. Gleason-González, S. Varoutis, V. Hauer, and C. Day. Simulation of neutral gas flow in a tokamak divertor using the Direct Simulation Monte Carlo method. *Fusion Engineering and Design*, 89(7-8), 1042–1047, 2014.

[170] V. Hauer and C. Day. Conductance modelling of ITER vacuum systems. *Fusion Engineering and Design*, 84(2-6), 903–907, 2009.

[171] M. Wykes, P. Andrew, C. Day, and G. Federici. Assessment of the ITER dwell pump-down. *Proceedings Symposium on Fusion Engineering*, 2005.

[172] V. Philipps and J. Ehrenberg. Analysis of outgassing after Joint European Torus discharges under beryllium first wall conditions. *Journal of Vacuum Science Technology A: Vacuum, Surfaces, and Films*, 11(2), 437–445, 1993.

[173] A. Santucci, M. Incelli, A. Hollingsworth, X. Lefebvre, and Z. Kollo. Tritium retention and outgassing from JET first wall materials due to tritiated atmosphere exposure: the Tritium Soaking Facility. *22nd International Conference on Plasma Surface Interactions in Controlled Fusion Devices*, 2016.

[174] S. Brezinsek et al. Fuel retention studies with the ITER-Like Wall in JET. *Nuclear Fusion*, 53(8), 083023, 2013.

[175] V. Philipps, T. Loarer, H. Esser, S. Vartanian, U. Kruezi, S. Brezinsek, and G. Matthews. Dynamic fuel retention and release under ITER like wall conditions in JET. *Journal of Nuclear Materials*, 438, 1067–1071, 2013.

[176] F. S. Sherman. A Survey of Experimental Results and Methods for the Transition Regime of Rarefied Gas Dynamics. In *Rarefied Gas Dynamics Vol. II*, New York, 1963. Press, Academic.

[177] S. K. Loyalka. Motion of a sphere in a gas: Numerical solution of the linearized Boltzmann equation. *Physics of Fluids A: Fluid Dynamics*, 4(5), 1049–1056, 1992.

[178] K. Koura and H. Matsumoto. Variable soft sphere molecular model for inverse-power-law or Lennard-Jones potential. *Physics of Fluids A: Fluid Dynamics*, 3(10), 2459–2465, 1991.

[179] C. Ericson. *Real-Time Collision Detection*. CRC Press, Boca Raton, 2004.

[180] S. Strobl, A. Formella, and T. Pöschel. Exact calculation of the overlap volume of spheres and mesh elements. *Journal of Computational Physics*, 311, 158–172, 2016.

[181] S. Stefanov, P. Gospodinov, and C. Cercignani. Monte Carlo simulation and Navier–Stokes finite difference calculation of unsteady-state rarefied gas flows. *Physics of Fluids*, 10(1), 289–300, 1998.

[182] C. T. Crowe, J. D. Schwarzkopf, M. Sommerfeld, and Y. Tsuji. *Multiphase Flows with Droplets and Particles*. CRC Press, 2011.

[183] L. Waldmann. Über die Kraft eines inhomogenen Gases auf kleine suspendierte Kugeln. *Zeitschrift für Naturforschung A*, 14(7), 589–599, 1959.

[184] H. Vestner. Forces on Small Particles in Nonhomogeneous Polyatomic Gases. *Zeitschrift für Naturforschung A*, 29(9), 1244–1252, 1974.

[185] G. S. Springer. Heat Transfer in Rarefied Gases. In *Advances In Heat Transfer*, pages 163–218. 1971.

[186] M. A. Gallis, D. J. Rader, and J. R. Torczynski. DSMC simulations of the thermophoretic force on a spherical macroscopic particle. In *35th AIAA Thermophysics Conference*, number c, Reston, Virigina, 2001. American Institute of Aeronautics and Astronautics.

[187] G. E. Uhlenbeck and L. S. Ornstein. On the Theory of the Brownian Motion. *Physical Review*, 36(5), 823–841, 1930.

[188] R. Kubo. The fluctuation-dissipation theorem. *Reports on Progress in Physics*, 29(1), 306, 1966.

[189] A. Einstein. *Investigations on the Theory of the Browian Movement.* Dover Publications, Inc., New York, 1st edition, 1956.

[190] P. S. Hubbard. Rotational Brownian Motion. *Physical Review A*, 6(6), 2421–2433, 1972.

[191] F. Sharipov. Onsager-Casimir reciprocal relations based on the Boltzmann equation and gas-surface interaction: Single gas. *Physical Review E*, 73(2), 026110, 2006.